Plasma Physics Reports, Vol. 27, No. 8, 2001, pp. 635–640. Translated from Fizika Plazmy, Vol. 27, No. 8, 2001, pp. 675–679.

MAGNETIC CONFINEMENT SYSTEMS

MHD Stability of a Plasma in an Axisymmetric Open Divertor Configuration

V. V. Arsenin and A. Yu. Kuyanov

Institute of Nuclear Fusion, Russian Research Centre Kurchatov Institute, pl. Kurchatova 1, Moscow, 123182 Russia

Received February 15, 2001; in final form, March 20, 2001

Abstract—For a plasma with $\beta \ll 1$ confined in a system of two simple axisymmetric mirror cells separated by a divertor cell, a radial plasma pressure profile is obtained that is stable against convective modes and drops off to zero at the separatrix. The shape of the marginally stable pressure profile depends on the geometric parameters (such as mirror ratios and the localization of the divertor cell), the ratio of the pressure in the mirrors cells to the pressure in the divertor cell, and the degree of pressure anisotropy. *© 2001 MAIK "Nauka/Interperiodica".*

1. INTRODUCTION

Among the methods for plasma stabilization in axisymmetric open confinement systems (see reviews [1–3]), stabilization by divertors [4–6] is especially attractive because of the simplicity and universality (roughness) of the main stabilizing effect [5, 6] and the possibility of placing the required number of stabilizers (divertors) at desired positions along the system (in contrast to, e.g., a cusp stabilizer, which can only be installed at the end of the device). Such stabilizers can also be used in systems with closed magnetic field lines, in which cusp stabilizers cannot be installed. The stabilizing effect of the divertor was observed in experiments on the TARA [7] and HIEI [8] devices.

Divertor stabilization has one point in common with the average minimum-B stabilization: the contribution of the stabilizing element to the potential energy W of the perturbation competes with that of the adjacent mirror cells. On the other hand, there is an important difference between these stabilization methods. In an average minimum-B mirror system, the cells with favorable magnetic field line curvature give rise to a "radial" magnetic well, which ensures the stability of any pressure profile that decreases with increasing radius (or, more precisely, flux coordinate ψ). In a divertor cell, the magnetic field line curvature in the vicinity of the equatorial plane (i.e., in the region that plays a decisive role in ensuring stability) is *unfavorable*, and the stabilizing effect comes from the nonparaxial nature of the magnetic field (the corresponding contribution to W is quadratic in the curvature). In this case, stability can only be achieved for a certain class of gradually decreasing profiles and not for an arbitrary decreasing pressure profile $p(\psi)$: for example, it is impossible to stabilize a sharp (in terms of ψ) boundary such that $dp/d\psi = -p\delta(\psi - \psi_*)$. This is an important feature in which divertor stabilization differs from average minimum-B stabilization.

The problem is to determine the marginally stable profile $p(\psi)$ corresponding to the stability boundary $\omega^2 = 0$. The marginal profile can be found from the Kruskal–Oberman criterion [9]. (In the models in which the potential energy W is replaced by a limiting expression like $W_< \propto \nabla p \cdot \nabla U + \gamma p(\nabla U)^2/U$, where $U = \int B^{-1} dl$, the marginal pressure profile obeys more stringent restrictions.) The related profile was calculated by Sokolov [6] for a periodic chain of cells with divertors and for a plasma with an isotropic pressure and $\beta = 0$. In fact, he found the profile corresponding to the self-stabilization of the divertor. The problem in a more general formulation should involve the following aspects. First, it is necessary to consider other types of confinement systems with built-in divertors, in which case the contributions to W that come from each of the cells (including the divertor cells) cannot be calculated independently because there are passing particles common to all of these cells. Second, anisotropic particle distributions that are characteristic of open confinement systems should be taken into consideration. Finally, the analysis should be extended to systems with finite β values (up to the maximum possible values consistent with equilibrium).

Here, we will focus on the aspects associated with the multicell character of a confinement system and the effects of anisotropic plasma pressure and will restrict the discussion to systems with $\beta \ll 1$ (formally, we assume that $\beta = 0$). We investigate plasma stability in a confinement system consisting of two simple identical mirror cells separated by a divertor cell. The magnetic field at the outer ends of the mirror cells is assumed to be stronger than that at the ends of the divertor cell, so that there exists a population of passing particles that ensures the electric coupling between the cells. The plasma pressure is assumed to be anisotropic, $p_\perp \neq p_\parallel$. We analyze how the shape of the marginally stable

1063-780X/01/2708-0635$21.00

ψ-profile of the plasma pressure depends on both the degree of pressure anisotropy and the ratio between the pressures of the particles trapped in the mirror cells and in the divertor cell.

2. FORMULATION OF THE PROBLEM

The Kruskal–Oberman criterion (a necessary and sufficient condition) for the stability of a low-pressure ($\beta \longrightarrow 0$) collisionless plasma against flute perturbations of the electric potential $\varphi(\psi)\exp(im\theta)$ (where θ is the azimuthal angle and the flux coordinate ψ is defined so that $d\psi = Br\,dn$, with r being the distance from the axis and dn being an element of length along the normal to the magnetic field line) has the form [10]

$$W = \int |\varphi(\psi)|^2 w(\psi) d\psi, \tag{1}$$

$$w = \int \frac{\partial J}{\partial \psi}\left[\frac{\partial F}{\partial \psi} - \frac{1}{\tau}\frac{\partial J}{\partial \psi}\frac{\partial F}{\partial \varepsilon}\right] d\mu\, d\varepsilon; \tag{2}$$

where $J(\varepsilon, \mu, \psi) = \int \sqrt{2(\varepsilon - \mu B)}\, dl$ is the longitudinal adiabatic invariant, $\tau(\varepsilon, \mu, \psi) = \int \frac{dl}{\sqrt{2(\varepsilon - \mu B)}}$, $\varepsilon = v^2/2$, $\mu = v_\perp^2/2B$, and the integration is carried out along a magnetic field line. For simplicity, we assume that one of the plasma components (electron or ion) is much hotter than the other; the distribution function F in expression (2) refers to the hotter component. The potential of the unperturbed electric field $e\Phi_0$ is assumed to be low in comparison with the mean energy of the hotter component and thus has no effect on the particle motion. For a multicell mirror system, the distribution function has the form $F = \sum_\zeta F(\varepsilon, \mu, \psi, \zeta)$, where the invariant ζ determines which cell the particle belongs to. In the problem as formulated, it is necessary to calculate the contribution of all of the particle populations in the system to the potential energy W. In considering a system of two mirror cells separated by a divertor, we deal with four particle populations, which can be treated independently: particles trapped in each of the two mirror cells, particles trapped in the divertor cell, and passing particles that are common to all of the cells. Each population is characterized by its own range of integration over l. We assume that the particle distributions in the mirror cells are the same. Since the passing particles cross the divertor's equatorial plane, which coincides with the symmetry plane of the system, they can be considered together with the particles trapped in the divertor cell. We will denote the quantities referring to the divertor cell by subscript 1, which will also be used to label the "combined" particle distribution. The quantities referring to the mirror cells (including the distribution of the particles that are trapped in the mirror cells and do not enter the divertor cell) will be marked by subscript 2, in which case the "variable" ζ is simply the number of the cell. Note that the contribution from the distribution function of the particle population 2 to W should be doubled, because there are two mirror cells. In the collisionless approximation, function F can be chosen with a certain freedom, because the particle and heat sources in different cells of the system are independent; in particular, the distribution function may be discontinuous in the pitch angle. However, in the problem of flute instability, which we are interested in here, these factors do not play a decisive role (although the ratio between the plasma pressures in the divertor cell and in the mirror cells that is required for stability and the exact shape of the marginally stable ψ-profile of the pressure, of course, both depend on the particle distribution, because the latter determines the quantities averaged over the magnetic field lines). Below, we will merely choose the distribution function F assuming a form convenient for calculations.

We assume that, in the divertor's equatorial plane, the particles obey the distribution function

$$F_1 = C_1 f_1(\varepsilon) G_1(\mu/\varepsilon, \psi) u(\psi). \tag{3}$$

We also assume that, along with the particles that escape from the divertor cell and obey distribution (3), each mirror cell contains a population of particles that obey the distribution function

$$F_2 = C_2 f_2(\varepsilon) G_2(\mu/\varepsilon, \psi) u(\psi). \tag{4}$$

It is expedient to express the normalizing constants $C_{1,2}$ in terms of the pressures in the equatorial plane in the divertor and mirror cells, e.g., in the following form:

$$C_{1,2} = 2p_{1,2}\left[u(\psi)\int \frac{MB(2\varepsilon - \mu B)}{\sqrt{2(\varepsilon - \mu B)}} f_{1,2} G_{1,2}\, d\mu\, d\varepsilon\right]^{-1}, \tag{5}$$

where

$$p_{1,2} = (p_\perp + p_\parallel)_{1,2}/2. \tag{6}$$

The condition for stability against convective modes that are arbitrarily localized in the ψ direction has the form

$$w \geq 0. \tag{7}$$

We introduce the variable $\lambda = \mu/\varepsilon$ in order to represent this stability condition as

$$A(\psi)\frac{du}{d\psi} + S(\psi)u(\psi) \geq 0, \tag{8}$$

where

$$A(\psi) = \sum D \int G(\lambda, \psi) h(\lambda, \psi) d\lambda, \tag{9}$$

$$S(\psi) = \sum D \int \left[\frac{\partial G}{\partial \psi} h + \left(\frac{5}{2}G + \lambda\frac{\partial G}{\partial \lambda}\right)\frac{h^2}{T}\right] d\lambda, \tag{10}$$

$$h(\lambda, \psi) = \sqrt{\frac{2}{\varepsilon}}\frac{\partial J}{\partial \psi} = -\int \frac{2 - \lambda B}{\sqrt{1 - \lambda B}}\frac{\partial \ln B}{\partial \psi} dl, \tag{11}$$

$$D = \int f(\varepsilon)\varepsilon^{3/2}d\varepsilon, \quad (12)$$

$$T(\lambda, \psi) = \int \frac{dl}{\sqrt{1-\lambda B}}, \quad (13)$$

and summation is implied over populations 1 and 2 (over ζ). This representation was used by K.M. Lobanov (Efremov Research Institute of Electrophysical Apparatus) for a particular form of G, and, later, it was applied, e.g., by Mikhailovskaya [11]. The left-hand side of condition (8) can be rewritten as

$$A\exp\left(-\int_0^\psi \frac{S}{A}d\psi'\right)\frac{d}{d\psi}\left[u\exp\left(\int_0^\psi \frac{S}{A}d\psi'\right)\right]. \quad (14)$$

Stable profiles are those for which the condition $u'/u \geq -S/A$ holds everywhere. The pressure profile at marginal stability ($w = 0$), which will be marked by an asterisk, is

$$u^*(\psi) = \text{const}\exp\left(-\int_0^\psi \frac{S}{A}d\psi'\right). \quad (15)$$

Note that, if the anisotropy of the plasma in one of the cells is so strong that the plasma is almost completely concentrated in an equatorial layer whose thickness is smaller than the radius of curvature of the magnetic field lines, then the contribution of this equatorial layer to w reduces to the expression $\text{const}\frac{d}{d\psi}\left(\frac{P_*}{B^3}\right)\frac{dB}{d\psi}$ [12, 13], where $P_* = \int p_\perp d\chi$, B is the magnetic field in the equatorial plane, and χ is a coordinate orthogonal to ψ ($\nabla\chi = \mathbf{B}$). For a single mirror cell with such a strong anisotropy, a marginally stable profile is determined from the condition $P_*/B^3 = \text{const}$.

In an open confinement system, there are no particles in the loss cone. However, in a periodic system (which models a chain of mirror cells with, e.g., ambipolar end plugs), function G can be nonzero even for $\lambda < 1/B_{\max}$. In order to take into consideration such distributions, we assume that, at the end plugs ($z = \pm z_{\max}$), the particles with $\lambda < 1/B_{\max}$ experience ideal reflection. Hence, for particles capable of traversing the entire periodic system of mirror cells, integration over dl can only be carried out for one period and the potential energy W can also only be calculated for one period.

As the distribution function F_1, we adopt the sum of an isotropic "pedestal," which produces pressure p_i, and the additional trapezoidal distribution function of the particles trapped in the divertor cell, i.e., between the magnetic mirrors $B_{1\max}$ (Fig. 1). We use P to denote the ratio of the pressure p_i to the total pressure $p_1 = (p_{\perp 1} + p_{\parallel 1})/2$ of the passing particles and all the populations of trapped particles. The anisotropy of the particles obeying the trapezoidal distribution function

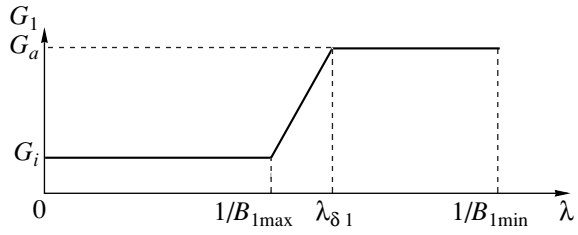

Fig. 1. Plot of the function $G_1(\lambda)$.

depends on the parameter $\delta_1 = (\lambda_{\delta 1} - 1/B_{1\max})/(1/B_{1\min} - 1/B_{1\max})$ in the following way: for $\delta_1 = 0$, the particle distribution outside the loss cone is uniform and, for $\delta_1 = 1$, this distribution is peaked at $\lambda = 1/B_{1\min}$, which corresponds to the particles that are accumulated near the surface on which the minima of the magnetic field are located. For the particles trapped in the mirror cells, we also assume a trapezoidal distribution function F_2 with its own parameter δ_2. The ratio between the pressures at the center of a mirror cell and at the center of a divertor cell, $p_2(0)/p_1(0)$, will be denoted by Π.

Since the configuration with a divertor exhibits a field null near which $|\partial \ln B/\partial\psi| \longrightarrow \infty$, we have $S/A \longrightarrow \infty$ as $\psi \longrightarrow \psi_s$ (where ψ_s is the flux coordinate of the separatrix), in which case function (15) that vanishes at the separatrix exists.

3. RESULTS OF CALCULATIONS

The magnetic field of a mirror system was calculated for given currents in a discrete set of external ring coils. Varying the current in the coils makes it possible to model different magnetic configurations (see Figs. 2–4).

Figure 2b shows marginal ($w = 0$) pressure profiles in the equatorial plane of the divertor cell for different distribution functions $G_1(\lambda)$. As ψ increases, the pressure profile is seen to fall off more gradually toward the separatrix than the profile $p = \text{const}\ U^{-5/3}$ in collisional MHD theory. Recall that, according to [6], in a plasma with isotropic pressure, the pressure profile that is marginally stable in the sense of the Kruskal–Oberman criterion satisfies the relationship $p|_{\psi\to\psi_s} \sim (\psi_s - \psi)^k$ with $k \approx 0.55$. In this case, the hydrodynamic model gives $p|_{\psi\to\psi_s} \sim |\ln(\psi_s - \psi)|^{-5/3}$. The fact that the profile $p(\psi)$ in the axial region falls off more sharply as the degree of anisotropy increases [compare the curves in pairs (*2*, *3*) and (*4*, *1*) in Fig. 2b] can be explained as follows. In condition (8), the contribution from the region in which the magnetic field is weak and the magnetic field line curvature is strong (i.e., the region where the anisotropic plasma is concentrated) to the terms that are quadratic in the curvature is larger (because of the additional power of $1/B$) than the contribution of this region

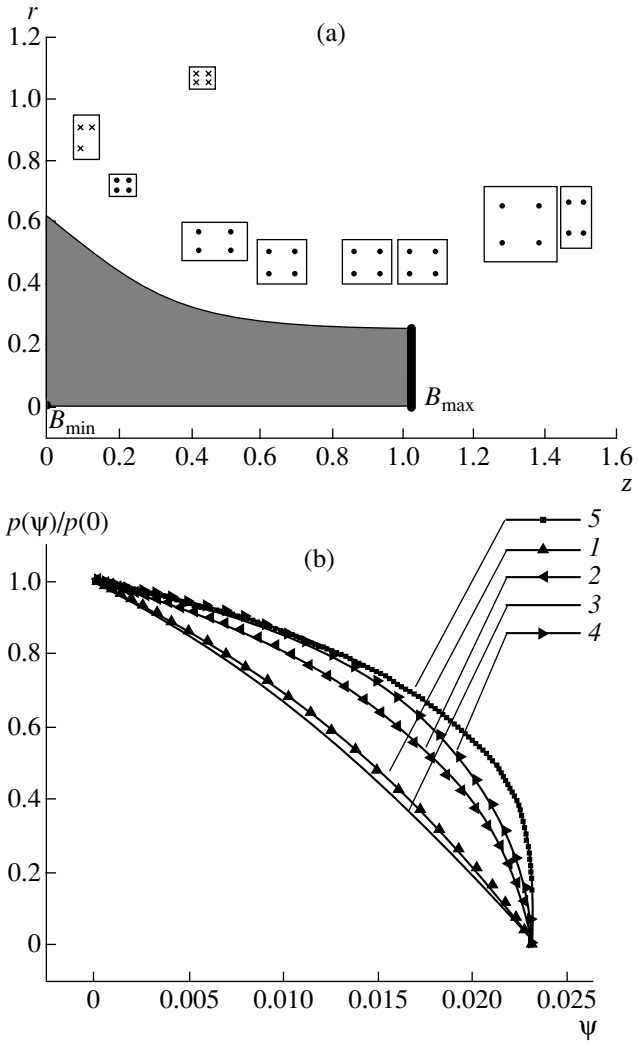

Fig. 2. The results of calculating a divertor in the absence of mirror cells: (a) divertor geometry (shown is half of the divertor; the current-carrying ring coils are indicated by the crosses and points in the rectangles) and (b) marginally stable pressure profiles for (*1*) $P = 0.2$ and $\delta = 0.9$, (*2*) $P = 0$ and $\delta = 0.1$, (*3*) $P = 0$ and $\delta = 0.9$, and (*4*) $P = 0.2$ and $\delta = 0.1$. Also shown is the profile const $U^{-5/3}$ (curve *5*). The mirror ratio at the axis is $B_{max}/B_{min} = 2.89$.

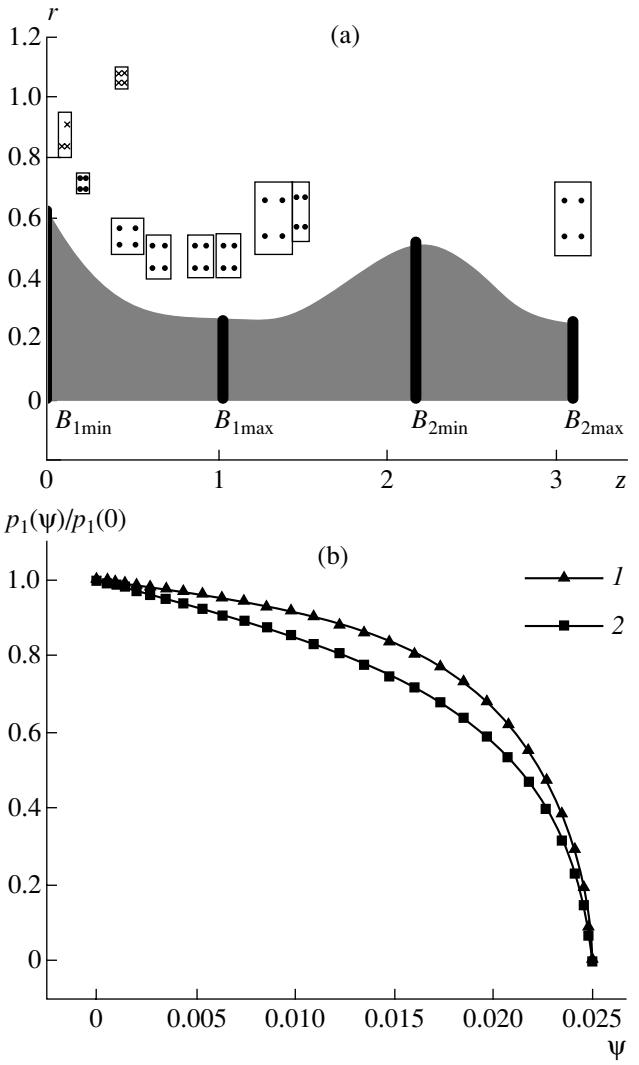

Fig. 3. The same as in Fig. 2 but for two mirror cells separated by a divertor: (a) geometry of the system and (b) marginally stable pressure profiles obtained for $\Pi = (1)$ 1.0 and (*2*) 3.0 and for the parameter values $P = 0.2$, $\delta_1 = 0.1$, and $\delta_2 = 0.1$. The mirror ratios at the axis are $B_{1max}/B_{1min} = 2.85$, $B_{2min}/B_{1min} = 0.92$, and $B_{2max}/B_{1min} = 2.96$.

to the term that is linear in the curvature and contains the derivative $du/d\psi$.

The law according to which the quantity $u^*(\psi)$ and, accordingly, the marginal profile $p(\psi)$ drop off to zero as the separatrix is approached is governed by the particles that cross the equatorial plane of the divertor cell, because their contributions to S and A become infinite as $\psi \longrightarrow \psi_s$, in which case the contributions of the particles trapped in the mirror cells remain finite. However, as illustrated in Fig. 3b, the plasma in the mirror cells affects the entire shape of the marginal pressure profile.

The stable pressure profiles that drop off to zero at the separatrix exist for any ratio between the pressures in the mirror cells and in the divertor cell. The larger the ratio $\Pi = p_2(0)/p_1(0)$ and the weaker the magnetic field in the mirror cells (and the stronger the magnetic field line curvature), the narrower the interval along the ψ direction near the separatrix in which the divertor manifests itself. This effect is illustrated in Fig. 4b, which refers to strongly nonparaxial, "fat" mirror cells, in which the magnetic field is weaker than in the main volume of the divertor cell and the curvature of the magnetic field lines is strong. Even for $\Pi \sim 1$, the shape of the stable pressure profile over almost the entire plasma

volume is governed by mirror cells (the allowable significant decrease—but not to zero—in the pressure away from the axis stems from the stabilizing effect of the magnetic field line curvature; see also [14]) rather than by the effect of the divertor, which only comes into play near the separatrix. This result is confirmed, in particular, by a comparison with curve *3*, which was calculated for $\Pi = 100$, i.e., for a system with a nearly empty divertor cell. Of course, in such a system, the divertor also manifests itself but in an even narrower layer near the separatrix (the nonmonotonic behavior of profile *3* is partially attributed to the ψ-dependence of the degree of anisotropy [15]).

4. DISCUSSION

The calculated pressure profiles that are stable in the sense of the Kruskal–Oberman criterion and drop off to zero at the separatrix differ from the profiles of the form $U^{-5/3}$ predicted by the simplest hydrodynamic model in that they decrease more sharply in the plasma interior (far from the separatrix).

This result is important because it indicates that only a small fraction of plasma particles experience nonadiabatic motion in the region near the magnetic field null-line and, especially, in a thin layer (with a thickness on the order of the Larmor radius ρ of the hotter plasma particles), from which they can escape (owing to the nonadiabatic nature of motion) through the separatrix in the transverse direction. Let us recall that the description of stability in the sense of the Kruskal–Oberman criterion is based on the conservation of μ, and, formally, criterion (1) was derived in the approximation $\rho = 0$. Theoretically, the fact that the pressure near the separatrix is low indicates that a more detailed description is only necessary for a small fraction of the particles. Note that stability is automatically guaranteed for pressure profiles that decrease in the region of adiabatic motion, $\psi < \psi_{ad}$, in the same manner as the marginal profile (15) and then, starting from the surface $\psi = \psi_{ad}$, approach a constant value. The smallness of the ratio $p(\psi_{ad})/p(0)$ makes such profiles easy to maintain in practice.

The restrictions imposed by the adiabaticity of the particle motion may be important in choosing both the divertor geometry and the ratio of the pressure in the mirror cells to the pressure in the divertor cell. The larger the ratio p_2/p_1 and the more "local" the divertor (or, equivalently, the lesser the extent to which the divertor perturbs the magnetic field near the axis), the smaller the thickness $\Delta\psi$ of the layer across which the marginal pressure profile (15) has the steepest drop near the separatrix and the larger the part of this layer where the particles experience nonadiabatic motion. (The same effect occurs in long rippled systems in which there are many mirror cells between neighboring divertors.) The pressure profiles corresponding to a relatively low energy content in particles near the separatrix exist when the ratio p_2/p_1 is not too large and the divertor is not too small, such that the derivative $\partial B/\partial\psi$ at the axis is on the order of R^{-2}, where R is the characteristic radius of the separatrix surface.

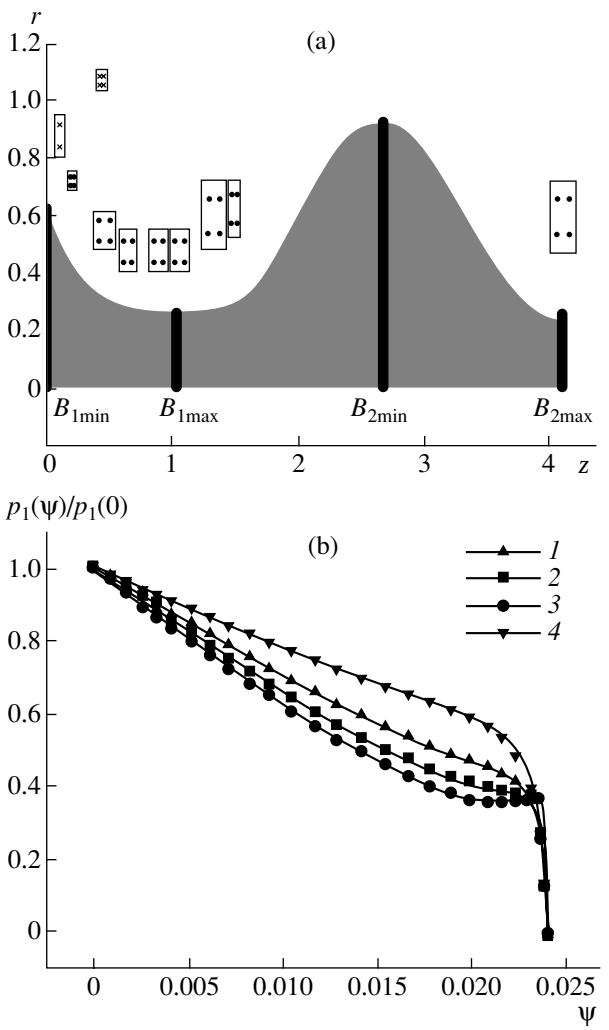

Fig. 4. The same as in Figs. 2 and 3 but for two essentially nonparaxial mirror cells separated by a divertor: (a) geometry of the system and (b) marginally stable pressure profiles obtained for $\Pi =$ (*1*) 1.0, (*2*) 3.0, (*3*) 100, and (*4*) 0.2 and for the parameter values $P = 0.2$, $\delta_1 = 0.1$, and $\delta_2 = 0.1$. The mirror ratios at the axis are $B_{1max}/B_{1min} = 2.86$, $B_{2min}/B_{1min} = 0.34$, and $B_{2max}/B_{1min} = 2.97$.

ACKNOWLEDGMENTS

This study was supported in part by the Russian Foundation for Basic Research, project no. 00-15-96526 (under the program "Leading Scientific Schools").

REFERENCES

1. D. D. Ryutov, Usp. Fiz. Nauk **154**, 565 (1988) [Sov. Phys. Usp. **31**, 300 (1988)].

2. G. I. Dimov, Fiz. Plazmy **23**, 883 (1997) [Plasma Phys. Rep. **23**, 813 (1997)].
3. V. V. Arsenin, Trans. Fusion Technol. **35** (1T), 3 (1999).
4. B. Lane, R. S. Post, and J. Kesner, Nucl. Fusion **27**, 227 (1987).
5. V. P. Pastukhov and A. Yu. Sokolov, Fiz. Plazmy **17**, 1043 (1991) [Sov. J. Plasma Phys. **17**, 603 (1991)].
6. A. Yu. Sokolov, Fiz. Plazmy **18**, 657 (1992) [Sov. J. Plasma Phys. **18**, 343 (1992)].
7. R. S. Post, K. Brau, J. Casey, *et al.*, in *Proceedings of the 12th International Conference on Plasma Physics and Controlled Nuclear Fusion Research, Nice, 1988* [Nucl. Fusion Suppl. **2**, 493 (1989)]; J. A. Casey, B. G. Lane, J. H. Irby, *et al.*, Phys. Fluids **31**, 2009 (1988).
8. Y. Yasaka, N. Takano, and H. Takeno, Trans. Fusion Technol. **39** (1T), 350 (2001).
9. M. D. Kruskal and C. R. Oberman, Phys. Fluids **1**, 275 (1958).
10. B. B. Kadomtsev, in *Plasma Physics and the Problem of Controlled Nuclear Fusion*, Ed. by M. A. Leontovich (Akad. Nauk SSSR, Moscow, 1958), Vol. IV, p. 370.
11. L. V. Mikhaĭlovskaya, Fiz. Plazmy **14**, 1241 (1988) [Sov. J. Plasma Phys. **14**, 727 (1988)].
12. V. V. Arsenin, Pis'ma Zh. Éksp. Teor. Fiz. **43**, 270 (1986) [JETP Lett. **43**, 346 (1986)].
13. D. D. Ryutov and G. V. Stupakov, Fiz. Plazmy **12**, 1411 (1986) [Sov. J. Plasma Phys. **12**, 815 (1986)].
14. E. A. Adler, Phys. Fluids **25**, 2053 (1982).
15. V. V. Arsenin, Fiz. Plazmy **25**, 307 (1999) [Plasma Phys. Rep. **25**, 277 (1999)].

Translated by I. A. Kalabalyk

Plasma Physics Reports, Vol. 27, No. 8, 2001, pp. 641–651. Translated from Fizika Plazmy, Vol. 27, No. 8, 2001, pp. 680–692.

NONLINEAR PHENOMENA

Slow Electromagnetic Solitons in Electron–Ion Plasmas

D. Farina* and S. V. Bulanov**

**Istituto di Fisica del Plasma, Consiglio Nazionale delle Ricerche, Milano, Italia*

***Institute of General Physics, Russian Academy of Sciences, ul. Vavilova 38, Moscow, 119991 Russia*

Received December 28, 2000

Abstract—A set of nonlinear differential equations that describe moving relativistic solitons is investigated analytically and solved numerically. The influence of the ion motion on the soliton structure is investigated. It is demonstrated that, depending on the propagation velocity, relativistic solitary waves can occur in the form of bright solitons, dark solitons, or collisionless electromagnetic shock waves. In the limit of a low propagation velocity, a dark soliton can trap the ions and accelerate them. In the case of a bright soliton, the effects of ion dynamics limit the soliton amplitude. The constraint on the maximum amplitude is related to either the breaking of ion motion or the intersection of electron trajectories. The soliton breaking provides a new mechanism for ion and electron acceleration in the interaction of high-intensity laser pulses with plasmas. © *2001 MAIK "Nauka/Interperiodica".*

1. INTRODUCTION

For a long time, solitons have attracted great attention because of their resilient, robust behavior [1]. In many cases, solitons are regarded as elementary entities comprising turbulence. Inside a soliton, the dispersion effects are balanced by the nonlinearity of the media. In the interaction of high-intensity laser pulses with plasmas, the dispersion effects come into play due to the finite electron inertia to respond the electromagnetic field action, while the nonlinearity is due to the relativistic increase in the electron mass, as well as to the plasma density redistribution under the action of the ponderomotive force, which pushes the plasma particles (electrons and, for a longer time, ions) away from the region where the electromagnetic field is maximum.

Relativistic solitons were observed in multidimensional particle-in-cell (PIC) simulations of the interaction of laser pulses with underdense [2–5] and overdense [6, 7] plasmas. Solitons are generated in the wake behind the laser pulse and propagate toward the plasma–vacuum interface with a velocity well below the speed of light. Here, they suddenly disappear, radiating away their energy in the form of low-frequency electromagnetic bursts [8]. Solitons can also be regarded as coherent structures that form electromagnetic turbulence and that can be detected via low-frequency backscattered radiation. In this context, we mention paper [9], in which an anomalous regime of stimulated backward Raman scattering with the frequency downshifting and spectrum broadening of backscattered laser radiation in an underdense plasma was observed. An analytical theory of relativistic electromagnetic solitons was developed in [10–17]. In those papers, apart from the paper by Kozlov *et al.* [12], the ions were assumed to be at rest. In [12], it was pointed out that the ion contribution limits the soliton propagation velocity from below and modifies the distribution of the electromagnetic field inside the soliton. For a relativistic soliton amplitude, which, however, is less than $a_c = \sqrt{m_i/m_e}$, the ions can be assumed to be at rest during approximately $\sqrt{m_i/m_e}$ periods of electromagnetic field oscillations inside the soliton. Here, $a = eE/m_e\omega c$ is the normalized amplitude and $\omega \approx \omega_{pe}$ is the frequency of electromagnetic field oscillations inside the soliton. The time $2\pi\sqrt{m_i/m_e}\omega_{pe}^{-1} = 2\pi\omega_{pi}^{-1}$, for which an analytical solution for a low-frequency zero-velocity soliton [16] provides a rather good description, is substantially longer than the period of electromagnetic field oscillations inside the soliton; in an underdense plasma, this time is much longer than the laser period. However, over a time period longer than $2\pi\omega_{pe}^{-1}$, the ponderomotive pressure of the electromagnetic field inside the soliton starts to dig a hole in the ion density and the parameters of the soliton change. We note that solitons were also observed in 2D PIC simulations of the interaction of laser pulses with plasmas with allowance for ion motion (see Fig. 1 in [8]).

When the laser power reaches the petawatt range [18], the ion dynamics begin to play the key role in laser–plasma interaction, even in the case of ultrashort (femtosecond) laser pulses. Particularly, for multiterawatt and petawatt laser pulses, ion acceleration becomes highly efficient [19–24]. The discussed mechanisms for ion acceleration are related to charged-particle acceleration in the charge-separation electric field [19–22, 25] and in the wake field behind an ultrashort laser pulse [20, 26]. On the other hand, solitary waves propagating with velocities close to the speed of light were discussed in [15, 27] in connection with charged-particle acceleration. In those papers, it was pointed out

that charged particles can gain energy when interacting with regular electric and magnetic fields inside the soliton. When a soliton propagates in an inhomogeneous plasma, the intersection of charged particle trajectories eventually occurs and the soliton energy transforms into the energy of fast particles (ions and electrons).

The aim of this paper is to investigate the role of ion dynamics in relativistic solitary waves in plasmas.

The paper is organized as follows. In Section 2, we derive a set of nonlinear differential equations describing solitons according to the method of [12]. In Section 3, we analyze the electric quasineutrality approximation. In Section 4, we obtain analytic solutions that describe finite-amplitude solitary waves in the limit of weak nonlinearity. In Section 5, we present the results of numerical solution of the equations obtained in Section 3 and discuss the properties of bright solitons. In the conclusion, the results obtained are summarized.

2. BASIC EQUATIONS

We use the hydrodynamic approximation to describe both the electron and ion components. We assume the plasma to be cold (both the ion and electron temperatures are zero). Maxwell's equations are written in the Coulomb gauge for the vector potential: $\nabla \cdot \mathbf{A} = 0$. As a result, we have

$$\Delta\mathbf{A} - \frac{1}{c^2}\frac{\partial^2}{\partial t^2}\mathbf{A} - \frac{\partial}{\partial t}\nabla\phi = \frac{4\pi e}{c}(n_e\mathbf{v}_e - n_i\mathbf{v}_i), \quad (1)$$

$$\Delta\phi = 4\pi e(n_e - n_i), \quad (2)$$

$$\frac{\partial}{\partial t}n_\alpha + \nabla\cdot(n_\alpha\mathbf{v}_\alpha) = 0, \quad (3)$$

$$\frac{\partial}{\partial t}\left(\mathbf{p}_\alpha + \frac{q_\alpha}{c}\mathbf{A}\right) = -\nabla(q_\alpha\phi + m_\alpha c^2\gamma_\alpha) + \mathbf{v}_\alpha\times\nabla\times\left(\mathbf{p}_\alpha + \frac{q_\alpha}{c}\mathbf{A}\right), \quad (4)$$

where the subscript $\alpha = e, i$ refers to electrons and ions, respectively; $\mathbf{p}_{e,i}$ is the particle momentum; $q_e = -e$ is the electron charge; $q_i = e$ is the ion charge; $\mathbf{v}_\alpha$ is the particle velocity; and

$$\gamma_\alpha = \sqrt{1 + |\mathbf{p}_\alpha|^2/m_\alpha^2c^2} \quad (5)$$

is the relativistic factor. By applying the curl operator to Eq. (4), we obtain

$$\partial_t\mathbf{\Omega}_\alpha = \nabla\times(\mathbf{v}_\alpha\times\mathbf{\Omega}_\alpha), \quad (6)$$

where $\mathbf{\Omega}_\alpha = \nabla\times(\mathbf{p}_\alpha + q_\alpha\mathbf{A}/c)$ is the curl of the generalized momentum, which is also referred to as the generalized vorticity. If we assume that at $t = 0$, $\mathbf{\Omega}_\alpha = 0$, then, in view of Eq. (6), it also holds at subsequent times.

We introduce the following dimensionless variables:

$$\frac{\mathbf{r}\omega_{pe}}{c}\longrightarrow\mathbf{r},\quad t\omega_{pe}\longrightarrow t,\quad \frac{\mathbf{v}_\alpha}{c}\longrightarrow\mathbf{v}_\alpha,$$
$$\frac{\mathbf{p}_\alpha}{m_\alpha c}\longrightarrow\mathbf{p}_\alpha,\quad \frac{e\mathbf{A}}{m_ec^2}\longrightarrow\mathbf{A},\quad \frac{e\phi}{m_ec^2}\longrightarrow\phi, \quad (7)$$

where $\omega_{pe} = (4\pi n_0e^2/m_e)^{1/2}$ is the electron plasma frequency and n_0 is the unperturbed electron density. We consider the 1D case, in which $\partial_y = \partial_z = 0$. For localized solutions, we have $A_\parallel = 0$. From Eq. (6), it follows that $\mathbf{p}_{\perp e} = \mathbf{A}_\perp$ and $\mathbf{p}_{\perp i} = -\rho\mathbf{A}_\perp$, where the subscripts $\parallel$ and $\perp$ refer to the x direction and the perpendicular direction, respectively, and $\rho = m_e/m_i$ is the electron-to-ion mass ratio.

We transform to the variables

$$\xi = x - Vt,\quad \tau = t - Vx \quad (8)$$

and look for a solution to set (1)–(4) in the form

$$A_y + iA_z = a(\xi)\exp(i\omega\tau), \quad (9)$$

while all the other quantities (ϕ, n_α, γ_α, and $p_{\parallel\alpha}$) are assumed to depend only on variable ξ. Here, ω is the wave frequency, V is the group velocity, $1/V$ is the phase velocity, and $k = V$ is the wavenumber. Then, set (1)–(4) transforms into

$$(1 - V^2)(a'' + \omega^2 a) = a\left(\frac{n_e}{\gamma_e} + \rho\frac{n_i}{\gamma_i}\right), \quad (10)$$

$$V\phi'' = n_e v_{\parallel e} - n_i v_{\parallel i}, \quad (11)$$

$$\phi'' = n_e - n_i, \quad (12)$$

$$[n_e(V - v_{\parallel e})]' = 0, \quad (13)$$

$$[n_i(V - v_{\parallel i})]' = 0, \quad (14)$$

$$(\gamma_e - Vp_{\parallel e} - \phi)' = 0, \quad (15)$$

$$(\gamma_i - Vp_{\parallel i} + \rho\phi)' = 0, \quad (16)$$

where the prime denotes the derivative with respect coordinate ξ,

$$\gamma_e = \sqrt{1 + p_{\parallel e}^2 + a^2} \text{ and } \gamma_i = \sqrt{1 + p_{\parallel i}^2 + \rho^2 a^2}. \quad (17)$$

From Eqs. (15) and (16), we find the x-component of the kinetic momentum and the energy as functions of the scalar and vector potentials:

$$p_{\parallel\alpha} = \frac{(V\psi_\alpha - R_\alpha)}{(1 - V^2)}, \quad (18)$$

$$\gamma_\alpha = \frac{(\psi_\alpha - VR_\alpha)}{(1 - V^2)}, \quad (19)$$

with $\psi_e = \mathscr{E}_e + \phi$, $\psi_i = \mathscr{E}_i - \rho\phi$, and

$$R_e = [\psi_e^2 - (1 - V^2)(1 + a^2)]^{1/2}, \quad (20)$$

$$R_i = [\psi_e^2 - (1 - V^2)(1 + \rho^2 a^2)]^{1/2}. \quad (21)$$

Constants $\mathscr{E}_e$ and $\mathscr{E}_i$ must be specified by the boundary conditions at infinity. If, at $x \longrightarrow \pm\infty$, the amplitude of the electromagnetic field vanishes ($a \longrightarrow 0$), $\phi \longrightarrow 0$, and the plasma is at rest ($p_{\|\alpha} = 0$), then we have $\mathscr{E}_e = \mathscr{E}_i = 1$. If, at $x \longrightarrow \pm\infty$, the amplitude of the electromagnetic field is finite ($a \longrightarrow \pm a_0$), $\phi \longrightarrow 0$, and the plasma is at rest ($p_{\|\alpha} = 0$), then we have $\mathscr{E}_e = \sqrt{1 + a_0^2}$ and $\mathscr{E}_i = \sqrt{1 + \rho^2 a_0^2}$.

From the electron and ion continuity equations (13) and (14), we obtain the relation for the density

$$n_\alpha = V\frac{(\psi_\alpha - VR_\alpha)}{R_\alpha(1 - V^2)}. \quad (22)$$

Finally, we obtain a closed set of equations for the potentials

$$\phi'' = \frac{V}{1 - V^2}\left(\frac{\psi_e}{R_e} - \frac{\psi_i}{R_i}\right), \quad (23)$$

$$a'' + \omega^2 a = a\frac{V}{1 - V^2}\left(\frac{1}{R_e} + \frac{\rho}{R_i}\right). \quad (24)$$

This set admits the first integral

$$\frac{1 - V^2}{2}(a'^2 + \omega^2 a^2) - \frac{1}{2}\phi'^2 + \frac{V}{1 - V^2}\left(R_e - V + \frac{R_i - V}{\rho}\right) = \frac{1 - V^2}{2}(a'^2 + \omega^2 a^2) - \frac{1}{2}\phi'^2 - (\gamma_e - 1) - \frac{\gamma_i - 1}{\rho} = \text{const}. \quad (25)$$

The limiting case of immobile ions (see [12, 15–17]) corresponds to setting $\rho = 0$ in Eqs. (23)–(25).

The set of Eqs. (23)–(24) describes the coupled longitudinal plasma wave and circularly polarized transverse electromagnetic wave. For $a = a_0 = 0$, it describes a longitudinal plasma wave,

$$\phi'' = \frac{V}{1 - V^2}\left[\frac{1 + \phi}{\sqrt{(1 + \phi)^2 - 1 + V^2}} - \frac{1 - \rho\phi}{\sqrt{(1 - \rho\phi)^2 - 1 + V^2}}\right]. \quad (26)$$

The influence of ion motion on the structure of a plasma wave was analyzed in [26, 28].

For a transverse electromagnetic wave with $\phi = 0$ and $a = a_0$, from Eq. (10) we have

$$(1 - V^2)\omega^2 a = a\left(\frac{1}{\sqrt{1 + a^2}} + \frac{\rho}{\sqrt{1 + \rho^2 a^2}}\right).$$

From this equation, we obtain the dispersion relation for the frequency as a function of the wave velocity and amplitude

$$\omega^2 = \frac{1}{1 - V^2}\left(\frac{1}{\mathscr{E}_e} + \frac{\rho}{\mathscr{E}_i}\right). \quad (27)$$

The dispersion relation can also be rewritten in the form containing the wavenumber k,

$$\omega^2 = k^2 + \left(\frac{1}{\mathscr{E}_e} + \frac{\rho}{\mathscr{E}_i}\right). \quad (28)$$

Dispersion relation (28) is a modification of the Akhiezer–Polovin result [29] to the case of mobile ions. In other words, the plasma frequency, modified with allowance for ion motion and relativistic effects, is equal to

$$\Omega = \sqrt{\frac{1}{\mathscr{E}_e} + \frac{\rho}{\mathscr{E}_i}}. \quad (29)$$

This expression can also be written as $\Omega^2 = \omega^2(1 - V^2)$. We see that, in view of Eq. (27), the effective plasma frequency Ω does not depend on the wave propagation velocity.

3. QUASINEUTRAL APPROXIMATION

In the quasineutral approximation, which is valid in the long-wavelength limit ($\phi'' \ll 4\pi e(n_e - n_i)$), the electron and ion densities are assumed to be equal to each other, $n_e = n_i$. As a result, we obtain the equation

$$\frac{\psi_e}{R_e} = \frac{\psi_i}{R_i}. \quad (30)$$

Its solution allows us to express the electrostatic potential via the vector potential:

$$\phi = \frac{(\mathscr{E}_i + \rho\mathscr{E}_e)\sqrt{(1 + a^2)(1 + \rho^2 a^2)} - \mathscr{E}_e(1 + \rho^2 a^2) - \rho\mathscr{E}_i(1 + a^2)}{1 - \rho^2}. \quad (31)$$

When $\mathscr{E}_e = \mathscr{E}_i = 1$, the electrostatic potential is equal to [12]

$$\phi = \frac{\sqrt{(1+a^2)(1+\rho^2 a^2)} - (1+\rho a^2)}{1-\rho}. \quad (32)$$

Using dispersion relation (28), we obtain the equation for the vector potential in the quasineutral approximation

$$(1-V^2)(a'' + \omega^2 a) = \frac{VaS^2}{\sqrt{(1+a^2)(1+\rho^2 a^2)}\sqrt{S_0^2 - S^2(1-V^2)}}, \quad (33)$$

where

$$S = \sqrt{1+\rho^2 a^2} + \rho\sqrt{1+a^2} \quad (34)$$

and

$$S_0 = \sqrt{1+\rho^2 a_0^2} + \rho\sqrt{1+a_0^2} \equiv \rho\mathscr{E}_e + \mathscr{E}_i. \quad (35)$$

The above equations have the following first integral

$$\frac{(a')^2}{2} + U(a) = K, \quad (36)$$

where K is a constant and

$$U(a) = \frac{1}{2}\omega^2 a^2 + \frac{V}{\rho(1-V^2)^2}\sqrt{S_0^2 - (1-V^2)S^2}. \quad (37)$$

The phase plane (a, a') of Eq. (36) can be investigated by varying V at a given value of a_0. The stationary points on the phase plane are given by

$$a' = 0, \quad a = 0, \quad (38)$$

$$a' = 0, \quad \frac{VS^2}{\sqrt{1+a^2}\sqrt{1+\rho^2 a^2}\sqrt{S_0^2 - (1-V^2)S^2}} = (1-V^2)\omega^2. \quad (39)$$

Equation (39) has the solution $a = a_0$ for any value of V.

We leave a detailed analytical study of the properties of nonlinear modes described by Eq. (36) in the electron–ion plasma for further publications. In this paper, we restrict ourselves to the weak nonlinearity limit.

4. WEAK NONLINEARITY LIMIT

We consider the limit of a small (but finite) wave amplitude ($|a_0|, |a| \ll 1$) and expand the right-hand side of Eq. (33) in powers of the amplitude. Then, in view of the smallness of parameter ρ, in the third order in a and in the first order in ρ, we obtain

$$a'' + \omega^2 a = a\frac{1}{1-V^2}\left[1 + \rho - \frac{a^2}{2} - \frac{\rho}{2V^2}(a_0^2 - a^2)\right]. \quad (40)$$

We rewrite this equation in the form

$$a'' + \omega^2 a = a\frac{1}{1-V^2}\left[1 + \rho - \frac{\rho a_0^2}{2V^2} - \left(1 - \frac{\rho}{V^2}\right)\frac{a^2}{2}\right]. \quad (41)$$

We see that the sign of $1 - \rho/V^2$ determines whether the nonlinear shift of the frequency is negative (for $V > \sqrt{\rho}$) or positive (for $V < \sqrt{\rho}$). It is well known that the nonlinear downshifting of the wave frequency corresponds to the breakup of a homogeneous wave into bright solitary waves. On the other hand, nonlinear frequency upshifting manifests the possibility of dark soliton formation [30].

4.1. Small-Amplitude Bright Soliton

We consider fast solitons with the propagation velocity $V > \sqrt{\rho}$. In this case, we have bright solitons whose amplitude is maximum at a certain point and vanishes at infinity. This solution to Eq. (40) is consistent with the boundary conditions when $a_0 = 0$. The bright soliton is described by the well known expression $a = a_m/\cosh(\kappa\xi)$ (see [12]) or

$$A_y + iA_z = \frac{a_m}{\cosh(\kappa(x - Vt))}\exp(i\omega(t - Vx)), \quad (42)$$

where the inverse soliton width is

$$\kappa = \frac{a_m}{2V}\sqrt{\frac{V^2 - \rho}{1-V^2}}, \quad (43)$$

and the frequency is

$$\omega = \sqrt{\frac{1+\rho}{1-V^2} - \frac{a_m^2}{4V^2}\left(\frac{V^2 - \rho}{1-V^2}\right)}. \quad (44)$$

It can be seen that, when the soliton propagation velocity approaches $\sqrt{\rho}$, the soliton width κ^{-1} tends to infinity for a fixed soliton amplitude a_m. On the other hand, if we assume the soliton width to be fixed, then its amplitude becomes infinite as $V \longrightarrow \sqrt{\rho}$. In this case, we can expect soliton breaking accompanied by the self-intersection of charged particle trajectories.

4.2. Small-Amplitude Dark Soliton

If velocity V is smaller than $\sqrt{\rho}$, then Eq. (40) has a solution which describes a dark soliton. Equation (40) has three equilibrium solutions: $a = 0$ and $a = \pm a_0$. It is easy to show that, in the vicinity of the first solution $a = 0$, we have a periodic wave. The second and third solutions, $a = \pm a_0$, require that the frequency be equal to

$$\omega = \sqrt{\frac{1+\rho}{1-V^2} - \frac{a_0^2}{2(1-V^2)}}. \quad (45)$$

Taking into account this relationship, we rewrite Eq. (40) as

$$a'' = \frac{(\rho - V^2)}{2V^2(1-V^2)} a(a_0^2 - a^2). \quad (46)$$

Equation (33) admits an exact solution for a dark soliton [30, 31], $a = a_0 \tanh(\kappa\xi)$ or

$$A_y = iA_z = a_0 \tanh(\kappa\xi)\exp(i\omega(t - Vx)), \quad (47)$$

where the soliton inverse width is given by

$$\kappa = \frac{a_0}{2V}\sqrt{\frac{\rho - V^2}{1-V^2}}, \quad (48)$$

and the frequency is given by Eq. (45). These expressions describe a small-amplitude dark soliton (kink state): the wave amplitude changes monotonically from $-a_0$ (or a_0) at $x = -\infty$ to a_0 (or $-a_0$) at $x = +\infty$.

In the case of a dark soliton, we have a minimum of the electromagnetic energy density and a minimum of the plasma density that propagate at velocity V without changing their shape. Dark solitons are known to occur in optical systems [30]. Recently, they were observed in the Bose–Einstein condensate [32]. We see that, at low propagation velocities, an electron–ion plasma exhibits properties similar to those in the Bose–Einstein condensate with a positive scattering length [33]. In an electron–positron plasma, dark solitons are natural nonlinear modes [34].

Calculating the electrostatic potential with expression (31), we obtain that there is an electrostatic well inside the soliton: $\phi = -a_0^2/\cosh^2(\kappa\xi)$. Thus, the dark soliton can trap positively charged ions and advect them. To illustrate this, we write the Hamiltonian of a charged particle:

$$H(P, x, t) = \sqrt{1 + P^2} - \frac{\rho a_0^2}{\cosh^2(\kappa(x - Vt))}. \quad (49)$$

Here, P is the longitudinal component of the ion momentum. Performing the canonical transformation to variables P and $\xi = x - Vt$, we obtain

$$H(P, \xi) = \sqrt{1 + P^2} - PV - \frac{\rho a_0^2}{\cosh^2(\kappa\xi)}. \quad (50)$$

Since this Hamiltonian is time-independent, it is conserved and the problem becomes integrable. At low soliton velocities ($V < \sqrt{\rho}$), we can use the nonrelativistic approximation. In this case, we obtain that the momentum of a trapped particle is given by

$$P_{\max,\min} = m_i V \pm \sqrt{\frac{m_e a_0^2}{\cosh^2(\kappa\xi)}}. \quad (51)$$

4.3. Weak Electromagnetic Shock Wave

The case $V = \sqrt{\rho}$ requires careful investigation because, in this case, the nonlinear term on the right-hand side of Eq. (41) vanishes. Assuming $a_0 = 0$, we expand the right-hand side of Eq. (33) in a power series up to the fifth order in a and the second order in ρ:

$$a'' + \omega^2 a = \frac{a}{1-V^2}\left[1 + \rho + \frac{3\rho^2}{2V^2} - \frac{1}{2}\left(1 - \frac{2\rho + \rho^2}{2V^2}\right)a^2 + \frac{3}{8}\left(1 - \frac{V^2\rho + \rho^2}{V^4}\right)a^4\right]. \quad (52)$$

Now, we assume that $V^2 = \rho(1 + \varepsilon)$, where $\varepsilon \ll 1$. Then, retaining the leading order terms, we obtain

$$a'' = \frac{1}{1-V^2}\left[(1 + \rho - (1-V^2)\omega^2)a - \frac{1}{2}\left(\varepsilon + \frac{\rho}{2}\right)a^3 + \frac{3}{8}a^5\right]. \quad (53)$$

This equation has the integral

$$\frac{(a')^2}{2} - \frac{a^2}{16(1-V^2)}\left[a^4 - 2\left(\varepsilon + \frac{\rho}{2}\right)a^2 + 8(1 + \rho - (1-V^2)\omega^2)\right] = \text{const}. \quad (54)$$

If we choose frequency ω to be equal to

$$\omega = \sqrt{\frac{8(1+\rho) - \varepsilon - \rho/2}{8(1-V^2)}} \quad (55)$$

and set the constant on the right-hand side of Eq. (54) to zero, then Eq. (53) can be rewritten as

$$\frac{(a')^2}{2} - \frac{1}{16(1-V^2)}a^2(a^2 - a_w^2)^2 = 0, \quad (56)$$

where $a_w = \sqrt{\varepsilon + \rho/2}$. The solution to this equation,

$$a(\xi) = \frac{a_w}{\sqrt{1 + \exp\left(\xi \frac{a_w^2}{2\sqrt{1-V^2}}\right)}} \quad (57)$$

describes a collisionless electromagnetic shock wave with an amplitude equal to a_w. The shock wave velocity is relatively low (on the order of $\sqrt{\rho}$). The shock wave is compressional; the carrying frequency of the electromagnetic field is equal to

$$\omega = \sqrt{\frac{8(1+\rho) - a_w^2}{8(1-V^2)}}. \quad (58)$$

The width of the shock wave front is equal to

$$\kappa^{-1} = 2\sqrt{1-V^2}/a_w^2. \quad (59)$$

We see that the larger the shock wave amplitude $a_w = \sqrt{\varepsilon + \rho/2}$, the steeper the shock wave front.

The above collisionless shock wave corresponds to a nonlinear regime of the penetration of a relativistically strong electromagnetic wave into an overdense plasma. Previously, the regimes of relativistic transparency were considered in which an electromagnetic wave could propagate through an overdense plasma due to the relativistic correction to the electron mass (see [29, 35–39]). In our case, the effective plasma frequency changes owing to both the relativistic correction to the electron mass and the change in the plasma density. In contrast to collisionless shock waves discovered by Sagdeev [40], the formation of the above collisionless shock wave with a steady-state monotonic profile does not require any dissipative process.

In what follows, we will address the detailed discussion of the properties of fast bright solitons, leaving a more detailed study of dark solitons and collisionless shock waves to our subsequent publications.

5. BRIGHT SOLITONS IN THE GENERIC CASE

So far, we have considered solitons in the plasma quasineutrality approximation. This approximation fails for narrow solitons with sufficiently high amplitudes. In particular, it fails for solitons that are close to breaking. To study these processes, we have to solve the full set of Eqs. (23) and (24). Due to the complexity of the problem, Eqs. (23) and (24) were solved numerically.

As was already pointed out in Section 2, the set of Eqs. (23) and (24) describes the coupled longitudinal plasma wave and circularly polarized transverse electromagnetic wave. It admits the following steady-state solutions consistent with the boundary conditions: $\phi = 0$ and $a = 0$ for $a_0 = 0$ and $\phi = 0$, $a = a_0$, and $\omega^2(1 - V^2) = 1/\mathscr{E}_e + \rho/\mathscr{E}_i$ for $a_0 \neq 0$. Linearizing Eqs. (23) and (24) for $\phi \ll 1$ and $|\delta a| \ll 1$ with $\delta a = a - a_0$, we obtain

$$\phi'' = b_{11}\phi + b_{12}\delta a, \quad (60)$$

$$\delta a'' = b_{21}\phi + b_{22}\delta a, \quad (61)$$

where

$$b_{11} = -\frac{1}{V^2}\left(\frac{1}{\mathscr{E}_e} + \frac{\rho}{\mathscr{E}_i}\right),$$

$$b_{12} = \frac{a_0^2(1-\rho^2)}{V^2\mathscr{E}_e^2\mathscr{E}_i^2},$$

$$b_{21} = -\frac{b_{12}}{1-V^2},$$

$$b_{22} = \omega_0^2 - \omega^2 + \frac{a_0^2}{V^2}\left(\frac{1}{\mathscr{E}_e^3} + \frac{\rho^3}{\mathscr{E}_i^3}\right).$$

Note that the set of linear equations (60) and (61) is decoupled for $a_0 = 0$ or $\rho = 1$. Below, we will focus on the case with $a_0 = 0$ (bright solitons). We will be looking for solutions of the form $\exp(\lambda\xi)$. Equation (60) has two purely imaginary eigenvalues

$$\lambda_L^2 = -\frac{1+\rho}{1-V^2}, \quad (62)$$

and Eq. (61) has two eigenvalues

$$\lambda_a^2 = \frac{1+\rho}{1-V^2} - \omega^2, \quad (63)$$

which are either real or imaginary for ω^2 smaller or larger than $(1 + \rho)/(1 - V^2)$, respectively. Thus, soliton solutions can occur for $\bar{\omega}^2 \equiv \omega^2(1 - V^2) < 1 + \rho$.

In this paper, we are interested in localized solutions to Eqs. (23) and (24). Note that these equations are reversible with respect to the transformation of the independent and dependent variables: $\xi \longrightarrow -\xi$, $\phi \longrightarrow \phi$, and $a \longrightarrow \pm a$. Thus, the solution for the vector potential a can either be symmetric or antisymmetric, while the electrostatic potential ϕ is always symmetric. In particular, we will look for solutions with single-humped ϕ profiles and a profiles with even or odd number p of the zeros (nodes) of the electromagnetic field.

Note that Eqs. (23) and (24) can be written in a Hamiltonian form. Thus, from the mathematical standpoint, the problem reduces to that of finding homoclinic orbits for a four-dimensional reversible autonomous Hamiltonian system, for which the point $\xi = 0$ is a saddle center (see [41]). To numerically obtain the soliton solution, we proceed in a way similar to that of [12]. For fixed V, we integrate the set of equations with the following initial conditions at $\xi = -\xi_1$: $\phi' = \phi = 0$ and

$a_1' = -\lambda a_1$, assuming that a_1 is small and $\lambda = [(1 + \rho)/(1 - V^2) - \omega^2]^{1/2}$. We look for ω values for which, at $\xi = 0$, we have $\phi' = 0$ and $a = 0$ (for odd p) or $\phi' = 0$ and $a' = 0$ (for even p).

5.1. Electron Relativistic Solitons

We first analyze the case in which the ion dynamics is neglected; i.e., we set $\rho = 0$. In this case, we can speak about purely electron solitons. For $p = 0$, no soliton solutions can be found for nonzero propagation velocities $V > 0$. For a number of nodes of the electromagnetic field $p \geq 1$ and $\rho = 0$, moving solitons are found to occur for V larger than a certain critical value V_c, which depends on p. For $p = 1$, the critical velocity is approximately 0.00165, which is substantially smaller than the lower limit for the propagation velocity of a weak bright soliton $\sqrt{\rho}$ at $\rho = 1/1836$. The critical velocity increases with increasing p. The corresponding frequency is an increasing function of V as can be seen in Fig. 1, in which the value of $\omega^2(1 - V^2) = \omega^2 - k^2$ is plotted versus the soliton velocity V for $p = 1$, 2, 3, and 4. Figure 1 also shows the square of the frequency of a soliton with a zero velocity and zero number of nodes ($p = 0$, $\rho = 0$) [16]. This dependence is shown at the $V = 0$ axis by a dotted line. According to Eq. (28), the value of $\omega^2 - k^2$ can be interpreted as the effective plasma frequency inside the soliton. The maximum values of ϕ and a occur at the critical soliton velocity V_c (see Fig. 2) and increase as the number of nodes p increases.

We see that there is no continuous transition from the $V = 0$ soliton (the so-called half-cycle soliton [16]) to moving solitons ($p \neq 0$). As is well known, an approximate analytical solution can be found in the small-amplitude limit at V close to 1 (see [12, 15, 42, 43]). The approximate analytical solution shows a continuous transition from moving solitons to $V = 0$ solitons. However, the full system does not allow for such a transition. The same result was obtained by Kuhel *et al.* [44] in the limit $\omega \gg 1$ and by Krammer *et al.* [45] for Langmuir solitons. We note that half-cycle standing solitons with $p = 0$ in the limit $\rho = 0$ exist and are stable [16] and that this type of soliton was observed in PIC simulations of laser–plasma interaction (see [2–4]).

As was mentioned above, in the case of a relativistic (but lower than $\sqrt{m_i/m_e}$) soliton amplitude, the ions can be assumed to be at rest during the period of time on the order of $2\pi\sqrt{m_i/m_e}\omega_{pe}^{-1} = 2\pi\omega_{pi}^{-1}$. Over this time period, the analytical solution obtained in [16] provides a rather good description of a low-frequency zero-velocity soliton. However, for times longer than $2\pi\omega_{pi}^{-1}$, the ponderomotive pressure of the electromagnetic field inside the soliton starts digging a hole in the ion density, and the parameters of the soliton change [46].

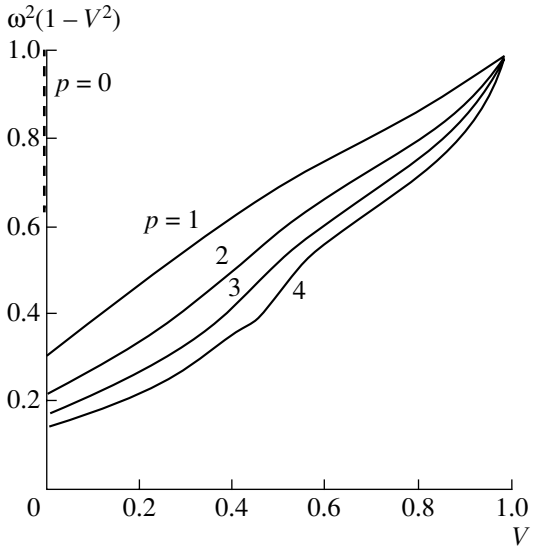

Fig. 1. The square of the effective plasma frequency inside the soliton, $\omega^2(1 - V^2)$, vs. the soliton velocity for $p = 1$, 2, 3, and 4 (the ions are assumed to be at rest) and the square of the frequency of a soliton with $p = 0$ and $V = 0$ (dotted line).

5.2. Electron–Ion Relativistic Solitons

When the ion dynamics is taken into account (i.e., $\rho \neq 0$), the picture drastically changes. In what follows, we choose $\rho = 1/1836$.

Let us first investigate the case $p = 1$ (which corresponds to a soliton with one node in the profile of the vector potential) in more detail. In Fig. 3, the value of $\omega^2(1 - V^2)$ is plotted versus V. At V smaller than the bifurcation velocity $V_{bif} \approx 0.175$, no solutions exist. For $V_{bif} < V < V_{br} \approx 0.32$, two solutions are found, while, for $V > V_{br}$, we have a single solution with a frequency close to that of a soliton obtained in the approximation of immobile ions ($\rho = 0$). In Fig. 3, the values of V_{bif} and V_{br} are shown for the $p = 1$ soliton.

We call V_{br} the breaking velocity, because, as will be shown below, at $V = V_{br}$, a singularity appears in the soliton solution described by the lower branch of the curves presented in Fig. 3. At high frequencies (and velocities), the ion dynamics is negligible. However, its role increases as the velocity decreases. The ions tend to pile up at the soliton center, while the electrons pile up at its edges. In the range $V_{bif} < V < V_{br}$, the lower branch has features quite different from the higher branch. In the solitons described by the lower branch, the amplitudes of the potentials are larger and the density profiles are much more peaked, as is seen in Fig. 4, in which the maximum value of the electrostatic potential (Fig. 4a) and the vector potential (Fig. 4b) inside the soliton are plotted versus V for the same parameters as in Fig. 3. At $V = V_{br}$ and $\omega^2 \approx 0.224$, the lower branch ends because of the soliton breaking; accordingly, n_i

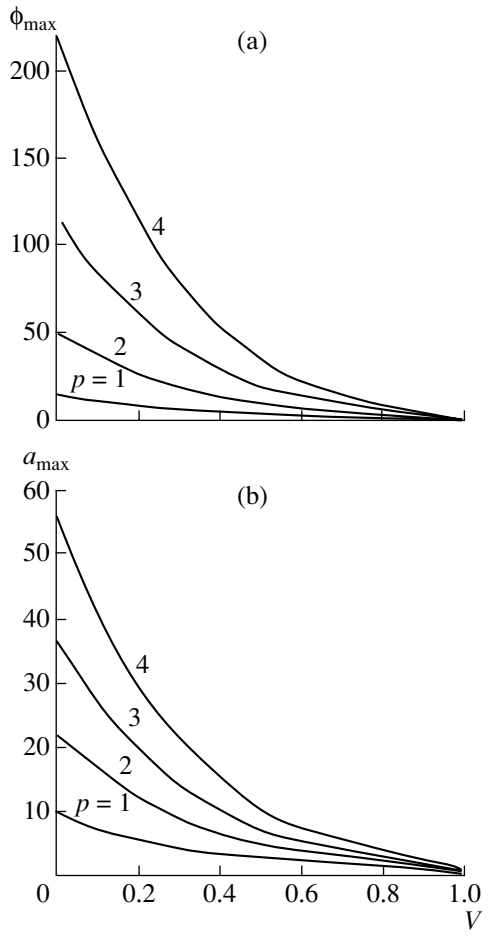

Fig. 2. The maximum values of (a) the electrostatic potential and (b) vector potential inside the soliton vs. the soliton velocity for the same parameters as in Fig. 1.

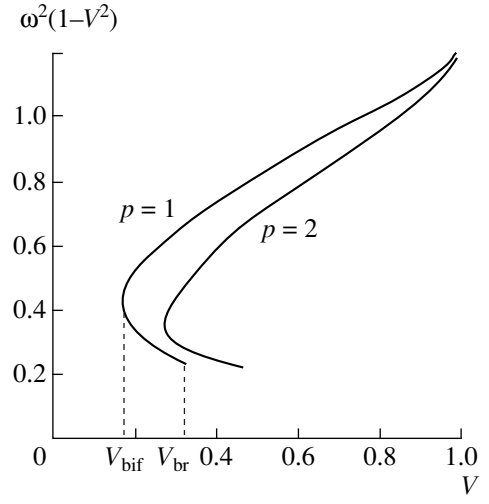

Fig. 3. The square of the effective plasma frequency inside the soliton, $\omega^2(1 - V^2)$, vs. the soliton velocity for $p = 1, 2$ in the case of mobile ions ($\rho = 1/1836$).

tends to infinity at $\xi = 0$ (i.e., $R_i \longrightarrow 0$). From the condition $R_i = 0$ [see Eq. (21)], we obtain the peak value of the potential

$$\phi_{br,0} = (1 - \sqrt{1 - V_{br}^2})/\rho. \quad (64)$$

It away seen in Fig. 4 that both the electrostatic potential and the vector potential are substantially larger at the breaking point than can be from it. For the $p = 1$ soliton, the breaking velocity is approximately equal to $V_{br} = 0.32$.

After breaking, a portion of ions are injected into the acceleration phase. Moving together with the soliton, the ions can be accelerated to higher energies. We can estimate the ion energy gain as

$$E_{ion} \approx \phi_{br,0}/(1 - V_{br}). \quad (65)$$

For $V_{br} = 0.32$, the energy of the accelerated ions is on the order of 70 MeV. This shows that the soliton breaking can provide an additional mechanism for the gener-

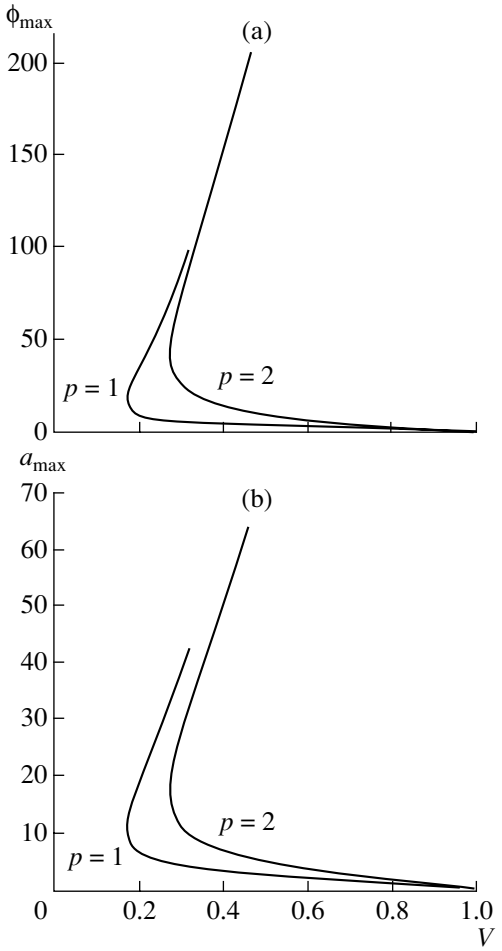

Fig. 4. The maximum values of (a) the electrostatic potential and (b) vector potential inside the soliton vs. the soliton velocity for the same parameters as in Fig. 3.

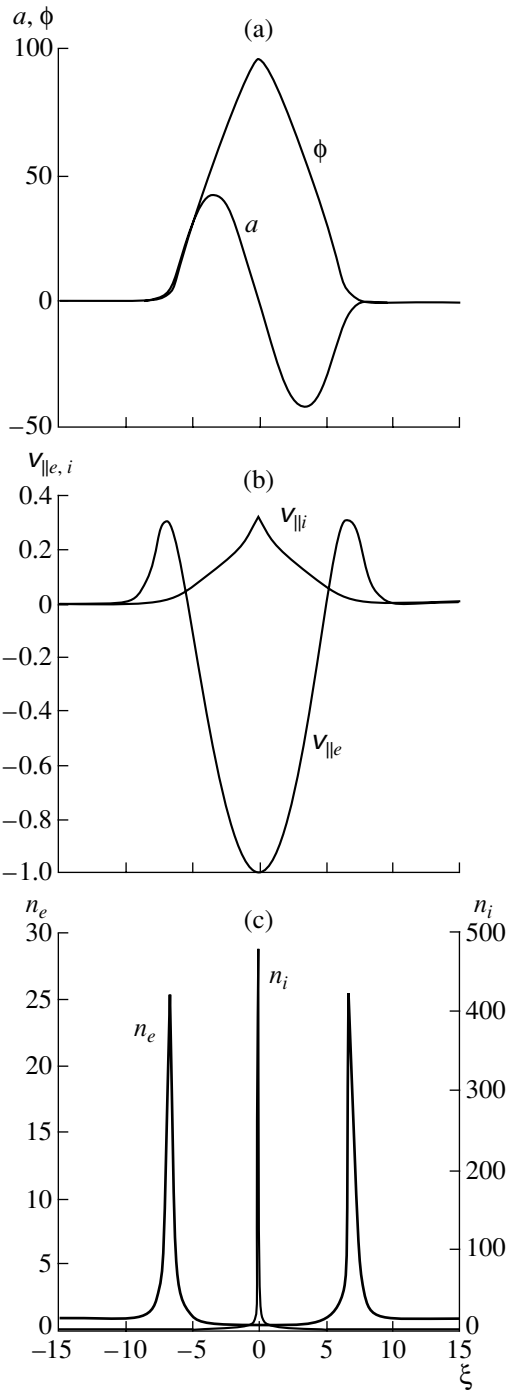

Fig. 5. (a) Electrostatic and vector potentials, ϕ and a; (b) electron and ion velocities, $v_{\|e}$ and $v_{\|i}$; and (c) electron and ion densities vs. ξ inside the $p = 1$ soliton for $V = 0.32$ (close to the breaking conditions).

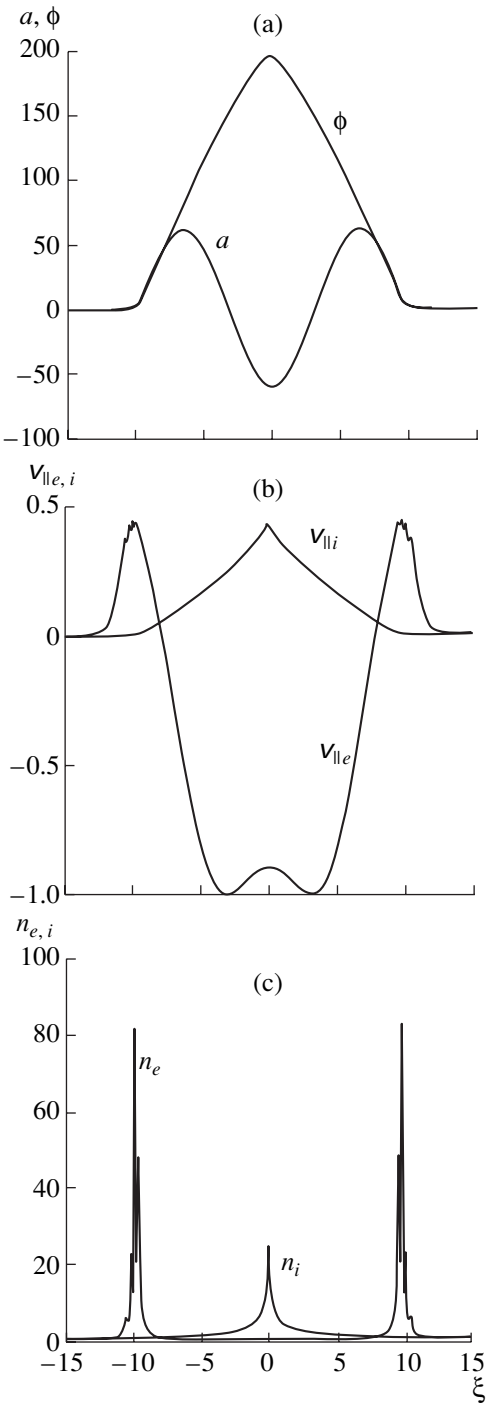

Fig. 6. Same as in Fig. 5 for the $p = 2$ soliton and $V = 0.45$.

ation of fast ions in plasmas irradiated with high-intensity lasers.

As can be seen in Fig. 5, the ion velocity becomes equal to $V_{\rm br}$ in the soliton center, while the electron velocity in the center is close to –1. For small ρ values, the electron velocity is equal to $v_{\|e}(\xi = 0) \approx -1 + O(\rho^2)$. Figure 5a shows the profiles of the electrostatic potential ϕ and the vector potential a, and Fig. 5b shows the velocity of electrons $v_{\|e}$ and ions $v_{\|i}$ versus ξ inside the $p = 1$ soliton. In Fig. 5b, a cusp in the ion velocity profile is seen. Such a cusp is evidence of nonlinear wave breaking. The corresponding dependence of the ion

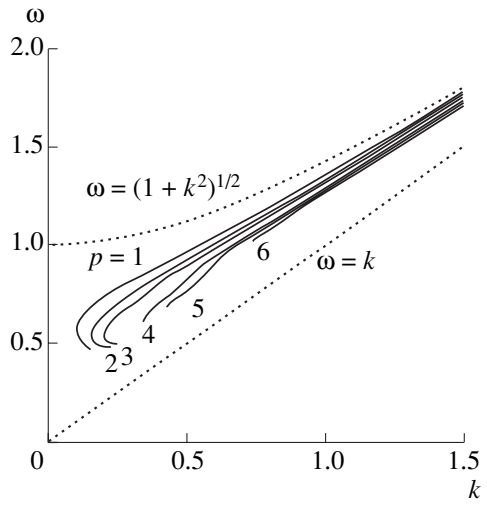

Fig. 7. Soliton frequency ω vs. the soliton wavenumber $k = V$ for solitons with $p = 1, \ldots, 6$.

density on ξ (see Fig. 5c) shows a very peaked distribution in the center (the ion density tends to infinity at this point).

For $p = 2$ (i.e., for a soliton with two nodes in the vector potential profile), similar behavior is observed (see Fig. 6). For $p \geq 3$, we still observe the soliton breaking at a certain finite velocity, but now it occurs due to the self-intersection of electron trajectories and the ion response is relatively weaker. Estimates show that, in this case, the fast electron energy is on the order of 125 MeV.

An analysis of the dependence of the maximum electron and ion velocities on the soliton propagation velocity (which in turn depends on p) demonstrates that, at relatively low propagation velocities, the ion velocity at the breaking point is higher than the electron velocity. At higher propagation velocities, the soliton breaking is related to electron motion.

As the number of the nodes inside the soliton increases, both the bifurcation velocity and the breaking velocity increase. This is seen in Fig. 7, in which the soliton carrier frequency ω is plotted versus the soliton wavenumber $k = V$ for $p = 1, \ldots, 6$. The dotted lines show the dispersion curves for linear electromagnetic waves in a vacuum ($\omega = k$) and in plasma ($\omega = \sqrt{k^2 + 1}$).

An analysis of the dependences of the soliton parameters (the soliton velocity V, the square of the soliton frequency ω^2, and square of the effective plasma frequency $\omega^2(1 - V^2)$) at the breaking point on p shows that they increase with the number of nodes inside the soliton. Also, the dependence of the maximum electron and ion velocities at the breaking point on p demonstrates that, for the lowest node number ($p = 1, 2$), the ion velocity is larger than the electron velocity. As p increases, the ion velocity becomes less than the electron velocity. This is in agreement with the previous results that demonstrate the increase in the electron velocity and the decrease in the ion velocity at the breaking point with increasing soliton propagation velocity.

The dependence of the soliton energy (the electromagnetic field energy plus the kinetic energy of the plasma) at the breaking point on the number of nodes is nonmonotonic. We found that, in the range of low node numbers, the soliton energy first increases; reaches its maximum at $p = 4, 5$; and then decreases.

6. CONCLUSION

We have investigated in detail the influence of ion motion on the dynamics of relativistic electromagnetic solitons in a collisionless plasma. We have found various nonlinear modes in the limit of low wave propagation velocities. It is shown that, in addition to the well-known bright solitons with a localized maximum of the electromagnetic energy density, there are also dark solitons with a localized minimum of the electromagnetic energy density and collisionless electromagnetic relativistic shock waves. We have shown that a dark soliton can advect the particles trapped inside an effective well formed by the radiation pressure. The trapped particles can gain an energy higher than the kinetic energy of the particles of the background plasma inside the soliton. The shock wave is compressional; it separates the region with no electromagnetic field and the region with a slowly propagating electromagnetic wave and the moving electron–ion plasma. The collisionless shock wave also describes the penetration of a relativistically strong electromagnetic wave into an overdense plasma.

We have studied bright solitons by numerically solving the boundary problem for the set of nonlinear differential equations. We have shown that, under the assumption that the ions are at rest, there is no continuous transition from the $V = 0$ soliton (the half-cycle soliton [16]) to moving ($p \neq 0$) solitons. In the small-amplitude limit, an approximate analytical solution can be found that shows a continuous transition from moving solitons to the $V = 0$ soliton. However, this solution does not satisfy the full set of equations.

When the ion dynamics is taken into account, the picture drastically changes. Solitons were found to exist at propagation velocities larger than V_{bif}. In the range $V_{bif} < V < V_{br}$, two types of solitons can exist. High-frequency solitons exist at $V > V_{bif}$, and low-frequency solitons exist in the velocity range $V_{bif} < V < V_{br}$. At $V = V_{br}$, the soliton breaks. As a result, some ions are injected into the acceleration phase and gain energy. Thus, the soliton breaking can provide a new mechanism for electron and ion acceleration in a plasma irradiated with high-intensity lasers. The investigation of mechanisms for ion acceleration is of great importance for various applications. Among them, the fast ignition of fusion targets by intense laser-accelerated proton beams is one of the most important [47, 48].

ACKNOWLEDGMENTS

We are grateful to F. Cattani and F. Pegoraro for fruitful discussions. S.V. Bulanov appreciates the support of the Russian Foundation on Basic Research (project no. 99-02-16997).

REFERENCES

1. G. B. Whitham, *Linear and Nonlinear Waves* (Wiley, New York, 1974; Mir, Moscow, 1977).
2. S. V. Bulanov, I. N. Inovenkov, V. I. Kirsanov, *et al.*, Phys. Fluids B **4**, 1935 (1992).
3. S. V. Bulanov, T. Zh. Esirkepov, N. M. Naumova, *et al.*, Phys. Rev. Lett. **82**, 3440 (1999).
4. S. V. Bulanov, F. Califano, T. Zh. Esirkepov, *et al.*, J. Plasma Fusion Res. **75**, 506 (1999).
5. S. V. Bulanov, F. Califano, T. Zh. Esirkepov, *et al.*, Physica D (Amsterdam) **152–153**, 682 (2001).
6. S. V. Bulanov, N. M. Naumova, and F. Pegoraro, Phys. Plasmas **1**, 745 (1994).
7. T. Honda, K. Nishihara, T. Okamoto, *et al.*, J. Plasma Fusion Res. **75**, 219 (1999).
8. Y. Sentoku, T. Zh. Esirkepov, K. Mima, *et al.*, Phys. Rev. Lett. **83**, 3434 (1999).
9. C. A. Coverdale, C. B. Darrow, C. D. Decker, *et al.*, Fiz. Plazmy **22**, 685 (1996) [Plasma Phys. Rep. **22**, 617 (1996)].
10. J. I. Gerstein and N. Tzoar, Phys. Rev. Lett. **35**, 934 (1975).
11. N. L. Tsintsadze and D. D. Tskhakaya, Zh. Éksp. Teor. Fiz. **72**, 480 (1977) [Sov. Phys. JETP **45**, 252 (1977)]; L. N. Tsintsadze, K. Nishikawa, T. Tajima, and T. Mendonca, Phys. Rev. E **60**, 7435 (1999).
12. V. A. Kozlov, A. G. Litvak, and E. V. Suvorov, Zh. Éksp. Teor. Fiz. **76**, 148 (1979) [Sov. Phys. JETP **49**, 75 (1979)].
13. P. K. Shukla, N. N. Rao, M. Y. Yu, and N. L. Tsintsadze, Phys. Rep. **138**, 1 (1986).
14. A. G. Litvak, in *Reviews of Plasma Physics*, Ed. by M. A. Leontovich (Atomizdat, Moscow, 1980; Consultants Bureau, New York, 1986), Vol. 10.
15. P. K. Kaw, A. Sen, and T. Katsouleas, Phys. Rev. Lett. **68**, 3172 (1992).
16. T. Zh. Esirkepov, F. F. Kamenets, S. V. Bulanov, and N. M. Naumova, Pis'ma Zh. Éksp. Teor. Fiz. **68**, 33 (1998) [JETP Lett. **68**, 36 (1998)].
17. D. Farina, M. Lontano, and S. V. Bulanov, Phys. Rev. E **62**, 4146 (2000).
18. G. A. Mourou, C. P. J. Barty, and D. Perry, Phys. Today **51** (1), 22 (1998).
19. G. S. Sarkisov, V. Yu. Bychenkov, V. N. Novikov, *et al.*, Phys. Rev. E **59**, 7042 (1999).
20. T. Zh. Esirkepov, Y. Sentoku, F. Califano, *et al.*, Pis'ma Zh. Éksp. Teor. Fiz. **70**, 80 (1999) [JETP Lett. **70**, 82 (1999)].
21. K. Krushelnik, E. L. Clark, M. Zepf, *et al.*, Phys. Plasmas **7**, 2055 (2000).
22. S. V. Bulanov, T. Zh. Esirkepov, F. Califano, *et al.*, Pis'ma Zh. Éksp. Teor. Fiz. **71**, 593 (2000) [JETP Lett. **71**, 407 (2000)].
23. R. A. Snavely, M. H. Key, S. P. Hatchett, *et al.*, Phys. Rev. Lett. **85**, 2945 (2000).
24. Y. Sentoku, T. V. Lisseikina, T. Zh. Esirkepov, *et al.*, Phys. Rev. E **62**, 7271 (2000).
25. A. V. Kuznetsov, T. Zh. Esirkepov, F. F. Kamenets, and S. V. Bulanov, Fiz. Plazmy **27**, 225 (2001) [Plasma Phys. Rep. **27**, 211 (2001)].
26. S. V. Bulanov, V. A. Vshivkov, G. I. Dudnikova, *et al.*, Fiz. Plazmy **25**, 764 (1999) [Plasma Phys. Rep. **25**, 701 (1999)].
27. K. Mima, T. Ohsuga, H. Takabe, *et al.*, Phys. Rev. Lett. **57**, 1421 (1986).
28. L. M. Gorbunov, P. Mora, R. R. Ramazashvili, and A. A. Solodov, Phys. Plasmas **7**, 375 (2000).
29. A. I. Akhiezer and R. V. Polovin, Zh. Éksp. Teor. Fiz. **30**, 915 (1956) [Sov. Phys. JETP **3**, 696 (1956)].
30. Yu. S. Kivshar and B. Luther-Davies, Phys. Rep. **298**, 8 (1998).
31. Yu. S. Kivshar and D. P. Pelinovsky, Phys. Rep. **331**, 117 (2000).
32. S. Burger, K. Bongs, S. Dettmer, *et al.*, Phys. Rev. Lett. **83**, 5198 (1999).
33. K. Burnett, M. Edwards, and C. W. Clark, Phys. Today **52**, 37 (1999).
34. D. Farina and S. V. Bulanov, Phys. Rev. Lett. (in press).
35. P. Kaw and J. M. Dawson, Phys. Fluids **13**, 477 (1970).
36. J. H. Marburger and R. F. Tooper, Phys. Rev. Lett. **35**, 1001 (1975).
37. V. V. Goloviznin and T. Schep, Pis'ma Zh. Éksp. Teor. Fiz. **70**, 445 (1999) [JETP Lett. **70**, 450 (1999)].
38. F. Cattani, A. Kim, D. Anderson, and M. Lisak, Phys. Rev. E **62**, 1234 (2000).
39. A. Kim, F. Cattani, D. Anderson, and M. Lisak, Pis'ma Zh. Éksp. Teor. Fiz. **72**, 335 (2000) [JETP Lett. **72**, 241 (2000)].
40. R. Z. Sagdeev, in *Reviews of Plasma Physics*, Ed. by M. A. Leontovich (Atomizdat, Moscow, 1964; Consultants Bureau, New York, 1968), Vol. 4.
41. A. R. Champneys, Physica D (Amsterdam) **112**, 158 (1998).
42. V. I. Berezhiani and S. M. Mahajan, Phys. Rev. Lett. **73**, 1110 (1994).
43. R. N. Sudan, Ya. S. Dimant, and O. B. Shiryaev, Phys. Plasmas **4**, 1489 (1997).
44. H. H. Kuehl and C. Y. Zhang, Phys. Rev. E **48**, 1316 (1993).
45. H. Krammer, E. W. Laedke, and K. H. Spatschek, Phys. Rev. Lett. **52**, 1226 (1984).
46. N. M. Naumova, S. V. Bulanov, T. Zh. Esirkepov, *et al.*, Phys. Rev. Lett. (in press).
47. M. Roth, T. E. Cowan, M. H. Key, *et al.*, Phys. Rev. Lett. **86**, 436 (2001).
48. H. Ruhl, S. V. Bulanov, T. E. Cowan, *et al.*, Fiz. Plazmy **27**, 387 (2001) [Plasma Phys. Rep. **27**, 363 (2001)].

Translated by the authors

Plasma Physics Reports, Vol. 27, No. 8, 2001, pp. 652–658. Translated from Fizika Plazmy, Vol. 27, No. 8, 2001, pp. 693–699.

PLASMA DYNAMICS

Heat Transport from the Region of Local Electron Heating in a Plasma

V. G. Ledenev and A. P. Starygin

Institute of Solar and Terrestrial Physics, Siberian Division, Russian Academy of Sciences, Irkutsk, 664033 Russia

Received July 26, 2000; in final form, January 18, 2001

Abstract—The initial stage of the one-dimensional expansion of a hot electron cloud into a "warm" plasma (i.e., into a plasma with a finite electron temperature) is studied with allowance for plasma turbulence. It is shown that, in a nonturbulent plasma or in a plasma with sufficiently weak turbulence, counterstreaming warm plasma flows interpenetrate one another; in this process, the plasma flows are accelerated and form beams escaping from the heating region. A stronger turbulence gives rise to electron heat waves that also propagate away from the heating region. © *2001 MAIK "Nauka/Interperiodica".*

Rapid local heating of plasma electrons is often observed in laboratory experiments [1] and space plasmas, e.g., in solar flares [2]. The initial stage of the expansion of hot electrons from the heating region in a collisionless plasma can be described under the assumption that hot electrons interact only with cold plasma electrons and do not interact with plasma ions. For a plasma in a magnetic field, the problem reduces to that of studying the one-dimensional expansion of hot electrons. In this case, it is also necessary to take into account the possible onset of plasma instability within the front of the expanding electron cloud [3]. In this formulation, the problem under consideration was solved by Ivanov *et al.* [4]. They determined the parameters of a so-called electron heat wave, or a jump in the density of hot electrons expanding from the heating region. On the other hand, it is of interest to investigate the behavior of the cold electrons that are accelerated by the electric field produced by an expanding hot electron cloud. It is clear that, sooner or later, the initial heating region will be dominated by cold electrons. If the temperature of the cold electrons is zero, the potential barrier produced by the excess electrons reflects the incoming electrons. If the temperature of the cold electrons is finite (such electrons will be called "warm" electrons), the potential barrier produced by the excess electrons, on the one hand, decelerates the incoming flows of cold electrons and, on the other, accelerates cold electrons with energies high enough to overcome the potential barrier, in which case the counterstreaming flows of cold electrons interpenetrate one another. These flows may give rise to a two-stream instability in the heating region [5]. It would be also of interest to analyze this aspect of the problem. Our purpose here is to trace the evolution of the distribution function of the cold electrons that fill the initial heating region and to follow the temporal and spatial evolutions of both the distribution function of the hot electrons and their density.

Let the plasma electrons be rapidly heated in a local plasma region. It is well known that locally heated electrons tend to escape from the heating region, thereby giving rise to a return current of cold electrons, which ensures plasma quasineutrality. In this case, the ions, having large inertial mass, remain essentially immobile. In the one-dimensional approximation, the electron motion and the interaction between hot electrons and cold electrons with a finite temperature (below, the latter will be called warm electrons) are described by the set of equations

$$\begin{aligned} &\partial f_h/\partial t + v(\partial f_h/\partial x) + (e/m)(\partial\varphi/\partial x)(\partial f_h/\partial v) = 0,\\ &\partial f_c/\partial t + v(\partial f_c/\partial x) + (e/m)(\partial\varphi/\partial x)(\partial f_c/\partial v) = 0,\\ &\partial^2\varphi/\partial x^2 = 4\pi e(\int f_c dv + \int f_h dv - n_0). \end{aligned} \quad (1)$$

Here, f_h and f_c are the distribution functions of the hot and warm electrons, respectively; φ is the electric potential; n_0 is the background plasma density; and e and m are the charge and mass of an electron. The first two equations in set (1) describe the behavior of the one-dimensional distribution functions of hot and warm electrons, and the third equation is Poisson's equation.

In simulations, we used a componentwise splitting scheme based on one-dimensional monotonic schemes with a SUPERBEE limiting procedure and Harten compression [6]. The length of the heating region was equal to four Debye radii, the spatial step was 0.2 of the Debye radius, and the temperature ratio between the warm and hot electrons was 1/100.

To illustrate the states of the system at different times, Figs. 1 and 2 show the contours of the distribution functions of the hot and warm electrons (Fig. 1),

1063-780X/01/2708-0652$21.00 © 2001 MAIK "Nauka/Interperiodica"

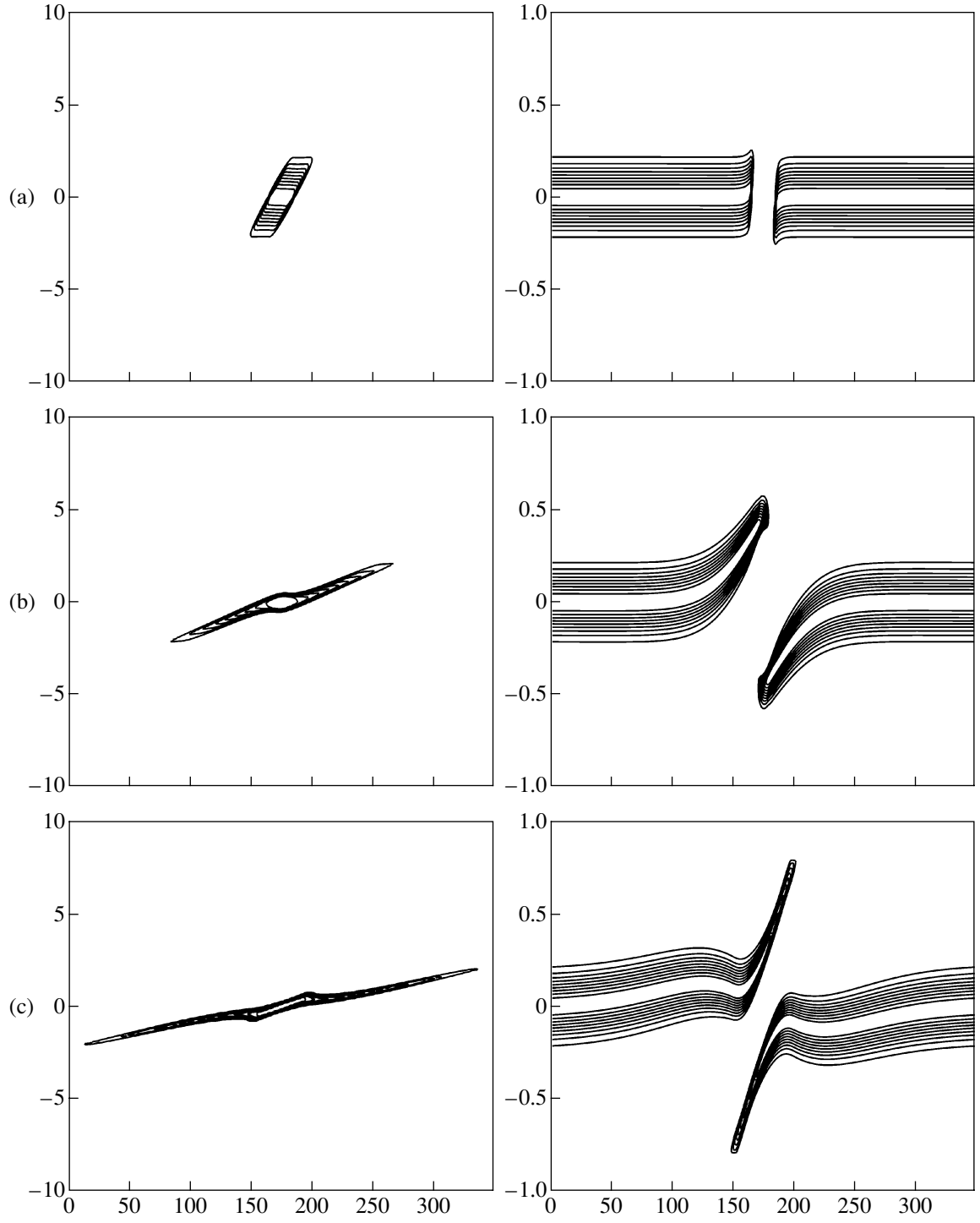

Fig. 1. Contours of the distribution functions of the hot (left) and warm (right) electrons at the times t = (a) $3.2/\omega_{pe}$, (b) $16/\omega_{pe}$, and (c) $30.4/\omega_{pe}$. On the abscissa, a division is the spatial step (0.2 of the Debye radius) adopted in simulations. The ordinate is the normalized electron velocity.

the density distributions of the hot (Fig. 2a) and warm (Fig. 2b) electrons, the distribution function of the hot electrons at the center of the heating region (Fig. 2c), and the electric potential distribution (Fig. 2d). The calculated results shown in Figs. 1 and 2 were obtained for Maxwellian initial distributions of the hot and warm electrons and a rectangular initial distribution of the density of hot electrons.

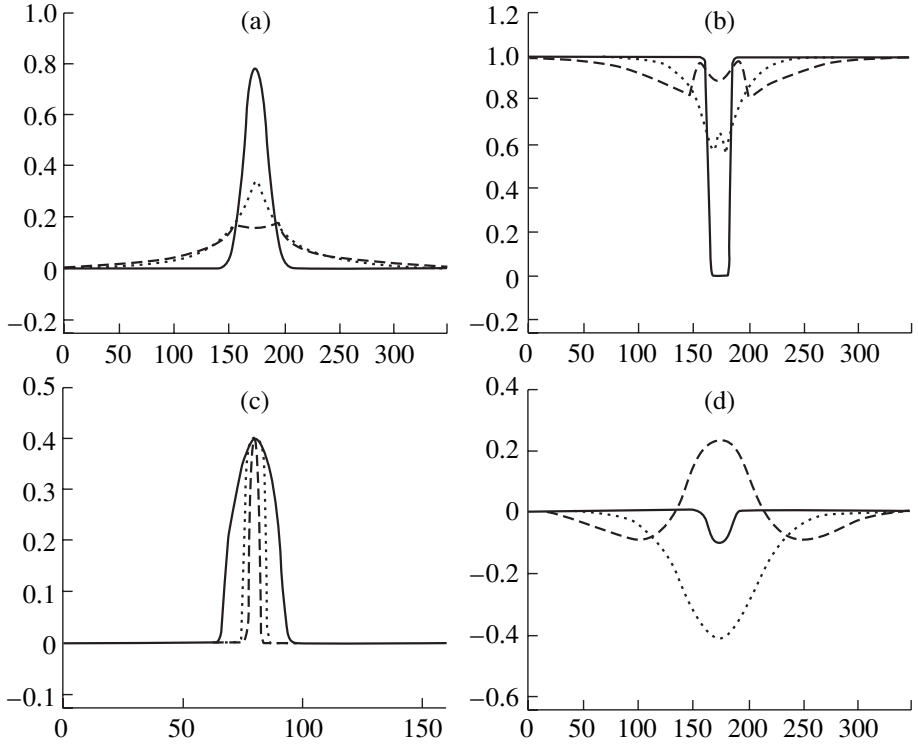

Fig. 2. Spatial distributions of the density of (a) hot and (b) warm electrons, (c) the distribution function of the hot electrons at the center of the heating region (the velocity is in arbitrary units), and (d) the spatial distribution of the electric potential, calculated at different times $t = 3.2/\omega_{pe}$ (solid curve), $16/\omega_{pe}$ (dotted curve), and $30.4/\omega_{pe}$ (dashed curve).

From Figs. 1 and 2, we can see that the expansion of hot electrons is accompanied by the acceleration of warm electrons, which form a counterstreaming flow and replace hot electrons in the heating region. As warm electrons accumulate in the heating region and produce a potential barrier, the counterstreaming electron flows interpenetrate one another, because the most energetic warm electrons overcome the barrier and are accelerated by the electric field produced by the excess electrons. In this case, the distribution function of the accelerated electrons that have overcome the potential barrier has a distinctly beamlike character (Fig. 1c). As for the two-stream instability, it does not occur in the case at hand, presumably because the counterstreaming electron flows interact in a finite-size region (although the initial stage of the formation of vortices in phase space is seen in Fig. 1b).

Another effect that should be taken into account is the possible onset of a plasma instability at the front of an expanding electron cloud [1, 3, 4]. In the case under consideration, this instability is most likely a beam instability [3], which develops as hot electrons escape from the heating region. The instability can be included in the analysis by supplementing the right-hand sides of the kinetic equations with diffusion terms in which the diffusion coefficients are proportional to the spectral energy density of the plasma turbulence. The related simulations were carried out by the method of separating the physical processes [7]. The basic set of equations for this case has the form

$$\begin{aligned}
&\partial f_h/\partial t + v(\partial f_h/\partial x) \\
&+ (e/m)(\partial\varphi/\partial x)(\partial f_h/\partial v) = 0, \\
&\partial f_h/\partial t - (\partial/\partial v)(A/v)(\partial/\partial v) f_h = 0, \\
&\partial f_c/\partial t + v(\partial f_c/\partial x) + (e/m)(\partial\varphi/\partial x)(\partial f_c/\partial v) = 0, \\
&\partial f_c/\partial t - (\partial/\partial v)(A/v)(\partial/\partial v) f_c = 0, \\
&\partial^2\varphi/\partial x^2 = 4\pi e(\int f_c dv + \int f_h dv - n_0),
\end{aligned} \tag{2}$$

where the constant A determines the level of plasma turbulence. In set (2), the first and third equations describe the expansion of hot and warm electrons with allowance for the electric field, and the second and fourth equations describe turbulence-driven electron diffusion in velocity space.

The results computed for $A = 10^{-4}$ are shown in Figs. 3 and 4, and the results obtained for $A = 10^{-2}$ are displayed in Figs. 5 and 6. In the simulations, the initial length of the heating region was equal to ten Debye radii and the spatial step was 0.5 of the Debye radius. In order of magnitude, coefficient A corresponds to the

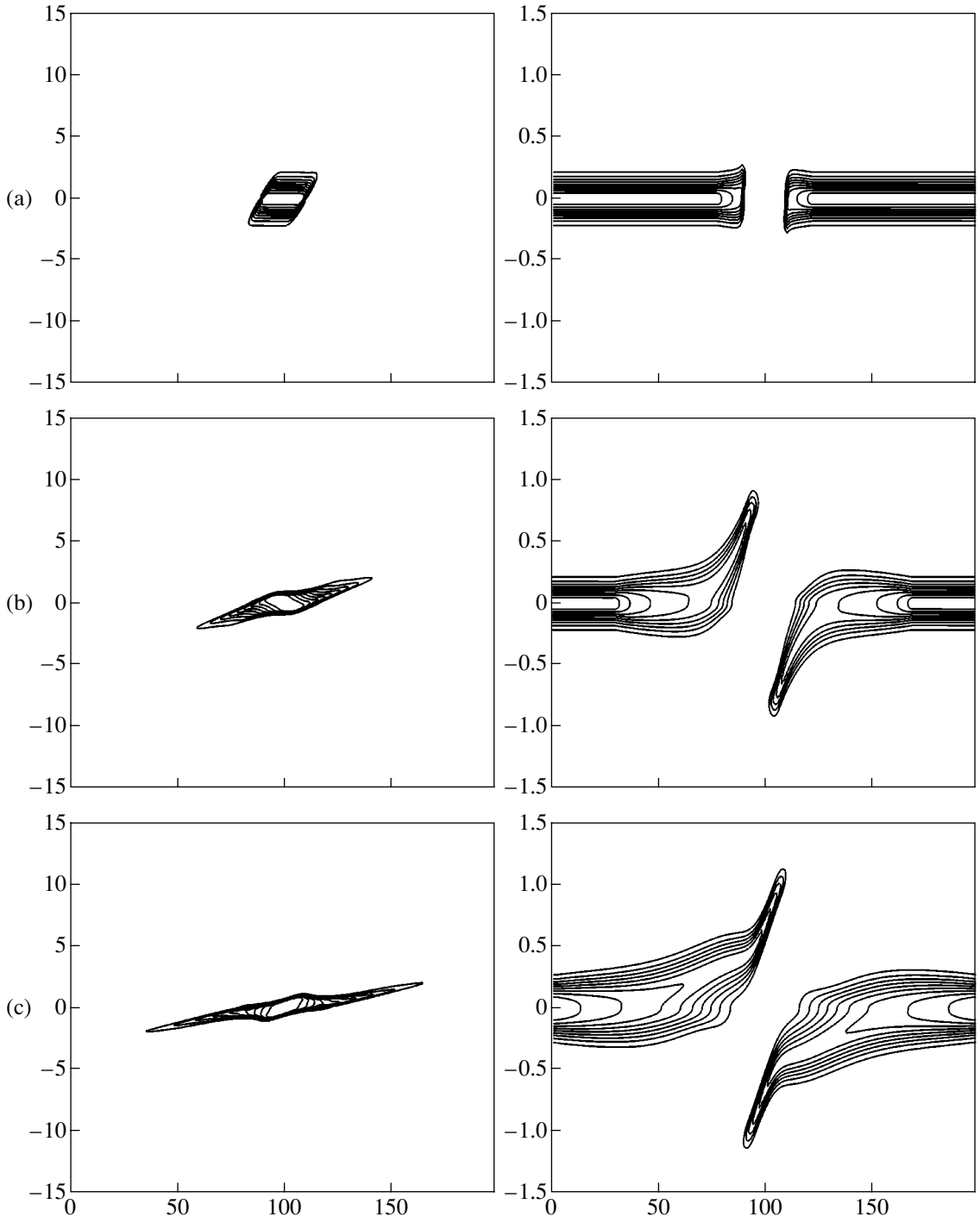

Fig. 3. The same as in Fig. 1 but for a low turbulence level at the times t = (a) $3.2/\omega_{pe}$, (b) $16/\omega_{pe}$, and (c) $28.8/\omega_{pe}$. On the abscissa, a division is the spatial step equal to 0.5 of the Debye radius.

ratio of the energy density of the plasma waves to the energy density of the hot electrons. Since $A \ll 1$, we can assume that, in our problem, plasma turbulence does not perturb the energy balance. For simplicity, we assumed that the energy density of the plasma turbulence is uniformly distributed in the region occupied by hot electrons. From Fig. 3–6, one can see that, at low and high levels of plasma turbulence, the interaction between hot and warm electrons occurs in different ways. At a lower turbulence level (Figs. 3, 4), electron

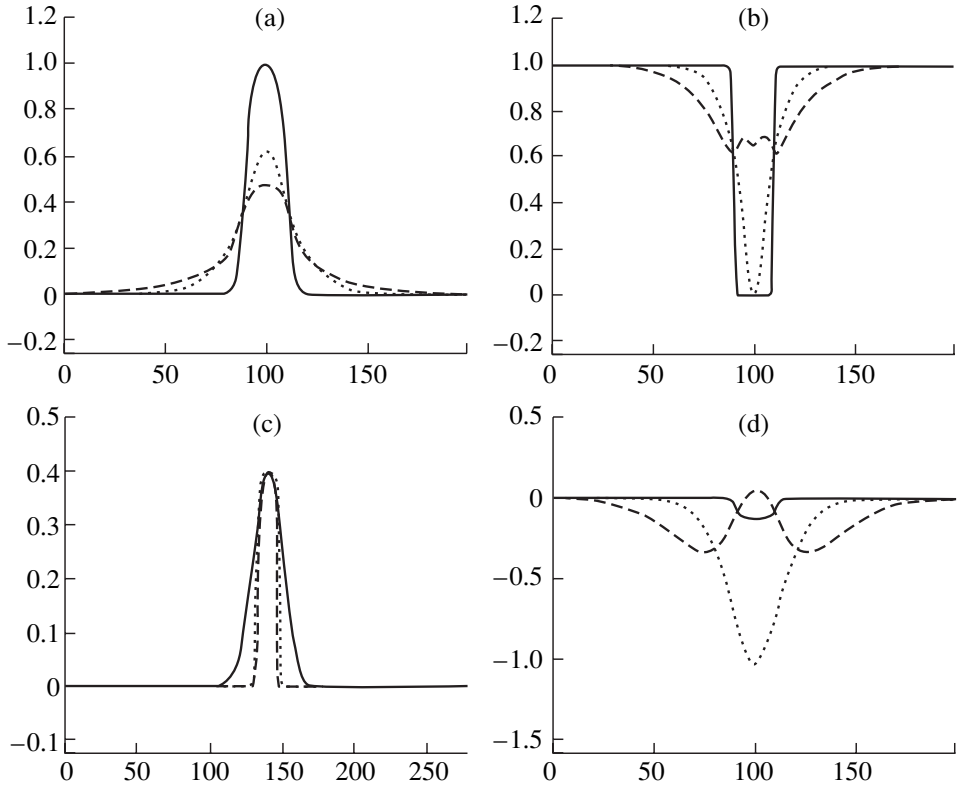

Fig. 4. The same as in Fig. 2 but for a low turbulence level at the times $t = 3.2/\omega_{pe}$ (solid curve), $16/\omega_{pe}$ (dotted curve), and $28.8/\omega_{pe}$ (dashed curve).

diffusion, although pronounced, does not play a dominant role. As is the case in a nonturbulent plasma, the main effect is the acceleration of warm electrons toward the heating region, followed by the formation of electron beams escaping from the heating region (Figs. 3b, 3c). At a higher turbulence level (Figs. 5, 6), the main effect is the diffusion of warm electrons in velocity space, i.e., their heating to substantially higher temperatures. In this case, the heated electrons occupy a finite-size region with sharp boundaries, thereby forming an electron heat wave moving away from the heating region at a speed on the order of the electron thermal velocity. On the other hand, Figs. 5 and 6 show that the rate at which the initial hot plasma region cools is markedly lower.

DISCUSSION

Our simulations of the initial stage of the expansion of hot electrons from the heating region and their replacement by warm electrons have shown that the expansion process is accompanied by the acceleration of warm electrons toward the heating region, in agreement with the simulation results described in monograph [1]. However, further evolution of the plasma may proceed in two different ways, depending on the level of turbulence that develops at the front of the expanding electron cloud. At a low turbulence level (for energy densities of $W < 10^{-3} W_0$, where W_0 is the energy density of the hot electrons), the main effect is the acceleration of a small fraction of warm electrons during the interpenetration of the counterstreaming electron flows moving toward the initial heating region (Figs. 3, 4). The accelerated electrons move away from the initial heating region, and their distribution functions are distinctly beamlike in character. The energy of these electrons is one order of magnitude higher than the warm-plasma energy, provided that the latter is two orders of magnitude lower than the hot-plasma energy. Although the electron diffusion is pronounced, it plays a very minor role. At higher energy densities of the plasma turbulence, $W > 10^{-3} W_0$ (Figs. 5, 6), the plasma evolution is radically different. The main effects are the diffusion of warm electrons in velocity space and the formation of an electron heat wave (Fig. 5) [4]. This wave is represented by the warm electrons that are heated to higher temperatures and occupy a region with sharp boundaries, whose characteristic dimension is approximately equal to the Debye radius. The wave front moves away from the heating region at a speed on the order of the thermal velocity of the heated electrons. Inside the heating region, the speed of the wave front is

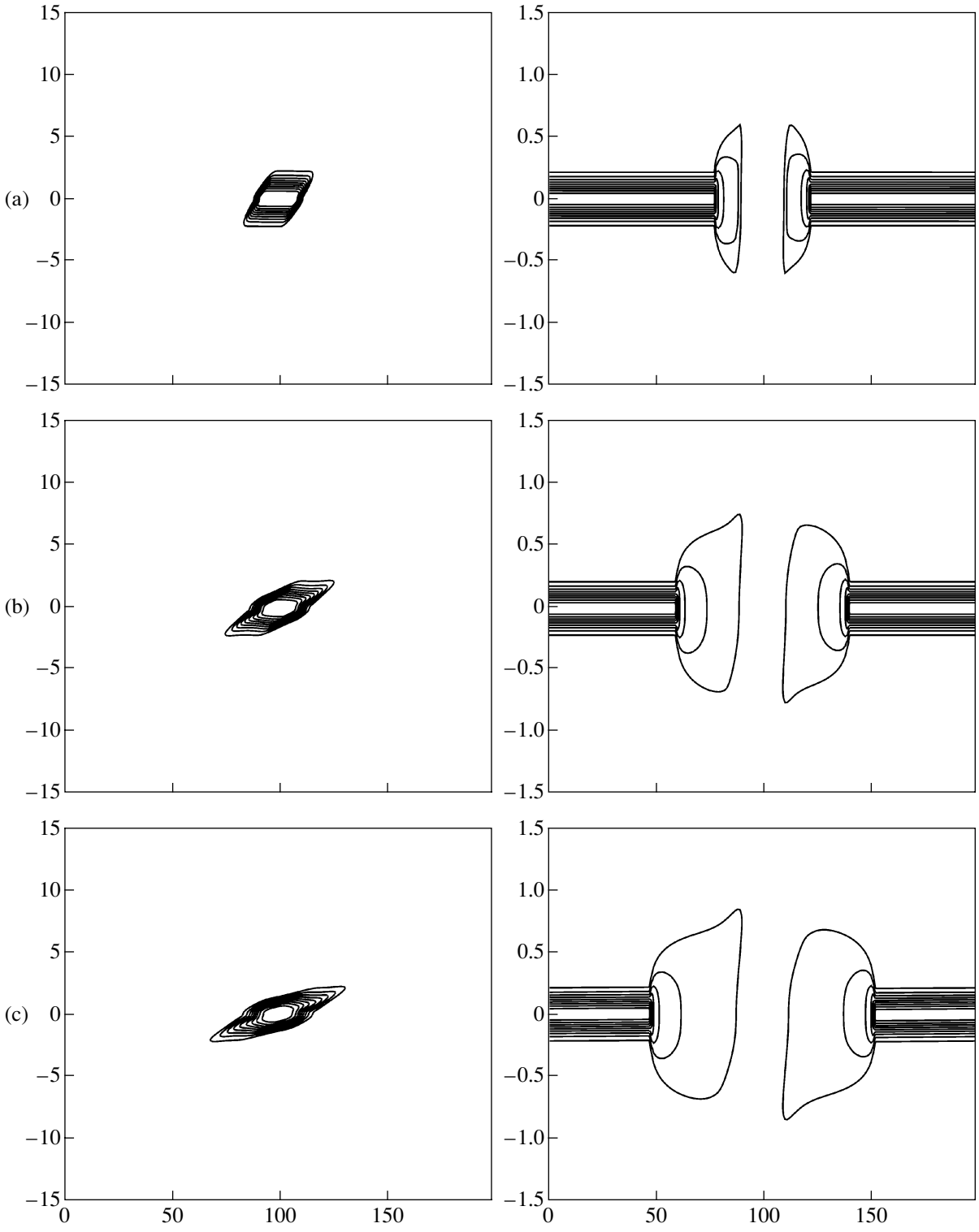

Fig. 5. The same as in Fig. 1 but for a high turbulence level at the times t = (a) $3.2/\omega_{pe}$, (b) $8/\omega_{pe}$, and (c) $11.2/\omega_{pe}$. On the abscissa, a division is the spatial step equal to 0.5 of the Debye radius.

significantly lower; this indicates a markedly lower rate at which the hot plasma region cools at a high turbulence level.

We emphasize that we have considered only the initial stage of cooling of the region of hot electrons, specifically, cooling on time scales shorter than the ion

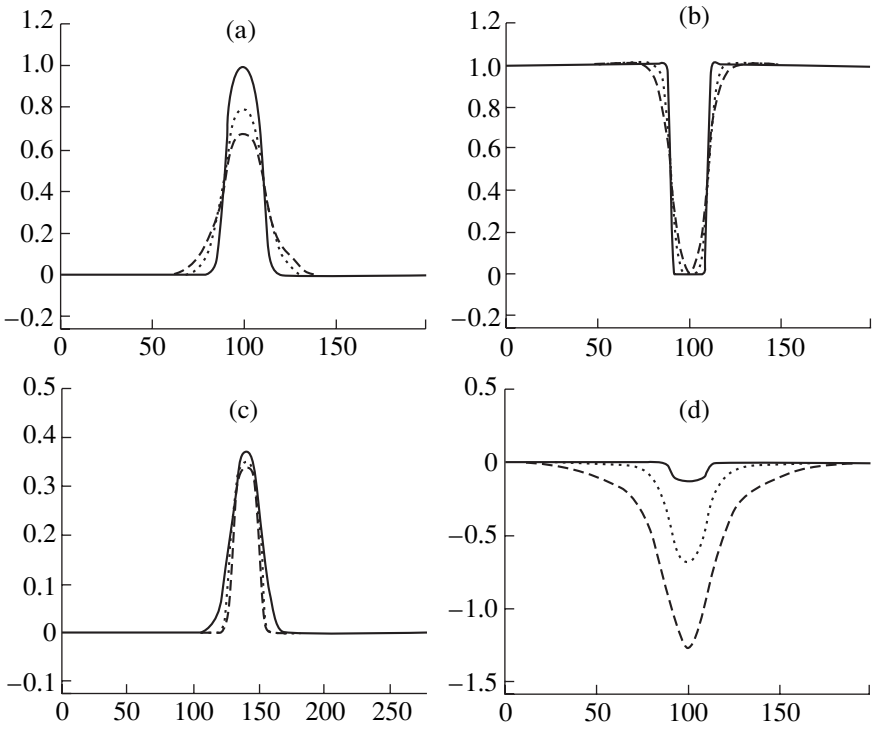

Fig. 6. The same as in Fig. 2 but for a high turbulence level at the times $t = 3.2/\omega_{pe}$ (solid curve), $8/\omega_{pe}$ (dotted curve), and $11.2/\omega_{pe}$ (dashed curve).

plasma period. At this stage, the plasma ions still remain almost immobile. On longer time scales, it is necessary to take into account ion motion under the action of an electrical potential gradient created in the initial heating region.

ACKNOWLEDGMENTS

This study was supported in part by the Russian Foundation for Basic Research, project no. 98-02-17727.

REFERENCES

1. A. A. Ivanov, *The Physics of Strongly Nonequilibrium Plasma* (Nauka, Moscow, 1977).
2. Z. Svestka, in *Solar Flares* (D. Reidel, Dordrecht, 1976), p. 399.
3. A. B. Mikhailovskii, *Theory of Plasma Instabilities* (Nauka, Moscow, 1975; Consultants Bureau, New York, 1974).
4. A. A. Ivanov, L. L. Kozorovitskiĭ, and V. D. Rusanov, Dokl. Akad. Nauk SSSR **184**, 811 (1969) [Sov. Phys. Dokl. **14**, 126 (1969)].
5. N. A. Krall and A. W. Trivelpiece, *Principles of Plasma Physics* (Academic, New York, 1973; Mir, Moscow, 1975).
6. G. S. Rivin and P. V. Voronina, Opt. Atmos. Okeana **10**, 6 (1997).
7. G. I. Marchuk, *Methods of Splitting* (Nauka, Moscow, 1988).

Translated by O. E. Khadin

Plasma Physics Reports, Vol. 27, No. 8, 2001, pp. 659–668. Translated from Fizika Plazmy, Vol. 27, No. 8, 2001, pp. 700–709.

PLASMA DYNAMICS

Hydrodynamic Model of the Penetration of a Magnetic Field into a Plasma with Two Ion Species

A. V. Gordeev

Russian Research Centre Kurchatov Institute, pl. Kurchatova 1, Moscow, 123182 Russia

Received June 1, 2000; in final form, April 2, 2001

Abstract—Hydrodynamic equations are presented that describe the dynamics of a plasma with two ion species in a magnetic field such that $B^2 \gg 8\pi p$. It is shown that there exists a range of values of the ratio of the plasma density to the magnetic field, $\nu_{ii}/\omega_{Bi} < (Z^2M/m)^{1/4}$, within which the frictional force caused by ion–ion collisions dominates over that caused by electron–ion collisions. In this range, the effective conductivity, which governs the magnetic field diffusion, is lower than the conventional electron–ion conductivity by a factor of $\sqrt{M/m}$ and can be as low as $\sigma \simeq enc/B$. The equations derived for this three-component plasma make it possible to self-consistently incorporate local changes in the partial mass and partial charge of each of the ion species in relative motion. The characteristic features of the equations obtained are analyzed by applying them to describe the propagation of a current sheath in a transmission line filled with a multispecies plasma. An analogy is drawn between magnetic phenomena in a plasma with two ion species and in a so-called dusty plasma. © *2001 MAIK "Nauka/Interperiodica".*

1. Vacuum transmission lines with magnetic self-insulation make it possible to efficiently transmit energy in the form of relatively short electromagnetic pulses from the generator to the load [1–3]. For generators in which the current rises fairly slowly, it is more convenient to use transmission lines filled with gas or plasma. In this case, the current in the generator rises as an electromagnetic pulse propagates in the line and becomes maximum when the pulse reaches the load. This peaking effect underlies the operation of various devices in which the transmission line is filled by a gas with an optimum density ensuring efficient energy transmission. A classical example of such systems is a plasma focus device [4–7], in which the current sheath is observed to propagate in a peculiar way along the surface of the positive electrode. For plasma focus devices, the transmission processes that occur before the focusing phase are usually investigated by numerical methods [8].

Here, hydrodynamic equations are presented that describe the dynamics of a current-carrying plasma in devices of the Mather type [5]. In such devices, the current sheath propagates along the coaxial line for a fairly long time before it reaches the edge region and gives rise to current focusing. The equations obtained are analyzed by applying them to describe precisely this initial stage of the propagation of a current sheath along a plasma-filled coaxial transmission line. The characteristic current in a coaxial line is assumed to be $J \geq 1$ MA, and the characteristic radius of the line is taken to be $r < 1$ cm, the coaxial electrodes being separated by a distance of the same order. These parameter values correspond to a magnetic field of $B \geq 10^5$ G. The characteristic plasma density in the interelectrode gap is assumed to be about $n_e \sim 10^{18}$–10^{19} cm^{-3}.

A current flowing through a gas-filled interelectrode gap ionizes the gas, causing the appearance of ions with different charge-to-mass ratios Z/M. Braginskii [9] showed that, in this situation, collisions between heavy particles may substantially increase transverse plasma resistance. This effect stems from the fact that the current flowing across the magnetic field gives rise to the relative motion of the various ion species present and, accordingly, to high friction between them, thereby resulting in additional energy dissipation. However, Braginskii [9] pointed out that, when the ion motion is slow, so that the plasma is in a nearly equilibrium state, the ion density obeys a Boltzmann temperature distribution and the plasma resistivity does not increase. In my paper [10], allowing for the inertial motion of the ions made it possible to demonstrate that the effect of a significant increase in transverse resistivity also takes place in a plasma with two ion species. The increase in transverse resistivity is accompanied by the spatial separation of ions with different ratios Z/M at the wave front [11, 12]. In this multispecies plasma, there exists a certain range of values of the ratio of the plasma density to the magnetic field, $\nu_{ii}/\omega_{Bi} < (Z^2M/m)^{1/4}$, within which the dissipation due to ion–ion collisions dominates over the conventional dissipation due to electron–ion collisions. Thus, it can be suggested that ion–ion collisions play a particularly important role in the formation of a plasma focus, because ion–ion dissipation is associated precisely with heavy ion species and occurs in the volume they occupy, while electron–ion dissipation can occur at a certain distance from the front

1063-780X/01/2708-0659$21.00

of the propagating ions, because the magnetic field is frozen in the electrons (this effect is known as "runaway" of the current sheath).

It should be noted that an analogous effect of the increase in resistivity will inevitably occur during the magnetic contraction of a liner. A significant decrease in resistivity due to ion–ion collisions should result in a partial suppression of the Rayleigh–Taylor instability and a more efficient contraction of the liner.

Note also that ion–ion collisions play a dominant role in the dynamics of dusty plasma, which contains, in addition to ordinary charged particles, dust grains carrying an electric charge. Modeling charged dust grains by very massive ions provides a qualitative description of the dynamics of a dusty plasma in a magnetic field.

The paper is organized as follows. The main estimates that confirm the applicability of the basic hydrodynamic equations are obtained in Section 2. In Sections 3 and 4, the basic equations are used to derive equations describing a plasma with two ion species and with zero thermal pressure. The equations derived are analyzed in Sections 5–8. In Section 9, the dissipation effect is explained and additional references are given to studies dealing with this effect. In Section 10, the equations derived are briefly analyzed by applying them to describe a dusty plasma. The results obtained are summed up in Section 11.

2. Below, we restrict ourselves to analyzing the effect of the increase in plasma resistivity due to ion–ion collisions and its influence on the plasma dynamics. To simplify matters, we start with the equations in which we exclude from consideration the effects that are irrelevant. We use the hydrodynamic equations derived by Braginskii in his review [9]. In these equations, we can neglect the thermal force because all of the quantities are independent of the coordinate along the magnetic field and the electrons are strongly magnetized, $\omega_{Be} \equiv eB/mc \gg \nu_{ei}$. For the same reason, the longitudinal conductivity can also be ignored.

The main assumption in our analysis is that the plasma thermal pressure is much lower than the magnetic field pressure,

$$\frac{B^2}{8\pi} \gg n_i T_i, \quad n_e T_e. \tag{1}$$

In this case, however, the particle temperature cannot be assumed to be zero if, e.g., $\omega_{Be} \gg \nu_{ei}$. Combining this inequality with conditions (1) and using the conductivity estimated in [9], $\sigma = 0.5 \times 10^{31} T^{3/2}$, we obtain the following inequality, which is important for further analysis:

$$B^2 \gg 1.9 \times 10^{-14} n^{5/4}. \tag{2}$$

Here, the magnetic field and density are expressed in G and cm^{-3}, respectively. It can be easily seen that inequality (2) holds for $B \sim 10^5$ G and $n \sim 10^{18}$ cm^{-3}. Note that using condition (50) (see below) instead of $\omega_{Be} \gg \nu_{ei}$ insignificantly affects inequality (2).

The question to be addressed is whether or not taking into account plasma heating by strong currents (for small radii of the current sheath and strong magnetic fields) and enhanced ion–ion dissipation will violate condition (1). To answer this question, we should, first of all, note that, in the stage of current propagation along the transmission line, a nonequilibrium plasma strongly emits radiation, so that the plasma temperature, as a rule, does not exceed $T \sim 10^2$ eV. However, in order to appreciate the level to which the plasma is heated, we make the required estimates under the characteristic heating conditions [9]:

$$\frac{3}{2} n \frac{\partial T}{\partial t} \simeq \frac{j_\perp^2}{\sigma_\perp}. \tag{3}$$

We set $B \sim 10^5$ G and $n \sim 10^{18}$ cm^{-3} and assume that the current rise time and characteristic length scale are $\tau \sim 10^{-7}$ s and $\delta \sim 1$ cm, respectively. As a result, we can estimate the plasma temperature for two limiting cases: (i) for the conventional electron–ion dissipation and (ii) for the effective conductivity $\sigma \simeq enc/B$ (see below).

In the first case, for the adopted parameter values, the above estimate for σ gives $T < 10$ eV. In the second case, in which the conductivity is $\sigma \simeq enc/B$, the corresponding estimate is $T \sim 10^2$ eV, which still satisfies inequality (1) for the above values of B and n. For stronger magnetic fields, this inequality may fail to hold. However, below we will assume that, in accordance with the measurement results, emission from the plasma and ion heat conduction substantially reduce the plasma temperature. Hence, the applicability of the equations to be derived is closely associated with the possibility of satisfying condition (1).

In order to determine whether the viscosity can be neglected, we estimate the ratio $|\mathbf{w}|/\delta\nu_{ii}$, where δ is the characteristic length scale and $\mathbf{w}$ is the relative ion velocity. Here, we are interested in estimating the maximum (ion) viscosity. Using formula (48) for the conductivity due to ion–ion collisions (see below) and taking into account the fact that the corresponding Hall parameter $\sigma B/enc$ is on the order of unity, we obtain

$$\frac{|\mathbf{w}|}{\delta\nu_{ii}} \sim \frac{c^2}{\delta^2 \omega_{pi}^2} \ll 1. \tag{4}$$

When $\delta \leq 1$ cm and $n \sim 10^{18}$ cm^{-3}, this inequality holds not only for a hydrogen plasma but also for plasmas with heavier ions. This estimate was derived by setting $|\mathbf{w}| \sim |\mathbf{j}|/en$.

Now, we consider the form of the dissipative terms that account for ion–ion collisions. According to the appendix to review [9], the form of the terms that incorporate ion–ion collisions into Eqs. (7)–(9) (see below) is consistent with, e.g., Maxwellian distribution func-

tions if the relative ion velocity is much lower that the characteristic ion thermal velocity, $|\mathbf{w}| \ll v_{Ti}$. This condition yields an additional restriction:

$$1 \ll \frac{B^2}{8\pi nT} \ll \frac{\delta^2 \omega_{pi}^2}{c^2}. \quad (5)$$

For a magnetic field $B \sim 10^5$ G and for a hydrogen plasma with the parameters $T \sim 30$–50 eV, $n \sim 10^{18}$ cm^{-3}, and $\delta \sim 1$ cm, the quantity $\delta^2\omega_{pi}^2/c^2$ is on the order of 3×10^3. This is why inequality (5) can be satisfied not only for a hydrogen plasma but also for plasmas with heavier ions.

The main feature of the equations to be derived is that the thermal effects are neglected compared to the effect of the magnetic field, in which case the plasma temperature will be chosen to lie in the range 30–50 eV because of the serious radiative losses from the plasma and high ion heat conduction to the wall. Since thermal effects are neglected, Eqs. (7)–(9) apply actually to individual particles whose accelerations are governed by the frictional forces between them and by the electromagnetic fields. Clearly, these equations cannot be used to describe the focusing stage of the plasma focus, when the plasma temperature significantly increases.

Hence, our aim here is to analyze the set of equations capable of describing, in particular, the propagation of a current sheath along a coaxial transmission line—a phenomenon that plays an important role in the formation of a plasma focus.

Of course, the fairly simple equations derived below do not provide a detailed description of the dynamics of a multispecies plasma in a magnetic field. The thermal effects in such a plasma are difficult to incorporate correctly (see, e.g., [13]); here, to demonstrate the role of these effects, the equations are used at their applicability limits. However, as will be shown below, even these simplified equations are capable of describing an interesting effect—the simultaneous diffusion of different ion species and the magnetic field in a frame of reference moving with the mass velocity. This effect is analogous to magnetoresistance, which is well known in solid-state physics and occupies an important place in modern plasma physics.

It is notable that, in the context of the present paper, the dominant role of ion–ion dissipation does not imply that the ions can be heated to high temperatures, e.g., due to ion heat conduction to the wall. Consequently, in what follows, the dominance of ion–ion dissipation means merely that the energy is transmitted preferentially via ion–ion collisions. In this case, the ion energy balance equation

$$\frac{3}{2} n_i \frac{d_i T_i}{dt} + p_i \nabla \cdot \mathbf{v}_i = Q_i + \nabla \cdot (\kappa_{i\perp} \nabla_\perp T_i) \quad (6)$$

implies that, for $\omega_{Bi} \sim \nu_0$ (which corresponds to unmagnetized ions) and $\sigma \sim enc/B$ [see formula (47)], at the validity limit $4\pi n_i T_i/B^2 \lesssim 1$ of our model, the ion heat loss Q_i to the wall is governed by the ion heat conduction due to ion–ion collisions.

In principle, the effect of the increase in resistivity can also be observed in a plasma with one (rather than two) ion species and one neutral species [14]. This issue has recently received much attention [15–17]. Also, multispecies plasmas attract increased interest because they are in a sense analogous to dusty plasma [18, 19].

3. Having obtained the necessary estimates, we go on to describe a multispecies plasma by the basic set of equations, which includes the equation for the electrons,

$$m\frac{d\mathbf{v}}{dt} = -e\mathbf{E} - \frac{e}{c}[\mathbf{v} \times \mathbf{B}] - m\nu_{e1}(\mathbf{v} - \mathbf{V}_1) - m\nu_{e2}(\mathbf{v} - \mathbf{V}_2) \quad (7)$$

and the equations for the two ion species,

$$M_1\frac{d_1\mathbf{V}_1}{dt} = Z_1 e\mathbf{E} + \frac{Z_1 e}{c}[\mathbf{V}_1 \times \mathbf{B}] - M_1\nu_{12}(\mathbf{V}_1 - \mathbf{V}_2) - M_1\nu_{1e}(\mathbf{V}_1 - \mathbf{v}), \quad (8)$$

$$M_2\frac{d_2\mathbf{V}_2}{dt} = Z_2 e\mathbf{E} + \frac{Z_2 e}{c}[\mathbf{V}_2 \times \mathbf{B}] - M_2\nu_{21}(\mathbf{V}_2 - \mathbf{V}_1) - M_2\nu_{2e}(\mathbf{V}_2 - \mathbf{v}). \quad (9)$$

Here, m is the mass of an electron, M_1 and M_2 are the masses of ions of different species, and Z_1 and Z_2 are the related ion charge numbers. The frequencies of collisions between the different ions, ν_{12}, and between the electrons and the ions, ν_{e1} and ν_{e2}, satisfy the obvious relationships

$$\alpha_1 = nm\nu_{e1} = N_1 M_1 \nu_{1e},$$
$$\alpha_2 = nm\nu_{e2} = N_2 m_2 \nu_{2e},$$
$$\alpha_{12} = N_1 M_1 \nu_{12} = N_2 M_2 \nu_{21}.$$

In Eqs. (7)–(9), the derivatives

$$\frac{d_k}{dt} = \frac{\partial}{\partial t} + (\mathbf{V}_k \cdot \nabla), \quad k = 1, 2$$

are the total derivatives along the trajectories of ions of different species. In what follows, we will assume that the electrons and ions move only in the r and z directions and do not move along the magnetic field, which has only the φ-component. We will also assume that all of the physical quantities do not depend on φ.

Equations (7)–(9) should be supplemented with the ion continuity equations

$$\frac{\partial N_k}{\partial t} + \nabla \cdot (N_k \mathbf{V}_k) = 0, \quad k = 1, 2 \quad (10)$$

and the quasineutrality condition

$$n = Z_1 N_1 + Z_2 N_2, \tag{11}$$

where n is the electron density and $N_{1,2}$ are the densities of the ions of different species.

For further analysis, it is expedient to introduce the relative charge and density of each ion species:

$$\xi_k = \frac{Z_k N_k}{n}, \quad \eta_k = \frac{M_k N_k}{\rho}, \quad k = 1, 2, \tag{12}$$

where $\rho = M_1 N_1 + M_2 N_2$ is the plasma density.

Using the expressions for the current density $\mathbf{j}$ and relative velocity $\mathbf{w}$ of the ion species,

$$\begin{aligned} \mathbf{j} &= eZ_1 N_1(\mathbf{V}_1 - \mathbf{v}) + eZ_2 N_2(\mathbf{V}_2 - \mathbf{v}), \\ \mathbf{w} &= \mathbf{V}_1 - \mathbf{V}_2, \end{aligned} \tag{13}$$

we obtain the following useful relationships, which make it possible to remove from consideration the electron velocity:

$$\mathbf{V}_1 - \mathbf{v} = \frac{\mathbf{j}}{en} + \xi_2 \mathbf{w}, \quad \mathbf{V}_2 - \mathbf{v} = \frac{\mathbf{j}}{en} - \xi_1 \mathbf{w}. \tag{14}$$

We neglect electron inertia and use Eq. (7) to eliminate the electric field in Eqs. (8) and (9). With the help of relationships (14), we reduce the equations of motion of the ion species to the form [10]

$$\eta_1 \rho \frac{d_1 \mathbf{V}_1}{dt} = \xi_1 \frac{1}{c}[\mathbf{j} \times \mathbf{B}] + \mathbf{F}, \tag{15}$$

$$\eta_2 \rho \frac{d_2 \mathbf{V}_2}{dt} = \xi_2 \frac{1}{c}[\mathbf{j} \times \mathbf{B}] - \mathbf{F}, \tag{16}$$

where $\mathbf{F} \equiv \xi_1 \xi_2 (en/c)[\mathbf{w} \times \mathbf{B}] - (\alpha_{12} + \alpha_e'')\mathbf{w} - \alpha_e' (\mathbf{j}/en)$. In accordance with [9], the kinetic coefficients in the expression for $\mathbf{F}$ are defined in the same manner as in [10]:

$$\alpha_e = \alpha_1 + \alpha_2, \ \alpha_e' = \alpha_1 \xi_2 - \alpha_2 \xi_1, \ \alpha_e'' = \alpha_1 \xi_2^2 + \alpha_2 \xi_1^2,$$

$$\alpha_k = n N_k \sqrt{m} \frac{4\sqrt{2\pi}}{3} \frac{Z_k^2 e^4 \lambda}{T^{3/2}}, \quad k = 1, 2,$$

$$\alpha_{12} = N_1 N_2 \sqrt{\frac{M_1 M_2}{M_1 + M_2}} \frac{4\sqrt{2\pi}}{3} \frac{Z_1^2 Z_2^2 e^4 \lambda}{T^{3/2}}.$$

For further analysis, it is important to write out the relationship $\alpha_{12}/\alpha_k \sim \sqrt{M/m} \gg 1$ and to note that, in a certain range of plasma parameters, the electric conductivity is governed by ion–ion (rather than electron–ion) collisions. In this relationship, M is the characteristic ion mass or the geometric mean mass (if the masses of the ions of different species are very different).

4. When studying a plasma with two ion species, it is convenient to switch from Eqs. (15) and (16) to their linear combination. The equation

$$\eta_1 \frac{d_1 \mathbf{V}_1}{dt} + \eta_2 \frac{d_2 \mathbf{V}_2}{dt} = \frac{1}{\rho c}[\mathbf{j} \times \mathbf{B}] \tag{17}$$

describes the motion of the center of mass of the two ion species. To see this, we introduce the mass velocity

$$\mathbf{V} \equiv \eta_1 \mathbf{V}_1 + \eta_2 \mathbf{V}_2 \tag{18}$$

and, using Eqs. (10), obtain

$$\frac{\partial \rho}{\partial t} + \nabla \cdot (\rho \mathbf{V}) = 0. \tag{19}$$

Consequently, the dynamics of the plasma density ρ is determined by the mass velocity $\mathbf{V}$. In this case, the velocities of the ion species are expressed in terms of the mass velocity $\mathbf{V}$ and relative velocity $\mathbf{w}$ as

$$\mathbf{V}_1 = \mathbf{V} + \eta_2 \mathbf{w}, \quad \mathbf{V}_2 = \mathbf{V} - \eta_1 \mathbf{w}. \tag{20}$$

We substitute expressions (20) for $\mathbf{V}_{1,2}$ into Eq. (17) and perform simple algebraic manipulations to obtain

$$\begin{aligned} &\frac{d\mathbf{V}}{dt} + \eta_1 \eta_2 (\mathbf{w} \cdot \nabla)\mathbf{w} + \mathbf{w}\left(\eta_1 \frac{d\eta_2}{dt} - \eta_2 \frac{d\eta_1}{dt}\right) \\ &\qquad = \frac{1}{\rho c}[\mathbf{j} \times \mathbf{B}], \end{aligned} \tag{21}$$

where the expression $\eta_1 d\eta_2/dt - \eta_2 d\eta_1/dt = -d\eta_1/dt$ can be changed from one form into another with the help of the equation

$$\frac{d\eta_1}{dt} + \frac{1}{\rho}\nabla \cdot (\rho \eta_1 \eta_2 \mathbf{w}) = 0, \tag{22}$$

which follows immediately from Eqs. (10) and (19) and relationships (20).

As a result, we arrive at the final form of the equation for the hydrodynamic mass velocity $\mathbf{V}$:

$$\frac{d\mathbf{V}}{dt} + \frac{1}{\rho}(\nabla \cdot \mathbf{w})\rho \eta_1 \eta_2 \mathbf{w} = \frac{1}{\rho c}[\mathbf{j} \times \mathbf{B}], \tag{23}$$

where

$$\frac{d}{dt} \equiv \frac{\partial}{\partial t} + (\mathbf{V} \cdot \nabla),$$

$$(\nabla \cdot \mathbf{w})\rho \eta_1 \eta_2 \mathbf{w} \equiv \rho \eta_1 \eta_2 \mathbf{w}(\nabla \cdot \mathbf{w}) + (\mathbf{w} \cdot \nabla)\rho \eta_1 \eta_2 \mathbf{w}.$$

We can see that the hydrodynamic equation of motion (23) contains a term that is similar in structure to the kinetic pressure tensor $p_{ik} = \rho \eta_1 \eta_2 w_i w_k$ and in which the relative velocity $\mathbf{w}$ plays the role of a thermal velocity.

The relative velocity $\mathbf{w}$ in Eqs. (22) and (23) can be deduced from the equation

$$\rho\left(\eta_1 \xi_2 \frac{d_1 \mathbf{V}_1}{dt} - \eta_2 \xi_1 \frac{d_2 \mathbf{V}_2}{dt}\right) = \mathbf{F}. \tag{24}$$

By analogy with the derivation of Eq. (21), the final equation for the relative velocity **w** can be obtained by inserting expressions (20) for the velocities $\mathbf{V}_{1,2}$ into Eq. (24) and using Eq. (21) for the total derivative of the mass velocity:

$$\frac{\mu}{c}[\mathbf{j}\times\mathbf{B}] + \rho\eta_1\eta_2 D\mathbf{w} = \xi_1\xi_2\frac{en}{c}[\mathbf{w}\times\mathbf{B}] - (\alpha_{12}+\alpha_e'')\mathbf{w} - \alpha_e'\frac{\mathbf{j}}{en}, \quad (25)$$

where $\mu \equiv \eta_1\xi_2 - \eta_2\xi_1$ and the inertial term $D\mathbf{w}$ has the form

$$D\mathbf{w} \equiv \frac{d\mathbf{w}}{dt} + (\mathbf{w}\cdot\nabla)\mathbf{V} + (\eta_2-\eta_1)(\mathbf{w}\cdot\nabla)\mathbf{w} + \mathbf{w}(\mathbf{w}\cdot\nabla\eta_2).$$

5. Equations (19), (22), (23), and (25) for functions ρ, η_1, **V**, and **w** describe the dynamics of a plasma with two ion species in a prescribed magnetic field B_φ. The equation for the magnetic field B_φ will be derived below. Now, we briefly discuss the equations obtained above. Equation (25) is in a sense analogous to the electron equation (7). Formally, we can say that Eq. (23) describes plasma mass motion with velocity **V** and Eq. (25) describes the relative motion of the ion components with velocity **w**. The latter equation is similar to the electron equation in the sense that the inertial term $D\mathbf{w}$ on the left-hand side of Eq. (25) is as important as the magnetic and collision terms on the right-hand side, which contain the relative velocity **w**. Note that, in place of the electron equation, the final set of equations includes an equation for the magnetic field. It is also necessary to take into account the fact that, over a broad range of plasma parameters, the inertial term in Eq. (25) can be significantly smaller than the magnetic and collision terms. In fact, we compare the inertial term with the magnetic term in order to show that the former can be discarded under the condition

$$\omega_{Bi} \gg \frac{1}{\tau}, \quad (26)$$

where ω_{Bi} is the ion cyclotron frequency and τ is the characteristic duration of an electromagnetic field pulse.

If we set $\tau \sim 10^{-8}$ s, then we can see that inequality (26) holds for a hydrogen plasma in the field $B_\varphi \gg 10^4$ G. An analogous inequality can be written for the collision term. Using the estimate that was obtained in [10] for the kinetic coefficient α_{12} and setting $T \sim 30$ eV, we can see that the condition

$$\alpha_{12} \gg \rho\frac{1}{\tau} \quad (27)$$

holds for $N \gg 10^{15}$ cm^{-3}. Of course, the shorter the pulse duration τ, the stronger the magnetic field and the higher the density for which conditions (26) and (27) are satisfied.

Under inequalities (26) and (27), Eq. (25) takes the form

$$\frac{\mu}{c}[\mathbf{j}\times\mathbf{B}] + \alpha_e'\frac{\mathbf{j}}{en} = \xi_1\xi_2\frac{en}{c}[\mathbf{w}\times\mathbf{B}] - (\alpha_{12}+\alpha_e'')\mathbf{w}. \quad (28)$$

We introduce the notation $\alpha \equiv \alpha_{12} + \alpha_e''$ and $\beta \equiv \xi_1\xi_2(enB_\varphi)/c$ in order to obtain an explicit expression for **w**:

$$\mathbf{w} = \left(\beta\frac{\mu}{c}B_\varphi - \frac{\alpha\alpha_e'}{en}\right)\frac{\mathbf{j}}{\alpha^2+\beta^2} - \left(\beta\frac{\alpha_e'}{enB_\varphi} + \alpha\frac{\mu}{c}\right)\frac{[\mathbf{j}\times\mathbf{B}]}{\alpha^2+\beta^2}. \quad (29)$$

Below, we will be interested primarily in the case in which the ion–ion dissipation dominates over the electron–ion dissipation. Following [10], the criterion of neglecting electron–ion dissipation can be derived from the law of energy conservation in the collisional plasma under consideration. The hydrodynamic equations and the evolutionary equation for the magnetic field,

$$\frac{\partial\mathbf{B}}{\partial t} = \nabla\times[\mathbf{v}\times\mathbf{B}] - \nabla\times\left(\frac{c\alpha_e}{e^2n^2}\mathbf{j} + \frac{c\alpha_e'}{en}\mathbf{w}\right) \quad (30)$$

yield the law of energy conservation in the form

$$\frac{\partial W}{\partial t} + \nabla\cdot\mathbf{P} = -(\alpha_{12}+\alpha_e'')\mathbf{w}^2 - \frac{\alpha_e\mathbf{j}^2}{e^2n^2} - \frac{2\alpha_e'\mathbf{w}\cdot\mathbf{j}}{en}, \quad (31)$$

where

$$W = N_1\frac{M_1\mathbf{V}_1^2}{2} + N_2\frac{M_2\mathbf{V}_2^2}{2} + \frac{\mathbf{B}^2+\mathbf{E}^2}{8\pi},$$

$$\mathbf{P} = N_1M_1\mathbf{V}_1 + N_2M_2\mathbf{V}_2 + \frac{[\mathbf{E}\times\mathbf{B}]}{4\pi c}.$$

By virtue of the relationship $\alpha_{12} \sim \sqrt{Z^2M/m}\alpha_e$, the ion–ion dissipation plays a dominant role under the condition

$$|\mathbf{w}| \gg \left(\frac{m}{Z^2M}\right)^{1/4}\frac{|\mathbf{j}|}{en}. \quad (32)$$

From Eq. (29), we can readily see that condition (32) can be satisfied for the following relationship between the plasma parameters:

$$\frac{\alpha_e'^2 + \beta^2(\mu/\xi_1\xi_2)^2}{\alpha^2+\beta^2} \gg \left(\frac{m}{Z^2M}\right)^{1/2}. \quad (33)$$

It is obvious that this inequality can only hold for $\beta \gg \alpha_e'$, which implies that the electrons are magnetized. In this case, it is also necessary to satisfy the condition $\beta/\alpha \gg (m/MZ^2)^{1/4}$; in other words, the ion–ion dissipation can dominate the plasma with unmagnetized ions when $1 \gg \beta/\alpha \gg (m/MZ^2)^{1/4}$.

6. Here, we derive an evolutionary equation for the magnetic field from Eq. (30). Equations (13) and (20) give the following expression for the electron velocity **v**:

$$\mathbf{v} = \mathbf{V} - \frac{\mathbf{j}}{en} - \mu\mathbf{w}. \tag{34}$$

Substituting expression (34) into Eq. (30), we obtain the following equation for the only nonzero component B_φ of the magnetic field:

$$\frac{\partial B_\varphi}{\partial t} + \nabla\cdot(\mathbf{V}B_\varphi)$$

$$= \frac{\partial}{\partial z}\left(\frac{j_z}{en}B_\varphi + \mu w_z B_\varphi - \frac{c\alpha_e}{e^2n^2}j_r - \frac{c\alpha_e'}{en}w_r\right) \tag{35}$$

$$+ \frac{\partial}{\partial r}\left(\frac{j_r}{en}B_\varphi + \mu w_r B_\varphi + \frac{c\alpha_e}{e^2n^2}j_z + \frac{c\alpha_e'}{en}w_z\right).$$

This equation closes the above set of hydrodynamic equations, thereby making it possible to calculate the dynamics of a plasma with two ion species in a magnetic field.

We substitute the above expression for **w** into Eq. (35) and express the current from Maxwell's equation

$$\nabla\times\mathbf{B} = \frac{4\pi}{c}\mathbf{j}. \tag{36}$$

As a result, we arrive at the final equation describing the magnetic field dynamics. Here, we write out this equation for a plasma with no electron–ion dissipation:

$$\frac{\partial B_\varphi}{\partial t} + \nabla\cdot(\mathbf{V}B_\varphi) = \frac{c}{4\pi}\frac{\partial}{\partial z}\frac{1}{\alpha^2+\beta^2}$$

$$\times\left\{\frac{\mu^2}{c}\alpha B_\varphi^2\frac{\partial B_\varphi}{\partial z} + \frac{B_\varphi}{r}\frac{\partial(rB_\varphi)}{\partial r}\left(\frac{\alpha^2+\beta^2}{en} + \frac{\mu^2}{c}\beta B_\varphi\right)\right\} \tag{37}$$

$$+ \frac{c}{4\pi}\frac{\partial}{\partial r}\frac{1}{\alpha^2+\beta^2}\left\{\frac{\mu^2}{c}\alpha B_\varphi^2\frac{1}{r}\frac{\partial(rB_\varphi)}{\partial r}\right.$$

$$\left. - B_\varphi\frac{\partial B_\varphi}{\partial z}\left(\frac{\alpha^2+\beta^2}{en} + \frac{\mu^2}{c}\beta B_\varphi\right)\right\}.$$

This is a diffusion equation incorporating the ion–ion dissipation and containing the convective terms that account for the Hall effect. It should be emphasized that electron–ion collisions are ignored and, by virtue of Eq. (30), the magnetic field is frozen in the electron plasma component. From the electron continuity equation, expression (34) for the electron velocity, and Eq. (29) for **w**, we can see that the electron density satisfies the following quasi-diffusion equation in a frame of reference moving with the mass velocity:

$$\frac{\partial n}{\partial t} + \nabla\cdot(n\mathbf{V}) = \nabla\cdot(n\mu\mathbf{w}). \tag{38}$$

Consequently, in order to satisfy the frozen-in condition

$$\left\{\frac{\partial}{\partial t} + (\mathbf{v}\cdot\nabla)\right\}\frac{B_\varphi}{rn} = 0 \tag{39}$$

the magnetic field should experience diffusive motion. The mechanism by which the ion motion affects the magnetic field can be understood in terms of the quasineutrality condition, which implies that the relative ion motion changes the electron density and, accordingly, the magnetic field, which is frozen in the electron component.

The ion density redistribution due to the magnetic field diffusion is described by the equation

$$\frac{d\eta_1}{dt} + \frac{1}{\rho}\frac{\partial}{\partial z}\rho\frac{c}{4\pi en}\mu\frac{\eta_1\eta_2}{\xi_1\xi_2}\frac{\beta}{\alpha^2+\beta^2}\left\{\alpha\frac{\partial B_\varphi}{\partial z} + \beta\frac{1}{r}\frac{\partial(rB_\varphi)}{\partial r}\right\}$$

$$+ \frac{1}{r\rho}\frac{\partial}{\partial r}r\rho\frac{c}{4\pi en}\mu\frac{\eta_1\eta_2}{\xi_1\xi_2}\frac{\beta}{\alpha^2+\beta^2} \tag{40}$$

$$\times\left\{\alpha\frac{1}{r}\frac{\partial(rB_\varphi)}{\partial r} - \beta\frac{\partial B_\varphi}{\partial z}\right\} = 0.$$

Hence, further analysis will be based on Eqs. (19), (23), (25), (37), and (40) for ρ, **V**, **w**, B_φ, and η_1. Of course, Eq. (23) should be taken with the above expression for the relative velocity **w**, in which case the remaining parameters, namely, $\xi_{1,2}$, η_2, μ, and the electron density n are expressed in terms of the calculated value of η_1. Thus, quantity μ has the form

$$\mu = \frac{\eta_1\eta_2(Z_2/M_2 - Z_1/M_1)}{\eta_1 Z_1/M_1 + \eta_2 Z_2/M_2}. \tag{41}$$

7. Now, we make some comments about the equations derived and discuss the relevant boundary conditions. We start by imposing the boundary conditions for the problem of the propagation of an electromagnetic pulse in a transmission line filled with a plasma with two ion species.

The standard boundary conditions for hydrodynamic equations imply that the flow velocities of the

ions of both species should vanish at the conducting surfaces:

$$V_r = 0 \quad \text{and} \quad w_r = 0. \tag{42}$$

We stress that it is not quite correct to describe the regions near the surfaces of the conducting electrodes using Eq. (28) instead of Eq. (25). Let us discuss this point in more detail. With the relationships $w_r = 0$ and $(D\mathbf{w})_r = 0$, which are both satisfied at the electrode surfaces, Eq. (25) yields the exact equations

$$\frac{\mu}{c} j_z B_\varphi = \xi_1\xi_2 \frac{en}{c} w_z B_\varphi + \alpha_e' \frac{j_r}{en}, \tag{43}$$

$$\frac{\mu}{\xi_1\xi_2}\beta j_r + \alpha_e j_z + en\rho\eta_1\eta_2 (D\mathbf{w})_z + \alpha en w_z = 0. \tag{44}$$

As was mentioned in Section 5, the term with $(D\mathbf{w})_z$ is usually much smaller than the remaining terms, and it seems likely that it can be omitted. However, this is not always the case. The reason is that, along with the above boundary conditions, there is an additional standard boundary condition at the surfaces of the conducting electrodes, specifically, $E_z = 0$. If we take into account this boundary condition and neglect electron inertia in Eq. (6), we obtain the relationship

$$\left(\frac{\beta^2}{\xi_1\xi_2} - \alpha_e'^2\right) j_r + \left(\alpha_e + \frac{\mu}{\xi_1\xi_2}\alpha_e'\right)\beta j_z = 0. \tag{45}$$

Comparing expression (45) with expression (44) taken with w_z extracted from formula (43), we can easily see that neglecting the small term with $(D\mathbf{w})_z$ leads to a homogeneous set of equations for j_r and j_z, in which case, at the conducting electrode surfaces, we have $j_z = j_r = 0$. This means that there is no magnetic field front at the electrode surfaces, $\partial B_\varphi/\partial z = 0$. Consequently, to describe a nonlinear magnetic field wave propagating along the electrode surfaces, it is necessary to keep the term with $D\mathbf{w}$ and to include electron–ion dissipation.

8. As was mentioned above, the dissipation due to ion–ion collisions may play an important role in the problem under study. Here, we explicitly introduce the conductivity due to ion–ion dissipation and briefly discuss its physical meaning. The coefficient of friction α_{12} can be represented as

$$\alpha_{12} \equiv n\frac{M_1M_2}{M_1 + M_2}\nu_0, \tag{46}$$

where

$$\nu_0 = \frac{N_1N_2}{n}\sqrt{\frac{M_1 + M_2}{M_1M_2}}\frac{4\sqrt{2\pi}}{3}\frac{Z_1^2Z_2^2e^4\lambda}{T^{3/2}}.$$

By analogy with the conventional conductivity $\sigma = e^2n/(m\nu_{ei})$, the effective conductivity in terms of ν_0 can be introduced through the relationship

$$\sigma_0 = \frac{\xi_1\xi_2 e^2 n}{M_1M_2/(M_1 + M_2)\nu_0}. \tag{47}$$

The final expression for the conductivity is

$$\sigma_0^{-1} = \frac{4\sqrt{2\pi}}{3}\frac{\lambda Z_1Z_2e^2}{T^{3/2}}\sqrt{\frac{M_1M_2}{M_1 + M_2}}, \tag{48}$$

in which case the above coefficients α_{12} and β are equal to

$$\alpha_{12} = \xi_1\xi_2\frac{e^2n^2}{\sigma_0}, \quad \beta = \xi_1\xi_2\frac{enB_\varphi}{c}. \tag{49}$$

The dimensionless ratio of these coefficients is the dimensionless Hall coefficient corresponding to ion–ion dissipation:

$$h_0 = \frac{\beta}{\alpha_{12}} = \frac{\sigma_0 B_\varphi}{enc} \gg \left(\frac{m}{Z^2M}\right)^{1/4}. \tag{50}$$

Hence, in order for the ion–ion dissipation to dominate over electron–ion dissipation, the dimensionless Hall coefficient should not be too small.

It should be noted that the dominant role of ion–ion dissipation is directly related to unsteady processes resulting in the separation of different ion species at the wave front [10–12]. In the absence of unsteady processes, the ion species evolve to steady-state distributions and the dissipation is governed by electron–ion collisions [9]. If the ion–ion dissipation dominates, we can neglect electron–ion collisions and assume that the magnetic field is frozen in the electron component. According to the quasineutrality condition, the electron density changes owing to the spatial separation of different ion species, leading to the redistribution of the frozen-in magnetic field. In this case, the relative ion motion is described by Eq. (40).

Collisions between ions of different species but with the same charge-to-mass ratio have no impact on dissipation. In this case, the above formula for μ gives $\mu = 0$, so that the relative velocity $\mathbf{w}$, which is associated directly with ion–ion dissipation, is governed by electron–ion collisions and turns out to be low. Consequently, ion–ion dissipation plays an important role only during the separation of ions of different species at the wave front.

Let us make one more remark. The value of the transverse electric conductivity adopted in [6, 8] when calculating the dynamics of a plasma focus was two orders of magnitude lower than the conventional conductivity, associated with electron–ion collisions. The primary reason for this choice was to take into account turbulence-driven anomalous conductivity. Although the possibility of this effect cannot be denied, it should be noted that an analogous effect of the decrease in con-

ductivity may also be associated with ion–ion dissipation [see formula (48)].

9. Here, we briefly discuss the physical causes of ion–ion dissipation. For this purpose, in Eq. (28), we neglect electron–ion collisions and, for simplicity, omit the Hall term, which is proportional to $\mathbf{w} \times \mathbf{B}$. We thus arrive at Ohm's law for the current carried by the ions:

$$\mathbf{j}_i = \sigma_0 \mathbf{E}_{\text{eff}}, \tag{51}$$

where

$$\mathbf{E}_{\text{eff}} = \frac{\mu^2}{\xi_1 \xi_2} \frac{1}{enc}[\mathbf{j} \times \mathbf{B}], \quad \mathbf{j}_i = -\mu e n \mathbf{w},$$

and σ_0 is the ion–ion conductivity introduced above. Consequently, the assumption that the magnetic field is completely frozen in the electron component [see Eq. (30) in which electron–ion collisions are neglected] indicates that, as compared to the frame of reference moving with the electron velocity **v**, the magnetic field in the frame moving with the mass velocity **V** [see expression (34)] experiences a diffusive motion. According to Ohm's law (51), the magnetic field diffusion is caused by the relative motion of different ion species in the effective electric field in a plasma in which ion–ion collisions play an important role.

It is clear that the relative velocity **w**, which determines the magnetic field diffusion in Eq. (35), can be significant only if the inertial term $\rho d\mathbf{V}/dt$ is taken into account and the ion species have different charge-to-mass ratios Z/M such that $\mu \neq 0$. If, in a quasi-equilibrium situation ($d\mathbf{V}/dt \simeq 0$), the inertial term is unimportant and the first term on the left-hand side of Eq. (28) is omitted, then the relative velocity **w** is determined by electron–ion dissipation and cannot lead to any significant effects. In this case, the isotope separation described by Eq. (40) is also determined by the value of the parameter μ and is certainly possible only for ions with different charge-to-mass ratios.

As early as 1963, Braginskiĭ [9] noted that plasma diffusion due to ion–ion friction may play a significant role only in the relaxation stage, in which the inertial term in Eq. (24) is important; in the subsequent quasisteady stage, the relative ion velocity **w** becomes low. Presumably, it is for this reason that, in review [20], devoted to tokamaks with multispecies plasmas, Hirshman and Sigmar did not analyze the related effect of ion–ion collisions on the transverse conductivity.

It should be kept in mind that, in solid-state physics, the effect of the increase in resistivity is analogous to magnetoresistance, whose description can be found, e.g., in [21]. In this context, of particular interest are kinetic simulations carried out by Surzhikov [22], which showed that the presence of two ion species in a shock wave that expels the magnetic field from the region occupied by an expanding plasma leads to an additional damping of this wave.

To conclude this section, note that the effect under consideration may play an important role in the dynamics of an imploding liner. Thus, in the paper by Deeney *et al.* [23], which was presented at the 13th International Conference on High-Power Particle Beams (Nagaoka, Japan), it was experimentally shown that a multiwire liner in which some of the metal wires are coated with a different metal can be contracted to more compact dimensions. Presumably, this can be explained by the high ion–ion dissipation, which partially suppresses the liner instability. For $\alpha \sim \beta$, Eq. (37) gives $\sigma \sim enc/B_\varphi$; consequently, for $n \sim 10^{19}$ cm^{-3} and $B_\varphi \sim 10^6$ G, the conductivity is on the order of $\sigma \sim 10^{14}$ s^{-1}. Such conductivity should act to help stabilize the liner against perturbations with characteristic spatial and temporal scales of $r \sim 1$ mm and $\tau \sim 10^{-8}$ s, respectively.

10. The above set of equations for a plasma with two ion species can also be applied to describe a dusty plasma [18, 19] in which dust grains with rather large dimensions (<1 μm) acquire a fairly large electric charge owing to collisions with electrons. In describing this plasma, the total mass of the electron and ion plasma components can be neglected in comparison with the mass of the grains and the charge of the grain can be assumed to be relatively small. Consequently, using subscript 2 to denote the quantities that refer to the dust grains, we can work under the condition $Z_2/M_2 \ll Z_1/M_1$. Of course, the above method fails to describe electron–ion collisions; however, the equations derived provide a qualitative description. Note also that, in a real dusty plasma, the dust grains differ in the charge number Z_2, which can, in addition, change with time. With allowance for the above considerations and under the assumption $\beta \gg \alpha$, we can neglect dissipation and write the dynamic equation for the magnetic field as

$$\frac{\partial B_\varphi}{\partial t} = \frac{\partial}{\partial z}\left\{\frac{cB_\varphi}{4\pi enr}\frac{\partial (rB_\varphi)}{\partial r}\left(1 + \frac{\mu^2}{\xi_1 \xi_2}\right)\right\} - \frac{\partial}{\partial r}\left\{\frac{cB_\varphi}{4\pi enr}\frac{\partial (rB_\varphi)}{\partial z}\left(1 + \frac{\mu^2}{\xi_1 \xi_2}\right)\right\}. \tag{52}$$

On the left-hand side of this equation, we also omitted the term that describes the motion of dust grains. As usual, we assume that the electron density n and the quantities μ, ξ_1, and ξ_2 depend only on r.

In such dusty plasma, the convective propagation of a magnetic field is described by the equation [24]

$$\frac{\partial B_\varphi}{\partial t} = -\frac{cr^2 B_\varphi}{4\pi e}\frac{\partial B_\varphi}{\partial z}\frac{\partial}{\partial r}\left\{\frac{1}{nr^2}\left(1 + \frac{\mu^2}{\xi_1 \xi_2}\right)\right\}, \tag{53}$$

in which case the convective velocity in the plasma has the form

$$u_{\text{conv}} = \frac{cB_\varphi}{4\pi e} r^2 \frac{\partial}{\partial r}\left\{\frac{1}{nr^2}\left(1 + \frac{\mu^2}{\xi_1\xi^2}\right)\right\}. \quad (54)$$

Since the mass of the plasma is mostly concentrated in the dust component, the definition of μ yields $\mu \equiv \eta_1\xi_2 - \eta_2\xi_1 \simeq -\eta_2\xi_1 \simeq -\xi_1$. As a result, we have $1 + \mu^2/\xi_1\xi_2 \simeq 1 + \xi_1/\xi_2 = 1/\xi_2$, so that the velocity of the convective propagation of the magnetic field is determined by the dust density gradient:

$$u_{\text{conv}} = \frac{cB_\varphi}{4\pi e} r^2 \frac{\partial}{\partial r}\left(\frac{1}{r^2 N_2}\right). \quad (55)$$

If we take into account a possible fractal structure of the spatial distribution of the dust density, we find that the convective velocity can increase substantially because the density profile N_2 is highly irregular. For dust grains with a characteristic dimension l, separated by the distance $d \ll l$, the relationship $\partial N_2^{-1}/\partial r \sim 1/(N_2 d)$ gives rise to the additional factor $l/d \gg 1$ in the expression for the convective velocity [25].

For a dusty plasma, Eq. (40), which now describes the motion of light ion species against the background of heavy grains, takes the form

$$\frac{\partial N_1}{\partial t} = \frac{c}{4\pi Z_2 e}\left\{\frac{\partial}{\partial z}\frac{N_1}{N_2}\frac{\beta}{\alpha^2+\beta^2}\left[\alpha\frac{\partial B_\varphi}{\partial z} + \beta\frac{1}{r}\frac{\partial(rB_\varphi)}{\partial r}\right]\right.$$
$$\left. + \frac{1}{r}\frac{\partial}{\partial r} r \frac{N_1}{N_2}\frac{\beta}{\alpha^2+\beta^2}\left[\alpha\frac{1}{r}\frac{\partial(rB_\varphi)}{\partial r} - \beta\frac{\partial B_\varphi}{\partial z}\right]\right\}. \quad (56)$$

On the left-hand side of this equation, we neglected the low macroscopic velocity **V**, which is governed by the inertia of heavy grains.

In the case of high dissipation ($\alpha^2 \gg \beta^2$), we arrive at the quasi-diffusion equation for N_1. When the dissipation is negligible ($\beta^2 \gg \alpha^2$), we deal with ion flows around immobile dust grains, in accordance with the equation

$$\frac{\partial N_1}{\partial t} + \nabla \cdot (N_1 \mathbf{u}) = 0, \quad (57)$$

where

$$\mathbf{u} = \frac{c}{4\pi Z_2 e N_2 r}\left[\frac{\mathbf{B}}{|\mathbf{B}|} \times \nabla(rB_\varphi)\right].$$

11. The set of equations describing a plasma with two ion species in a magnetic field such that $B^2 \gg 8\pi p$ has been analyzed with allowance for friction between ions of different species. In this limiting case, the hydrodynamic equations (7)–(9) are actually one-particle equations accounting for friction between the particles. The plasma thermal pressure can be neglected because of the intense emission from the plasma and high ion heat conduction to the wall. Of course, the effects related to ion–ion collisions also remain in the presence of thermal effects. It is shown that there exists a certain range of values of the ratio of the plasma density to the magnetic field, $\nu_{ii}/\omega_{Bi} < (MZ^2/m)^{1/4}$, within which ion–ion dissipation dominates over the conventional electron–ion dissipation, in which case the lowest value of conductivity is about $\sigma \sim enc/|B_\varphi|$. Such a low conductivity may partially suppress the Rayleigh–Taylor instability of an imploding liner. Also, the effect of the decrease in conductivity may play an important role in the physics of a plasma focus: a decrease of two orders of magnitude in the conductivity (as is usually assumed in simulations) may be caused not only by plasma turbulence but also by the effects of ion–ion dissipation. Another important property of the ion–ion dissipation is that it always occurs within the front of a nonlinear wave.

The equations obtained can be used to describe a current-carrying dusty plasma in which the magnetic field dynamics plays an important role. The main dissipative effect in a dusty plasma with a magnetic field is related to collisions of ions with individual grains (along with time variations in the dust grain charge). The new equations (37) and (40) provide a qualitative description of the magnetic-field and particle dynamics in a dusty plasma.

ACKNOWLEDGMENTS

This study was supported in part by the Russian Foundation for Basic Research (project no. 00-02-16305) and INTAS (grant no. 97-00-21).

REFERENCES

1. A. V. Gordeev, Preprint No. 3076 (Kurchatov Institute of Atomic Energy, Moscow, 1978) [Preprint No. PIIR-12-79 (Physical International Company, San Leandro, CA, 1979)].
2. E. I. Baranchikov, A. V. Gordeev, V. D. Korolev, and V. P. Smirnov, Zh. Éksp. Teor. Fiz. **75**, 2102 (1978) [Sov. Phys. JETP **48**, 1058 (1978)].
3. L. I. Rudakov, M. V. Babykin, A. V. Gordeev, *et al.*, *Generation and Focusing of High-Current Relativistic Electron Beams*, Ed. by L. I. Rudakov (Énergoatomizdat, Moscow, 1990).
4. N. V. Filippov, T. I. Filippova, and V. P. Vinogradov, Nucl. Fusion Suppl. **2**, 571 (1962).
5. J. W. Mather, Phys. Fluids **8**, 366 (1965).
6. V. F. D'yachenko and V. S. Imshennik, *Reviews of Plasma Physics*, Ed. by M. A. Leontovich (Atomizdat, Moscow, 1974; Consultants Bureau, New York, 1980), Vol. 8.
7. V. V. Vikhrev and S. I. Braginskii, *Reviews of Plasma Physics*, Ed. by M. A. Leontovich (Atomizdat, Moscow, 1980; Consultants Bureau, New York, 1986), Vol. 10.

8. V. S. Imshennik and N. A. Bobrova, *Collisional Plasma Dynamics* (Énergoatomizdat, Moscow, 1997).
9. S. I. Braginskii, in *Reviews of Plasma Physics*, Ed. by M. A. Leontovich (Gosatomizdat, Moscow, 1963; Consultants Bureau, New York, 1963), Vol. 1.
10. A. V. Gordeev, Fiz. Plazmy **13**, 1235 (1987) [Sov. J. Plasma Phys. **13**, 713 (1987)].
11. G. Barak and N. Rostoker, Appl. Phys. Lett. **41**, 918 (1982).
12. H. U. Rahman, P. Amendt, and N. Rostoker, Phys. Fluids **28**, 1528 (1985).
13. N. A. Bobrova and P. V. Sasorov, Fiz. Plazmy **19**, 789 (1993) [Plasma Phys. Rep. **19**, 409 (1993)].
14. T. G. Cowling, *Magnetohydrodynamics* (Interscience, New York, 1957; Inostrannaya Literatura, Moscow, 1959).
15. L. I. Rudakov, Phys. Plasmas **2**, 2940 (1995).
16. A. I. Smolyakov and I. Khabibrakhmanov, Phys. Rev. Lett. **81**, 4871 (1998).
17. I. V. Sokolov and J. I. Sakai, Fiz. Plazmy **26**, 529 (2000) [Plasma Phys. Rep. **26**, 493 (2000)].
18. Ya. K. Khodataev, R. Bingkhem, V. P. Tarakanov, and V. N. Tsytovich, Fiz. Plazmy **22**, 1028 (1996) [Plasma Phys. Rep. **22**, 932 (1996)].
19. O. S. Vaulina, A. A. Samaryan, A. V. Chernyshev, *et al.*, Fiz. Plazmy **25**, 191 (1999) [Plasma Phys. Rep. **25**, 170 (1999)].
20. S. P. Hirshman and D. J. Sigmar, Nucl. Fusion **21**, 1079 (1981).
21. V. V. Vladimirov, A. F. Volkov, and E. Z. Meĭlikhov, *Semiconductor Plasmas* (Atomizdat, Moscow, 1979).
22. S. T. Surzhikov, Fiz. Plazmy **26**, 811 (2000) [Plasma Phys. Rep. **26**, 759 (2000)].
23. C. Deeney, C. A. Coverdale, M. R. Douglas, *et al.*, in *Proceedings of the 13th International Conference on High Power Particle Beams, Nagaoka, 2000*, p. 336.
24. A. V. Gordeev, A. S. Kingsep, and L. I. Rudakov, Phys. Rep. **243**, 215 (1994).
25. A. V. Gordeev, Preprint No. 5924/6 (Russian Research Centre Kurchatov Institute, Moscow, 1995).

Translated by O. E. Khadin

Plasma Physics Reports, Vol. 27, No. 8, 2001, pp. 669–691. Translated from Fizika Plazmy, Vol. 27, No. 8, 2001, pp. 710–733.

PLASMA ELECTRONICS

Plasma Relativistic Microwave Electronics

M. V. Kuzelev, O. T. Loza, A. A. Rukhadze, P. S. Strelkov, and A. G. Shkvarunets

Institute of General Physics, Russian Academy of Sciences, ul. Vavilova 38, Moscow, 119991 Russia

Received March 22, 2001

Abstract—The principles of plasma relativistic microwave electronics based on the stimulated Cherenkov emission of electromagnetic waves during the interaction of a relativistic electron beam with a plasma are formulated. A theory of relativistic Cherenkov plasma microwave oscillators and amplifiers is developed, and model experimental devices are elaborated and investigated. The emission mechanisms are studied theoretically. The efficiencies and frequency spectra of relativistic Cherenkov plasma microwave oscillators and amplifiers are calculated. The theoretical predictions are confirmed by the experimental data: the power of the devices attains 500 MW, the microwave frequency can be continuously tuned over a wide band with an upper-to-lower boundary frequency ratio of 7 (from 4 to 28 GHz), and the emission frequency bandwidth can be varied from several percent to 100 percent. These microwave sources have no analogs in vacuum microwave electronics.

1. INTRODUCTION

1.1. The Subject of Plasma Relativistic Microwave Electronics

Microwave electronics is one of the main branches of physical electronics—an extensive (fundamental and applied) science. The subjects of investigation of microwave electronics are oscillations and waves in the frequency band 1–100 GHz, how these may be excited by electron beams, and many practical applications.

Since a plasma consists of charged particles (electrons and ions), it is subject to numerous natural oscillations in the microwave frequency range. For this reason, a device filled with plasma may serve as a source of microwave radiation.

There are two types of plasma-filled microwave sources. Devices of the first type are conventional vacuum microwave sources filled with plasma. Filling a vacuum source with plasma makes it possible to improve some of its parameters (to increase the microwave power, to vary the frequency, etc.). Such sources are called *hybrid* microwave devices. Since the mechanism for microwave excitation in hybrid devices is essentially the same as that in vacuum analogs (backward-wave tubes, gyrotrons, etc.), they can also operate in plasma-free modes. That is why such hybrid devices are not a significant concern for plasma microwave electronics.

Plasma-filled devices of the second type are based on the resonant interaction of an electron beam with a plasma. This interaction leads to the excitation of eigenmodes of plasma-filled systems (plasma waveguides or plasma resonators), which cannot be excited in the absence of plasma. For this reason, such sources are called *plasma* microwave devices. Plasma microwave electronics is primarily concerned with the mechanisms for microwave excitation (emission) by an electron beam in plasma systems and the creation of related plasma microwave devices. Accordingly, plasma microwave devices and their physical justification are the focus of our investigation.

The considerable progress in plasma microwave electronics is associated with the development of methods for generating relativistic electron beams (REBs) (i.e., beams in which the electron velocity is close to the speed of light). In a plasma, REBs excite electromagnetic waves with relativistic phase velocities. Plasma microwave electronics dealing with REBs are called relativistic.

Below, we will review the results obtained in studies on plasma relativistic microwave electronics. We also formulate the general principles underlying this new area of modern physics, survey the relevant theoretical and experimental advances, and discuss the prospects of plasma relativistic microwave devices as well as their possible practical applications.

1.2. Historical Review

The beam–plasma instability was discovered as early as 1949 by A.I. Akhiezer and Ya.B. Fainberg [1] and independently by D. Bohm and E. Gross [2]. Further research on this instability gave birth to plasma microwave electronics. Physically, the beam–plasma instability consists in an anomalously strong interaction of a fast electron beam with a dense plasma. The theory predicted that a monoenergetic electron beam should be fairly efficiently decelerated by a plasma, thereby giving rise to plasma oscillations. In a spatially unbounded beam–plasma system, the characteristic time scale on which an electron beam is decelerated has the form

$$\tau = 1/\delta, \quad \delta = \omega_p (n_b/2n_p)^{1/3}. \qquad (1.2.1)$$

1063-780X/01/2708-0669$21.00

Here, n_b and n_p are the electron densities of the beam and plasma, respectively (it is assumed that $n_b \ll n_p$); ω_p is the Langmuir frequency of the plasma electrons; and δ is the temporal growth rate of the beam instability. The characteristic distance l over which the beam electrons are decelerated is approximately equal to $l \approx u\tau = u/\delta$, where u is the electron beam velocity.

The growth rate δ and, accordingly, the deceleration distance l are achieved when the frequency ω of the excited plasma waves satisfies the condition

$$\omega \approx \omega_p \approx ku, \tag{1.2.2}$$

i.e., when the phase velocity of the plasma wave is close to the beam velocity. Here, k is the projection of the wave vector of the plasma wave onto the propagation direction of the beam. Condition (1.2.2) made it possible to understand the mechanism for the anomalously strong interaction of a dense electron beam with a plasma as being due to the stimulated emission of plasma waves by the beam electrons (stimulated Cherenkov effect). As a result, the beam kinetic energy is converted into the energy of plasma waves. The conversion efficiency Q, which can also be regarded as the emission efficiency of plasma waves by an electron beam, is estimated to be

$$Q = \left(\frac{E^2}{8\pi}\right)\Big/\left(n_b\frac{mu^2}{2}\right) \approx \left(\frac{n_b}{2n_p}\right)^{1/3}, \tag{1.2.3}$$

where $E^2/8\pi$ is the field energy in a plasma wave and $mu^2/2$ is the kinetic energy of a beam electron. This estimate implies that, for $n_b \approx 0.01n_p$ and $u \approx 10^{10}$ cm/s (which corresponds to a beam electron energy of about 30 keV), the fraction of the beam energy that can be converted into the energy of plasma waves amounts to 20%. If, in addition, $n_p \approx 10^{12}$ cm^{-3} and $n_b \approx 10^{10}$ cm^{-3} (which corresponds to the beam current density $j_b \approx 15$ A/cm^2), then the electron beam loses 75 kW/cm^2 of its initial energy; this energy loss occurs during a time interval of 10^{-10} s, i.e., over a distance of about $l \sim 1$ cm.

The first experiments in this field, which were carried out in 1960 in the Soviet Union (at the Kharkov Institute of Physics and Technology [3] and the Vekua Institute of Physics and Technology [4]) and abroad confirmed that the efficiency of a collective interaction of the electron beam and the plasma is fairly high. On the other hand, electromagnetic radiation emitted from the plasma turned out to be insignificant: the fraction of the beam energy lost in the form of microwaves was smaller than 1%.

An investigation of the general properties of the beam–plasma instability was followed by research on the possibility of creating microwave emitters based on this instability, thereby marking the beginning of plasma nonrelativistic microwave electronics. Significant contributions to this scientific direction were made by the physicists of the Institute of Radio Engineering and Electronics of the Russian Academy of Sciences, who published the first review [5] on plasma nonrelativistic microwave electronics. This review, as well as review [6], demonstrated that it is possible to excite different modes of the plasma waveguide by an electron beam and thus create the relevant Cherenkov plasma microwave oscillators and amplifiers.

A serious difficulty in creating effective plasma microwave emitters is associated with the development of a system for transforming a slow plasma wave into a fast mode of a vacuum waveguide. The most difficult point in this way is that of making the device broadband. That is why it was impossible to make use of an important advantage of plasma microwave devices over vacuum ones—the possibility of tuning the radiation frequency over a broad band by varying the plasma density. As a result, plasma microwave devices driven by nonrelativistic electron beams have not been implemented in practice.

The situation in plasma microwave electronics had changed drastically by the early 1970s, when, first, encouraging theoretical results were obtained and, then, scientists learned to produce high-current REBs with current densities of 1–10 kA/cm^2 and electron energies of about 1 MeV. As the relativistic factor γ of the electron beam increases, the growth rate δ of the beam instability decreases [7, 8],

$$\delta = \left(\frac{n_b}{2n_p}\right)^{1/3}\frac{\omega_p}{\gamma}, \quad \gamma = \frac{1}{\sqrt{1 - u^2/c^2}}, \tag{1.2.4}$$

and, accordingly, the relaxation length $l \approx u/\delta$ of the beam in the plasma increases, which seems to be evidence of a weakening of the beam–plasma interaction. However, in actuality, this is not the case: it is precisely because of the longer beam relaxation length that the efficiency of the beam energy transfer to plasma waves increases up to the value [9]

$$Q \approx \frac{1}{2}\left(\frac{n_b}{2n_p}\right)^{1/3}(\gamma + 1). \tag{1.2.5}$$

Notably, for large values of γ, the approximate formula (1.2.5) implies that the efficiency can be on the order of unity. However, this formula is valid only when the efficiency is low. Actually, numerical experiments [10] show that the maximum conversion efficiency is usually at most 20–30%.

We should also mention two theoretical results that had an important impact on the development of plasma relativistic microwave electronics. The first is the formula for the limiting current at which an electron beam can be transported through a vacuum waveguide. In particular, in a cylindrical metal vacuum (plasma-free) waveguide, the current of a thin-walled annular beam cannot exceed the limit known as the Bogdankevich–Rukhadze current [11]

$$J_0 \approx 17\frac{(\gamma^{2/3} - 1)^{3/2}}{\Delta_b/r_b + 2\ln R/r_b}\ \text{kA}, \tag{1.2.6}$$

where R is the waveguide radius, r_b is the mean beam radius, and Δ_b is the beam wall thickness. The current (1.2.6) stems from the deceleration of the beam electrons by the field of their own space charge and is thus the limiting beam current for vacuum microwave devices. However, even if the electron beam current is neutralized either by the ions or by the plasma, there is another limit, which is known as the Pierce current and is governed by the condition for the beam transport to be stable [12]:

$$J_{\mathrm{P}} = J_0\left(\frac{\gamma^2-1}{\gamma^{2/3}-1}\right)^{3/2} > J_0\gamma^2. \qquad (1.2.7)$$

Consequently, owing to the complete (or partial) neutralization of the beam charge, plasma-filled systems can operate with beam currents that are not attainable in vacuum microwave devices.

The second important theoretical result is the condition for exciting the eigenmodes of a plasma waveguide by an electron beam. The eigenmodes can be excited only in a sufficiently dense plasma, such that the plasma frequency ω_p is higher than a certain threshold frequency ω_{thr} [13]:

$$\omega_p^2 > \omega_{\mathrm{thr}}^2 = k_{\perp p}^2 u^2\gamma^2, \qquad (1.2.8)$$

where the transverse wavenumber $k_{\perp p}$ of the plasma wave is determined by the plasma density profile and waveguide radius (see below) [10].

The currents J_0 and J_{P} are the characteristic limiting currents of electron beams in vacuum and plasma relativistic microwave sources, respectively. Condition (1.2.8) determines the threshold plasma density above which the plasma wave can be excited by an REB.

By 1976, the basic elements of plasma relativistic microwave electronics were comprehended in general principles [14–16]. Since that time, a long-term close collaboration between experimental and theoretical groups began, which led to the development a new branch of microwave electronics—plasma relativistic microwave electronics. Our combined efforts made it possible to devise an optimum scheme of plasma relativistic microwave sources—an annular REB and an annular plasma column in a metal waveguide with a strong longitudinal external magnetic field. We constructed linear and nonlinear theories of plasma relativistic microwave oscillators and amplifiers, investigated the emission mechanisms in these devices, and calculated the emission efficiency and emission spectra.

Our first successful experiment with a relativistic Cherenkov plasma maser (RCPM) was carried out in 1982 at the Institute of General Physics of the Russian Academy of Sciences [17, 18]. Then, the theory developed was used to design and investigate high-power Cherenkov plasma microwave oscillators and amplifiers tunable over a broad frequency band. We also elaborated new original diagnostics for measuring and controlling the parameters of high-current pulsed relativistic electron beams and high-power microwave radiation.

2. THEORETICAL PLASMA RELATIVISTIC MICROWAVE ELECTRONICS

2.1. Linear Theory of the Plasma Relativistic Microwave Amplifier

The simplest theoretical model of a plasma microwave amplifier assumes a straight REB propagating along the axis of a plasma-filled metal waveguide of radius R in a strong longitudinal external magnetic field. The beam is injected into the waveguide through the plane $z = 0$. A collector is placed in the plane $z = L$ and is coupled to the emitter (the outlet horn). The beam and plasma are homogeneous along the waveguide axis, cold, and completely charge- and current-neutralized. In the waveguide cross section, the plasma and beam are annular, with the mean radii $r_b < R$ and $r_p < R$ and wall thicknesses Δ_b and Δ_p such that $\Delta_{b,p} \ll r_{b,p}$.

In the linear approximation, the spectra of the natural oscillations in this waveguide system are determined from the following dispersion relation [19, 20], which is derived from Maxwell's equations, the hydrodynamic equation for a cold plasma, and the Vlasov equation for the beam electrons:

$$D_pD_b = \theta\omega_p^2\omega_b^2\gamma^{-3}\frac{\chi^4}{k_{\perp p}^2k_{\perp b}^2}. \qquad (2.1.1)$$

Here,

$$D_p \equiv \omega^2 - \omega_p^2\frac{\chi^2}{k_{\perp p}^2},\quad D_b \equiv (\omega - k_z u)^2 - \omega_b^2\gamma^{-3}\frac{\chi^2}{k_{\perp b}^2} \qquad (2.1.2)$$

are the dispersion functions, whose zeros determine the wave spectra in the plasma and electron beam, provided that they do not interact with one another [10]; parameter θ characterizes the degree to which the beam and plasma waves are coupled; and quantities $k_{\perp p}^2$ and $k_{\perp b}^2$ are the squared transverse wavenumbers of the beam and plasma waves. The rest of the notation in formulas (2.1.1) and (2.1.2) is as follows: ω is the frequency, k_z is the longitudinal wavenumber, ω_p and ω_b are the Langmuir frequencies of the plasma and beam electrons, $\chi^2 = k_z^2 - \omega^2/c^2$, u is the unperturbed velocity of the beam electrons, and $\gamma = (1 - u^2/c^2)^{-1/2}$ is the relativistic factor.

The coupling parameter θ possesses an important property: $\theta = 1$ for $r_b = r_p$ and $\theta < 0$ in other cases. Thus, for azimuthally symmetric low-frequency perturbations such that $\omega R/u\gamma \ll 1$, parameter θ is equal to

$$\theta = \begin{cases} \ln(R/r_p)/\ln(R/r_b), & r_b < r_p, \\ \ln(R/r_b)/\ln(R/r_p), & r_b > r_p. \end{cases} \qquad (2.1.3)$$

As the frequency ω increases, the coupling parameter θ decreases substantially in comparison with that in formula (2.1.3).

The values of ω and k_z that are close to those at which the dispersion functions (2.1.2) vanish simultaneously correspond to a strong (single-particle or collective) Cherenkov resonance between the beam and plasma. Cherenkov resonance can occur only in the frequency range $\omega < k_z c$, in which the beam and plasma waves are surface waves. In particular, in the most important long-wavelength limit ($k_z \longrightarrow 0$), the dispersion relation for the surface plasma wave has the form [10]

$$\omega = \omega_p \frac{k_z c}{\sqrt{k_{\perp p}^2 c^2 + \omega_p^2}}, \qquad (2.1.4)$$

where the squared transverse wavenumber of the plasma wave is equal to

$$k_{\perp p}^2 = \begin{cases} [r_p \Delta_p \ln(R/r_p)]^{-1}, & l = 0, \\ 2l[r_p \Delta_p (1 - (r_p/R)^{2l})]^{-1}, & l \neq 0; \end{cases} \qquad (2.1.5)$$

with l being the azimuthal wavenumber. An azimuthally symmetric wave that obeys dispersion relation (2.1.4) with $l = 0$ is also called a cable plasma wave [10, 21]. This wave has the highest phase velocity and thus plays an especially important role in plasma relativistic microwave electronics. In the classification accepted in the waveguide theory, this wave is designated as E_{01}. As the wavenumber increases ($k_z R > 1$), the wave phase velocity (2.1.4) decreases abruptly, so that the wave acquires the nature of a potential wave and becomes trapped in the plasma.

In the long-wavelength limit, the squared transverse wavenumber $k_{\perp b}^2$ is also described by formula (2.1.5) with subscript b in place of p, in which case the spectra of both fast and slow beam waves can easily be found from the dispersion functions (2.1.2) (see [10, 19, 20] for details). A slow beam wave has negative energy, so that the beam in the plasma is unstable. The frequency at which the phase velocity of a surface plasma wave with frequency (2.1.4) coincides with the beam velocity is called the frequency of the single-particle Cherenkov resonance (the wave–particle resonance). The frequency at which the phase velocity of the plasma wave is equal to the phase velocity of the slow beam wave is referred to as the frequency of the collective Cherenkov resonance (the wave–wave resonance). One can readily show that the frequency of the single-particle resonance decreases with ω_p and vanishes at [19, 20]

$$\omega_p^2 = \omega_{p0}^2 = k_{\perp p}^2 u^2 \gamma^2. \qquad (2.1.6)$$

If the plasma frequency is below the threshold frequency (2.1.6), then the single-particle Cherenkov resonance is impossible. The threshold frequency (2.1.6) is the lowest for an azimuthally symmetric cable plasma wave. The absence of resonance does not imply that there is no stimulated Cherenkov emission and, accordingly, that the generated microwaves are not amplified. Below, we will show that, for electron beams with sufficiently high densities, the threshold plasma frequency ω_p is significantly below the threshold (2.1.6) [19, 20].

In a beam–plasma system, microwaves can be amplified in different frequency bands, depending on the system parameters (primarily, on ω_p and $|r_b - r_p|/R$). Thus, if the coupling coefficient is close to unity ($\theta \simeq 1$), then the microwaves are amplified over a broad frequency band—from nearly zero to a frequency higher than the wave–wave resonance frequency. In the literature, such broadband plasma microwave sources are referred to as Thomson amplifiers [19, 20, 24]. If the coupling coefficient is much smaller than unity ($\theta \ll 1$), then microwaves are amplified in a narrow frequency band. In the literature, such narrowband plasma microwave sources are referred to as Raman amplifiers [19, 20, 22].

The frequency characteristics that are most important for the beam–plasma interaction are shown in Fig. 1 as functions of the plasma frequency ω_p. Curves *1* and *2* are, respectively, the upper and lower boundary frequencies of the amplification band: the amplification is possible only at frequencies lying between curves *1* and *2*. Curve *3* shows the frequencies at which the amplification coefficient is maximum. Curves *4* and *5* reflect the collective and single-particle resonance frequencies, respectively. All of the curves were computed for an experimental waveguide with the parameters R = 1.8 cm, r_p = 1.1 cm, r_b = 0.6 cm, $\Delta_b = \Delta_p$ = 0.1 cm, I_b = 2 kA, and $\gamma = 2$ ($u = 2.6 \times 10^{10}$ cm/s).

As can be seen in Fig. 1, microwaves can be amplified only when the plasma frequency ω_p is above a certain threshold, which is marked by the vertical line *A* and, because of the high beam current, is lower than the threshold (2.1.6) by a factor of approximately two. For higher plasma frequencies (i.e., those lying between the vertical lines *A* and *D*), the lower boundary frequency of the amplification band is equal to zero (the zone of Thomson amplification). For even higher plasma frequencies (i.e., those lying to the right of the vertical line *D*), the lower boundary frequency of the amplification band becomes nonzero and the amplification band itself narrows as ω_p increases (the zone of Raman amplification). In turn, the zones of Thomson and Raman amplification regimes can be divided into subzones (bounded by the vertical lines *B*, *C*, and *E*). From Fig. 1, we can also see that, as ω_p increases, the amplification band becomes significantly narrower and the frequency at which the amplification is most efficient (curve *3*) increases and eventually becomes equal to the

collective resonance frequency (curve *4*). Consequently, the higher the plasma frequency and the beam current, the clearer the collective nature of the beam–plasma interaction, because coefficient θ decreases as ω increases. In contrast, as the plasma frequency increases, the single-particle resonance frequency (curve *5*) progressively deviates from the frequency at which the amplification coefficient is maximum (curve *3*). Moreover, Fig. 1 demonstrates that amplification at the single-particle resonance frequency ceases above a certain plasma frequency [19].

In Fig. 2, curve *1* shows the maximum amplification coefficient (the quantity $\delta k = |\mathrm{Im}(k_z)|$) calculated as a function of ω_p along curve *3* in Fig. 1 for microwave sources with the same parameters as in Fig. 1. We can see that there is a certain optimum plasma frequency at which the amplification coefficient has an absolute maximum.

Figure 3 illustrates the amplification coefficients for a system with the same parameters as in the previous two figures but calculated as functions of the frequency ω for different plasma frequencies ω_p: 15×10^{10}, 25×10^{10}, 35×10^{10}, and 45×10^{10} rad/s. In this figure, curves *1* and *2* are very similar to the ω-profiles of the amplification coefficients for a broadband Thomson amplifier, whereas curves *3* and *4* are characteristic of the Raman amplification regime.

Figures 1 and 3 and curve *1* in Fig. 2 refer to an azimuthally symmetric cable plasma mode E_{01}. The other waves described by dispersion relation (2.1.4) obey analogous dependences. The mode with the phase velocity closest to the phase velocity of the E_{01} mode is the first azimuthally asymmetric E_{11} ($l = 1$) mode, whose amplification coefficient is represented by curve *2* in Fig. 2. For high plasma densities, the amplification coefficients of these two modes are approximately the same. Consequently, in terms of the transverse wavenumber $k_{\perp p}$ defined by formula (2.1.5), the plasma microwave amplifier is not, generally speaking, a single-mode amplifier. The single-mode regime takes place only in a comparatively narrow range of plasma frequencies (as is shown in Fig. 2). The dependences displayed in Figs. 1–3 make it possible to determine (in the linear approximation) the frequency spectra of the microwave radiation and the frequency bandwidths for microwave amplification in a plasma relativistic microwave amplifier.

2.2. Nonlinear Theory of the Plasma Relativistic Microwave Amplifier

The general nonlinear equations for the electromagnetic field of an E-wave and the currents induced in the plasma and beam in a plasma relativistic microwave

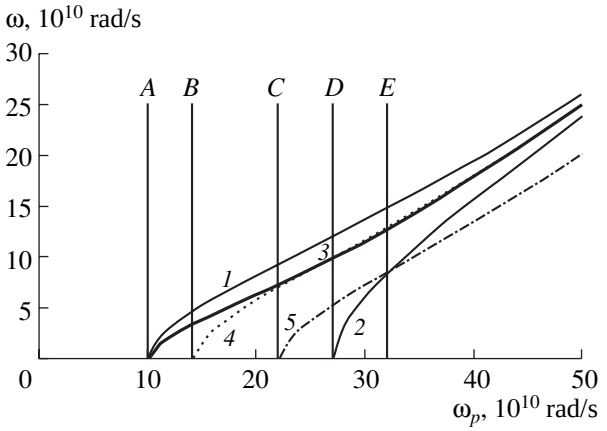

Fig. 1. The most important frequencies of a plasma amplifier vs. the plasma frequency: ω_p: (*1*) upper boundary of the amplification band, (*2*) lower boundary of the amplification band, (*3*) frequency corresponding to the maximum amplification coefficient, (*4*) collective-resonance frequency, and (*5*) one-particle resonance frequency. The curves are calculated for a system with the following parameters: R = 1.8 cm, r_p = 1.1 cm, r_b = 0.6 cm, $\Delta_b = \Delta_p$ = 0.1 cm, I_b = 2 kA, and γ = 2.

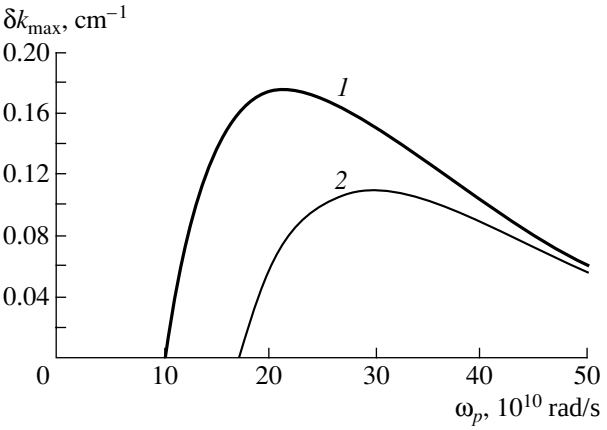

Fig. 2. Maximum amplification coefficient vs. the plasma frequency: (*1*) azimuthally symmetric E_{01} mode and (*2*) azimuthally asymmetric E_{11} mode.

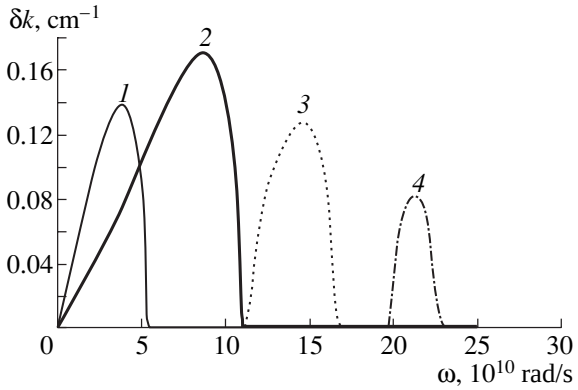

Fig. 3. Frequency dependences of the amplification coefficient for different plasma frequencies: ω_p = (*1*) 15×10^{10}, (*2*) 25×10^{10}, (*3*) 35×10^{10}, and (*4*) 45×10^{10} rad/s.

amplifier have the form [19, 20]

$$\frac{\partial}{\partial t}\left(\frac{1}{r}\frac{\partial}{\partial r}r\frac{\partial}{\partial r}+\frac{\partial^2}{\partial z^2}-\frac{1}{c^2}\frac{\partial^2}{\partial t^2}\right)\psi$$
$$= -4\pi(\Delta_b\delta(r-r_b)j_b+\Delta_p\delta(r-r_p)j_{pz}),$$
$$j_b = en_b\int v(z,t_0)\delta[t-t(z,t_0)]dt_0, \qquad (2.2.1)$$
$$\frac{\partial j_p}{\partial t} = \frac{\omega_p^2}{4\pi}E_z, \quad E_z = \left(\frac{\partial^2}{\partial z^2}-\frac{1}{c^2}\frac{\partial^2}{\partial t^2}\right)\psi,$$

where E_z is the longitudinal electric field, ψ is the polarization potential, and n_b is the unperturbed density of the beam electrons. In Eqs. (2.2.1), current j_p induced in the plasma is described in the linear approximation (the effects of plasma nonlinearity and the possibility of neglecting them were considered in [23]), and the beam current j_b is determined using a model based on the calculation of the characteristics of the Vlasov equation for the beam electrons and the representation of the distribution function of the beam electrons by an integral over the initial conditions [10, 24]. In this case, $t(z, t_0)$ and $v(z, t_0)$ are solutions to the characteristic set of equations for the Vlasov equation,

$$\frac{dt}{dz} = \frac{1}{v}, \quad v\frac{dv}{dz} = \frac{e}{m}(1-v^2/c^2)^{3/2}E_z, \qquad (2.2.2)$$

supplemented with the initial (injection) conditions $t(z = 0) = t_0$ and $v(z = 0) = u$. Equations (2.2.1) and (2.2.2) yield dispersion relation (2.1.1) and, hence, the remaining results of linear theory.

The general equations (2.2.1) and (2.2.2) can be reduced to a form that is convenient for solving the problem of microwave amplification with allowance for the following circumstances: (a) in a beam–plasma waveguide, the transverse structure is not known *a priori* and is established self-consistently with increasing distance from the injection plane along the *z*-axis; (b) the frequency spectrum of an amplified signal may not be specified *a priori*, so that it is necessary to consider the simultaneous amplification of waves with different frequencies, which interact with each other in the nonlinear stage; and (c) the longitudinal wavenumbers of the waves that are efficiently amplified by the beam are close to the wave frequency divided by the unperturbed beam velocity. These considerations allow the polarization field potential ψ to be represented as [19, 20]

$$\psi = \frac{1}{2}\sum_{n=1}^{\infty}\left\{\varphi_n(\mathbf{r}_\perp)\right.$$
$$\left.\times\sum_{s=1}\left[A_{ns}(z)\exp\left(-is\Omega t+is\frac{\Omega}{u}z\right)+\text{c.c.}\right]\right\}. \qquad (2.2.3)$$

Here, Ω is a certain small frequency value, which serves to "discretize" the frequency spectrum of the amplified signal and is equal in order of magnitude to $\Omega = 2\pi/T$, where T is the characteristic time scale on which the current of an electron beam changes (the beam pulse duration). With expression (2.2.3), Eqs. (2.2.1) and (2.2.2) reduce to the following nonlinear equations for a plasma relativistic microwave amplifier [19, 20]:

$$\frac{dy}{d\xi} = \eta,$$
$$\frac{d\eta}{d\xi} = \frac{i}{2}\left(1+2\gamma^2\frac{u^2}{c^2}\eta\right)^{3/2}$$
$$\times\sum_{s=1}[s\exp(-isy)\hat{L}_s(\alpha_{bs}\rho_s+j_s)-\text{c.c.}], \qquad (2.2.4)$$
$$\frac{dj_s}{d\xi} = \frac{is}{2\gamma^2}\left[\left(\frac{1}{\alpha_{ps}}-1\right)j_s-\theta(s)\alpha_{bs}\hat{L}_s\rho_s\right].$$

Here,

$$\rho_s = \frac{1}{\pi}\int_0^{2\pi}\exp(isy)dy_0, \quad \hat{L}_s = 1-2i\gamma^2\frac{1}{s}\frac{d}{d\xi},$$
$$\alpha_{ps} = \frac{\omega_p^2}{k_{\perp p}^2(s)u^2\gamma^2}, \quad \alpha_{bs} = \frac{\omega_b^2\gamma^{-3}}{k_{\perp b}^2(s)u^2\gamma^2}, \qquad (2.2.5)$$

and the quantities $k_{\perp p}^2(s)$, $k_{\perp b}^2(s)$, and $\theta(s)$ coincide with their linear analogs correct to the replacement $\omega \longrightarrow s\Omega$. The dimensionless parameters and variables in Eqs. (2.2.4) are defined as

$$y = \Omega[t(z,t_0)-z/u], \quad \eta = \frac{u-v(z,t_0)}{v(z,t_0)},$$
$$y_0 = \Omega t_0, \quad \xi = \frac{\Omega}{u}z. \qquad (2.2.6)$$

The amplification efficiency is defined as a relative fraction of the kinetic energy flux of the beam electrons that is transferred into the microwave energy flux:

$$Q = 1-\frac{1}{2\pi}\int_0^{2\pi}(1+2\gamma^2(u/c)^2\eta)^{-1/2}dy_0. \qquad (2.2.7)$$

For a spatially unbounded beam–plasma system, the amplification efficiency (2.2.7) reduces to the efficiency described by formula (1.2.5) in linear theory.

Equations (2.2.4) should be supplemented with the boundary conditions. In the amplification problem,

they are specified in the injection plane $z = 0$ [19, 20]:

$$j_s|_{\xi=0} = j_{s0}, \quad \eta|_{\xi=0} = 0,$$
$$y|_{\xi=0} = y_0 + \frac{1}{2}\sum_{s=1}(b_s \exp(isy_0 + i\phi_s) + \text{c.c.}). \quad (2.2.8)$$

Here, j_{s0} are the amplitudes of the current harmonics of the plasma oscillations at the entrance to an amplifier, $y_0 \in [0, 2\pi]$ refers to an unperturbed beam, and the second term on the right-hand side of the third condition describes the electron density modulation of a beam. Generally, nonlinear theory deals with problems in which there are no plasma oscillations at the entrance to an amplifier (i.e., all of the amplitudes of the plasma-current harmonics j_{s0} are equal to zero), whereas the density of the injected beam is assumed to be weakly modulated: $|b_s| = 0.01$–0.05.

Below, we will present the maximum amplification efficiency, the length corresponding to the maximum output power (the optimum length), and the spectrum of the amplified signal, all obtained by numerically solving the nonlinear equations for a plasma amplifier with the same parameters as in Figs. 1–3. In order to find the maximum amplification efficiency and optimum length, it is sufficient to consider the amplification of a monochromatic signal, i.e., to use the boundary conditions (2.2.9) with only one nonzero term $b_1 \neq 0$, setting the remaining terms, $b_{2, 3, \ldots} = 0$, to zero. On the other hand, determining the spectrum requires taking into account many nonzero terms $b_s \neq 0$, which corresponds to the amplification of a large number of waves.

Figure 4 shows the maximum amplification efficiency of a monochromatic signal as a function of ω_p, and Fig. 5 displays the optimum length L on which the maximum efficiency is achieved. These results were obtained for frequency Ω [see formula (2.2.3)] corresponding to curve *3* in Fig. 1 and for $b_1 = 0.01$.

As can be seen from Figs. 4 and 5, the operation efficiency of the amplifier is fairly high over the entire range of the plasma frequencies under consideration [25] and the length of the amplifier is not too large and is essentially independent of ω_p over a fairly broad frequency range.

The operation efficiency is especially high near the threshold for amplification [19, 20, 25], in which case the length of the amplifier sharply increases (in Figs. 4 and 5, the threshold plasma frequency $\omega_p = 10.1 \times 10^{10}$ rad/s is shown by the vertical line). Of course, the optimum length depends on the depth b_1 of the initial beam modulation, but this dependence is weak and, for a beam with a different initial modulation depth b_1', it can be recalculated from the formula $L' - L = \delta k^{-1} \ln|b_1'/b_1|$, where δk is represented in Fig. 2.

For several plasma frequencies, Fig. 6 illustrates the spectral densities of microwave radiation at the exit from an amplifier with an optimum length corresponding to the maximum output power. The spectral density of the input signal was assumed to be uniform over the entire frequency range under consideration. Curves *1–4*

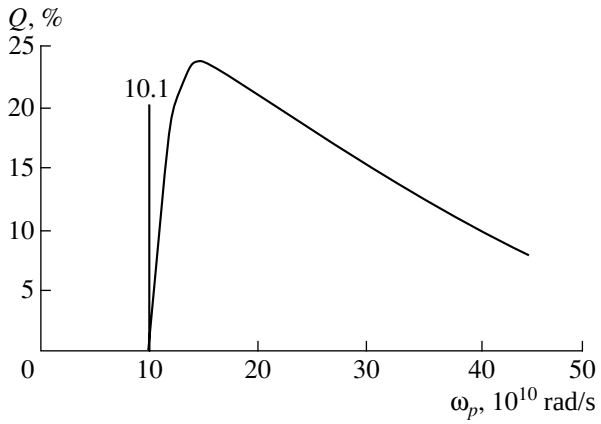

Fig. 4. Amplification efficiency Q vs. the plasma frequency ω_p.

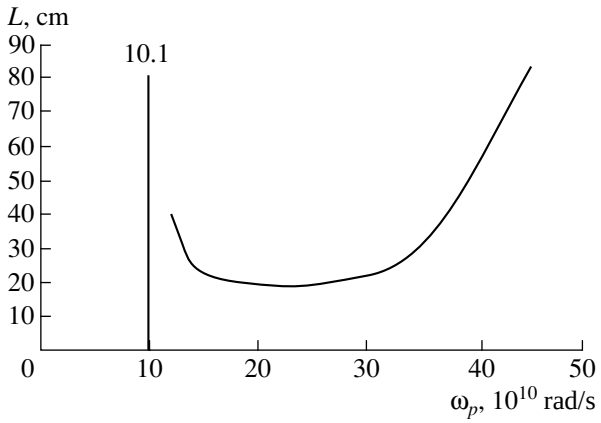

Fig. 5. Optimum accelerator length L vs. the plasma frequency ω_p.

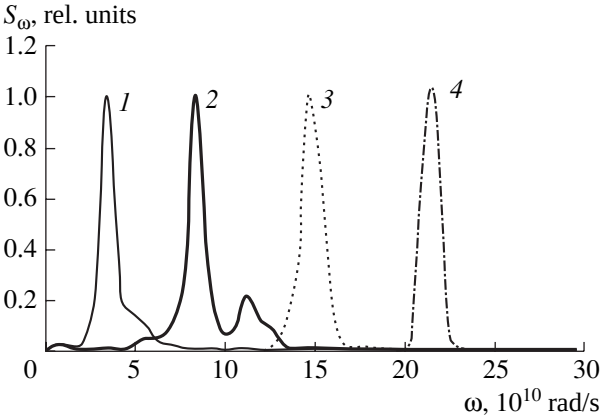

Fig. 6. Spectral density of radiation at the amplifier output for different plasma frequencies: ω_p = (*1*) 15×10^{10}, (*2*) 25×10^{10}, (*3*) 35×10^{10}, and (*4*) 45×10^{10} rad/s.

were computed for the same parameters for which the relevant curves $\delta k(\omega)$ in Fig. 3 were obtained from linear theory. We can see that, because of the nonlinear competition between different microwaves, the emission spectra are somewhat narrower than those predicted by linear theory. On the other hand, the maximum spectral density corresponds to the maximum in the linear amplification coefficient $\delta k(\omega)$. The relative widths of the emission spectra and their central frequencies depend strongly on the plasma frequency.

2.3. Linear Theory of the RCPM

The theory behind a plasma relativistic microwave amplifier assumes that electromagnetic radiation amplified by the beam escapes freely from the amplifier through the boundary $z = L$. However, in reality, the plasma wave amplified by the beam is partially reflected from the exit boundary $z = L$ and returns to the entrance plane $z = 0$. This effect may result in the self-excitation of the amplifier (i.e., in the start-up of microwave generation). An RCPM is usually assumed to be equipped with a metal grid that is placed at the entrance boundary $z = 0$, is transparent to the beam electrons, and is opaque to radiation. The exit boundary $z = L$ of the plasma waveguide is coupled to the emitter (the outlet horn) in the form of a coaxial vacuum waveguide with an outer radius R equal to that of the plasma waveguide and with an inner radius r_0 somewhat larger than the radius r_p of the plasma tube. When passing through the boundary $z = L$, a cable plasma wave converts into a cable vacuum wave, in which case the phase velocity of the microwave field and its structure change. As a result, the plasma wave incident on the emitting horn from the left is partially reflected.

Special numerical methods [26] developed to determine the reflection coefficients of the boundary $z = L$ for a plasma wave in terms of the power (κ^2) and amplitude (κ) are based either on the direct solution of the steady-state diffraction problem or on the determination of the time during which the microwave field escapes from a plasma resonator. The reflection coefficients can also be obtained from approximate analytic formulas [27]. Since all of these approaches yield nearly the same results, the RCPM theory is constructed under the assumption that the reflection coefficient in terms of the field amplitude, κ, is known. Figure 7 illustrates the frequency dependence of the reflection coefficient in terms of the amplitude, calculated for $r_p = 1.1$ cm and $r_0 = 1.15$ cm and for the same four values of the plasma frequency as in Figs. 3 and 6.

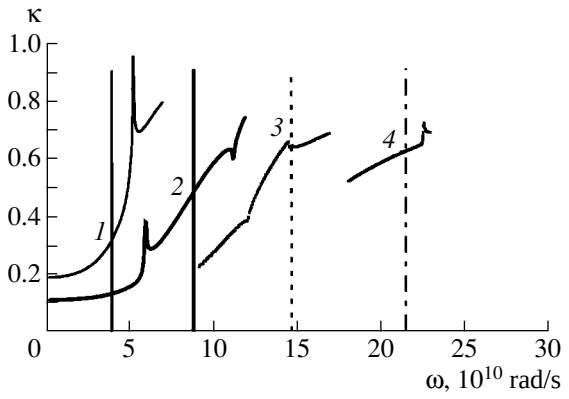

Fig. 7. Frequency dependences of the reflection coefficient for different plasma frequencies: ω_p = (*1*) 15×10^{10}, (*2*) 25×10^{10}, (*3*) 35×10^{10}, and (*4*) 45×10^{10} rad/s.

The vertical lines in Fig. 7 refer to the frequencies at which the amplification coefficients (Fig. 3) and the spectral densities of microwave radiation at the exit from an amplifier (Fig. 6) reach their maxima. The reflection coefficients are seen to be fairly large, although, in the cases at hand, the reflection coefficient in terms of the power, κ^2, does not exceed 0.5. The peaks and breaks in the profiles in Fig. 7 occur at frequencies close to any of the cutoff frequencies of the system.

The basic equations of the linear theory of the RCPM are the linearized equations (2.2.1), whose general solution in the plasma region of the system ($0 < z < L$) has the form

$$\psi = \sum_{j=1}^{4} A_j \exp(ik_{zj}z), \qquad (2.3.1)$$

where $k_{zj} = k_{zj}(\omega)$ are the roots of dispersion relation (2.1.1). Since this dispersion relation is fourth-order in k_z, solution (2.3.1) contains four terms, in which constants A_j are determined with allowance for the above properties of the boundaries $z = 0$ and $z = L$. This approach results in the following equation for the complex frequencies of an RCPM [10, 27]:

$$1 = \kappa(\omega)\sum_{j=1}^{3} \alpha_{j4}(\omega)\exp[i(k_{zj}(\omega) - k_{z4}(\omega))L], \qquad (2.3.2)$$

where α_{j4} are known theoretical wave conversion coefficients at the boundary $z = 0$ [10]. Hence, if the dependence $\kappa(\omega)$ is known, then an RCPM can be calculated in the linear approximation by solving a complicated but purely algebraic problem (2.3.2).

The main result of linear theory is that the expression for the working frequency of an RCPM (i.e., a frequency close to the collective resonance frequency) contains an imaginary correction introduced by the energy transfer from the beam to the resonator and the escape of microwave energy through the horn [10, 27, 28]:

$$\delta\omega = i\frac{u}{2L}\left(|\mathrm{Im}\,\delta k(\omega)|L - \ln\frac{q}{|\kappa(\omega)|}\right), \qquad (2.3.3)$$

where ω is the resonant frequency, the amplification coefficient δk is determined from Fig. 2, and q is a constant whose value lies between 2 and 3. Formula (2.3.3), which is a simplified version of a far more general expression [10, 28], is valid if $\omega L/u \gg 1$ and the group velocity of the plasma wave is close to the beam velocity u.

Formula (2.3.3) gives the self-excitation condition for a beam–plasma resonator [19, 20, 28]:

$$|\mathrm{Im}\,\delta k(\omega)|L = \ln\frac{q}{|\kappa(\omega)|}, \tag{2.3.4}$$

which determines the parameters for the onset of microwave generation (usually, these are the starting beam current and starting resonator length). If the beam current and/or resonator length exceed their starting values, the amplification regime goes over to the generation regime. From Figs. 2 and 7, one can readily estimate the starting length. If the plasma frequency is not too close to the critical frequency, then the starting length is between 10 and 20 cm and equals, on average, 15 cm. However, as can be seen from Fig. 5, the optimum length of the amplifier exceeds the starting length. Consequently, such an amplifier will operate in the generation regime. There are two ways of achieving the amplification regime: first, to make the amplifier shorter while simultaneously increasing the level of the input signal (in order to keep the efficiency optimum) and, second, to improve the coupling of the plasma resonator to the outlet horn.

2.4. Nonlinear Theory of the RCPM

The general nonlinear equations for an RCPM are Eqs. (2.2.1) with the beam current j_b represented by a different expression. In the RCPM theory, the most convenient model for determining the beam current is that based on the macroparticle method, which yields [27–29]

$$j_b = en_b\frac{\lambda}{N}\sum_j v_j(t)\delta(z - z_j(t)). \tag{2.4.1}$$

Here, λ is a characteristic length, N is the number of macroparticles (electrons) in an unperturbed beam region of length λ, and $z_j(t)$ and $v_j(t)$ are solutions to the equations of motion for the jth macroparticle:

$$\begin{aligned}\frac{dz_j}{dt} &= v_j,\\ \frac{dv_j}{dt} &= \frac{e}{m}(1 - v_j^2/c^2)^{3/2}E_z.\end{aligned} \tag{2.4.2}$$

These equations are supplemented with the initial (injection) conditions $z_j(t = t_{0j}) = 0$ and $v_j(t = t_{0j}) = u$, where t_{0j} is the time of injection of the jth macroparticle into a plasma resonator. Length λ is usually determined using the procedure for regularizing the delta-functions in expression (2.4.1); however, this length can also be chosen in a different way.

Clearly, the most general approach to the RCPM problem consists in the direct solution of nonlinear equations (2.2.1) and (2.4.1), which should be supplemented with an additional boundary condition for the polarization potential at the open end $z = L$ of the plasma resonator. This unsteady partial condition for the emission of microwave radiation into the coaxial waveguide was stated by Bobylev *et al.* [30] and was applied to solving the RCPM problem in the most general formulation (paper [30] also contains a detailed bibliography on the subject). One of the most important results of the general nonlinear theory of an RCPM is that the spectrum of electromagnetic radiation excited during a long-term quasisteady injection of an electron beam is fairly narrow:

$$\Delta\omega \ll \omega, \tag{2.4.3}$$

which agrees with the predictions made in the nonlinear theory of a plasma microwave amplifier (Fig. 6). Of course, in the low-frequency range, in which the spectral density of the microwave radiation is described by curve *1* in Fig. 6, inequality (2.4.3) fails to hold, so that the only way to adequately describe the nonlinear regime of RCPM operation is to solve the general nonlinear equations (2.2.1), (2.4.1), and (2.4.2).

Assuming that inequality (2.4.3) is satisfied, we can construct a fairly simple and very illustrative physical model that allows a detailed analysis of the main parameters of an RCPM. Based on this inequality, we consider a wave with a fixed mean frequency and a slowly varying amplitude. In particular, we use the following representation of the polarization potential of the plasma wave that accompanies (resonates with) the beam [see formula (2.2.3)]:

$$\psi = \frac{1}{2}\sum_{n=1}^{\infty}\varphi_n(\mathbf{r}_\perp)\left[A_n(z, t)\exp\left(-i\omega t + i\frac{\omega}{u}z\right) + \text{c.c.}\right], \tag{2.4.4}$$

where the amplitudes A_n vary with the z coordinate and time much more slowly in comparison to the related exponential functions. The equations for the slowly varying amplitudes can be obtained using the averaging procedure

$$\langle\Phi\rangle = \frac{1}{\lambda}\int_{z-\lambda/2}^{z+\lambda/2}\Phi(z')\exp\left(i\omega t - i\frac{\omega}{u}z'\right)dz', \tag{2.4.5}$$

where Φ is the quantity to be averaged and λ is the characteristic length in representation (2.4.1). The expression for λ can be found from formulas (2.4.4) and (2.4.5):

$$\lambda = \frac{2\pi u}{\omega}. \tag{2.4.6}$$

We substitute representation (2.4.4) into Eqs. (2.1.1) and (2.4.1), apply the above averaging procedure, and

perform fairly involved manipulations. As a result, we arrive at the following RCPM equations [27–29]:

$$\left(\frac{\partial}{\partial\xi}+\tilde{v}\frac{\partial}{\partial\tau}\right)J^+ = \frac{i}{2\gamma^2}\left[\left(\frac{1}{\alpha_p}-1\right)J^+ - \theta\alpha_b\hat{L}\langle\rho\rangle\right],$$
$$\frac{dy_j}{d\tau} = \eta_j,$$
$$\frac{d}{d\tau}\left(\frac{\eta_j}{\sqrt{1-\beta^2\eta_j^2}}\right) = -\frac{i}{2}\gamma^3[\exp(-i\tau+iy_j)\hat{L}(\alpha_b\langle\rho\rangle+J^+)-\text{c.c.}]. \quad (2.4.7)$$

Here,

$$\langle\rho\rangle = \frac{2}{N}\sum_j f(\tau_{0j})\exp(i\tau-iy_j),$$
$$\hat{L}_s = 1-2i\gamma^2\left(\frac{\partial}{\partial\xi}+\beta^2\frac{\partial}{\partial\tau}\right), \quad (2.4.8)$$

θ is the coupling coefficient for beam and plasma waves; quantities α_b and α_p are defined by formulas (2.2.5); and the remaining dimensionless variables have the form

$$\tau = \omega t, \quad \xi = \frac{\omega}{u}z, \quad y_j = \frac{\omega}{u}z_j, \quad \eta_j = \frac{v_j}{u}, \quad \beta = u/c, \quad \tilde{v} = V_g/u, \quad (2.4.9)$$

where V_g is the group velocity of a plasma wave obeying dispersion relation (2.1.4).

Although Eqs. (2.4.7) and expressions (2.4.8) are time-dependent, they correspond exactly to the above equations for the plasma amplifier, specifically, to Eqs. (2.2.4) and (2.2.5) with $s = 1$. Quantity $\langle\rho\rangle$ is the complex amplitude of the perturbed beam charge density and corresponds to one of the quantities ρ_s in the equations for the plasma amplifier. In formula (2.4.8) for $\langle\rho\rangle$, we introduced the function $f(\tau_{0j})$ (where τ_{0j} is the time at which the jth electron enters the plasma resonator) in order to model the fronts and density modulation of the beam. Quantity J^+ is a slowly varying amplitude of the plasma wave accompanying the beam and corresponds to one of the functions j_s in Eqs. (2.2.4).

The RCPM theory cannot be constructed only on the basis of Eqs. (2.4.7). We must also take into account the counterpropagating plasma wave, which is responsible for feedback in an RCPM. The counterpropagating wave does not resonate with the beam and, on the average, does not even interact with it. The accompanying and counterpropagating waves interact only at the side boundaries of the plasma resonator, at which they transform into one another. This transformation can be described by the following feedback boundary condition [10, 28]:

$$J^+(\xi=0,\tau) = -\kappa J^+(\xi=\xi^+,\tau-\xi^+/\tilde{v}), \quad (2.4.10)$$

where κ is the reflection coefficient introduced above, $\xi^+ = \omega L/u$ is the dimensionless length of a plasma resonator, and the minus sign indicates that the wave phase changes as the wave is reflected from the metal grid at the boundary $z = 0$. Equations (2.4.7) with boundary condition (2.4.10) constitute a closed set of equations of the nonlinear RCPM theory [27–29]. The results of linear theory that were presented in Section 2.3 can naturally be obtained from the above sets of equations and the feedback condition.

Equations (2.4.7) with boundary condition (2.4.10) can be successfully used in the theory of an RCPM based on pulsed electron beams, provided that $\omega T \gg 1$ [see condition (2.4.3)], where T is the characteristic time scale on which the beam current changes. Thus, under certain conditions during the steady injection of an electron beam, it is possible to achieve a steady-state regime of microwave generation [31], in which case we have $\partial/\partial\tau = 0$, so that Eqs. (2.4.7) pass over to Eqs. (2.2.4) (in which J^+ should be replaced by j_s) and the feedback condition (2.4.10) becomes

$$J^+(\xi=0) = -\kappa J^+(\xi=\xi^+). \quad (2.4.11)$$

Equations (2.2.4) with boundary condition (2.4.11) constitute an eigenvalue problem whose solutions determine the steady-state regimes of RCPM operation. In this problem, the eigenvalue is $J^+(\xi = 0)$. Whether or not steady-state operation regimes exist is not *a priori* clear. However, if steady-state regimes do exist, they can be determined through a simple iteration procedure. First, for a very small value of $J^+(\xi = 0)$, it is necessary to solve Eqs. (2.2.4) and to determine the new value $J^+(\xi = \xi^+)$. Then, it is necessary to calculate the new value $J^+(\xi = 0)$, to solve Eqs. (2.2.4) again, and so on. If this iteration process converges, then a possible steady-state regime of RCPM operation will be determined. However, instead of iterating, one can directly look for a solution to the time-dependent equations (2.4.7) with boundary condition (2.4.10). This somewhat more involved approach makes it possible to investigate the achievement of not only steady-state but also quasi-steady-state generation regimes.

Let us consider some results of modeling an RCPM operating with a steady injection of an electron beam [31]. In the corresponding calculations, we varied the plasma frequency and the length of the plasma resonator while keeping the remaining parameters fixed: I_b = 2 kA, R = 1.8 cm, r_b = 0.6 cm, $\Delta_b = \Delta_p$ = 0.1 cm, $\gamma = 2$, and r_p = 1.1 cm (see above). Figure 8 shows the generation efficiency obtained as a function of the length L of the plasma resonator for the same four values of the plasma frequency as in Figs. 3, 6, and 7 and for the reflection coefficients in Fig. 7. A sharp increase in the

generation efficiency from zero to a fairly high level stems from the fact that the resonator length exceeds its starting value. As can be seen from Fig. 8, the starting lengths are very close to those determined by condition (2.3.4). In a longer plasma resonator, the generation efficiency is seen to oscillate, because the point of saturation of the beam instability is periodically displaced from the exit boundary $z = L$ toward smaller values of z and back. In this case, the maximum values of the generation efficiency even turn out to be somewhat higher than those in the case of the amplification of a monochromatic signal. However, a comparison between Figs. 8 and 4 confirms that the generation efficiency decreases as the plasma frequency increases. On the whole, different methods and models for calculating Cherenkov plasma microwave oscillators and amplifiers based on dense electron beams yield close results on the efficiencies, spectra, critical plasma frequencies, starting characteristics, and the dependences on the main parameters of the beam–plasma system. These theoretical results agree well with the data from the experimental investigations that will be described below.

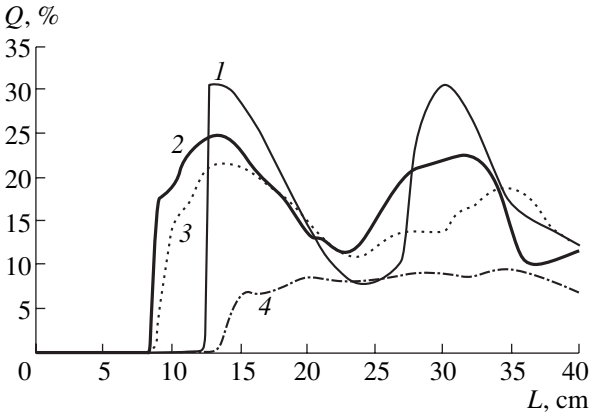

Fig. 8. Maximum generation efficiency Q vs. the plasma-resonator length for different plasma frequencies: ω_p = (*1*) 15×10^{10}, (*2*) 25×10^{10}, (*3*) 35×10^{10}, and (*4*) 45×10^{10} rad/s.

3. EXPERIMENTAL PLASMA RELATIVISTIC MICROWAVE ELECTRONICS

3.1. Relativistic Cherenkov Plasma Maser

3.1.1. Scheme of the RCPM. The first experiments on the excitation of waves in a plasma waveguide by a high-current REB were carried out in 1982 [17, 18]. The RCPM scheme, which has changed insignificantly since that time, is illustrated in Fig. 9. A high-voltage pulse is applied to an accelerator cathode (*1*). An REB *2* is injected along the axis of a circular metal waveguide (*3*) prefilled with an annular plasma (*4*). The beam and the plasma are immersed in a uniform longitudinal magnetic field **B**. The beam electrons have a longitudinal velocity component only. The electron beam terminates at the end of the central conductor (*5*) of the coaxial emitter (*6*). Microwaves are generated in the plasma waveguide, propagate through the vacuum coaxial waveguide (*6*) and are emitted through the outlet horn (*7*). The basic ideas underlying this scheme are the following.

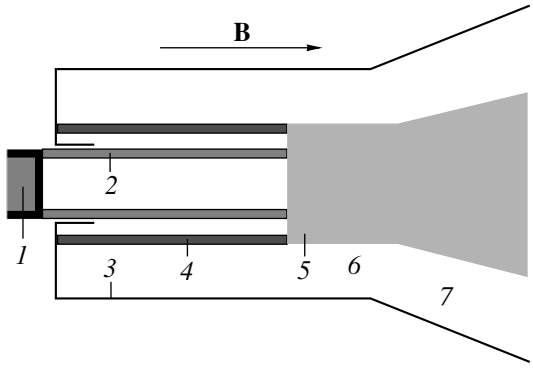

Fig. 9. Schematic of the RCPM: (*1*) accelerator cathode, (*2*) REB, (*3*) metal waveguide, (*4*) plasma, (*5*) REB collector, (*6*) coaxial vacuum waveguide, and (*7*) output horn.

The annular plasma diameter is larger than that of the electron beam, so that the plasma does not penetrate into the diode of the high-current accelerator. In experiments on the injection of an REB into a plasma, the method of separating the diode from the plasma with the help of a thin metal foil transparent to relativistic electrons was also used. However, the use of a foil leads to the appearance of the transverse velocity component of the beam electrons, which substantially decreases the efficiency of the Cherenkov interaction.

The transverse dimensions of the waveguide, beam, and plasma, as well as the electron densities in the plasma and beam and the magnitude of the magnetic field, are constant along the device axis. This circumstance significantly simplifies the theoretical analysis. The plasma is immersed in a strong uniform magnetic field such that the electron cyclotron frequency Ω_e is higher than the microwave radiation frequency ω ($\Omega_e > \omega$). This ensures the absence of a resonant absorbing layer in which the radiation frequency is equal to the hybrid frequency: $\omega^2 = \omega_p^2 + \Omega_e^2$.

A substantial fraction of the energy of the excited plasma wave is concentrated inside the vacuum gap between the plasma and the waveguide wall. In this region, the field structure of the plasma wave is similar to that of the TEM mode of the coaxial outlet emitter. This fact, along with a high phase velocity close to the speed of light guarantees the high conversion efficiency of the energy of the slow plasma wave into microwave energy. The coaxial outlet emitter used in the scheme provides efficient extraction of radiation from the RCPM in a broad frequency band.

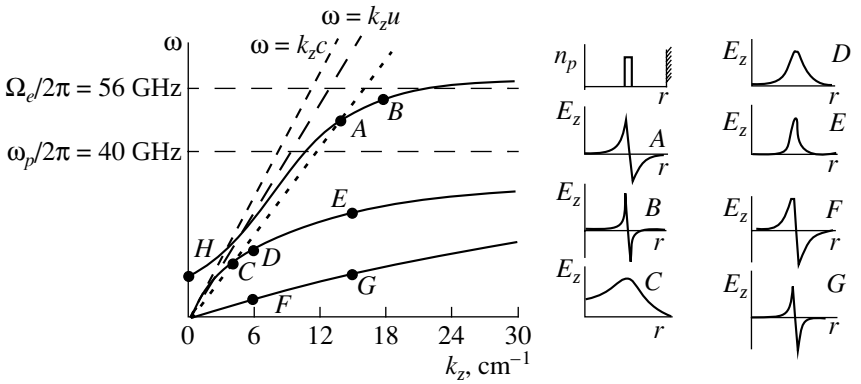

Fig. 10. Dispersion of modes of a plasma waveguide in a finite magnetic field at $\Omega_e = 1.4\omega_p$ (on the left) and the radial profiles of the plasma density $n_p(r)$ and longitudinal component $E_z(r)$ of the microwave electric field for points *A*–*G* (on the right). Curve *HAB* corresponds to the vacuum E_{01} mode modified in the presence of a plasma; curve 0*CDE* corresponds to the lowest radial mode ($i = 1$) of the slow azimuthally symmetric plasma wave; curve 0*FG* is the same for $i = 2$; and the dashed line 0*CA* corresponds to the slow wave of the beam space charge.

The maximum value of δk in Fig. 3 at fixed values of the electron energy and the electron beam current depends on the coupling between the beam and the plasma wave. In the experiment, the coupling was varied by varying the gap length between the annular REB and plasma. As the gap length decreases, both field E_z in the electron beam (see the distribution $E_z(r)$ at point *C* in Fig. 10) and δk increase.

Figure 10 shows the calculated dispersion curves for the waves in the plasma waveguide and the radial profiles of the electric field of the plasma wave for the following experimental conditions: the radius of the metal waveguide is $R = 1.8$ cm, the radius of the annular plasma is $r_p = 1$ cm, the plasma thickness is $\Delta r_p = 0.1$ cm, $\gamma = 2$, $I_b = 2$ kA, and $\Omega_e = 1.4\omega_p$.

When the waveguide is filled with a plasma, the fast wave of the vacuum waveguide E_{01} (whose phase velocity exceeds the speed of light) is converted into the mode presented by curve *HAB*. This mode of the plasma waveguide remains fast at low frequencies, but it becomes slow as the frequency increases: $\omega \longrightarrow \Omega_e$ for $k_z \longrightarrow \infty$. In Fig. 10 (on the right), the radial profiles of the component E_z of the microwave electric field are also shown. It is seen that, as k_z increases, field E_z becomes more concentrated inside the plasma (compare the $E_z(r)$ profiles for points *A* and *B*).

Now, we consider the dispersion of slow plasma waves whose frequencies lie below ω_p. Figure 10 shows the dispersion curves of two axisymmetric plasma modes 0*CDE* and 0*FG*. For large values of the longitudinal wavenumber k_z, the frequency ω of both modes approaches ω_p. The 0*CDE* mode is the lowest radial mode (see the $E_z(r)$ profiles for points *C*, *D*, and *E*), whereas the 0*FG* mode is a higher radial mode (see the $E_z(r)$ profiles for points *F* and *G*). As is the case for the faster mode represented by curve *HAB*, field E_z becomes more concentrated inside the plasma as k_z increases (compare the $E_z(r)$ profiles for points *C* and *E* and points *F* and *G*, respectively). This means that, at large k_z values, the wave transforms into the longitudinal wave of an infinite cold plasma with frequency ω_p and the group velocity close to zero.

The straight line $\omega = k_z u$ in Fig. 10 corresponds to a beam with an electron energy of 500 keV. For the finite value of the beam electron density, the dispersion curve of the slow beam wave takes the form of line 0*CA*. The electron beam interacts with only one of two slow plasma waves 0*CDE* and 0*FG*, namely, with the lowest radial mode: curve 0*CA* (electron beam) intersects curve 0*CDE* (plasma) at point *C*, but does not intersect curve 0*FG*. Thus, it is possible to avoid the intersection of curve 0*CA* with all the curves (curve 0*FG* and, maybe, another) except one (curve 0*CE*), if the slope of these curves near the coordinate origin is sufficiently low. This example illustrates the principle of mode selection for the slow plasma waves: it is possible to suppress the excitation of all of the slow plasma waves except one if their group velocities are sufficiently low at $k_z \longrightarrow 0$.

The intersection of the curves at point *A* in Fig. 10 shows that there is a possibility of coupling between the electron beam (curve 0*CA*) and the wave represented by curve *HAB*. In this case, the selection of modes (the plasma wave 0*CDE* and wave *HAB*) is based on another principle, namely, on the difference between the electric field profiles $E_z(r)$ shown on the right in Fig. 10. We note that, near the waveguide axis (at small values of *r*), the field E_z of the fast wave at point *A* almost vanishes. In the same region near the axis, the slow plasma wave (at point *C*) has a substantially higher amplitude of the longitudinal electric field E_z. In the case of the Cherenkov interaction with the electron beam, the wave with a higher field will predominantly be excited. Therefore,

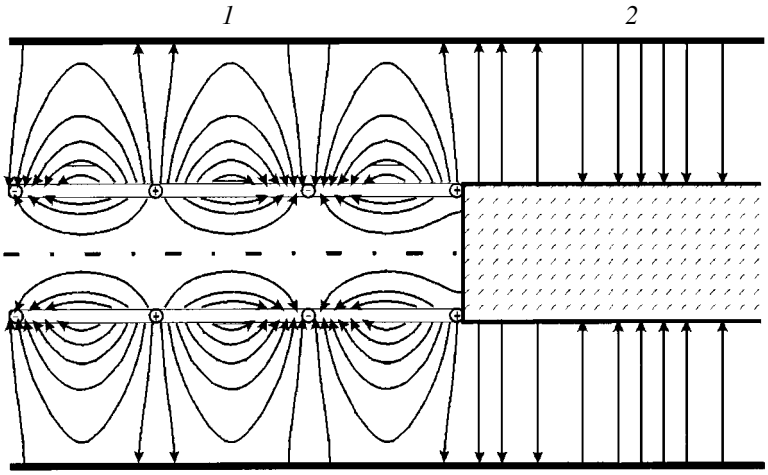

Fig. 11. Pattern of the electric field in a plasma waveguide for point *D* in Fig. 10: (*1*) plasma waveguide region and (*2*) metal coaxial waveguide.

the slow plasma wave will only be excited if the electron beam radius is not too large.

Figure 11 shows the pattern of the electric field at point *C*; this picture qualitatively confirms the $E_z(r)$ profile presented in Fig. 10.

It can be seen in Fig. 11 that the field E_z is maximum inside the plasma and decreases both toward the axis and toward the waveguide wall. It is also easy to infer that the field outside the plasma is high when the wavelength satisfies the inequality $2\pi/k_z > R - r_p$.

From Fig. 11, we can draw two important inferences. First, the field distribution in the gap between the plasma and the waveguide wall is similar to the field distribution of the TEM mode of a coaxial plasma waveguide. This favors the good conversion of this wave into the wave of the metal coaxial waveguide, through which microwave energy is emitted into space. Second, the field at the wall of the metal waveguide is relatively low (particularly, at short wavelengths) and only has a radial component. This circumstance, along with the presence of a strong external longitudinal magnetic field, decreases the probability of microwave breakdown on the waveguide wall.

The frequency dependence of the electric field amplification coefficient δk for different values of the plasma density was given above in Fig. 3. It is seen that, for a fixed value of the plasma density, the linear theory predicts the broadband microwave excitation. An important point is that, over a wide range of plasma densities, the maximum value of the amplification coefficient varies only slightly within a wide frequency band (in our case, from 12 to 20 GHz). This shows promise for creating an oscillator (or amplifier) in which a broadband frequency tuning at a constant efficiency could be achieved by varying only the plasma density, without changing the geometry of the device.

3.1.2. Experimental results and comparison with theory. Typical parameters of RCPMs are the following. In different experiments [17, 32–35], the radius of the metal waveguide was in the range R = 18–35 mm, the waveguide length was L = 10–50 cm, the REB radius was r_b = 6–14 mm, and the plasma radius was r_p = 7–20 mm. The plasma waveguide was in a uniform magnetic field B = 1.7–2.2 T. The energy of beam electrons was in the range 500–700 keV; the beam current was I_b = 2–3 kA; and the current pulse duration in different experiments was 30, 100, or 1000 ns.

The presence of a threshold plasma density [see formula (1.2.8)] above which microwave radiation is generated confirms the Cherenkov mechanism for the plasma wave excitation. For comparison, the experimental [35] and calculated values of the threshold plasma density are presented in the table for two plasma resonator lengths L = 10 and 20 cm. The other parameters are the following: R = 1.8 cm, r_p = 1 cm, r_b = 0.6 cm, $\Delta_p = \Delta_b$ = 0.1 cm, γ = 2, and I_b = 2 kA.

Taking into account the measurement accuracy and the inevitable difference between the experiment and the theoretical model, we can conclude that the table demonstrates quantitative agreement between calculations and experiment.

Figure 12 shows the RCPM spectra [35] for R = 1.8 cm, r_p = 1 cm, r_b = 0.6 cm, L = 20 cm, γ = 2, I_b = 2 kA, B = 2.2 T, and different values of the plasma density. It follows from the figure that the mean microwave

Threshold plasma density

	Experiment	Calculation
L = 10 cm	5×10^{13} cm^{-3}	2×10^{13} cm^{-3}
L = 20 cm	3×10^{12} cm^{-3}	2×10^{12} cm^{-3}

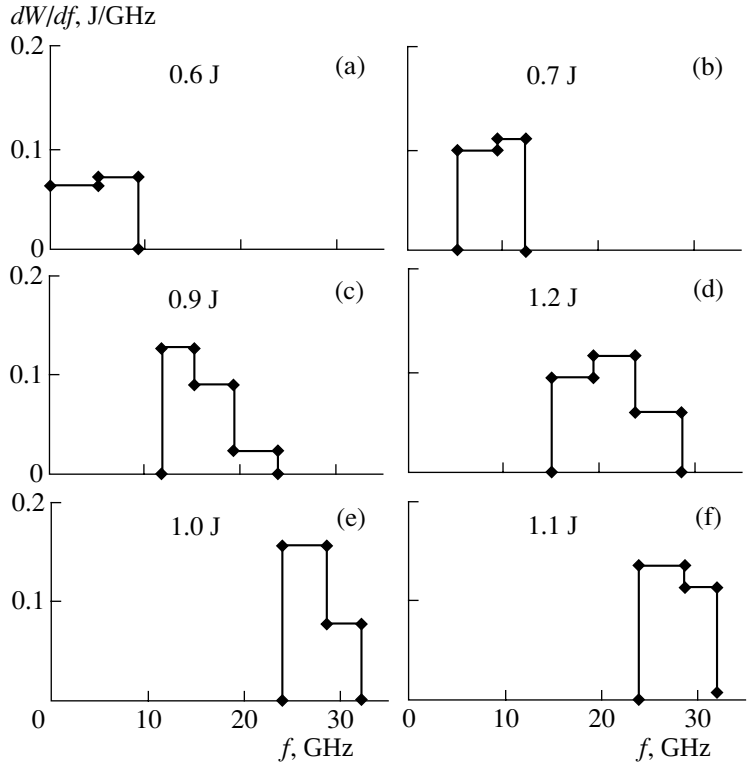

Fig. 12. Spectra of an RCPM for several values of the plasma density: n_p = (a) 4×10^{12}, (b) 9×10^{12}, (c) 2×10^{13}, (d) 4.5×10^{13}, (e) 6×10^{13}, and (f) 7×10^{13} cm^{-3}. The total energy of the microwave pulse is given in each figure.

frequency increases from 4 to 28 GHz as the plasma density increases from 4×10^{12} to 7×10^{13} cm^{-3}.

In Fig. 13, the experimental dependence of the mean RCPM frequency on the plasma density is compared with the results of calculations. Calculations were performed for an amplifier at given input frequencies from 0 to 40 GHz. We stress the fact that calculations were carried out for an amplifier; i.e., we did not take into account the possible effect of the reflection of the generated radiation from the ends of the plasma waveguide (as is in the experiment) on the emission spectrum. Nevertheless, the experimental dependence of the mean frequency on the plasma density, for the most part, coincides well with calculations; the discrepancy is only observed at high plasma densities.

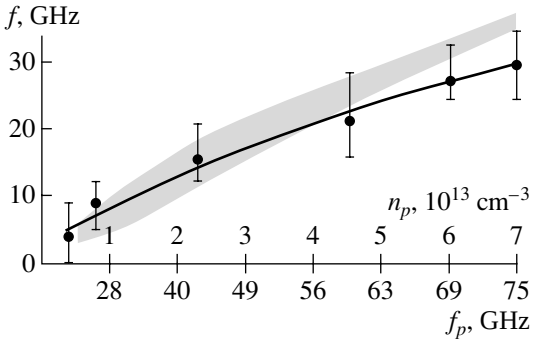

Fig. 13. Microwave frequency f vs. the plasma density n_p and the plasma frequency $f_p = \omega_p/2\pi$. The bold line and points correspond to the experiment, the vertical bars show the measured spectral width (corresponding to Fig. 12). The calculated spectrum width at a level of 0.3 of the maximum value of the emission spectral density is shown by shading. The calculation is performed for $\Omega_e/2\pi \gg f_p$; in the experiment, we have $\Omega_e/2\pi$ = 62 GHz.

The experimental spectrum width is shown in Fig. 13. However, the accuracy of measurements of the spectrum width was rather low; it may be only asserted that the spectrum width is no larger than the value given in the figure and is no less than one-half of this value. Therefore, it follows from Fig. 13 that the RCPM spectrum width is greater than or equal to the calculated value of the amplifier spectrum width. The microwave pulse duration was equal to 25 ns over the entire range of plasma densities. Consequently, 1 J corresponds to a power of 40 MW. Note that, as the plasma density varies from 9×10^{12} to 7×10^{13} cm^{-3}, the microwave power varies insignificantly (from 30 to 50 MW) and the efficiency varies from 3 to 5%.

According to calculations (Fig. 8), the efficiency of a microwave oscillator of length L = 20 cm varies from 13 to 8% as the plasma density varies from 7×10^{12} to 6×10^{13} cm^{-3}. Consequently, the degree to which the

calculated power is constant within this range of plasma densities coincides well with the experiment: the ratio between the maximum and minimum efficiencies is equal to 1.6. However, the experimental value of the efficiency is nearly half as large as the calculated one. According to Fig. 8, the maximum value of the calculated efficiency is achieved at a plasma resonator length of $L = 12$ cm. Qualitatively the same dependence (i.e., the increase in the efficiency with decreasing length L) was observed in the experiment: as the length decreased from 20 to 10 cm, the power increased from 50 to 60 MW and the efficiency reached 6%.

The results presented in Figs. 12 and 13 were obtained with a plasma waveguide length of $L = 20$ cm, $B = 2.2$ T, and $n_p = (0.4–7) \times 10^{13}$ cm^{-3}, in which case we have $\Omega_e/\omega_p = 3.5–0.82$. We note that, in calculations, it was assumed that $\Omega_e \gg \omega_p$. From Fig. 13, it can be seen that the calculated and experimental data coincide at $\omega_p < \Omega_e$. Note that, in the experiment with a lower magnetic field of $B = 1.2$ T, the coincidence between calculations and experiment was also observed at $\omega_p < \Omega_e$.

Hence, the characteristic experimental dependences are qualitatively confirmed by calculations (except for the absolute value of the efficiency). The coincidence of the calculated and experimental dependences of the emission frequency on the plasma density implies that, indeed, an axisymmetric lowest radial mode of the slow plasma wave is excited in the experiment. The width of the emission spectrum and the generation efficiency are determined by the frequency dependence of the linear amplification coefficient $\delta k(\omega)$ and the nonlinear processes of trapping the beam electrons by the microwave field.

Thus, an RCPM has been created whose mean frequency can be continuously tuned over a wide band with an upper-to-lower boundary frequency ratio of 7. The frequency can be tuned during ~30 μs; the tuning time is limited from below by the rate at which the plasma density can be varied in the electrodynamic system. Such a tuning cannot be achieved in vacuum relativistic oscillators. The maximum microwave power (0.5 GW) in our experiments was obtained by using an electron beam with an energy of 1 MeV and current of 5 kA (i.e., at an efficiency of 10%) [36].

As was mentioned in the Introduction, one of the advantages of plasma-filled microwave devices is the possibility of transporting the currents exceeding the vacuum limiting current [see formula (1.2.6)]. At the same time, calculations [28] show that the RCPM efficiency is maximum when the current is nearly half as large as the vacuum limiting current. In the experiment described above, we used a current of 2.0 kA, whereas the vacuum limiting current was equal to $I_0 = 3.5$ kA. The increase in the REB current up to 3 kA [35] is not accompanied by the increase in the microwave power, which confirms the results of calculations [28].

The limiting electron beam current in RCPMs can also be increased by increasing the electron beam radius. In [32], the waveguide radius was $R = 14.5$ cm and the electron beam radius was $r_b = 10$ or 12.7 mm. The corresponding values of the vacuum limiting current were 10 and 30 kA, respectively. In this case, the diameter of the annular plasma was smaller than that of the REB and was equal to $r_p = 7$ mm. For a beam with a current of 6 kA, an electron energy of 420 keV, and a radius of $r_b = 12.7$ mm, the microwave power was ≈300 MW; i.e., the efficiency reached ≈12%. Further increase in the current did not result in an increase in the microwave power.

For some applications, it is important to excite the H_{11} mode at the output of the microwave oscillator. In [32], a TEM-to-H_{11} mode converter was installed at the RCPM output. It was shown that an REB with an electron energy of 570 keV and a current of 3 kA generated only the H_{11} mode in the emitting horn, the emission power being 100 MW and the efficiency being ≈6%.

3.1.3. Microsecond RCPMs. One of the main problems of high-power microwave electronics is the "microwave pulse shortening" effect which shows up as follows. After injecting into the electrodynamic system, the REB starts to generate high-power microwaves; however, after a certain time, the generation terminates although the electron beam continues to propagate through the device. Because of the shortening effect, the duration of the microwave pulse is limited by tens of nanoseconds. This effect is the most pronounced in microwave oscillators with a relatively long duration of the current pulse (on the order of one microsecond and longer).

The cause of the microwave pulse shortening is the appearance of a plasma in different sections of the device. The plasma produced by the explosive-emission cathode expands across the magnetic field; as a result, the shape of the REB changes and the conditions for its optimum interaction with the electrodynamic structure are violated. The plasma produced at the collector bombarded by electrons expands toward the high-current REB at a velocity of up to 10^8 cm/s and can penetrate into the electrodynamic structure or merely lock-in microwaves, which thus cannot be emitted from the device. Furthermore, a plasma can be produced immediately in the electrodynamic structure by microwave breakdown.

Our long-term investigations permitted us to resolve the problem of the cathode plasma. We have created an original magnetically insulated diode [37, 38] in which the shape of an annular thin-walled REB formed at an explosive-emission cathode remained unchanged for one microsecond. It turned out that the diode also had other advantages. By using the method we developed [39] for measuring the transverse velocities of relativistic electrons in a strong magnetic field, we revealed that their pitch angles did not exceed several degrees over the entire cross section of the dense electron beam

throughout the entire microsecond current pulse. This means that such an electron beam completely satisfies all the requirements for using it in high-power long-pulse microwave oscillators.

We have also created an original collector unit with unique properties [40]. This unit not only completely protects the oscillator from the penetration of the collector plasma into it, but also acts so that relativistic electrons reflected from the collector do not propagate along the magnetic field lines back into the electrodynamic structure.

The most serious problem associated with the microwave pulse shortening effect is the generation of a plasma on the walls of the electrodynamic structure. We have revealed the mechanism for the formation and accumulation of this plasma [41]. This mechanism is as follows. When passing through the electrodynamic structure, the electron beam is partially degraded under the action of the strong microwave field. A relatively small fraction of electrons fall onto the wall. Nevertheless, the bombardment of the wall by electrons initiates the formation of a plasma, the amount of which increases rapidly due to the surface microwave discharge on the wall.

The only way of decreasing the number of electrons arriving at the wall and increasing the microwave pulse duration is to increase the distance between the electron beam and the surface of the electrodynamic structure. Unfortunately, in vacuum high-current electronics, the possibility of increasing this distance is strongly limited by the electron-beam space charge (which also determines the REB vacuum limiting current (1.2.6)). Indeed, as the distance increases, the electrostatic potential of the beam increases and the kinetic energy of electrons and, consequently, the microwave power decrease. In actual high-current electronic devices, the gap between the electron beam and the metal wall usually does not exceed several millimeters.

Thus, there is a mechanism limiting the microwave pulse duration. This effect is difficult to avoid in vacuum relativistic electronic devices; however, this problem can be resolved in plasma electronics.

As was mentioned above, the electron beam in a coaxial RCPM (Fig. 9) is shielded from outside by a dense plasma that is placed at a short distance (on the order of several millimeters) from the beam. In this case, the electrostatic field of the REB does not penetrate into the plasma. Both the electron beam and the plasma can be placed inside a metal waveguide with an arbitrarily large radius, in which case the REB electrons cannot reach the wall. In addition, the electric component of the microwave field decreases rapidly with distance away from the plasma (Fig. 10) and the electric field amplitude at the waveguide wall is much less than that in the plasma–beam coaxial line. Therefore, in the RCPM, it is relatively easy to avoid one of the main causes of the microwave pulse shortening—microwave breakdown on the wall of the electrodynamic structure.

Increasing the waveguide cross section is one of the traditional ways of decreasing the microwave field amplitude and, consequently, the probability of breakdown. In vacuum microwave electronics, this problem involves difficulties because efforts to suppress the generation of modes other than the main oscillation mode (the so-called "multimode oscillation") are not always successful. The described structure of the microwave field in the RCPM provides an opportunity to avoid multimode oscillation, which arises when the waveguide radius is increased, and to obtain a single-mode generation over a broad frequency band.

The advantages of using a plasma were realized in an RCPM designed by us [42]. In this device, we used a microsecond REB (500 keV, 2 kA, 1000 ns) to obtain microwave pulses with a duration of 800 ns at a power of 40 MW.

3.2. Plasma Relativistic Microwave Amplifier

Experiments with the RCPM demonstrated its unique property: the possibility of varying the microwave generation frequency over a wide range (4–28 GHz) by varying the plasma density at an almost constant microwave power. The broad spectrum of the RCPM (~30% of the mean frequency) is of interest for solving a number of applied problems. However, the creation of monochromatic microwave sources that can be tuned over a frequency range as wide as in RCPMs is also of great practical importance.

The problem of the amplification of a monochromatic signal is the simplest for theoretical consideration and allows a detailed theoretical description. Therefore, it was reasonable to begin experimental studies with investigations of a plasma relativistic microwave amplifier rather than of an oscillator. However, the experimental implementation of a microwave amplifier occurred to be very complicated. The reason for this was the self-excitation of the device, i.e., the change of the amplification operating mode to the generation mode. The amplification of the microwave field over a broad frequency band and the simultaneous suppression of self-oscillations turned out to be a very laborious problem. That is why experiments on the plasma relativistic microwave amplifier have only been performed recently [43, 44].

3.2.1. Scheme of the microwave amplifier. The scheme of a plasma relativistic microwave amplifier [44] is shown in Fig. 14. An annular plasma (*1*) with a mean radius of $r_p = 7.5$ mm and thickness of $\Delta_p = 1$ mm is immersed in a uniform longitudinal magnetic field $B = 1.6$ T in a cylindrical metal waveguide (*2*) of radius $R = 22$ mm. A hollow thin-walled REB (*3*) with an electron energy of 550 keV, a current of 1.5 kA, and a pulse duration of 150 ns propagates along the waveguide axis. The mean radius of the electron beam is $r_b = 10$ mm, and the beam thickness is $\Delta_b = 1$mm.

At the amplifier input, there is a microwave converter (*4*) exciting the TEM mode, which is converted into a fast and slow eigenmodes of the plasma waveguide (Fig. 10). The slow plasma wave is amplified by the REB. Then, it is converted into the TEM mode of the output metal coaxial waveguide and the latter is emitted by an output coaxial horn (*5*) with a large cross section. The plasma waveguide length over which the REB interacts with the plasma is 29 cm.

A microwave absorber (*6*) with an outer radius of 22 mm, an inner radius of 11.5 mm, and a length of 14 cm is placed at a distance of 3 cm from the conical collector of the REB at the outlet from the system. The absorber is intended to prevent the self-excitation of the device. The microwave absorption coefficient is equal to 20 dB for the TEM mode of a coaxial waveguide with an inner radius of 5 mm and an outer radius of 22 mm, and it is equal to 50 dB for the TM_{01} mode of a circular waveguide with a radius of 22 mm. The measurements were conducted at a frequency of 9.1 GHz.

As a source of input microwave signals, we used one of two pulsed magnetrons. One of them had a frequency of $f_1 = 12.9$ GHz, pulse duration of 2 μs, and power of $P_{in} = 75$ kW. The parameters of the second magnetron were $f_2 = 9.1$ GHz, 20 μs, and 40 kW, respectively.

The output microwave power and the emission spectrum were measured by two detectors installed in a 23×10 mm^2 receiving waveguide. The first (broadband) detector measured the total microwave power in the receiving duct. At the input of the second (narrowband) detector, there was one of two narrowband microwave filters tuned to the magnetron frequency; the filter passband was $\Delta f = 0.29$ GHz for $f_1 = 12.9$ GHz and $\Delta f = 0.51$ GHz for $f_2 = 9.1$. GHz. Both detectors had nearly the same sensitivity. When the emission spectrum was narrower than the microwave filter passband, the ratio between the signals from the narrowband and broadband detectors was equal to unity. When the emission spectrum was wider than the microwave filter passband, this ratio decreased. In this way, we could estimate the spectrum width of the output microwave radiation.

3.2.2. Experimental results. Figure 15 shows the ratio between the signals from the narrowband and broadband detectors 75 ns after the REB has started to be injected into the amplifier. It can be seen that, in the range of plasma densities $5 \times 10^{12} < n_p < 1.5 \times 10^{13}$ cm^{-3}, the output signal of the microwave amplifier always lies within the passband of the narrowband detector (the power ratio is close to unity). The power of the amplified signals in this range of plasma densities always exceeded a level of 3 MW, the maximum power being 8 MW.

A comparison of the experimental dependence P/P_f (Fig. 15a) with the calculated dependence for the single-pass linear power amplification coefficient K on the plasma density (Fig. 15b) shows that the effect of

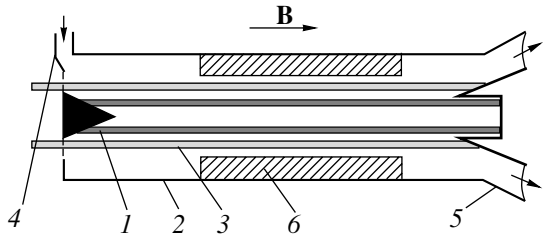

Fig. 14. Schematic of the plasma relativistic microwave amplifier: (*1*) plasma, (*2*) metal waveguide, (*3*) REB, (*4*) amplifier inlet, (*5*) coaxial conical emitting horn, and (*6*) microwave absorber.

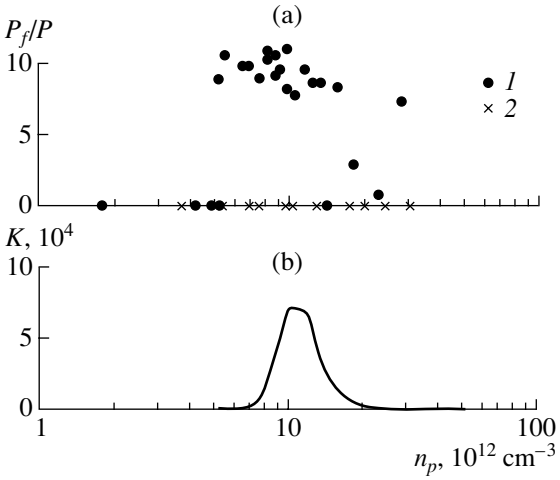

Fig. 15. (a) Ratio of the powers measured by the narrowband P_f and broadband (P) detectors at a frequency of $f_2 = 9.1$ GHz (*1*) in the presence of an input signal with a power of 40 kW and (*2*) in the absence of an input signal; (b) single-pass linear power amplification coefficient K as a function of the plasma density n_p.

microwave amplification takes place for the range of plasma densities predicted by the theory.

We note that, in the absence of an input microwave signal, no microwave radiation was detected in this range of plasma densities. This means that Fig. 15 demonstrates the amplification effect, rather than another well-known effect—the narrowing of the spectrum of a microwave oscillator under the action of an external controlling monochromatic signal.

Calculations show the frequency of the amplified radiation can be tuned over a broad band (Fig. 3). To verify this theoretical result, we also carried out experiments on microwave amplification at the frequency $f_1 = 12.9$ GHz ($P_{in} = 75$ kW). At this frequency, amplification was observed for higher plasma densities, namely, in the range $10^{13} < n_p < 3 \times 10^{13}$ cm^{-3}, which coincides with the calculation results.

Thus, a stable amplification regime was obtained for the first time for the slow plasma wave in a beam–

plasma system. It is shown that, at an input signal frequency of 9.1 GHz, there is a range of plasma densities for which the spectrum of output microwave radiation lies within the 0.5-GHz band during the entire period of REB propagation through the plasma (150 ns). The output power of the amplified signals attains 8 MW, and the power amplification coefficient is on the order of 200. It was experimentally demonstrated that the same device can also operate at a frequency of 12.9 GHz. The experiment has confirmed the theoretical prediction that there is a plasma density value at which the beam–plasma system amplifies radiation at both frequencies.

4. EXPERIMENTAL TECHNIQUES

4.1. Diagnostic of a High-Current REB and High-Power Pulsed Microwave Radiation

A high-current relativistic electron flow is a specific medium that had no analogues in the experimental physics until the advent of high-current accelerators in the early 1970s. Of course, voltages of hundreds of kilovolts and powers of several gigawatts had been used before in electrical power engineering. However, these were slowly varying (50 Hz) voltages and the power was transferred with the help of facilities tens of meters in size. Nanosecond current pulses can be generated using relatively small-sized devices; however, the requirements on the electric strength remain as stringent as earlier.

These mutually contradictory requirements, namely, that the devices should be compact and could withstand voltages up to hundreds of kilowatts and carry kiloampere currents, determine the specifics of the facilities employed in high-current relativistic electronics, in particular, the diagnostic equipment. For this reason, it was necessary to develop special methods for measuring the parameters of high-current REBs.

Concurrently, methods for diagnosing microwave pulses of unique (for those times) power (on the order of 10^8 W) generated with REBs were developed.

4.1.1. Diagnostics of a high-current REB. In the first place, the complex diagnostics of a high-current REB includes the measurements of the electron energy (the absolute value of the electron velocity) and the total current of an electron beam. Another important parameter is the distribution of the electron current over the beam cross section. Moreover, since the electron beam propagates in the magnetic field, it is also no less important to have information about the direction of the electron velocity with respect to the field.

The total electron energy depends on the potential of the accelerator cathode, at which the electron beam is produced. The cathode potential was measured with a capacitive divider. However, in order to be convinced that the diode of the high-current accelerator indeed forms a monoenergetic electron beam and also to calibrate the capacitive divider, the electron energy was measured directly (in absolute units) with the help of an original electrostatic analyzer [45].

The total electron beam current is difficult to measure because it is fairly high (several kiloamperes) and the current pulse is rather short. To resolve this problem, we designed special shunts made of metal conductors [46, 47] and low-inductance shunts based on conducting rubber [48].

The spatial and temporal uniformity of the electron current density over the beam cross section is the key requirement for various devices of high-current relativistic electronics. In all of our experiments, an explosive-emission cathode was used to generate the REB. The plasma emitter of this cathode varies with time, which can result in the variations in the electron beam size. To measure the distribution of the electron beam current density over the beam cross section, we designed a sectioned current-density meter [49] using a slit diaphragm.

The REB phase portrait depends on the electron kinetic energy and the orientation of the electron velocity relative the magnetic field, along which the beam propagates. The pitch angle is the angle between the electron velocity and the magnetic field. At a fixed value of the cathode potential, it is the pitch angles of electron trajectories that determine the efficiency with which the electron beam is used during plasma heating, microwave generation, etc. The development of the methods for measuring the pitch angles of electron trajectories is the most important component of the REB diagnostics.

Our first experiment on the measurements of the electron distribution over pitch angles with the help of the "pinhole method" was described in [50]. In [51], for the first time, this method was grounded theoretically and the criterion of its applicability was determined. The use of rapidly varying magnetic fields allowed us to further improve this method and substantially increase the accuracy of measurements [39]. In addition, the domain of applicability of the method was extended so that it became possible to perform measurements in stronger magnetic fields and longer (by one order of magnitude) electron current pulses.

We also mention a unique method for visualizing the electron trajectories [52], which is based on the glow of a thin dielectric film under the action of relativistic electrons penetrating through it. This method allowed us to carry out the first simultaneous measurements of the electron energy and the transverse size of the beam and estimate the angular distribution of particle trajectories simultaneously at different points over the beam cross section.

4.1.2. Diagnostics of high-power microwave pulses. The methods for measuring the parameters of microwave pulses produced with high-current REBs differ substantially from the methods that existed before the advent of gigawatt microwave electronics. In the first place, the requirements on the electric strength

of the facilities have changed, because the microwave field amplitude in relativistic microwave electronic devices reaches 10^6 V/cm. Certain difficulties arise from the short pulse duration. Moreover, microwave pulses are usually generated in individual shots; i.e., the pulses appear rather rarely (one pulse per several minutes). The latter circumstance, as well as the rather high cost of each microwave pulse, makes it necessary to search for techniques capable of measuring all the parameters of the generated microwave radiation during a single pulse. Original methods developed by us make it possible to trace the behavior of microwave radiation throughout the entire pulse and resolve the spatial structure of radiation.

For a number of reasons, conventional semiconductor microwave detectors are difficult to use to record high-power radiation pulses in high-current microwave devices. First, they do not withstand overloads. Second, they produce very weak response signals that are difficult to discriminate against the stray background that unavoidably arises during the operation of high-current accelerators. To study the time characteristics of microwave radiation, an original method for measuring the microwave pulse envelope was proposed in [53] (and then improved in [54]). The method is based on the effect of "hot electrons" in semiconductors. A special semiconductor monocrystal does not break down at almost any incident microwave power and reproduces the shape of the microwave pulse envelope with an accuracy of up to $\approx$1 ns, the signal amplitude being from tens to hundreds of volts. This instrument allows the direct detection (without preliminary attenuation) of the microwave power in a waveguide at a level of hundreds of kilowatts and substantially increases the accuracy and reliability of measurements. At present, this method is standard in both Russia and other countries.

An important microwave characteristic is the wave mode. We have proposed an original method for determining the wave mode [55] from the trace produced by the microwave pulse on a dielectric surface with a special coating. As compared to the other ways of visualizing the microwave mode (e.g., a thermovisor or a panel of gas-discharge lamps), this method has an important advantage: we have a direct print of a nanosecond microwave pulse and need no additional equipment.

The methods described above allow us to trace the spatial and temporal characteristics of the microwave field, but do not ensure a sufficient accuracy in determining the total microwave energy. In the early experiments, the procedure of calculating the power was the following. The microwave power was measured (in relative units) in different points over the cross section of the radiation flow with the help of a microwave detector (see, e.g., [54]). Then, the detector was calibrated with a reference microwave source whose frequency was close to the frequency of the measured radiation. Finally, the results obtained were recalculated to the total pulse power.

This procedure was time-consuming, required good reproducibility of experimental results, could not ensure a necessary accuracy, and, more importantly, was unsuitable for studying microwave oscillators with broad emission spectra. For this reason, we have designed an original wide-aperture broadband calorimeter [56].

The energy of a single pulse of a relativistic microwave oscillator is difficult to measure because the pulse power is high (~100 MW), whereas its energy is low ($W \approx 2$ J at $T \approx 20$ ns). Because of the high pulse power, the diameter of the window through which the generated radiation is output from the vacuum chamber into atmosphere should be sufficiently large in order to avoid microwave breakdown on the window surface, as well on the surfaces of microwave receivers. It follows from this that the calorimeter surface should also be large; in view of this circumstance, the problem of detecting low microwave energy by a large-area (large-volume) absorber arises.

This problem was successfully resolved in [56]: a microwave calorimeter with a diameter of 40 cm and sensitivity of 0.05 J was created. The calorimeter was situated in air behind the emitting microwave horn. The operation principle of the calorimeter is to detect how the volume of an absorbing liquid increases under the action of microwave radiation. It is important that the calorimeter has nearly the same sensitivity within a broad frequency band: the microwave absorption coefficient of the calorimeter varies from 0.8 to 0.95 as the frequency varies from 5 to 40 GHz.

With this instrument, along with the methods described above, we were able to measure the microwave power in each pulse with a sufficient accuracy and reliability, determine its absolute value, and find its distribution in space and time.

One of the most important characteristics of microwave radiation is its spectrum. The traditional methods dealing with continuous or pulse-periodic radiation are of little use for measuring the radiation frequency in single short high-power pulses. We have developed and successfully used two methods (local and integral) for measuring microwave spectra.

The local method [57] is intended to measure the time-resolved microwave spectrum at one spatial point and is based on the use of "hot-carrier" microwave detectors [54]. Several detectors are built into low-Q resonators (necessary for measuring short pulses) fed with radiation arriving from the same resonator. This spectrometer has a relatively narrow frequency band (a few tens percent) determined by the waveguide dimensions. In this case, the instrument has all the above advantages: it is reliable, withstands overload, does not require preliminary attenuation of the microwave power, and produces output signals on the order of tens of volts.

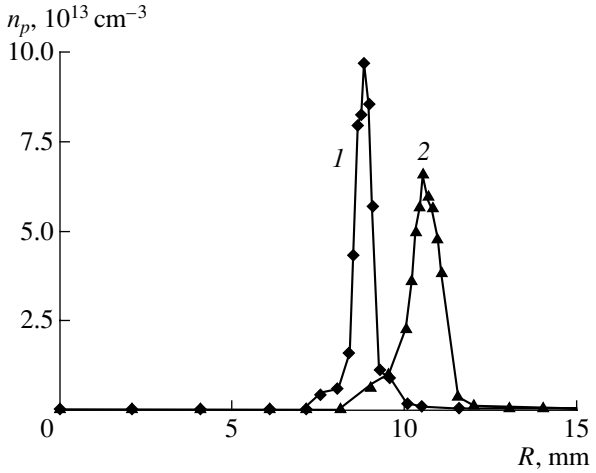

Fig. 16. Radial profile of the plasma density n_p: (*1*) magnetic field in the cathode region B_c is less than the magnetic field in the drift space B ($B_c < B$) and (*2*) $B_c = B$.

The integral method is needed to measure the spectrum of the total radiation flux integrated over the microwave pulse. Such an instrument is necessary for studying a broadband microwave source (RCPM) whose mean frequency can be varied severalfold (from 4 to 28 GHz). In microwave electronics, spectral measurements are usually conducted for a small fraction of the total radiation flux. If the spectrum is broadband, then the spectral density can be different in different cross sections of the microwave beam, so that it is hardly possible to reconstruct the integral microwave spectrum from these measurements. The integral spectrum measured in absolute units (in MW/GHz) is the fundamental RCPM characteristic, which is calculated numerically and is important for applications.

To measure the integral radiation spectrum, we have designed a calorimetric spectrometer [58]. It is based on a wide-aperture calorimeter [56] that is successively masked with microwave filters with different cutoff frequencies. The filter is shaped as a disc with apertures of the same diameter; each aperture is a waveguide whose diameter determines the threshold frequency of the filter. By comparing the energy measured in two shots by the calorimeter with two filters that have different threshold frequencies, we can measure the microwave energy in the frequency range between the threshold frequencies of these filters. The calorimetric spectrometer [58] measures the energy spectrum in units of J/GHz. Independent measurements of the envelope of the microwave pulse allow us to determine the spectrum of the total radiation power in units of MW/GHz.

Thus, all the parameters of high-current REBs and high-power microwave pulses were carefully measured. Often, the same parameter was measured by several methods. For the most part, we used original measurement methods; the reason is merely the absence of available alternatives to most of them.

4.2. Method of Plasma Creation

The successful creation of an RCPM would have been impossible if had we been unable to find a method for creating a thin-walled annular plasma. A potential of –600 V relative to the vacuum chamber wall was applied to a tungsten wire ring heated to a temperature of ~2100 K. The tungsten cathode immersed in a strong longitudinal magnetic field created an annular electron beam whose cross-section area was equal to that of the cathode. The annular electron beam ionized the gas (xenon at a pressure of 5×10^{-3} torr) and produced a plasma by impact ionization. However, it is hardly possible to create the plasma with a necessary density of 10^{12}–10^{13} cm^{-3} at currents of up to 100 A and a plasma length of ~30 cm by impact ionization only. The dense plasma was produced in a beam–plasma discharge due to the onset of the beam–plasma instability and the ionization of the gas by the microwave field. These effects are well known. A new and fundamentally important experimental observation is that ionization by the microwave field does not increase the thickness of the annular plasma.

Figure 16 shows the radial profile of the plasma density. It can be seen that the thickness of the annular plasma is nearly equal to the thickness of the tungsten cathode wire. Due to the sharp outer plasma boundary, the diameter of the plasma is equal to that of the collector (Fig. 9). This, in turn, makes it possible to produce a transition from the plasma waveguide to the vacuum coaxial waveguide (Fig. 11) with a minimal reflection coefficient. The sharp inner boundary of the annular plasma allows us to have a narrow gap between the electron beam and the plasma and, at the same time, to ensure the absence of plasma in the accelerator diode.

The coupling between the beam electrons and the electric field of the slow plasma wave depends on the gap length between the electron beam and the plasma. For this reason, we have developed a method for controlling the plasma diameter in the course of the experiment [59].

The possibility of varying the plasma diameter from 17 to 21 mm is demonstrated in Fig. 16. The plasma diameter is varied by the pulsed decrease in the magnetic field near the plasma source cathode. The REB was surrounded by a shield, so that the pulsed magnetic field did not penetrate into the axial region where the REB propagated. As a result, the REB propagated in a uniform magnetic field from the accelerator cathode to the collector. This eliminates the possibility of pumping the transverse electron velocity of the REB in a nonuniform magnetic field.

The plasma source operated in the pulsed mode and was switched on usually 30 μs before the accelerator current pulse. The plasma density at the time the beam current was switched on could be controlled by varying the delay time between switching on the plasma source and the accelerator and by varying the gas pressure or the plasma-source current.

It turned out that the plasma source had a disadvantage: the annular plasma was azimuthally nonuniform. It was proved experimentally that this nonuniformity was caused by the drift instability of the radially nonuniform plasma placed in the longitudinal magnetic field [59]. In particular, according to theoretical predictions, the increase in the annular plasma thickness resulted in a decrease in the measured azimuthal modulation depth. Fortunately, the azimuthal plasma nonuniformity had no effect on the RCPM efficiency and, in this sense, was unimportant.

5. APPLICATION OF PLASMA RELATIVISTIC MICROWAVE SOURCES IN SCIENCE AND TECHNOLOGY

The unique frequency characteristics of high-power plasma relativistic microwave sources can find wide applications in different fields of science and technology such as plasma chemistry and plasma technologies [including fusion reactors, plasma sources (plasmotrons), and plasma thrusters]. These problems have been discussed in many reviews and monographs. Here, we only consider the possible applications of high-power plasma relativistic microwave sources in plasma chemistry and radiolocation.

5.1. Plasma Chemistry

Short high-power microwave pulses make it possible to efficiently excite electronic and vibrational states of molecules, thus increasing the rates of chemical reactions by several orders of magnitude as compared to traditional methods. In this case, the gas temperature varies only slightly, which is very important for plasmochemical processes involving weakly bonded reaction products, such as complex ions. The swiping of the microwave frequency can be useful, e.g., in ECR plasmochemical reactors. In the case of a nonuniform magnetic field, the frequency swiping is equivalent to the spatial scanning of the discharge region. This makes it possible to excite a discharge in a larger volume, in particular, in a gas layer adjacent to a large-area surface, in accordance with the technological requirements of modern microelectronics.

5. 2. Radiolocation

In radiolocation, the maximum distance at which the target L_d can be located is given by the formula [60]

$$L_d = \left(\frac{PG_A^2\sigma\lambda^2}{(4\pi)^3 P_{\min} K}\right)^{1/4} \text{ km}. \qquad (5.2.1)$$

Here, P is the radar power (in W), λ is the wavelength (in m), $G_A = 4\pi S_{\text{eff}}/\lambda^2$ is the antenna emission coefficient (where $S_{\text{eff}} = \beta S_g$ is the effective antenna area, $\beta \approx 0.5$–0.7 is the antenna utilization factor, and S_g is the geometric area of the antenna), σ is the effective reflecting area of the target (in m^2), $P_{\min}$ is the dimensionless factor characterizing the sensitivity of the radar, and $K \approx 5$ is the resultant loss factor.

It follows from formula (5.2.1) that, in order to locate a small-sized target with $\sigma = 0.01$ m^2 (this is the effective area of the reflecting surface of modern aircrafts made by stealth technology) at a distance of $L_d =$ 100 km at $S_g = 4$ m^2 and $P_{\min} = 0.1$, the radar should have a power of $P \approx 50$ MW in the centimeter wavelength range. Actually, a radar operating at this power level was successfully used to locate a long-range aircraft [61]. The plasma relativistic microwave sources provide this power level.

However, there is a problem in radiolocation that is difficult to solve using vacuum microwave sources, but which can be solved by plasma relativistic microwave electronics. This is the location of aircrafts coated with materials that absorbant microwaves. The absorbant coating is applied to the surface by sputtering the microwave-absorbing materials with plasma and by implanting charge carriers or magnetic domains into the surface layer. From a variety of the microwave-absorbing materials, we can distinguish two main classes: the resonant narrowband absorbers and nonresonant broadband absorbers. The resonant coatings efficiently absorb microwaves within a relatively narrow frequency band; e.g., radiation in the X band (8–12 GHz) is absorbed completely. The broadband absorbing materials are based on composite semiconductors consisting of free charge carriers and different kinds of implanted magnetic domains. Different domains resonantly absorb microwaves at different frequencies. Consequently, to absorb microwaves in a broad frequency band, the resonant absorption bands of different domains should overlap. The materials absorbing microwaves in the 1.5- to 15-GHz frequency range are produced precisely in this way.

It is obvious that, aircrafts coated with microwave-absorbing materials can be located only with a broadband microwave source or a tunable source. It is necessary that the frequency band of the emitter be wider than the frequency band of the absorbing coating. Such broadband high-power pulses can be produced by plasma relativistic microwave sources.

6. CONCLUSION

In recent years, a new field of physical electronics—plasma relativistic microwave electronics—has been created. The theory has been developed and new high-power microwave sources with broadband frequency tuning—plasma relativistic microwave oscillators and amplifiers—have been designed. The unique properties of these devices distinguish them from other high-power microwave sources. The results obtained can be summarized as follows:

(i) The emission frequency of plasma relativistic microwave sources can rapidly be varied within a very wide band. An RCPM whose frequency can be continuously tuned in a band with an upper-to-lower boundary frequency ratio of 7 (from 4 to 28 GHz) at a power of 50 MW has been created. The frequency can be retuned within several tens of microseconds.

(ii) The emission spectrum width of a plasma relativistic source can be varied in a wide range. We have obtained high-power microwave radiation with a spectrum width from <5% (in a plasma relativistic microwave amplifier) to 20–100% (in an RCPM). There are no other tunable high-power microwave sources with such a wide spectrum.

(iii) The level of microwave power achieved (0.5 GW at an efficiency of 10%) does not exceed the maximum parameters of vacuum microwave sources. However, in plasma relativistic microwave sources, it is possible to use electron currents comparable to or even exceeding the limiting current in a vacuum system of the same geometry. Moreover, the maximum efficiency of vacuum relativistic microwave sources is achieved when the current is about 20–25% of the limiting current, whereas, in plasma devices, the maximum efficiency is achieved at nearly 50–70% of the vacuum limiting current. This provides the possibility of substantially increasing the microwave power and utilizing the resources of high-current accelerators more efficiently.

(iv) We have clarified the mechanism responsible for the suppression of high-power microwave generation in relativistic microwave devices and the shortening of microwave pulses to several tens of nanoseconds. Because of the specific design of vacuum microwave oscillators, it is hard to eliminate this effect. Plasma relativistic microwave devices can generate microwave pulses with considerably longer durations and higher powers.

The reliability of the results obtained is confirmed by unique diagnostic methods that we have developed. Among these, we should mention a wide-aperture broadband microwave calorimeter, a high-power microwave radiation spectrometer, and a method for visualizing electrons in an REB.

ACKNOWLEDGMENTS

This study was supported in part by the International Science Foundation (grant nos. MO 3000 and MO 3300), the Ministry of Industry, Science, and Technology (MIST) of the Russian Federation under the Program for Supporting Unique Devices (Cherenkov Plasma Maser device, registration no. 01-04), the Russian Foundation for Basic Research (project nos. 94-02-03437 and 97-02-16948), and the MIST Scientific Program “Physics of Microwaves” (project 1.11. Plasma Relativistic Microwave Sources with Controlled Radiation Parameters).

REFERENCES

1. A. I. Akhiezer and Ya. B. Faĭnberg, Dokl. Akad. Nauk SSSR **69**, 551 (1949).
2. D. Bohm and E. Gross, Phys. Rev. **75**, 1851 (1949).
3. I. F. Kharchenko, Ya. B. Faĭnberg, R. M. Nikolaev, *et al.*, Zh. Éksp. Teor. Fiz. **38**, 685 (1960) [Sov. Phys. JETP **11**, 493 (1960)].
4. R. A. Demirkhanov, A. K. Gevorkov, A. F. Popov, and G. I. Zverev, Zh. Tekh. Fiz. **30**, 306 (1960) [Sov. Phys. Tech. Phys. **5**, 282 (1960)].
5. G. A. Bernashevskiĭ, E. V. Bogdanov, V. Ya. Kislov, and Z. S. Chernov, *Plasma and Electronic Microwave Amplifiers and Oscillators* (Sov. Radio, Moscow, 1965).
6. D. I. Trubetskov and L. A. Pishchik, Fiz. Plazmy **15**, 266 (1989) [Sov. J. Plasma Phys. **15**, 200 (1989)].
7. A. A. Rukhadze, Zh. Tekh. Fiz. **31**, 1236 (1961) [Sov. Phys. Tech. Phys. **6**, 900 (1962)].
8. A. A. Rukhadze, Zh. Tekh. Fiz. **32**, 669 (1962) [Sov. Phys. Tech. Phys. **7**, 488 (1962)].
9. R. I. Kovtun and A. A. Rukhadze, Zh. Éksp. Teor. Fiz. **58**, 1219 (1970) [Sov. Phys. JETP **31**, 655 (1970)].
10. M. V. Kuzelev and A. A. Rukhadze, *Electrodynamics of Dense Electron Beams in Plasma* (Nauka, Moscow, 1990).
11. L. S. Bogdankevich and A. A. Rukhadze, Usp. Fiz. Nauk **103**, 609 (1971) [Sov. Phys. Usp. **14**, 163 (1971)].
12. A. A. Rukhadze, L. S. Bogdankevich, S. E. Rosinskiĭ, and V. G. Rukhlin, *Physics of High-Current Relativistic Electron Beams* (Atomizdat, Moscow, 1980).
13. B. I. Aronov, L. S. Bogdankevich, and A. A. Rukhadze, Plasma Phys. **16**, 101 (1976).
14. M. S. Rabinovich and A. A. Rukhadze, Fiz. Plazmy **2**, 715 (1976) [Sov. J. Plasma Phys. **2**, 397 (1976)].
15. L. S. Bogdankevich, M. S. Rabinovich, and A. A. Rukhadze, Izv. Vyssh. Uchebn. Zaved., Fiz. **10**, 47 (1979).
16. L. S. Bogdankevich, M. V. Kuzelev, and A. A. Rukhadze, Usp. Fiz. Nauk **133**, 3 (1981) [Sov. Phys. Usp. **24**, 1 (1981)].
17. M. V. Kuzelev, F. Kh. Mukhametzyanov, M. S. Rabinovich, *et al.*, Zh. Éksp. Teor. Fiz. **83**, 1358 (1982) [Sov. Phys. JETP **56**, 780 (1982)].
18. M. V. Kuzelev, F. Kh. Mukhametzyanov, M. S. Rabinovich, *et al.*, Dokl. Akad. Nauk. SSSR **267**, 829 (1982) [Sov. Phys. Dokl. **27**, 1030 (1982)].
19. M. V. Kuzelev and A. A. Rukhadze, Fiz. Plazmy **26**, 250 (2000) [Plasma Phys. Rep. **26**, 231 (2000)].
20. M. Birau, M. A. Krasil’nikov, M. V. Kuzelev, and A. A. Rukhadze, Usp. Fiz. Nauk **167**, 1025 (1997) [Phys. Usp. **40**, 975 (1997)].
21. M. V. Kuzelev, F. Kh. Mukhametzyanov, and A. G. Shkvarunets, Fiz. Plazmy **9**, 1137 (1983) [Sov. J. Plasma Phys. **9**, 655 (1983)].
22. M. V. Kuzelev and A. A. Rukhadze, Usp. Fiz. Nauk **152**, 285 (1987) [Sov. Phys. Usp. **30**, 507 (1987)].
23. M. V. Kuzelev, O. V. Lazutchenko, and A. A. Rukhadze, Izv. Vyssh. Uchebn. Zaved., Radiofiz. **42**, 958 (1999).
24. M. V. Kuzelev and A. A. Rukhadze, Izv. Vyssh. Uchebn. Zaved., Radiofiz. **36**, 867 (1993).
25. M. V. Kuzelev and A. A. Rukhadze, Fiz. Plazmy **24**, 530 (1998) [Plasma Phys. Rep. **24**, 486 (1998)].

26. I. N. Kartashov, M. A. Krasil'nikov, and M. V. Kuzelev, Radiotekh. Élektron. (Moscow) **44**, 1502 (1999).
27. M. Birau, M. A. Krasil'nikov, M. V. Kuzelev, and A. A. Rukhadze, Zh. Éksp. Teor. Fiz. **111**, 1258 (1997) [JETP **84**, 694 (1997)].
28. M. A. Krasil'nikov, M. V. Kuzelev, and A. A. Rukhadze, Zh. Éksp. Teor. Fiz. **108**, 521 (1995) [JETP **81**, 280 (1995)].
29. M. A. Krasil'nikov, M. V. Kuzelev, and A. A. Rukhadze, Zh. Éksp. Teor. Fiz. **112**, 1299 (1997) [JETP **85**, 705 (1997)].
30. Yu. V. Bobylev, M. V. Kuzelev, A. A. Rukhadze, and A. G. Sveshnikov, Fiz. Plazmy **25**, 615 (1999) [Plasma Phys. Rep. **25**, 561 (1999)].
31. M. A. Krasil'nikov, M. V. Kuzelev, and A. A. Rukhadze, Kratk. Soobshch. Fiz., Nos. 7–8, 22 (1996).
32. I. A. Selivanov, P. S. Strelkov, A. V. Fedotov, and A. G. Shkvarunets, Fiz. Plazmy **15**, 1283 (1989) [Sov. J. Plasma Phys. **15**, 744 (1989)].
33. O. T. Loza and P. S. Strelkov, in *Proceedings of the 10th International Conference on High-Power Particle Beams, San-Diego, 1994*, Vol. 2, p. 958.
34. M. V. Kuzelev, O. T. Loza, A. V. Ponomarev, *et al.*, Zh. Éksp. Teor. Fiz. **109**, 2048 (1996) [JETP **82**, 1102 (1996)].
35. P. S. Strelkov and D. K. Ul'yanov, Fiz. Plazmy **26**, 329 (2000) [Plasma Phys. Rep. **26**, 303 (2000)].
36. M. Birau, J-M. Buzzi, Y. Caillez, *et al.*, in *Proceedings of the 23rd International Conference on Phenomena in Ionized Gases, Toulouse, 1997*, Vol. 3, p. 46.
37. P. S. Strelkov, O. T. Loza, and S. N. Voronkov, Patent RF No. 2030135 (1995); Priority from May 8, 1992; Application No. 5041576.
38. P. S. Strelkov and O. T. Loza, Patent RF No. 2061307 (1996); Priority from June 2, 1993; Application No. 93028127.
39. O. T. Loza and I. E. Ivanov, in *Proceedings of the 13th International Conference on High-Power Particle Beams, Nagaoka, 2000*, p. 603.
40. O. T. Loza, P. S. Strelkov, and S. N. Voronkov, Fiz. Plazmy **20**, 686 (1994) [Plasma Phys. Rep. **20**, 617 (1994)].
41. O. T. Loza, P. S. Strelkov, and S. N. Voronkov, Fiz. Plazmy **20**, 418 (1994) [Plasma Phys. Rep. **20**, 374 (1994)].
42. O. T. Loza, P. S. Strelkov, and I. E. Ivanov, IEEE Trans. Plasma Sci. **26**, 336 (1998).
43. A. V. Ponomarev, P. S. Strelkov, and A. G. Shkvarunets, Fiz. Plazmy **24**, 53 (1998) [Plasma Phys. Rep. **24**, 48 (1998)].
44. A. V. Ponomarev, P. S. Strelkov, and A. G. Shkvarunets, Fiz. Plazmy **26**, 633 (2000) [Plasma Phys. Rep. **26**, 592 (2000)].
45. Yu. F. Bondar', B. M. Koval'chuk, A. M. Rybalov, and P. S. Strelkov, Prib. Tekh. Éksp., No. 1, 25 (1974).
46. O. D. Klok, V. I. Krementsov, P. S. Strelkov, and A. G. Shkvarunets, Zh. Éksp. Teor. Fiz. **67**, 1401 (1974) [Sov. Phys. JETP **40**, 696 (1974)].
47. V. I. Krementsov, M. S. Rabinovich, A. A. Rukhadze, *et al.*, Zh. Éksp. Teor. Fiz. **69**, 1218 (1975) [Sov. Phys. JETP **42**, 622 (1975)].
48. Yu. F. Bondar', S. I. Zavorotnyĭ, A. L. Ipatov, *et al.*, Fiz. Plazmy **8**, 941 (1982) [Sov. J. Plasma Phys. **8**, 528 (1982)].
49. S. N. Voronkov, O. T. Loza, A. A. Ravaev, *et al.*, Fiz. Plazmy **14**, 1259 (1988) [Sov. J. Plasma Phys. **14**, 737 (1988)].
50. P. H. de-Haan, R. N. Singh, H. J. Hopman, *et al.*, J. Phys. E **14**, 373 (1981).
51. P. S. Strelkov, A. G. Shkvarunets, and P. Shunka, Fiz. Plazmy **7**, 564 (1981) [Sov. J. Plasma Phys. **7**, 305 (1981)].
52. V. I. Krementsov, P. S. Strelkov, and A. G. Shkvarunets, Zh. Tekh. Fiz. **50**, 2469 (1980) [Sov. Phys. Tech. Phys. **25**, 1447 (1980)].
53. M. D. Raĭzer and L. É. Tsopp, Radiotekh. Élektron. (Moscow) **20**, 1691 (1975).
54. O. T. Loza and L. É. Tsopp, Kratk. Soobshch. Fiz., No. 1, 8 (1982).
55. E. A. Vinogradov, V. I. Golovanov, N. A. Irisova, *et al.*, Zh. Tekh. Fiz. **52**, 1458 (1982) [Sov. Phys. Tech. Phys. **27**, 893 (1982)].
56. A. G. Shkvarunets, Prib. Tekh. Éksp., No. 4, 72 (1996).
57. A. A. Rukhadze, P. S. Strelkov, and A. G. Shkvarunets, Fiz. Plazmy **20**, 686 (1994) [Plasma Phys. Rep. **20**, 617 (1994)].
58. I. L. Bogdankevich, P. S. Strelkov, V. P. Tarakanov, *et al.*, Prib. Tekh. Éksp., No. 1, 92 (2000).
59. O. T. Loza, A. V. Ponomarev, P. S. Strelkov, *et al.*, Fiz. Plazmy **23**, 222 (1997) [Plasma Phys. Rep. **23**, 201 (1997)].
60. V. P. Kalinushkin, M. V. Kuzelev, I. M. Minaev, and A. A. Rukhadze, in *Physicotechnical Problems of Electrical Energy Transfer*, Ed. by A. F. D'yakov (Mosk. Énerg. Inst., Moscow, 1998), Vol. 1, p. 11.
61. B. V. Bunkin, A. V. Gaponov-Grekhov, A. S. Elchaninov, *et al.*, in *Proceedings of the 9th International Conference on High-Power Particle Beams, Washington, 1992*, p. 195.

Translated by I. A. Kalabalyk and N. F. Larionova

Plasma Physics Reports, Vol. 27, No. 8, 2001, pp. 692–698. Translated from Fizika Plazmy, Vol. 27, No. 8, 2001, pp. 734–740.

PLASMA DIAGNOSTICS

Diagnostic of an Ionized Gas by Recording Linearly Polarized Radiation

M. B. Shapochkin

Moscow Power Engineering Institute (Technical University), ul. Krasnokazarmennaya 14, Moscow, 111250 Russia

Received October 14, 1999; in final form, May 20, 2000

Abstract—The degree of linear polarization of radiation from an ionized gas is calculated analytically. The analytical results on the resonant transition in Al XII atoms agree (to within 4%) with the numerical results obtained from the ATOM code. The applicability of the analytic expressions derived to the analysis of the degree of linear polarization of radiation from this atomic transition and the related excitation cross section is discussed. The plots of the degree of linear polarization of radiation from an ionized gas as a function of the electron parameters are presented. The question of whether the spectropolarimetry can provide an independent optical diagnostic tool is discussed. © *2001 MAIK "Nauka/Interperiodica".*

1. INTRODUCTION

Measurements of the Stokes parameters of radiation from an ionized gas make it possible to determine the anisotropic properties of electrons. The degree of linear polarization of radiation can be found from the quadrupole moment of the electron distribution function [1–5]. The parameters characterizing the anisotropy of electrons can be calculated using the model of superthermal electrons [6, 7].

In order to interpret the diagnostic data on the degree of linear polarization of radiation from a vacuum spark plasma and, in particular, the data on the line emission from the Al XII resonant transition, Walden *et al.* [4] calculated the excitation cross sections for the *m* sublevels in the Born–Coulomb approximation by using the ATOM code package [8–10]. The results of their calculations of the degree of linear polarization of line radiation from the Al XII resonant transition excited by a monoenergetic electron beam agree with the results obtained by Kieffer *et al.* [11] to within 5%.

The anisotropy of an ionized gas leads to the alignment of atomic states, i.e., to the spatial ordering of the angular momenta of the atoms. In this case, the degree of linear polarization of radiation can be calculated with the help of the electron impact alignment cross section [1, 12, 13]. In turn, this cross section can be calculated from the excitation cross sections for the magnetic sublevels or obtained as the quadrupole moment of the total excitation cross sections of the level, e.g., the cross section found experimentally for ArI [3].

2. FORMULATION OF THE PROBLEM

In [1, 5, 14], it was shown that the electron impact alignment cross section can be expressed in terms of the total excitation cross section of the level and the degree of linear polarization of radiation from the transition in a collision between a beam electron and an atom. By using the analytic expressions for the total cross section [15–24] and for the degree of linear polarization of radiation from the transition in beam experiments [25] and by choosing an appropriate model, it is possible not only to analytically calculate the degree of linear polarization of radiation from an ionized gas but also to analyze how this degree depends on the model parameters [8].

The degree of linear polarization of radiation from an ionized gas can be written as

$$P = \frac{I^{(2)}}{I^{(0)}}, \tag{1}$$

where

$$I^{(0)} = \int_0^{\pi/2} \sin\Theta d\Theta \int_0^{2\pi} d\varphi \times \int_{\Lambda\varepsilon}^{\infty} \frac{Q(\varepsilon)}{\Gamma} \frac{1 - P_0(\varepsilon)\cos^2\Theta}{1 - P_0(\varepsilon)/3} f(\varepsilon, \Theta, \varphi)\sqrt{2\varepsilon}d\varepsilon, \tag{2}$$

$$I^{(2)} = 4\sqrt{\frac{2\pi}{15}} \int_{\Delta\varepsilon}^{\infty} \frac{W(J, J_1)Q^{(2)}(\varepsilon)}{\Gamma^{(2)}} f_{2+}^{(2)}(\varepsilon)\sqrt{2\varepsilon}d\varepsilon. \tag{3}$$

In formulas (2) and (3), we introduce the following notation: $I^{(0)}$ and $I^{(2)}$ are the total and quadrupole intensities of radiation emitted by an atom per unit solid angle, $Q(\varepsilon)$ is the total excitation cross section, Γ is the decay constant, $Q^{(2)}(\varepsilon)$ is the electron impact alignment cross section, $\Gamma^{(2)}$ is the quadrupole moment of the decay constant, $W(J, J_1)$ is the polarization moment of the transition, $f(\varepsilon, \Theta, \varphi)$ is the electron distribution function, $f_{2+}^{(2)}(\varepsilon)$ is the quadrupole moment of the electron

distribution function, and $P_0(\varepsilon)$ is the degree of linear polarization of radiation from the transition excited by an electron beam.

The calculations will be carried out in the atomic system of units in which $e = h = m = 1$ and the energy is expressed in rydbergs (1 Ry = 13.6 eV).

3. MODEL FOR PLASMA ELECTRONS

For an axisymmetric (about the z-axis) plasma, the total electron distribution function (with allowance for thermal and nonthermal electrons) can be written as [17]

$$f(\varepsilon, \Theta, \varphi) = \frac{N_t}{4\pi} f_t(\varepsilon) + N_{nt} f_{nt}(\varepsilon, \Theta) f_{nt}(\varepsilon). \quad (4)$$

Here, N_t is the density of thermal electrons; the Maxwellian distribution function $f_t(\varepsilon)$ for thermal electrons with the temperature T_0 has the form

$$f_t(\varepsilon) = 2\pi^{-1/2} T_0^{-3/2} \sqrt{\varepsilon} \exp\left(-\frac{\varepsilon}{T_0}\right), \quad (5)$$

N_{nt} is the density of superthermal electrons; and the high-energy part $f_{nt}(\varepsilon)$ of the distribution function of the superthermal electrons can be either a Maxwellian function with the temperature $T_1 \gg T_0$ or a power function of the form [4]

$$f_{nt}(\varepsilon) = \frac{1-\gamma}{\varepsilon_1}\left(\frac{\varepsilon}{\varepsilon_1}\right)^{-\gamma}, \quad (6)$$

where ε_1 and γ are the characteristic constants. An analysis of the spectral line intensities [4] calculated for Maxwellian and power distribution functions shows that the power function is more preferable for describing superthermal electrons. Haug [6] proposed the following angular dependence for the distribution function of the superthermal electrons:

$$f_{nt}(\varepsilon, \Theta) = \begin{cases} \dfrac{a+1}{2\pi}\cos^a\Theta & \text{for} \quad 0 < \Theta \le \dfrac{\pi}{2} \\ 0 & \text{for} \quad \dfrac{\pi}{2} \le \Theta \le \pi \end{cases}, \quad (7)$$

where $a = \dfrac{\bar{\varepsilon}}{\varepsilon_2}$ and ε_2 is the anisotropy constant. The dependence of the pitch angle of the superthermal electron distribution on a can be found in [6]. Thus, for a beam, we have $a \longrightarrow \infty$, whereas, as $a \longrightarrow 0$, the distribution function becomes isotropic. Using the angular dependence (7), the authors of [4, 26] calculated the general polarization of radiation from an ionized gas.

The energy dependence of the quadrupole moment $f_{2+}^{(2)}(\varepsilon)$ of the distribution function can be found by the method of expansion in spherical functions [27]:

$$f_q^{(k)}(\varepsilon) = \int_0^{2\pi} d\varphi \int_0^{\pi/2} f(\varepsilon, \theta, \varphi) Y_q^{(k)*}(\Theta, \varphi) \sin\Theta d\Theta.$$

By using formulas (4)–(6) for $f_{nt}(\varepsilon, \Theta)$ and the relationship $Y_{2+}^{(2)}(\Theta, \varphi) = \dfrac{1}{4}\sqrt{\dfrac{15}{2\pi}} \sin^2\Theta e^{i2\varphi}$ [27], we obtain

$$f_{2+}^{(2)}(\varepsilon) = \int_1^0 (a+1)\cos^a(\Theta)\frac{1}{4}\sqrt{\frac{15}{2\pi}}\sin^2\Theta f_{nt}(\varepsilon) d(\cos\Theta)$$

$$= \frac{1}{4}\sqrt{\frac{15}{2\pi}}(a+1)\int_1^0 \cos\Theta(1-\cos^2\Theta) f_{nt}(\varepsilon) d(\cos\Theta) \quad (8)$$

$$= -\frac{1}{2}\sqrt{\frac{15}{2\pi}} N_{nt} \frac{f_{nt}(\varepsilon)}{a+3}.$$

4. ANALYTIC EXPRESSIONS FOR THE EXCITATION CROSS SECTION AND THE POLARIZATION OF RADIATION FROM THE TRANSITION

Analytical expressions for the total excitation cross section can be taken from [15–24]. As a rule, semiempirical expressions for the excitation cross sections are derived from the Bethe formula for dipole transitions by modifying the functional dependence on the electron energy and by analyzing the experimental data in order to determine the necessary parameter values. However, the parameter values obtained in this way cannot be regarded as being universal; i.e., they do not ensure the same accuracy of calculations for different atomic systems. In addition, some of the semiempirical expressions are fairly involved and, accordingly, are difficult to apply to practical analytic calculations of the degree of linear polarization of radiation from an ionized gas.

The excitation cross sections for dipole transitions in various highly ionized atoms can be calculated from the expression [16]

$$Q(\varepsilon) = \frac{8f}{\varepsilon\Delta\varepsilon}\ln\left(\frac{1.36\sqrt{\varepsilon}}{R_0\Delta\varepsilon}\right), \quad (9)$$

where f is the dipole oscillator strength, R_0 is a constant, and $\Delta\varepsilon$ is the threshold energy.

Formula (9) is based on the model dipolar interaction potential. A comparison between the results obtained from formula (9) and from the ATOM code [28] on the excitation cross sections for dipole transitions in ions (including highly ionized atoms such as Al XII) makes it possible to determine the accuracy of formula (9). Near the excitation threshold, it gives accuracies of 100%, and, in the energy range above the five excitation thresholds, the accuracy is within 20%.

Below, the polarization of radiation from multicharged ions will be calculated using formula (9).

In the literature, the question of whether it is expedient to calculate the degree of linear polarization of radiation from atoms and ions by using semiempirical expressions has been studied to a much lesser extent. The degree of linear polarization of radiation from the resonant dipole S–P transition is well described by the interpolation formula [12]

$$P_0(\varepsilon) = P_1\frac{\ln(\varepsilon_0/\varepsilon)}{\ln(13\varepsilon/\Delta\varepsilon)}, \tag{10}$$

where ε_0 is the energy at which the polarization passes through zero and then changes sign and P_1 is the polarization at the threshold energy. Formula (10) for the polarization of radiation from atoms and singly and multiply charged ions gives an accuracy of no worse than 10%.

5. GENERAL EXPRESSIONS FOR THE INTENSITIES $I^{(0)}$ AND $I^{(2)}$ OF RADIATION FROM THE RESONANT S–P TRANSITION IN A MULTICHARGED ATOM

The general analytic expression for $I^{(2)}$ can be obtained by substituting expression (8) for the quadrupole moment $f_{2+}^{(2)}(\varepsilon)$ of the electron distribution function into formula (3):

$$I^{(2)} = -2\frac{N_{nt}}{\Gamma}\int_{\Delta\varepsilon}^{\infty}\frac{Q(\varepsilon)P_0(\varepsilon)}{1-P(\varepsilon)/3}\frac{f_{nt}(\varepsilon)}{a+3}\sqrt{2\varepsilon}d\varepsilon. \tag{11}$$

In order to calculate the intensity I^0, we substitute expressions (4)–(7) for the electron distribution function into formula (2) and integrate the resulting formula, first, over the angles Θ and φ and, then, over the energy:

$$\begin{aligned}
I^{(0)} &= \int_1^0 d(\cos\Theta)\int_0^{2\pi}d\varphi\int_{\Delta\varepsilon}^{\infty}\frac{Q(\varepsilon)}{\Gamma}\frac{1-P_0(\varepsilon)\cos^2\Theta}{1-P_0(\varepsilon)/3}\\
&\times\left(\frac{N_t}{4\pi}f_t(\varepsilon)+N_{nt}\frac{a+1}{2\pi}\cos^a\Theta\right)\sqrt{2\varepsilon}d\varepsilon\\
&= \int_1^0\frac{1-P_0(\varepsilon)\cos^2\Theta}{1-P_0(\varepsilon)/3}d(\cos\Theta)\\
&\times\int_{\Delta\varepsilon}^{\infty}\frac{Q(\varepsilon)}{\Gamma}\frac{N_t}{2}f_t(\varepsilon)\sqrt{2\varepsilon}d\varepsilon\\
&+\int_1^0(a+1)\cos^a(\Theta)\frac{1-P_0(\varepsilon)\cos^a(\Theta)}{1-P_0(\varepsilon)/3}d(\cos\Theta)\\
&\times\int_{\Delta\varepsilon}^{\infty}\frac{Q(\varepsilon)}{\Gamma}N_{nt}f_{nt}(\varepsilon)\sqrt{2\varepsilon} = -\frac{N_{nt}}{2\Gamma}\int_{\Delta\varepsilon}^{\infty}Q(\varepsilon)f_t(\varepsilon)\sqrt{2\varepsilon}d\varepsilon\\
&-\frac{N_{nt}}{\Gamma}\int_{\Delta\varepsilon}^{\infty}\frac{Q(\varepsilon)}{1-P_0(\varepsilon)/3}f_{nt}(\varepsilon)\sqrt{2\varepsilon}d\varepsilon\\
&+\frac{N_{nt}}{\Gamma}\int_{\Delta\varepsilon}^{\infty}\frac{Q(\varepsilon)P_0(\varepsilon)}{1-P_0(\varepsilon)/3}\frac{a+1}{a+3}f_{nt}(\varepsilon)\sqrt{2\varepsilon}d\varepsilon.
\end{aligned} \tag{12}$$

We insert expressions (11) and (12) for $I^{(2)}$ and $I^{(0)}$ into formula (1) and introduce the notation $n = N_t/N_{nt}$. As a result, we arrive at the final expression for the degree of linear polarization of radiation from an ionized gas:

$$P = \frac{2\int_{\Delta\varepsilon}^{\infty}\frac{Q(\varepsilon)P_0(\varepsilon)}{1-P_0(\varepsilon)/3}\frac{f_{nt}(\varepsilon)}{a+3}\sqrt{\varepsilon}d\varepsilon}{\frac{n}{2}\int_{\Delta\varepsilon}^{\infty}Q(\varepsilon)f_t(\varepsilon)\sqrt{\varepsilon}d\varepsilon+\int_{\Delta\varepsilon}^{\infty}\frac{Q(\varepsilon)}{1-P_0(\varepsilon)/3}f_{nt}(\varepsilon)\sqrt{\varepsilon}d\varepsilon-\int_{\Delta\varepsilon}^{\infty}\frac{Q(\varepsilon)P_0(\varepsilon)}{1-P_0(\varepsilon)/3}\frac{a+1}{a+3}f_{nt}(\varepsilon)\sqrt{\varepsilon}d\varepsilon}. \tag{13}$$

In order to simplify expression (13) into a form suitable for calculating the degree of linear polarization, we must consider the following four integrals:

$$I_0 = \int_{\Delta\varepsilon}^{\infty}Q(\varepsilon)f_t(\varepsilon)\sqrt{\varepsilon}d\varepsilon, \tag{14a}$$

$$I_1 = \int_{\Delta\varepsilon}^{\infty}\frac{Q(\varepsilon)P_0(\varepsilon)}{1-P_0(\varepsilon)/3}\frac{f_{nt}(\varepsilon)}{a+3}\sqrt{\varepsilon}d\varepsilon, \tag{14b}$$

$$I_2 = \int_{\Delta\varepsilon}^{\infty}\frac{Q(\varepsilon)}{1-P_0(\varepsilon)/3}f_{nt}(\varepsilon)\sqrt{\varepsilon}d\varepsilon, \tag{14c}$$

$$I_3 = \int_{\Delta\varepsilon}^{\infty} \frac{Q(\varepsilon)P_0(\varepsilon)}{1-P_0(\varepsilon)/3}\frac{a}{a+3} f_{nt}(\varepsilon)\sqrt{\varepsilon}d\varepsilon. \quad (14d)$$

First, we rewrite expression (13) in terms of the symbol notation for the integrals:

$$P = \frac{2I_1}{(n/2)I_0 + I_2 - I_3 - I_1}. \quad (15)$$

Before evaluating expression (15) with formula (9) for the total excitation cross section $Q(\varepsilon)$ for the transition, formula (10) for the degree of linear polarization of radiation $P_0(\varepsilon)$, formula (5) for the Maxwellian distribution function $f_t(\varepsilon)$ of the thermal electrons, and formula (6) for the power distribution function $f_{nt}(\varepsilon)$ of the superthermal electrons, we make the identity replacement $\frac{a}{a+3} = 1 - \frac{3}{a+3}$ in the integral I_3 in expression (14d):

$$I_3 = \int_{\Delta\varepsilon}^{\infty} \frac{Q(\varepsilon)P_0(\varepsilon)}{1-P_0(\varepsilon)/3} f_{nt}(\varepsilon)\sqrt{\varepsilon}d\varepsilon - 3\int_{\Delta\varepsilon}^{\infty} \frac{Q(\varepsilon)P_0(\varepsilon)}{1-P_0(\varepsilon)/3}\frac{f_{nt}(\varepsilon)}{a+3}\sqrt{\varepsilon}d\varepsilon.$$

In terms of the integrals I_2 and I_1 in expressions (14c) and (14b), the integral I_3 takes the form

$$I_3 = I_2 - 3I_1,$$

in which case the expression for the degree of linear polarization reduces to

$$P = \frac{2I_1}{(n/2)I_0 + 2I_1}. \quad (16)$$

Expression (16) is similar in structure to the expressions derived in [1, 29]. If we insert the explicit expressions for $Q(\varepsilon)$, $P_0(\varepsilon)$, $f_t(\varepsilon)$, and $f_{nt}(\varepsilon)$ into formulas (14), we obtain the integrals I_0 and I_1 in explicit form and thus arrive at the following formula for the degree of linear polarization of radiation from an ionized gas:

$$P = \frac{\frac{8f(\gamma-1)\varepsilon_1^{\gamma-1}\varepsilon_2}{\Delta\varepsilon}\frac{3P_0}{3+P_0}F_1}{\frac{n}{2}\frac{8f}{\Delta\varepsilon\sqrt{\pi}}F_0 + \frac{8f(\gamma-1)\varepsilon_1^{\gamma-1}\varepsilon_2}{\Delta\varepsilon}\frac{3P_0}{3+P_0}F_1}. \quad (17)$$

We divide the right-hand side of expression (17) by f and $\Delta\varepsilon$ and perform the necessary manipulations. As a result, we obtain

$$P = \frac{(\gamma-1)\varepsilon_1^{\gamma-1}\varepsilon_2\frac{3P_0}{3+P_0}F_1}{0.094nF_0 + (\gamma-1)\varepsilon_1^{\gamma-1}\varepsilon_2\frac{3P_0}{3+P_0}F_1}. \quad (18)$$

The functionals F_0 and F_1 are governed by the parameters of the ionized gas and atomic system. Thus, the functional F_0 is determined by the quantities $\Delta\varepsilon$, R_0, and T_0, and the functional F_1 depends on $\Delta\varepsilon$, R_0, P_0, ε_0, ε_2, and γ. The degree of linear polarization of radiation from an ionized gas is independent of both the dipole oscillator strength and the decay constant for the transition. Recall that the calculations were carried out in the atomic system of units in which the energy is expressed in rydbergs. The method of calculation restricts the parameter γ to half-integer values.

The analytical expression derived for the polarization of radiation from the resonant S–P transition in an ion in an ionized gas makes it possible to analyze the polarization as a function of the parameters characterizing the distribution of superthermal electrons. With the given characteristics $\Delta\varepsilon$, R_0, P_0, and ε_0 of the atomic system, expression (18) contains five parameters of the plasma electrons: n, T_0, ε_1, γ, and ε_2. Therefore, we can say that spectropolarimetric methods provide an additional diagnostic tool, supplementing the well-known techniques used to diagnose ionized gases in order to determine the parameters ε_1, γ, and ε_2 of the model of anisotropic electron distribution.

The radiation intensity can be analyzed using expression (2) for $I^{(0)}$; in the above notation, this expression takes the form

$$I^{(0)} = \frac{2^{5/2}N_t f}{\pi^{1/2}\Delta\varepsilon\Gamma}F_0 + \frac{2^{7/2}N_{nt}f(\gamma-1)\varepsilon_2\varepsilon_1^{\gamma-1}}{\Delta\varepsilon\Gamma}\frac{3P_0}{3+P_0}F_1. \quad (19)$$

6. CALCULATION OF THE DEGREE OF LINEAR POLARIZATION OF RADIATION FROM THE RESONANT *S–P* TRANSITION IN Al XII ATOMS

The analytic calculations based on expression (18) for the degree of linear polarization of radiation from an ionized gas were carried out with the help of the MATHCAD package, which provides, in particular, a graphical illustration of the numerical results.

The accuracy of the analytic model was tested by repeating the calculations done by Walden *et al.* [4] with the ATOM code in order to interpret the measurement data on the polarization of the line radiation from the Al XII resonant transition in a vacuum spark plasma. It seems that, at present, the results from these

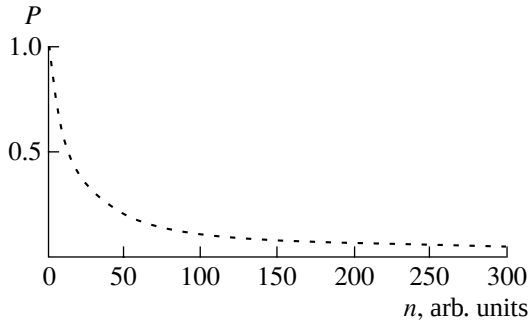

Fig. 1. Degree of linear polarization of radiation from an ionized gas vs. the ratio n of the number of thermal electrons to the number of superthermal electrons for $\gamma = 4.5$, $\varepsilon_1 = 139$, and $\varepsilon_2 = 110$.

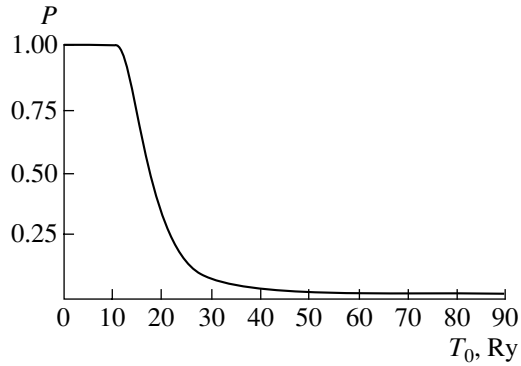

Fig. 2. Degree of linear polarization of radiation from an ionized gas vs. the temperature T_0 for $\gamma = 4.5$, $\varepsilon_1 = 139$, and $\varepsilon_2 = 110$.

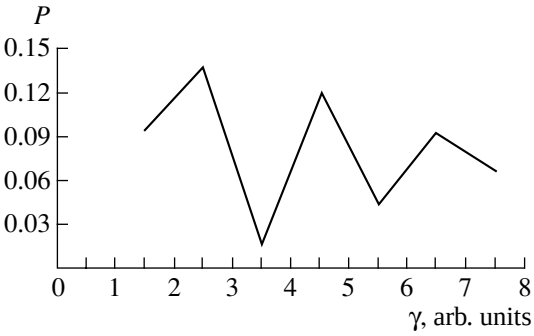

Fig. 3. Degree of linear polarization of radiation from an ionized gas vs. γ for $\varepsilon_1 = 139$ and $\varepsilon_2 = 110$.

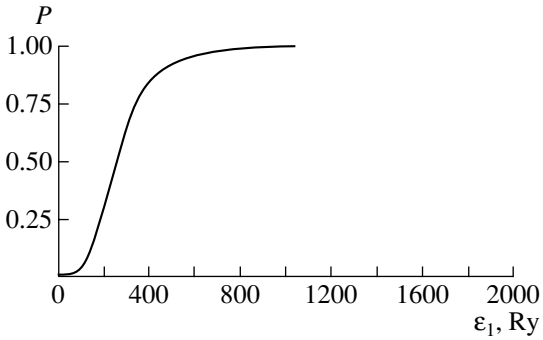

Fig. 4. Degree of linear polarization of radiation from an ionized gas vs. ε_1 for $\gamma = 4.5$ and $\varepsilon_2 = 110$ ($P = 0.12$ for $\varepsilon_1 = 139$).

calculations are the most reliable. In accordance with the data of [4], we can work with the known parameter values $n = 100$ and $T = 26$. In [4], for the measured polarization $P = 0.12$, the pitch angle was calculated to be 50°.

According to the analytical calculations carried out in [4] for $\gamma = 4.5$, the analytic formula (18) with the energies $\varepsilon_1 = 139$ and $\varepsilon_2 = 110$ (expressed in rydbergs) gives a polarization degree of 0.12. In order to calculate the pitch angle, it is necessary to find the ratio $a = \dfrac{\bar{\varepsilon}}{\varepsilon_2}$ of the mean energy $\bar{\varepsilon}$ of superthermal electrons, whose distribution function $f_{nt}(\varepsilon)$ is described by formulas (4)–(6), to the anisotropy constant ε_2 (7). The mean energy for the power distribution function $f_{nt}(\varepsilon)$ (6) is found to be

$$\bar{\varepsilon} = \int_{\varepsilon 1}^{\infty} \varepsilon f_{nt}(\varepsilon) d\varepsilon = \frac{\gamma - 1}{\gamma - 2}\varepsilon_1. \qquad (20)$$

In this case, for $\gamma = 4.5$ and $\varepsilon_1 = 139$, we obtain $\bar{\varepsilon} = 194$ and, accordingly, $a = 1.76$. In [6], the pitch angle was calculated to be 48°, and, in [4], it was found to be 50°. Thus, we can conclude that the above analytic calculations agree to a high accuracy with the numerical calculations based on the ATOM code [4].

A polarization degree of 0.12 can also be obtained analytically with other numerical combinations of the parameters γ, ε_1, and ε_2 of superthermal electrons. For example, the degree of polarization turns out to be equal to $P = 0.12$ for the combination $\gamma = 3.5$, $\varepsilon_1 = 173$, and $\varepsilon_2 = 270$, for which the pitch angle is about 59°. Consequently, for an adequate description of superthermal electrons, the range of the parameters γ, ε_1, and ε_2 should be determined, e.g., from the spectral measurements of the intensity ratio [4], in which case it is possible to use expression (19).

Analytic expression (18) for the degree of linear polarization of radiation from an ionized gas allows the polarization to be analyzed as a function of all of the parameters of the plasma electrons.

Figures 1 and 2 show how the polarization depends on n and T_0. The shapes of the profiles in these figures are governed by the form of the functional F_0.

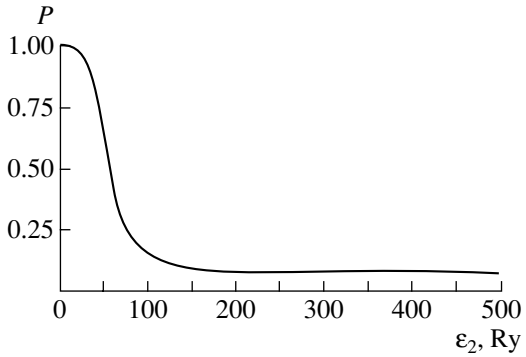

Fig. 5. Degree of linear polarization of radiation from an ionized gas vs. ε_2 for $\gamma = 4.5$ and $\varepsilon_1 = 139$ ($P = 0.12$ for $\varepsilon_2 = 110$).

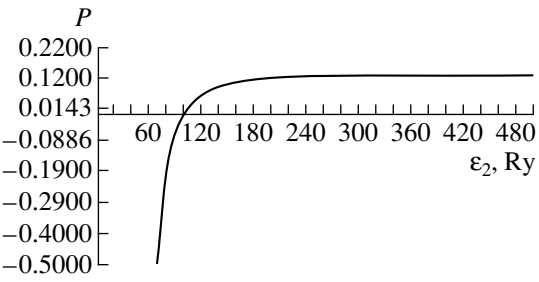

Fig. 6. Degree of linear polarization of radiation from an ionized gas vs. ε_2 for $\gamma = 3.5$ and $\varepsilon_1 = 173$ ($P = 0.12$ for $\varepsilon_2 = 270$).

Figure 3 displays the polarization as a function of the parameter γ.

Figure 4 shows the dependence of the degree of linear polarization on the parameter ε_1 for $\gamma = 4.5$ and $\varepsilon_2 = 110$. Notably, in the limit $\varepsilon_1 \longrightarrow \infty$, the polarization approaches $P = 1$. Formulas (4)–(7) imply that, in this limit, $a \longrightarrow \infty$ and the pitch angle vanishes. Consequently, this limit can be regarded as the "beam" limit, in which, however, the maximum degree of linear polarization of radiation from a gas ionized by a beam is equal to 0.6. Presumably, the analytical model makes it possible to predict a certain collective effect for which the degree of linear polarization of radiation from the atoms in an ionized gas exceeds the threshold value in the beam experiment. The shape of the profile in Fig. 4 is independent of the value of γ.

Figures 5 and 6 show the degree of linear polarization as a function of the parameter ε_2 of the electrons in an ionized gas for $\gamma = 4.5$ and 3.5, respectively. We can see that the profiles calculated for these γ values are radically different. For $\gamma = 2l + 1/2$, where l is an integer, the degree of linear polarization remains positive over the entire range of the parameter ε_2. According to formula (7), the limit $\varepsilon_2 \longrightarrow 0$ is analogous to the beam limit. For $\gamma = 2l + 3/2$, the degree of linear polarization changes sign at a certain value of ε_2. This dependence is similar to the energy dependence of the degree of linear polarization in the case of excitation by the beam. An analysis of the profiles presented in Figs. 5 and 6 clearly shows that spectropolarimetric measurements should be supplemented with measurements that would make it possible to adequately determine the parameters of superthermal electrons. However, the parameter ε_2 can be determined only by spectropolarimetric techniques.

7. CONCLUSION

The analytical results on the degree of linear polarization of radiation from the resonant S–P transition in multicharged Al XII ions in an ionized gas agree with the numerical results from the ATOM code to within 4%. The accuracy of the analytic model is governed by the accuracy of expression (9) for the excitation cross sections for the resonant transition and expression (10) for the degree of linear polarization. We can anticipate that the polarization of radiation from the S–P transitions in other ions can be described by expression (18) for the degree of linear polarization within an accuracy of 20%. This circumstance may extend the applicability range of the analytic model developed here.

The above model can also be used to calculate the degree of linear polarization of radiation from atomic transitions. To do this, the analytic expression for the excitation cross section for each particular atomic transition should be chosen so as to provide a good calculation accuracy and to take integrals (14a) and (14b) explicitly.

An obvious advantage of the analytic model is that the degree of linear polarization of radiation from an ionized gas is derived as an explicit function of the parameters of both thermal and superthermal electrons. This circumstance makes it possible to analyze the dependence of the degree of linear polarization on all of the parameters of superthermal electrons and to plan the operating modes of technical devices.

ACKNOWLEDGMENTS

I am grateful to A.M. Urnov for his interest in this study and his useful remarks.

REFERENCES

1. S. A. Kazantsev and J. C. Henoux, *Polarization Spectroscopy of Ionized Gases* (KAP, London, 1995).
2. S. A. Kazantsev, N. Ya. Polynovskaya, L. I. Pyatnitskiĭ, and S. A. Édel'man, Usp. Fiz. Nauk **156**, 3 (1988) [Sov. Phys. Usp. **31**, 785 (1988)].
3. L. Ya. Margolin, N. Ya. Polynovskaya, L. I. Pyatnitskiĭ, *et al.*, Teplofiz. Vys. Temp. **22**, 193 (1984).
4. F. Walden, H.-J. Kunze, A. Petoyan, *et al.*, Phys. Rev. E **59**, 3562 (1999).
5. M. Shapochkin, J. Mosc. Phys. Soc. **9**, 361 (1999).
6. E. Haug, Sol. Phys. **61**, 129 (1979).

7. V. L. Ginzburg and A. V. Gurevich, Usp. Fiz. Nauk **70**, 261 (1960).
8. A. V. Vinogradov, A. M. Urnov, and A. S. Shlyapnikova, Tr. Fiz. Inst. Akad. Nauk SSSR **195**, 89 (1989).
9. A. V. Vinogradov, A. M. Urnov, and A. S. Shlyapnikova, Tr. Fiz. Inst. Akad. Nauk SSSR **194**, 72 (1981).
10. I. L. Beĭgman, S. N. Oparin, and A. M. Urnov, Tr. Fiz. Inst. Akad. Nauk SSSR **195**, 47 (1989).
11. J. C. Kieffer, J. P. Matte, H. Pepin, *et al.*, Phys. Rev. Lett. **68**, 480 (1992).
12. M. Shapochkin, J. Mosc. Phys. Soc. **9**, 245 (1999).
13. K. Blum, in *Progress in Atomic Spectroscopy*, Ed. by W. Hanle and H. Kleinpoppen (Plenum, New York, 1973), p. 337.
14. H. Kleinpoppen and A. Scharmann, in *Progress in Atomic Spectroscopy*, Ed. by W. Hanle and H. Kleinpoppen (Plenum, New York, 1978), Part A, p. 329.
15. I. I. Sobelman, L. A. Vainshtein, and E. A. Yukov, *Excitation of Atoms and Broadening of Spectral Lines* (Nauka, Moscow, 1979; Springer-Verlag, Berlin, 1981).
16. V. P. Shevelko, Phys. Scr. **46**, 531 (1992).
17. L. A. Vaĭnshteĭn, L. P. Presnyakov, and I. I. Sobel'man, Zh. Éksp. Teor. Fiz. **45**, 2015 (1963) [Sov. Phys. JETP **18**, 1382 (1963)].
18. M. J. Seaton, in *Atomic and Molecular Processes*, Ed. by D. Bates (Academic, New York, 1962; Mir, Moscow, 1964).
19. A. V. Eletskiĭ and B. M. Smirnov, Zh. Tekh. Fiz. **38**, 3 (1968) [Sov. Phys. Tech. Phys. **13**, 1 (1968)].
20. H. van Regemorther, Astrophys. J. **136**, 906 (1962).
21. S. M. Younger and W. Wiese, J. Quant. Spectrosc. Radiat. Transf. **22**, 161 (1979).
22. L. C. Johnson, Astrophys. J. **174**, 227 (1972).
23. R. Mewe, Astron. Astrophys. **20**, 215 (1972).
24. L. Vriens and A. H. M. Smeets, Phys. Rev. A **22**, 940 (1980).
25. M. Shapochkin, Phys. Scr. **60**, 335 (1999).
26. M. K. Inal and J. Dubau, J. Phys. B **20**, 4221 (1987).
27. D. A. Varshalovich, A. N. Moskalev, and V. K. Khersonskii, *Quantum Theory of Angular Momentum* (Nauka, Leningrad, 1975; World Scientific, Singapore, 1988).
28. L. A. Vaĭnshteĭn and V. P. Shevel'ko, *Structure and Characteristics of Ions in a Hot Plasma* (Nauka, Moscow, 1986).
29. A. S. Kazantsev and A. G. Petrashen', Opt. Spektrosk. **84**, 375 (1998) [Opt. Spectrosc. **84**, 324 (1998)].

Translated by O. E. Khadin

Plasma Physics Reports, Vol. 27, No. 8, 2001, pp. 699–707. Translated from Fizika Plazmy, Vol. 27, No. 8, 2001, pp. 741–749.

LOW-TEMPERATURE PLASMA

Helicon Plasma in a Nonuniform Magnetic Field

O. V. Braginskiĭ, A. N. Vasil'eva, and A. S. Kovalev

Institute of Nuclear Physics, Moscow State University, Vorob'evy gory, Moscow, 119899 Russia

Received November 8, 2000; in final form, February 7, 2001

Abstract—The distributions of the electron density in a plasma produced by helicon waves and the corresponding wave amplitudes and phases are studied experimentally. The measurements were carried out in an argon plasma at a pressure of 3 mtorr and at an input RF power of up to 600 W. The magnetic field was varied in the range from 0 to 200 G. The efficiency of plasma production in both uniform and nonuniform fields is investigated. It is shown that, in a nonuniform magnetic field, the electron density can be substantially increased (up to 5×10^{12} cm^{-3}) by placing an antenna in the region in which the magnetic field is weaker than in the main plasma. © *2001 MAIK "Nauka/Interperiodica".*

1. INTRODUCTION

At present, helicon plasma sources hold great promise for plasmochemical technologies in microelectronics. Helicon sources are capable of creating a plasma with an electron density from 10^{12} to 10^{13} cm^{-3} at a gas pressure of about 1 mtorr in relatively weak magnetic fields in the range 50 to 100 G. In such a plasma, the electron temperature is, as a rule, no higher than 3–4 eV. The parameters of a helicon plasma and the structure of helicon waves (helicons) were studied in [1–8]. Among the most challenging problems are those related to the observed rapid damping of helicons and the high efficiency of gas ionization in the field of a helicon wave. Thus, in order to interpret the experimentally observed values of the absorption coefficients of helicon waves, it is necessary to introduce an effective electron collision frequency that exceeds the binary collision frequency by one order of magnitude or more.

The main collisionless mechanisms responsible for high ionization efficiency are the trapping of electrons by the longitudinal electric field of a helicon wave [8]. The phase velocities of helicons along the magnetic field correspond to electron energies in the range 20–100 eV and, accordingly, to peaks in the ionization cross sections for most gases. That these mechanisms are indeed important is confirmed by the observed emission spectra of argon ions (ArII) that move along the magnetic field at a speed corresponding to the phase velocity of a helicon wave [8, 9]. However, the lack of data about the amplitude of the longitudinal electric field of a helicon wave raises the question of whether the wave is capable of trapping a sufficient number of electrons to provide the observed level of ionization and the wave damping rate [10].

A mechanism for the efficient damping of a helicon wave was proposed in [11, 12] and was refined in [13–17]. This mechanism is associated with the possible conversion of helicons into electrostatic waves in a magnetized plasma [18]. In contrast to helicon waves, electrostatic waves, which are often referred to as Trivelpiece–Gould (TG) waves, are damped in a plasma at a fairly high rate. In particular, in [11, 13, 14], it was suggested that both helicons and TG waves can be strongly coupled at the jump in the plasma density near the dielectric wall that confines the plasma. As a result, helicons are damped by their linear conversion into TG waves at the plasma boundary, while TG waves experience a strong collisional damping by the plasma electrons. Strictly speaking, at the plasma boundary, the electron density does not undergo a jump but instead decreases to zero across a transitional layer, so that the question remains open of whether the plasma inhomogeneities are strong enough to explain the damping of helicon waves as being due to their conversion into electrostatic waves.

Most studies devoted to helicon waves deal with a uniform magnetic field. As was shown by Chen [19], who studied helicon waves in a plasma column 4 cm in diameter in a nonuniform magnetic field of 560 G, the magnetic field nonuniformities may act to substantially increase the electron density. However, the physical nature of this phenomenon remained unclear. Further research on helicon plasma sources [20–22] showed that, even for the same input power, the electron density in a nonuniform magnetic field may be markedly higher than in a uniform field. Our purpose here is to investigate the spatial distribution of the electron density and to determine the structure of a helicon wave in both uniform and nonuniform magnetic fields for plasma dimensions characteristic of helicon plasma sources used in microelectronic technologies.

2. EXPERIMENTAL DEVICE

A schematic of the helicon plasma source is shown in Fig. 1. The plasma is produced in a cylindrical glass tube 15 cm in diameter and 40 cm in length. A steel chamber 26 cm in diameter and 24 cm in length is con-

1063-780X/01/2708-0699$21.00 © 2001 MAIK "Nauka/Interperiodica"

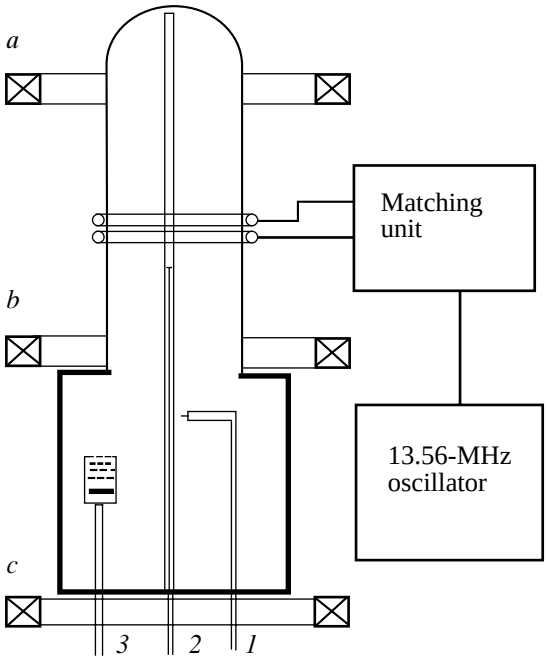

Fig. 1. Schematic of the experimental device: (*1*) Langmuir probe, (*2*) magnetic probe for measuring the magnetic field of a helicon wave, and (*3*) ion energy analyzer.

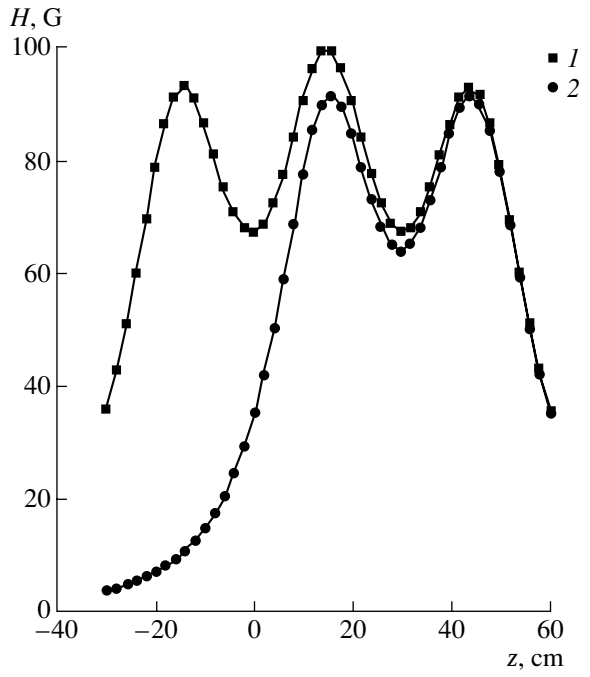

Fig. 2. Configurations of (*1*) uniform and (*2*) constant nonuniform magnetic fields *H*.

nected to the tube. The tube and the chamber are placed in a constant magnetic field created by three 32-cm-diameter individual coils (*a*, *b*, and *c*) separated by a distance of 30 cm. The magnetic field was varied from 0 to 200 G. The three coils make it possible to create a uniform magnetic field as well as a magnetic field with the desired gradients inside the tube and chamber. The experiments were carried out with two magnetic configurations: a uniform configuration created by the three coils carrying the same current and a nonuniform configuration created by the two lower coils (the current in the upper coil *a* was switched off). Figure 2 illustrates the magnetic field strength along the common symmetry axis of the tube and the discharge chamber for both of these configurations. The zero point of the *z*-axis corresponds to the position of the antenna. Helicon waves are excited by a loop antenna in the form of a two-turn coil 16 cm in diameter wrapped around the glass tube in the plane perpendicular to the symmetry axis. The antenna, which excites an $m = 0$ helicon wave, is connected by a matching unit to a 13.56-MHz RF oscillator with a power of up to 700 W. In the experiments, we measured the powers of the incident and reflected waves and the RF voltage at the antenna. The power of the reflected wave was always measured to be lower than 7% of the power of the incident wave. The experiments were carried out with the discharge chamber, which was pre-evacuated to a pressure of 10^{-5} torr and through which argon was passed at a pressure of 3 mtorr.

The electron density and plasma potential were measured by a Langmuir probe (*1*) 300 μm in diameter and 2 mm in length. Inside the chamber, the probe could be moved in both the longitudinal and radial directions. The electron density was determined from the ion saturation current at a probe potential of −100 eV:

$$N_e = (I_{\text{sat}}/0.54eA)\sqrt{\frac{m_i}{T_e}}, \quad (1)$$

where I_{sat} is the ion saturation current, e is the electron charge, A is the probe area, m_i is the mass of an ion, and T_e is the electron temperature.

The RF magnetic field of a helicon wave (or, more precisely, the B_z-component, parallel to a constant magnetic field) was measured by a one-turn magnetic probe 10 mm in diameter oriented perpendicular to the constant magnetic field. The magnetic probe was placed inside a quartz tube 15 mm in diameter coaxial with the discharge chamber and could be moved in the longitudinal direction. Our investigations of helicon discharges showed that placing the quartz tube at the discharge axis reduces the electron plasma density by at most 10%. The signal from the probe was fed to an oscillograph through a cable loaded with a resistance equal to the wave impedance. The voltage $V(t)$ at the probe was calculated by the formula

$$V(t) = \pi r^2 \frac{\omega}{c} B_z, \quad (2)$$

where B_z is the z-component of the magnetic field of a helicon wave, r is the probe radius, ω is the angular frequency of the RF magnetic field, and c is the speed of light.

3. EXPERIMENTAL RESULTS

Figure 3 shows how the electron density N_e in a helicon discharge plasma depends on the strength H of the constant magnetic field. The profiles presented were measured in a uniform magnetic field at different distances z from the center of the antenna for an input power of 300 W. The input power is defined as the difference between the powers of the incident and reflected waves.

From Fig. 3, we can see that, near the antenna (z = 4.5 cm), the electron density reaches its maximum at $H \sim 25$ G and then decreases with increasing magnetic field. At distances farther away from the antenna (z = 10 cm), the electron density decreases from its maximum value more gradually and then starts to increase again, reaching a second maximum at $H \sim 45$ G. At distances of 15 and 22 cm, the electron density in a plasma produced by helicons propagating from the antenna is the highest at a magnetic field of about 60 G. We can also see that, the stronger the magnetic field, the more gradual is the decrease in the electron density with distance from the antenna.

An analysis of Fig. 3 allows us to conclude that, for an input power of 300 W, the optimum magnetic field near the loop antenna is about 20 G. Within about 20 cm from the antenna, the optimum magnetic field for plasma production ranges between 50 and 60 G. These two optimum magnetic field strengths can be made consistent by reducing the magnetic field in a local region near the antenna (or, in other words, by producing the plasma in a nonuniform magnetic field). For this purpose, we carried out a series of experiments in which the current in magnetic coil a was switched off. As a result, the magnetic field near the antenna became approximately two times weaker than in the discharge chamber (Fig. 2). Figure 4 displays the dependence of the electron density on the strength of a nonuniform magnetic field at the chamber axis at a distance of 30 cm from the antenna. The profiles shown in Fig. 4 were measured for an input power of 300 W. A comparison between Figs. 3 and 4 shows that, in a nonuniform magnetic field, the behavior of the electron density differs radically from that in a uniform magnetic field. In fact, even near the antenna, we observe no substantial reduction in N_e as the magnetic field increases. At a distance of 22 cm from the antenna, the electron density N_e increases monotonically with the magnetic field; this indicates that, in a nonuniform field, the electron density decreases far more gradually with distance from the antenna. As a result, at distances of 15 and 20 cm, the electron density in a nonuniform field is, respectively, three and seven times the maximum electron density of the plasma produced in a uniform magnetic field, provided that the input RF power is the same (300 W). Hence, with a nonuniform magnetic field, it is possible to achieve significantly higher electron densi-

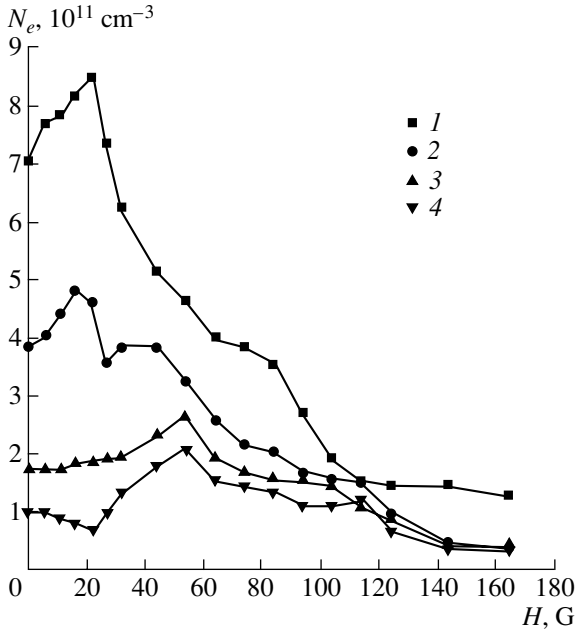

Fig. 3. Electron density N_e vs. uniform magnetic field H for W = 300 W at different distances from the antenna: z = (*1*) 4.5, (*2*) 10, (*3*) 15, and (*4*) 22 cm.

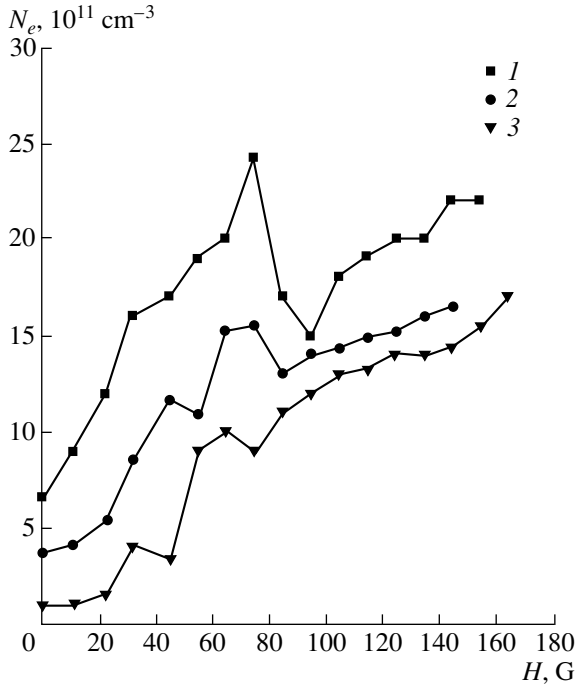

Fig. 4. Electron density N_e vs. nonuniform magnetic field H for W = 300 W at different distances from the antenna: z = (*1*) 4.5, (*2*) 15, and (*3*) 22 cm.

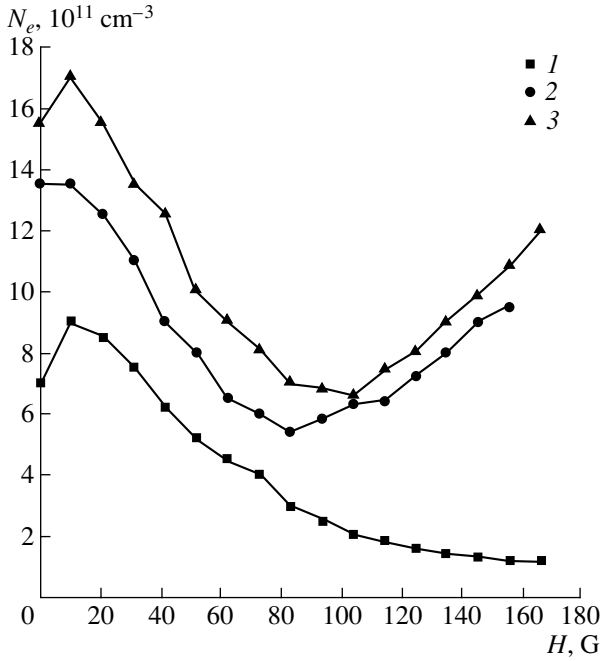

Fig. 5. Electron density N_e vs. uniform magnetic field H at a distance of 4.5 cm from the antenna for different input RF powers: W = (*1*) 300, (*2*) 450, and (*3*) 600 W.

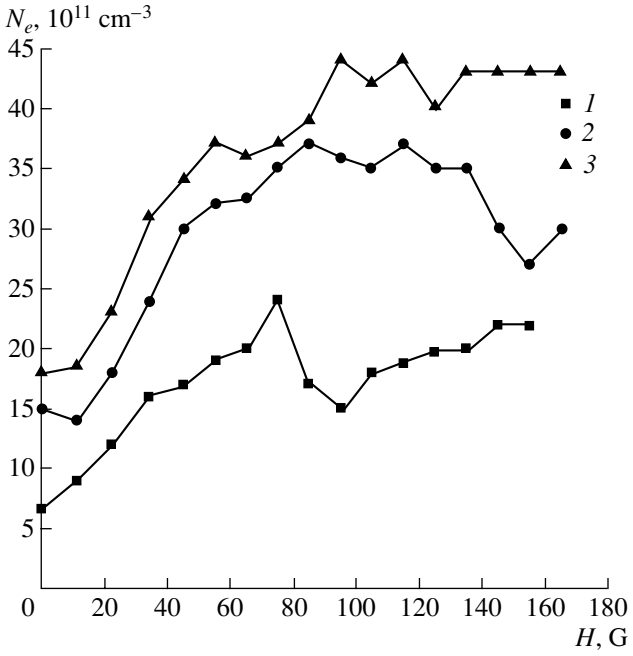

Fig. 6. Electron density N_e vs. nonuniform magnetic field H at a distance of 4.5 cm from the antenna for W = (*1*) 300, (*2*) 450, and (*3*) 600 W.

ties; moreover, the greater the distance from the antenna, the larger is the amount by which the electron density N_e can be increased.

In order to gain a clearer insight into the effect of the magnetic field nonuniformity on the plasma properties of a helicon discharge, we measured the electron density as a function of the strength of both uniform and nonuniform magnetic fields for three different input powers (300, 450, and 600 W) at two fixed distances from the antenna (4.5 and 22 cm). For a uniform magnetic field, the profiles of the electron density N_e measured at a distance of 4.5 cm from the antenna for input RF powers of 300, 450, and 600 W are displayed in Fig. 5. Figure 6 presents the same profiles but for a nonuniform magnetic field. We see from Fig. 5 that, regardless of the value of the input power, the electron density N_e decreases as the magnetic field is increased to more than 20 G. However, for input powers of 450 and 600 W, the electron density N_e starts to increase again when the magnetic field exceeds 100 G. For a nonuniform magnetic field, the electron density behaves in a radically different manner (Fig. 6): for an input power of 300 W, N_e increases as the magnetic field is increased up to 80 G; for an input power of 450 W, it increases as the field is increased up to 100 G; and, for an input power of 600 W, it increases as the field is increased up to 120 G. Moreover, the maximum achievable electron density is approximately three times that for a uniform magnetic field. Analogous profiles measured at a distance of 22 cm from the antenna are displayed in Figs. 7 and 8. We again see that, for a nonuniform magnetic field, the electron density N_e increases monotonically with the magnetic field and reaches values seven times higher than those for a uniform magnetic field.

An important point here is that, in a nonuniform magnetic field, the electron density increases only when the field near the antenna is weaker than the field in the main plasma. If this is not the case, the situation is reversed.

Radial profiles of the electron density measured at distances of 4.5 and 22 cm from the antenna for an input power of 300 W are shown in Figs. 9 and 10, respectively. We can see that, in a nonuniform magnetic field, the profiles are somewhat narrower. Consequently, the increase in the electron density at the discharge axis in a nonuniform magnetic field cannot be attributed to the radial redistribution of the electron density N_e. The density N_e increases because, in a nonuniform field, the helicon wave field ionizes the gas more efficiently.

In order to clarify the physical nature of such a significant increase in the efficiency of plasma production in a nonuniform magnetic field, we carried out magnetic probe measurements of the amplitude and phase of a helicon wave as well as their profiles along the plasma axis. Specifically, we measured the B_z component of the RF magnetic field of a helicon. Figure 11 shows the amplitude of a standing helicon wave measured as a function of distance from the antenna for an input power of 600 W in uniform magnetic fields of 50,

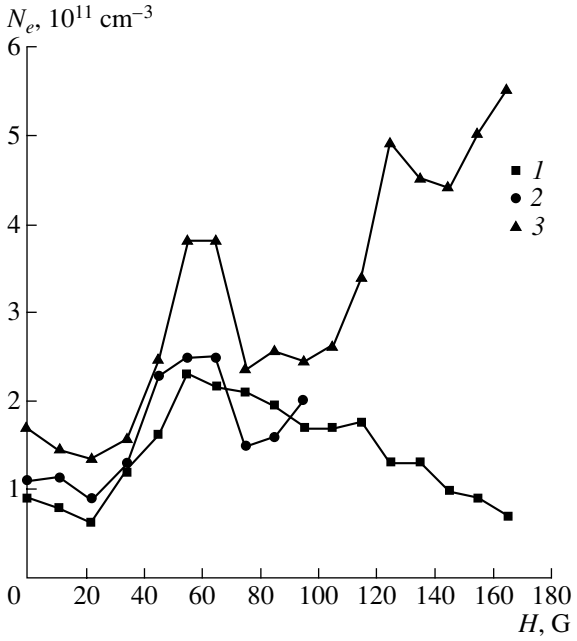

Fig. 7. Electron density N_e vs. uniform magnetic field H at a distance of 22 cm from the antenna for W = (*1*) 300, (*2*) 450, and (*3*) 600 W.

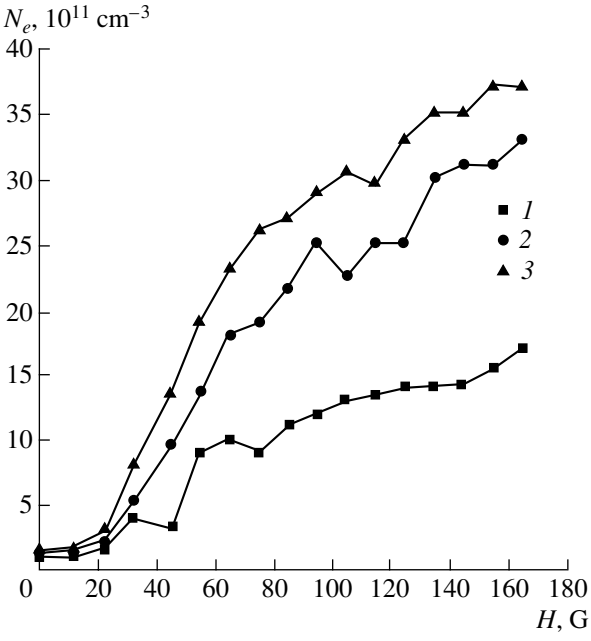

Fig. 8. Electron density N_e vs. nonuniform magnetic field H at a distance of 22 cm from the antenna for W = (*1*) 300, (*2*) 450, and (*3*) 600 W.

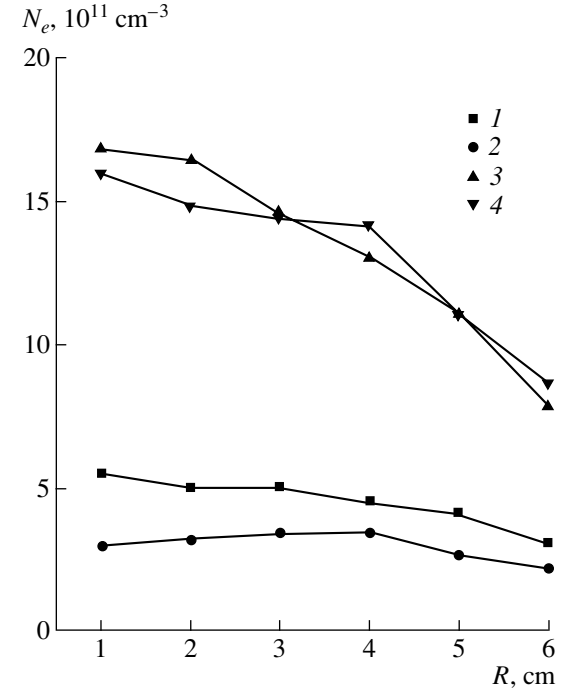

Fig. 9. Radial profiles of N_e at a distance of 4.5 cm from the antenna in uniform magnetic fields of H = (*1*) 45 and (*2*) 90 G and in nonuniform magnetic fields of H = (*3*) 45 and (*4*) 90 G.

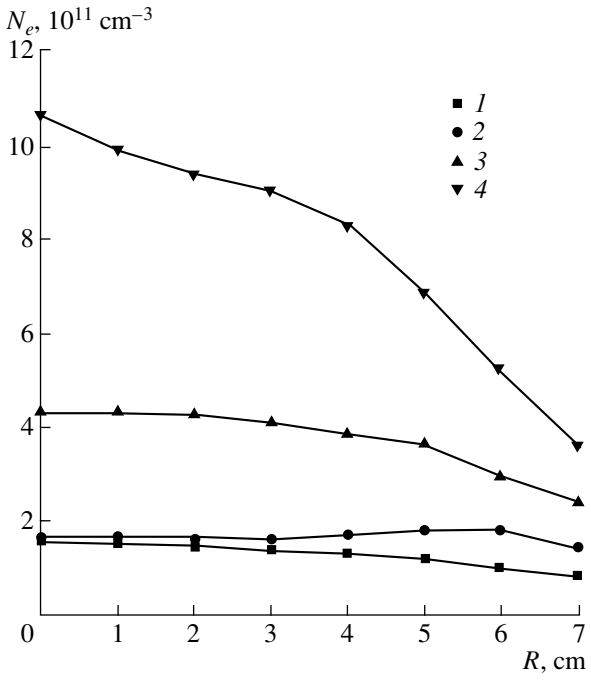

Fig. 10. Radial profiles of N_e at a distance of 22 cm from the antenna in uniform magnetic fields of H = (*1*) 45 and (*2*) 90 G and in nonuniform magnetic fields of H = (*3*) 45 and (*4*) 90 G.

100, and 150 G, which correspond to the regions where the electron density N_e in Figs. 5 and 7 is decreasing, at a minimum, and increasing, respectively. Analogous longitudinal profiles measured in nonuniform magnetic fields are presented in Fig. 12. It is of interest to note that, the stronger the magnetic field, the larger the amplitude of a helicon wave, although there is a dip in the dependence of N_e on the uniform field H at

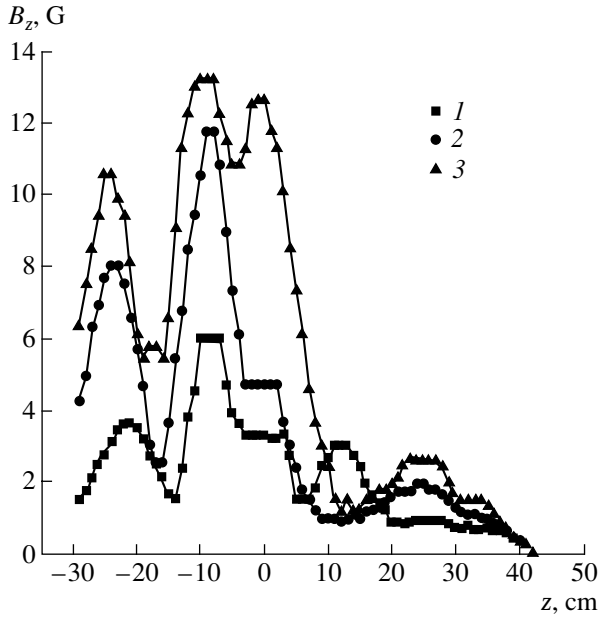

Fig. 11. Amplitude B_z of the longitudinal component of the helicon field vs. z for W = 600 W in uniform magnetic fields of H = (*1*) 60, (*2*) 100, and (*3*) 140 G.

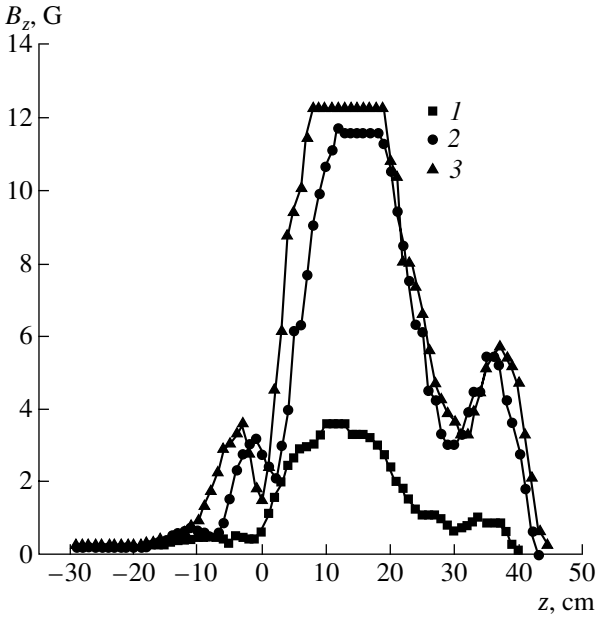

Fig. 12. Amplitude B_z of the longitudinal component of the helicon field vs. z for W = 600 W in nonuniform magnetic fields of H = (*1*) 60, (*2*) 100, and (*3*) 140 G.

$H \sim 100$ G. It can be seen in Figs. 11 and 12 that the wave amplitudes in uniform and nonuniform magnetic fields are comparable. An important difference is that, in a uniform magnetic field, the main peaks in the wave amplitude occur to the left of the antenna (i.e., they are remote from the reaction chamber). In a nonuniform magnetic field, the main peaks occur in the region where the field is stronger (i.e., they are closer to the reaction chamber). Thus, at a distance of 22 cm from the antenna, the wave amplitudes in uniform and nonuniform magnetic fields differ by a factor of approximately five. This value is close to the ratio of the related electron densities N_e. However, at a distance of 4.5 cm from the antenna, the wave amplitudes are comparable, while the corresponding electron densities N_e differ by a factor of three. Hence, we can conclude that there is no direct correlation between the amplitude of a helicon wave and the electron plasma density.

Figure 13 shows how the phase of a helicon wave changes with distance from the antenna in both uniform and nonuniform magnetic fields. The longitudinal profiles were measured in a plasma with a magnetic field of 100 G for an input power of 600 W. One can see that the wave phase velocities in uniform and nonuniform fields differ only slightly: in both cases, they are equal to about $\sim 3.5 \times 10^8$ cm/s.

4. DISCUSSION OF THE RESULTS

In order to estimate the efficiency of a helicon discharge, we determine the fraction of the input RF power that is expended directly in ionizing the gas. To do this, we must find the electron losses from the plasma. In a plasma cylinder in a longitudinal uniform magnetic field, the diffusion equation for the electrons can be written as [23]

$$D_a \frac{\partial^2 n}{\partial z^2} + D_h \Delta_r n + S_i(r, z) = 0. \qquad (3)$$

Here, D_a is the coefficient of the ambipolar diffusion of the electrons along the magnetic field (for an argon pressure of 3 mtorr and an electron temperature of about 3 eV, we have $D_a = 10^6$ cm^2/s) and $S_i(r, z)$ [cm^{-3} s^{-1}] is the number of electrons produced in a unit gas volume per second. The coefficient of electron diffusion across the magnetic field, D_h, has the form

$$D_h = \frac{\mu_i D_e + \mu_e D_i}{\mu_i(1 + \omega_{ce}^2/\nu_e^2) + \mu_e(1 + \omega_{ci}^2/\nu_i^2)}; \qquad (4)$$

where D_e and D_i are the electron and ion diffusion coefficients, μ_e and μ_i are the electron and ion mobilities, ω_{ce} and ω_{ci} are the electron and ion cyclotron frequencies, and ν_e and ν_i are the electron–neutral and ion–neutral collision frequencies.

The term $S_i(r, z)$ can be represented as

$$S_i(r, z) = S J_0\left(\frac{\chi_{01} r}{R}\right) \exp(-z/l_i); \qquad (5)$$

where R is the plasma radius, l_i is the characteristic ionization length (for the conditions of our experiments, it is approximately equal to 10 cm), $\chi_{01} = 2.44$ is the root

of the Bessel function, and S is the number of electrons produced near the antenna at the discharge axis per 1 cm^3. As a result, Eq. (3) reduces to

$$\frac{\partial^2 n}{\partial z^2} - K^2 n = \frac{S}{D_a}\exp(-z/l_i), \qquad (6)$$

where $K = \frac{\chi_{01}}{R}\sqrt{\frac{D_h}{D_a}}$.

The boundary conditions for Eq. (6) have the form $\left.\frac{dn}{dz}\right|_{z=0} = 0$ and $n(L) = 0$, where $L = 35$ cm and the point $z = 0$ corresponds to the position of the antenna.

The total power P_i expended on gas ionization is equal to

$$P_i = 2\varepsilon_i \int_0^L dz \int_0^R N_i(r, z) 2\pi r dr = 4\varepsilon_i S l_i \pi R^2 J_1(\chi_{01})/\chi_{01}. \qquad (7)$$

The results of calculations of the electron density at distances of 4.5 and 22 cm from the antenna and the total power P_i for magnetic fields of 50, 100, and 150 G are summarized in the table. The ionization rate was chosen so as to equate the electron densities to those shown in Figs. 5 and 7 for an input power of 600 W. In the table, the fraction of the input power expended on ionizing the gas is denoted by η.

The electron temperature can be estimated from the calculated results by using the empirical formula $K_i = 7.93 \times 10^{-8}\exp(-18.9/T_e)$ [cm^3/s] for the ionization rate of argon gas [24] (see the corresponding column in the table). The calculated temperatures are close to the temperatures typical of helicon plasmas (about 3 eV). Note that the calculations carried out with a Maxwellian distribution function and an ionization cross section in the form of a step function with the height $\sigma_i = 2 \times 10^{-16}$ cm^2 yield somewhat higher temperatures: 3.7, 3.2, and 3 eV for magnetic fields of 50, 100, and 150 G, respectively.

We can see that, in weak magnetic fields, the fraction of the input power expended on gas ionization is fairly high and amounts to 10%.

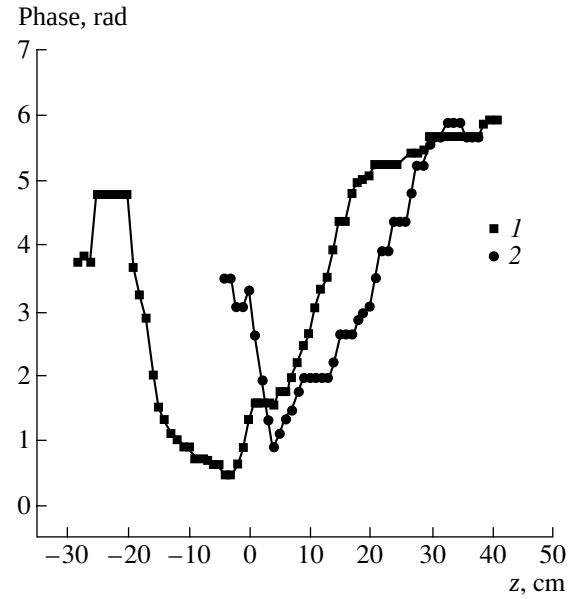

Fig. 13. Phase of a helicon wave vs. z for $W = 600$ W in (*1*) a uniform magnetic field of $H = 100$ G and (*2*) a nonuniform magnetic field of $H = 100$ G.

In a nonuniform magnetic field, the electron losses from the plasma are far more difficult to estimate. Nevertheless, even under the assumption that the electron losses in a nonuniform field are comparable to those in the uniform field, the power expended on gas ionization is markedly higher than 10% of the total input power.

Hence, the observed electron density can be maintained by heating the electrons to a temperature of about 3 eV. The damping of helicons by electron collisions is too weak to explain why the wave amplitude decreases with distance from the antenna (as is shown in Figs. 11 and 12). Consequently, the most probable mechanism for gas ionization in a helicon discharge is the conversion of helicon waves into electrostatic waves, which are strongly damped by collisions of electrons with neutral gas atoms, in which case the electrons are heated to a temperature of about 3 eV.

Another possible mechanism by which the helicons ionize the gas is the trapping of electrons by the helicon field and subsequent gas ionization by the trapped electrons, which move at the phase velocity of the wave. Figure 11 shows that the longitudinal component B_z of the magnetic field of a running helicon wave is about

Table

H, G	$D_h \times 10^{-4}$	$N_e \times 10^{-11}$ (z = 22 cm)	$N_e \times 10^{-11}$ (z = 4.5 cm)	$S \times 10^{-16}$	P_i, W	T_e, eV	η, %
50	7.3	3.2	10	2	65	3.1	11
100	2	2.7	7	0.62	20	2.8	3.3
150	0.87	4.7	10	0.63	20.5	2.65	3.4

6 G. The component B_z is related to the longitudinal component E_z of the helicon field by [16]

$$E_z = i\gamma\frac{\omega c}{\omega_p^2}kB_z; \quad (8)$$

where $\gamma = 1 + i\nu_e/\omega$, ω_p is the plasma frequency, the total wave vector k of a helicon wave is defined as $k = \sqrt{k_\parallel^2 + k_\perp^2}$; $k_\perp = 3.83/R$ is the transverse wave vector, and $k_\parallel$ is the longitudinal wave vector. From Fig. 10, we can see that $k_\parallel \sim 0.2$–0.3 cm^{-1} and $k = 0.56$ cm^{-1}. As a result, using relationship (8), we find that the longitudinal component E_z of the helicon field is about 1 V/cm.

The number of electrons that can be trapped by a helicon wave is equal to [10]

$$n_{\rm tr} = \frac{n}{2}\left\{\mathrm{erf}\left(\frac{V_{\rm ph}+V_{\rm tr}}{V_t}\right) - \mathrm{erf}\left(\frac{V_{\rm ph}-V_{\rm tr}}{V_t}\right)\right\}\frac{\omega_{\rm tr}}{\omega_{\rm tr}+\nu_{\rm ph}}, \quad (9)$$

where n is the number of electrons per unit volume, $V_{\rm ph}$ is the wave phase velocity (for our experimental conditions, it is about $\sim 3.5 \times 10^8$ cm/s), V_t is the thermal velocity of electrons with a temperature of 3 eV, $V_{\rm tr}$ denotes the width of the velocity range in which the electrons can be trapped by the helicon field, ω_{tr} is the bounce frequency of the trapped electrons, and $\nu_{\rm ph}$ is the rate of elastic collisions of an electron moving at the wave phase velocity with neutral gas atoms. The quantities $V_{\rm tr}$, $\omega_{\rm tr}$, and $\nu_{\rm ph}$ have the form

$$V_{\rm tr} = 2\left(\frac{eE_z}{mk_\parallel}\right)^{1/2}, \quad \omega_{\rm tr} = \left(\frac{eE_z\omega}{mV_{\rm ph}}\right)^{1/2}, \quad \nu_{\rm th} = N_0\sigma_e V_{\rm ph}, \quad (10)$$

where m is the mass of an electron, σ_e is the elastic collision cross section, and N_0 is the gas density.

Using expression (9), we find that, for $n = 10^{12}$ cm^{-3}, the number of electrons that can be trapped by a helicon wave per unit volume is equal to $n_{\rm tr} = 2.3 \times 10^9$ cm^{-3}. For a mean electron energy of 35 eV (which corresponds to $V_{\rm ph} = 3.5 \times 10^8$ cm/s), the ionization cross section for argon atoms can be set equal to $\sigma_I = 2 \times 10^{-16}$ cm^2. As a result, the rate at which argon gas is ionized by the trapped electrons is estimated as $S = 1.6 \times 10^{16}$ cm^{-3} s^{-1}, which is comparable to the above values of the rates of the ionization of argon atoms by thermal electrons with a temperature of about 3 eV (see table). Hence, under our experimental conditions, both of the possible ionization mechanisms are comparable in importance.

We emphasize that a substantial increase in the electron density in a nonuniform magnetic field can also be explained in terms of the collisionless ionization mechanism. According to formula (9), the number of electrons that can be trapped by a helicon wave increases sharply as the wave phase velocity decreases. In turn, the weaker the magnetic field, the lower the phase velocity of a helicon. Consequently, in a nonuniform magnetic field, a helicon wave near the antenna (where the magnetic field is weaker and, accordingly, the phase velocity is lower) can trap a larger number of electrons than a wave with a phase velocity corresponding to the strongest magnetic field. As the wave phase velocity increases, the trapped electrons are accelerated to higher energies [21]. However, the wave phase velocity also depends on the electron plasma density N_e, $V_{\rm ph} \sim N_e^{-1/2}$, which is, in turn, far from being uniform. In Fig. 11, the behavior of the wave phase in uniform and nonuniform magnetic fields is nearly the same. However, since the number n_{tr} of electrons that can be trapped by the wave per unit volume is highly sensitive to the wave phase velocity, even a slight difference in the phase velocity may result in a significant difference in the gas ionization rates.

It should be noted that the magnetic field gradients in a plasma can enhance the coupling between the helicon and electrostatic waves, thereby causing the helicons to damp at a higher rate and the electron density to increase. In fact, if there is a surface in the plasma column at which the wave vectors of the helicon and electrostatic waves are the same, then the helicons are efficiently converted into electrostatic waves near this surface. The critical magnetic field at this surface is equal to [13]

$$H_c = 2\omega_p\frac{m\omega}{ek_\parallel}. \quad (11)$$

This formula shows that, for electron densities of $(3$–$4) \times 10^{12}$ cm^{-3} (Fig. 6), the critical magnetic field ranges between 120 and 140 G. Recall that, in the nonuniform magnetic configuration under investigation, the magnetic field near the antenna is two times weaker than in the main plasma. Consequently, near the antenna, the magnetic field is approximately equal to 30–60 G. This indicates that, between the antenna and the main plasma, there may be a critical magnetic-field region, in which the helicon waves are efficiently converted into electrostatic waves.

5. CONCLUSION

We have investigated the electron density distribution in a magnetized plasma produced by helicon waves. The measurements were carried out in both uniform and nonuniform magnetic fields. We have shown that, in certain nonuniform magnetic configurations, the efficiency of plasma production can be significantly higher than in uniform configurations. We have also investigated the distributions of the amplitude and phase of a helicon wave in uniform and nonuniform magnetic fields. We have analyzed the relative importance of two principal mechanisms for the damping of helicons: the trapping of electrons by the longitudinal

helicon field and the conversion of helicon waves into electrostatic waves. We have found that, under our experimental conditions, these mechanisms may be equally important.

ACKNOWLEDGMENTS

This study was supported in part by the Russian Foundation for Basic Research (project no. 01-02-17476) and the State Program for Science and Technology "Promising Technologies and Devices in Micro- and Nanoelectronics."

REFERENCES

1. R. W. Boswell and F. F. Chen, IEEE Trans. Plasma Sci. **25**, 1229 (1997).
2. R. W. Boswell and F. F. Chen, IEEE Trans. Plasma Sci. **25**, 1245 (1997).
3. T. Lho, N. Hershkowitz, J. Miller, *et al.*, Phys. Plasmas **5**, 3135 (1998).
4. J. P. Rayner and A. D. Cheetham, Plasma Sources Sci. Technol. **8**, 79 (1999).
5. K. K. Chi, T. E. Sheridan, and R. W. Boswell, Plasma Sources Sci. Technol. **8**, 421 (1999).
6. C. Carter and J. Khachan, Plasma Sources Sci. Technol. **8**, 432 (1999).
7. O. V. Braginskiĭ, A. N. Vasil'eva, and A. S. Kovalev, Fiz. Plazmy **24**, 821 (1998) [Plasma Phys. Rep. **24**, 762 (1998)].
8. A. R. Ellingboe, R. W. Boswell, J. P. Booth, and N. Sadeghi, Phys. Plasmas **2**, 1807 (1995).
9. A. W. Degeling, T. E. Sheridan, and R. W. Boswell, Phys. Plasmas **6**, 3664 (1999).
10. A. W. Degeling, T. E. Sheridan, and R. W. Boswell, Phys. Plasmas **6**, 1641 (1999).
11. K. P. Shamrai and V. B. Taranov, Plasma Phys. Controlled Fusion **36**, 1719 (1994).
12. N. F. Vorob'ev and A. A. Rukhadze, Fiz. Plazmy **20**, 1065 (1994) [Plasma Phys. Rep. **20**, 955 (1994)].
13. K. P. Shamrai and V. B. Taranov, Plasma Sources Sci. Technol. **5**, 474 (1996).
14. K. P. Shamrai, V. P. Pavlenko, and V. B. Taranov, Plasma Phys. Controlled Fusion **39**, 505 (1997).
15. K. P. Shamraĭ, Fiz. Plazmy **25**, 934 (1999) [Plasma Phys. Rep. **25**, 860 (1999)].
16. F. F. Chen and D. Arnush, Phys. Plasmas **4**, 3411 (1997).
17. F. F. Chen and D. Arnush, Phys. Plasmas **5**, 1239 (1998).
18. N. Krall and A. Trivelpiece, *Principles of Plasma Physics* (Academic, New York, 1973; Mir, Moscow, 1975).
19. F. F. Chen, J. Vac. Sci. Technol. A **10**, 1389 (1992).
20. O. V. Braginskiy, A. S. Kovalev, and A. N. Vasilieva, in *Proceedings of the International Conference on Plasma Physics, Touluse, 1997*, Vol. 3, p. 76.
21. X. M. Guo, J. Scharer, Y. Mouzouris, and L. Louis, Phys. Plasmas **6**, 3400 (1999).
22. O. V. Braginskiĭ, A. N. Vasil'eva, and A. S. Kovalev, Mikroélektronika **29**, 410 (2000).
23. M. A. Lieberman and R. W. Boswell, J. Phys. IV **8** (7), 145 (1998).
24. J. T. Gudmundsson, T. Kimura, and M. A. Lieberman, Plasma Sources Sci. Technol. **8**, 22 (1999).

Translated by O. E. Khadin

Plasma Physics Reports, Vol. 27, No. 8, 2001, pp. 708–714. Translated from Fizika Plazmy, Vol. 27, No. 8, 2001, pp. 750–756.

LOW-TEMPERATURE PLASMA

Simulation of Ethylene Conversion Initiated by a Streamer Corona in an Air Flow

E. A. Filimonova and R. Kh. Amirov

Associated Institute of High Temperatures, Russian Academy of Sciences, Izhorskaya ul. 13/19, Moscow, 127412 Russia

Received December 8, 2000

Abstract—The conversion of ethylene (C_2H_4) at concentrations of 400 and 930 ppm in an air flow at a temperature of 295 K is simulated. Ethylene is added to air either upstream of the discharge chamber or in the reaction tube, downstream of a pulsed corona discharge. It is taken into account that the distribution of the gas components in the discharge zone is nonuniform due to the streamer nature of the discharge. In the reaction tube, all of the components are assumed to be uniform. Simulation results agree with the experiments carried out at voltage pulse amplitudes of 30 and 40 kV, a gas flow rate of 2–10 l/min, and a specific energy deposition of up to 0.15 J/cm^3. It is shown that the ozone produced plays a governing role in the C_2H_4 conversion. It is found that it is possible to minimize the energy spent on conversion by choosing the optimum pulse repetition rate and the specific energy deposited per pulse. The presence of water vapor impedes the ethylene conversion and increases the concentration of formaldehyde and methane. © *2001 MAIK "Nauka/Interperiodica".*

1. INTRODUCTION

Current interest in the conversion of hydrocarbons with the help of nonequilibrium plasmas is related, on one hand, to the problem of decreasing their concentration in diesel engine exhaust and, on the other hand, to the influence of hydrocarbons on the decomposition of nitrogen oxides.

The conversion of hydrocarbons in a barrier or streamer discharge was studied experimentally in [1–5]. The results from simulations [6] of the conversion of some hydrocarbons (including ethylene, which is one of the constituents of diesel engine exhaust) in a barrier discharge are in reasonable agreement with the experimental data. In [6], ethylene was assumed to be oxidized by an OH radical via the production of an activated complex and the rate constants for the reactions of the further ethylene conversion were estimated. However, ozone was not considered to be a reagent, although it was shown experimentally [1, 7] that O_3 plays a governing role in the conversion of a number of volatile organic compounds, including ethylene.

Interest in ethylene oxidation kinetics stems from the following. Ethylene is one of the simplest hydrocarbons, and its oxidation exhibits features typical of the oxidation of unsaturated hydrocarbons. For example, in the production of soot, ethylene is an intermediate reagent in the process of decomposition of more complex hydrocarbons. It is also a key agent in the photochemical production of urban smog. The mechanism for C_2H_4 conversion depends substantially on the temperature, pressure, and composition of the bulk gas and the impurity composition [2, 8–11].

This paper is devoted to simulations of the removal of ethylene from air with the help of a nanosecond streamer corona discharge. The experimental data are taken from [7].

2. EXPERIMENTAL SETUP

Experiments on the removal of ethylene from air were performed at the Institute for Environmental Protection Technology (Berlin, Germany). The experimental setup is described in [1, 7]. Air at atmospheric pressure and room temperature was pumped through a reactor, which consisted of a discharge chamber and reaction tube. The gas composition was analyzed after leaving the reaction tube. The discharge chamber was a 900-mm-long metal cylinder with an inner diameter of 100 mm. Voltage pulses were applied to a 2-mm-diameter wire electrode located at the cylinder axis. The reaction tube volume was 3.77 l. The energy deposition in the streamer corona was varied by changing the repetition rate f of nanosecond pulses from 1.1 to 26 Hz at a constant voltage pulse amplitude. The maximum value of the specific energy deposition W was 0.15 J/cm^3 (42 W h m^{-3}).

Three series of experiments were carried out. In the first series, the direct and indirect methods for treating synthetic air (20.5% of O_2 in N_2) at a constant gas flow rate were compared in regard to the ethylene removal efficiency. When treating air directly, ethylene was added to the air before entering the discharge chamber. When treating air indirectly, ethylene was added to the air after passing through the discharge chamber, just upstream of the reaction tube. The voltage pulse amplitude was 30 kV. In the second series of experiments, the efficiency of ethylene removal from synthetic air via direct treatment was studied as a function of the gas flow rate at a constant voltage pulse amplitude of 40 kV.

1063-780X/01/2708-0708$21.00 © 2001 MAIK "Nauka/Interperiodica"

In the third series of experiments, the removal of ethylene from room air was studied under the same conditions.

3. SIMULATION OF ETHYLENE CONVERSION

Numerical simulations of ethylene removal are based on an approximate mathematical model for cleaning gas of toxic additives using a pulsed streamer discharge [12–15]. The model takes into account that the distribution of gas components in the discharge chamber is nonuniform because of the production of active particles in the streamer channels. Calculations were performed for a sequence of pulses. After each pulse, the change in the gas composition caused by chemical reactions and diffusion processes inside and outside the streamer channel was examined. The gas composition at the outlet of the discharge chamber was taken as the initial composition in simulations of chemical kinetics in the reaction tube. The distribution of gas components in the reaction tube was assumed to be uniform. The RADICAL numerical code [12, 13, 16] and a chemical kinetics code developed by M.B. Zheleznyak and E.A. Filimonova [16] were employed to model the processes in the discharge chamber and reaction tube, respectively. Simulations incorporated 179 components and 881 reactions.

In simulations, we used the following experimental data: the energy deposited in the gas in the discharge chamber (both per pulse W_{dc} and total W), the discharge pulse repetition rate f, the gas flow rate Q, and the volumes of the discharge chamber and reaction tube. We specified the streamer radius (according to calculations [17]); the specific energy deposited in the streamer W_{st}; its fraction q spent on the production of active particles; and the parameter $F_0 = W_{dc}/W_{st}$, which determines the volume fraction of the discharge chamber occupied by streamers immediately after the end of the current pulse. The parameter q, which depends on the discharge conditions, implicitly accounts for the deviation of the effective electric field from the theoretical value, the mutual influence of the streamers, etc. It was set so as to match the results of calculations to the experimental data. The value of q was assumed to be independent of the species and concentration of the toxic additive and, for a given gas composition, independent of the pulse repetition rate and gas flow rate.

The densities of active particles immediately after the discharge pulse are determined by formula

$$n_i = \frac{\sum_j G_{ij} x_j w_{st}}{100}, \qquad (1)$$

where n_i is the density of the ith component, which is produced in collisions between the molecules of the jth component of the bulk gas with electrons; x_j is the mole fraction of the jth component; $w_{st} = qW_{st}$ is the specific energy spent on the production of active particles; and G_{ij} are the G factors, which determine the number of particles of the ith species produced from the molecules of the jth species per 100 eV of energy deposited in the gas. The G factors depend on the electric field E at the streamer head and the gas composition. They were taken from [17, 18] for E = 100 kV/cm, which is characteristic of a streamer discharge in air [17], and were recalculated taking into account the gas molar composition.

The variations in the concentrations of the gas components due to chemical reactions and diffusion inside and outside the streamer channel were determined by solving the set of ordinary differential equations [12–15]. The densities calculated by formula (1) were taken as the initial conditions.

4. RESULTS AND DISCUSSION

4.1 Comparison of the Direct and Indirect Methods for Treating Synthetic Air

The simulated dependences of the ethylene removal efficiency (with allowance for chemical processes in the reaction tube) on the specific deposited energy W are shown in Fig. 1. The figure also shows the experimental data from [7]. Each point (both experimental and simulated) corresponds to a certain repetition rate within the 1.79- to 11.13-Hz range and the specific energy deposition $W_{dc} = (1.9–3.5) \times 10^{-5}$ J/cm^3. The initial ethylene concentration $[C_2H_4]_0$ was 400 ppm; for both direct and indirect treating, the gas flow rate was Q = 2 l/min. The simulation results are in good agreement with the experiment. The gas stays in the discharge chamber and reaction tube for 212 and 113 s, respectively. It can be seen in Fig. 1 that the ethylene removal efficiency is higher when ethylene is prelimi-

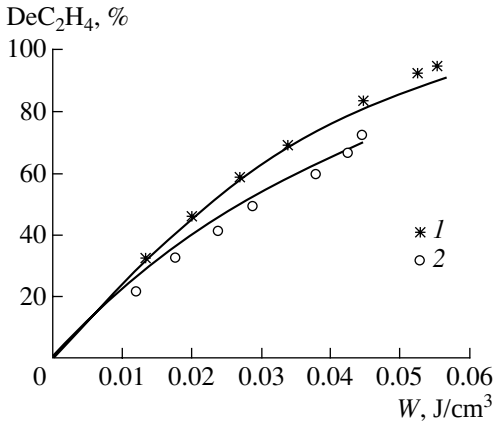

Fig. 1. Degree of ethylene removal vs. specific energy deposition for (*1*) direct and (*2*) indirect treating of synthetic air at a voltage pulse amplitude of 30 kV and gas flow rate of 2 l/min. The curves and symbols show the simulation and experimental results, respectively.

Initial densities of active particles in the streamer

No.	Component	Density, cm^{-3}
1	O	2.25×10^{14}
2	O_2 ($^1\Delta$)	2.15×10^{13}
3	N	8.43×10^{13}
4	O_2^+	3.00×10^{13}
5	e	1.31×10^{14}
6	O(^{1}D)	1.34×10^{14}
7	N^+	7.93×10^{12}
8	N_2^+	9.32×10^{13}
9	N_2^*	3.74×10^{14}
10	N(^{2}D)	7.93×10^{11}
11	N(^{2}P)	3.97×10^{11}

narily treated in the discharge chamber. For a degree of ethylene removal of 90%, the energy spent on the decomposition of one C_2H_4 molecule is about 40 eV.

When modeling these experiments, it was assumed that all of the specific energy W_{st} deposited in the streamer was spent on the production of active particles; i.e., $q = 1$. In simulations, W_{st} was set at 0.002 J/cm^3. The initial densities of active particles calculated by formula (1) are shown in the table.

The main reactions governing the ethylene conversion in the discharge chamber after the first and 380th discharge pulse at $f = 1.79$ Hz, $W_{dc} = 3.5 \times 10^{-5}$ J/cm^3, and $W = 0.0133$ J/cm^3 are presented in diagrams in Fig. 2. In both diagrams, there is a horizontal separating string that indicates the sign of the time derivative of the ethylene density. The main reactions (numbered as in the full list of reactions) that lead to ethylene production or loss are listed above and below this string, respectively. Arrows show the directions of the processes. The reactions are arranged in descending order of their integral contribution, which is shown in the right column in cm^{-3}. The resultant change in the ethylene density is shown at the right end of the separating string. The numerals in the central parts of the diagrams show the time evolution of the reaction ratings. The minus sign indicates that the rating is the same as at the previous instant; a blank means that the rating is lower than a certain threshold value. The rating is determined by the absolute value of the time derivative of the density of the corresponding component due to its production or loss at a given instant. The time scale and the ethylene density are given at the bottom and top of each diagram, respectively. Because of limited space, we do not present here the data on the other reactions incorporated in the model.

It is seen in Fig. 2 that the reactions involving oxygen atoms are the most important in the initial phase of the diffusive expansion of the streamer channel during a time of up to 10^{-3} s (reaction nos. 237 and 206). Within the time interval 10^{-3}–1 s, the reaction with ozone (no. 875) is dominant. The rating of this reaction changes with time: from 7 after the first pulse to 3 after the 380th pulse. The rate constants of the reactions governing ethylene removal were taken as follows:

$$O + C_2H_4 \Rightarrow CHO + CH_3,$$

$$k = 3.45 \times 10^{-18} T^{2.08} \text{ cm}^3/\text{s [19]},$$

$$O + C_2H_4 \Rightarrow CH_2CHO + H,$$

$$k = 2.0 \times 10^{-18} T^{2.08} \text{ cm}^3/\text{s [20]},$$

$$O_3 + C_2H_4 \Rightarrow \text{products},$$

$$k = 1.2 \times 10^{-14} \exp(-2630/T) \text{ cm}^3/\text{s [21]}.$$

The time evolutions of the densities of some components are plotted in Fig. 3. The ethylene density has a feeble minimum due to the diffusive expansion of the streamer channel and changes only slightly during one pulse. In the reaction tube, the main reaction is the reaction with ozone, which is produced in the discharge chamber and does not react there. Thus, at $f = 11.13$ Hz and $W_{dc} = 3.5 \times 10^{-5}$ J/cm^3, the ethylene concentration decreases from 400 ppm to 136 ppm in the discharge chamber and to 88 ppm downstream of the reaction tube.

Simulations show (Fig. 4) that the ethylene concentration after the discharge chamber and before the reaction tube is determined not only by the total energy deposition but also the energy deposited per pulse, the pulse repetition rate, and the duration of air treatment. When treating air directly, the decrease in the pulse repetition rate and the increase in the time during which air stays in the discharge chamber (i.e., the increase in the effective length of the chamber) stimulate ethylene conversion in the discharge chamber. The circles in Fig. 4 show the final value of the ethylene concentration after treating air in the reaction tube.

A comparison of curves *2* and *4* in Fig. 4 shows that, for the same total energy deposition $W = 0.0133$ J/cm^3 and the same energy W_{dc} deposited per pulse, the conversion efficiency in the discharge chamber is higher for a lower repetition rate. Thus, at a repetition rate of $f = 1.79$ Hz (mode *2*), the decrease in the ethylene concentration in the discharge chamber is larger than that at $f = 11.13$ Hz (mode *4*) by 55 ppm. However, the amount of ozone produced in mode *4* is larger; as a result, the resultant degree of ethylene conversion downstream of the reaction tube in mode *2* is higher than that in mode *4* by only 2.5%. The reason for this is that ozone begins to be produced with a certain delay after the current pulse; hence, it starts to actively react with ethylene only at the end of the pause between the pulses (see Figs. 2, 3). The longer the pause between the pulses (i.e., lesser the repetition rate *f*), the larger the number of ozone molecules that react with C_2H_4.

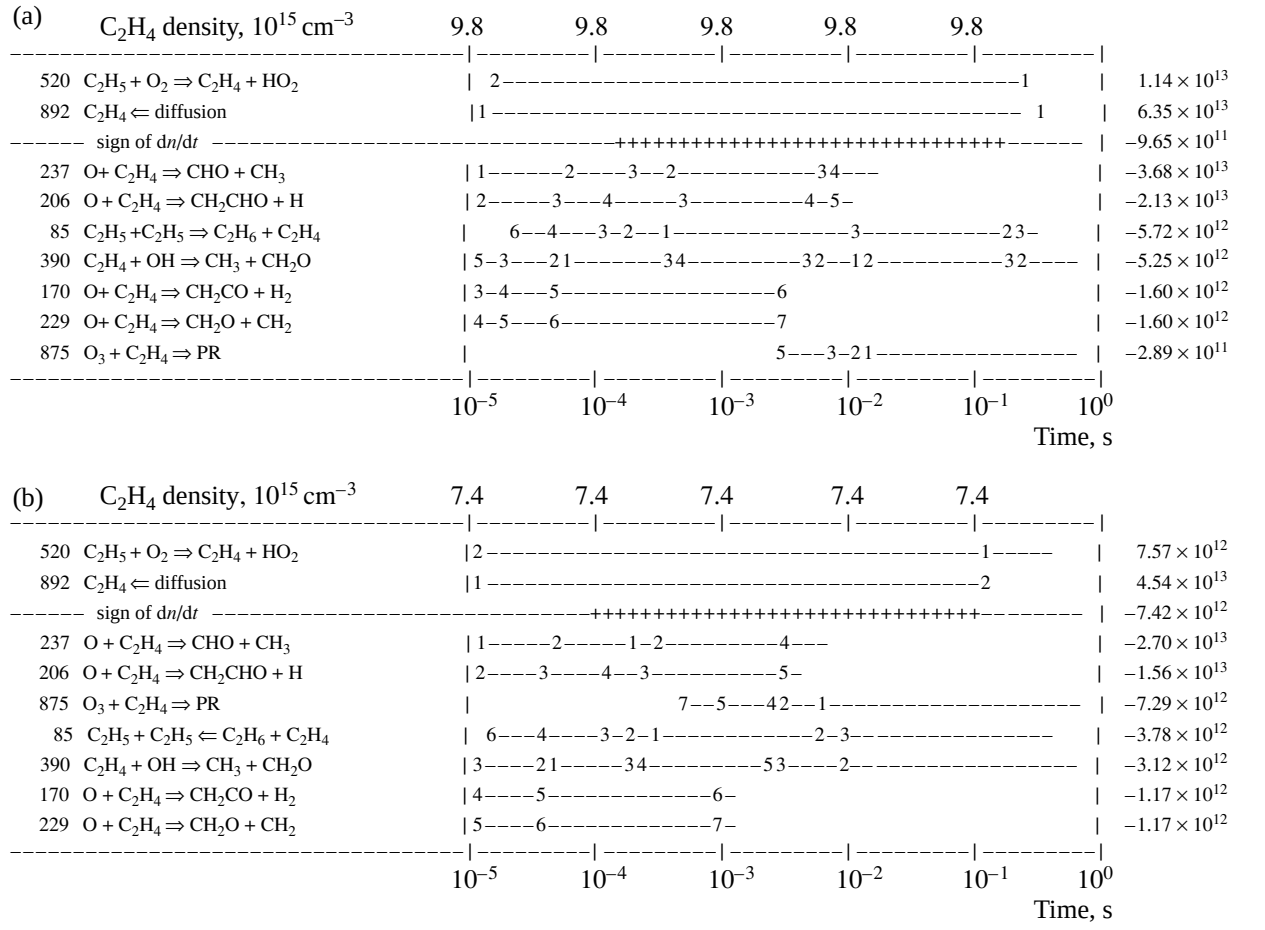

Fig. 2. Main reactions governing ethylene conversion in the discharge chamber after (a) the first and (b) 380th discharge for f = 1.79 Hz, $W_{dc} = 3.5 \times 10^{-5}$ J/cm^3, and $W = 0.0133$ J/cm^3.

For the same repetition rate and a fixed value of W, it is preferable to decrease the energy deposited per pulse and increase the duration of gas treatment. This is seen from the comparison of curves *3* and *4* in Fig. 4 for $W = 0.0566$ J/cm^3 and $f = 11.13$ Hz. At $W_{dc} = 2.4 \times 10^{-5}$ J/cm^3 (mode *3*), the decrease in the ethylene concentration in the discharge chamber is higher than that at $W_{dc} = 3.5 \times 10^{-5}$ J/cm^3 (mode *4*) by 30 ppm. Again, since the amount of ozone produced in mode *4* is larger, the resultant degree of ethylene conversion downstream of the reaction tube in mode *3* is higher than that in mode *4* by only 3%. The reason for this is that the number of pulses in mode *3* is larger than in mode *4* (2360 and 1586, respectively) and the rate at which active particles are produced increases from pulse to pulse.

We note that, in simulations, not only the energy deposited per pulse, but also the volume fraction occupied by streamers is larger for mode *4* [15]. In principle, this stimulates the conversion process in the discharge chamber. Thus, for $W_{dc} = 3.5 \times 10^{-5}$ J/cm^3 (mode *4*), we have $F_0 = 0.0175$, whereas for $W_{dc} = 2.4 \times 10^{-5}$ J/cm^3 (mode *3*), we have $F_0 = 0.012$. However, this factor has a smaller effect on the conversion efficiency than the increase in the number of pulses at a constant repetition rate.

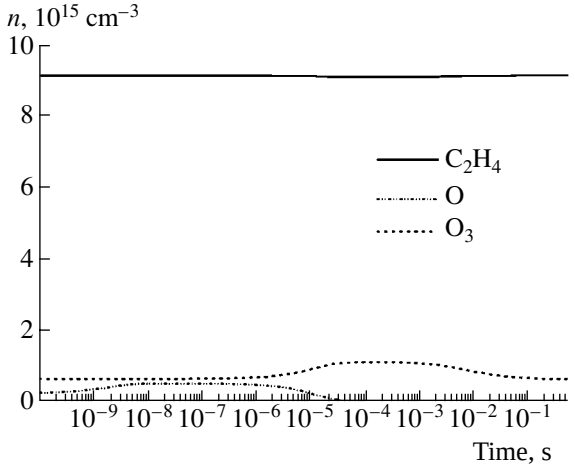

Fig. 3. Densities of the components vs. time after the 151th discharge at $W = 0.0053$ J/cm^3, the other parameters being the same as in Fig. 2.

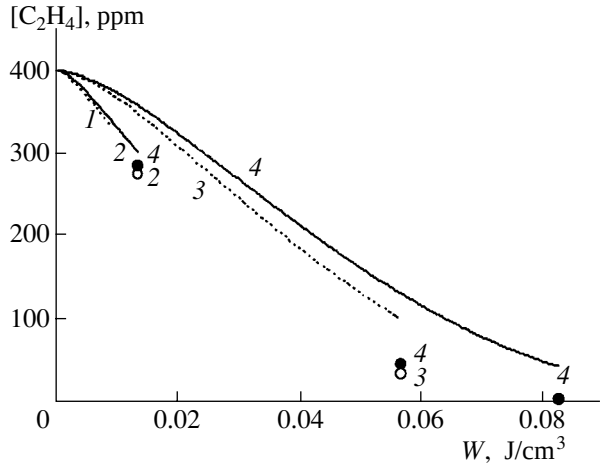

Fig. 4. Simulated ethylene concentration vs. specific energy deposition under different conditions: (*1*) f = 1.79 Hz and $W_{dc} = 2.4 \times 10^{-5}$ J/cm^3, (*2*) f = 1.79 Hz and $W_{dc} = 3.5 \times 10^{-5}$ J/cm^3, (*3*) f = 11.13 Hz and $W_{dc} = 2.4 \times 10^{-5}$ J/cm^3, and (*4*) f = 11.13 Hz and $W_{dc} = 3.5 \times 10^{-5}$ J/cm^3. The curves and the circles show the simulated concentrations in the discharge chamber and downstream of the reaction tube, respectively. Conditions *2* and *3* are the same as in experiment.

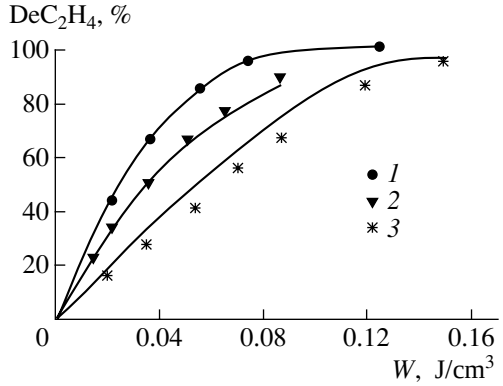

Fig. 5. Degree of ethylene removal from synthetic air vs. specific energy deposition for (*1*) Q = 2 l/min and $[C_2H_4]_0$ = 400 ppm, (*2*) Q = 5 l/min and $[C_2H_4]_0$ = 400 ppm, and (*3*) Q = 2 l/min and $[C_2H_4]_0$ = 934 ppm. The voltage pulse amplitude is 40 kV. The curves and symbols show the simulation and experimental results, respectively.

In experiment [7], the value of W_{dc} was fairly large (larger than in many experiments with corona streamer discharges). Consequently, the volume fraction occupied by streamers was also high, which means that the experimental conditions of [7] were not optimum for ethylene conversion (providing that conversion occurs in the discharge chamber only).

This is not the case for indirect treating because the ozone production in the discharge chamber is independent of both f and W_{dc} and depends only on the total energy deposition W (e.g., for W = 0.045 J/cm^3, the ozone concentration amounts to 425 ppm). In the discharge chamber, only ozone is produced; i.e., the discharge chamber acts as an ozonizer and O_3 reacts with ethylene only in the reaction tube.

4.2. Efficiency of Ethylene Removal from Synthetic Air as a Function of the Gas Flow Rate and Initial Ethylene Concentration

The data on the ethylene removal efficiency for different gas flow rates and initial concentrations of C_2H_4 are presented in Fig. 5. Experiments were carried out at a voltage pulse amplitude of 40 kV. In this series of simulations, we set q = 0.85 and $w_{st} = 0.85 \times W_{st}$; consequently, the concentration of active particles amounted to 85% of the previous value. Such an approach was previously used in [12–17]. Each experimental point corresponds to a certain pulse repetition rate at a nearly constant deposited energy of $W_{dc} = 9 \times 10^{-5}$ J/cm^3. For an initial concentration of $[C_2H_4]_0$ = 400 ppm, the repetition rate varied from 1.1 to 6.42 Hz for a gas flow rate of Q = 2 l/min and from 1.81 to 12.5 Hz for Q = 5 l/min. For $[C_2H_4]_0$ = 934 ppm, the repetition rate varied from 1.1 to 8.3 Hz. The lower energy deposition W corresponded to the lower repetition rate.

In both simulations and experiments, for an intermediate energy deposition of W = 0.04–0.09 J/cm^3, the degree of ethylene conversion at Q = 2 l/min was higher than at Q = 5 l/min by 15%. This is related to the different repetition rates f (and, therefore, different durations of gas treatment between the pulses) and different times during which the gas stays in the reaction tube: 113 s for Q = 2 l/min and 45 s for Q = 5 l/min.

It can be seen in Fig. 5 that, under the above parameters, simulations are in reasonable agreement with the experiment.

4.3 Efficiency of Ethylene Removal from Room Air as a Function of the Gas Flow Rate

Both simulations and experiments were carried out under the same conditions as for synthetic air (see Section 4.2). According to the measurements of the dew point, the concentration of water vapor in air was approximately 0.45%. The simulation results for $[C_2H_4]_0$ = 400 ppm and Q = 2, 5, and 10 l/min are shown in Fig. 6. As in the case of synthetic air, for Q = 2 and 5 l/min, agreement between the simulations and experiment is good, whereas for Q = 10 l/min, it is worse. It is experimentally shown that ozone production is linearly proportional to the gas flow rate and decreases as the water content in air (both room and synthetic) increases in the absence of ethylene. This behavior is more pronounced at a voltage pulse amplitude of 30 kV than at 40 kV. The production of ozone at Q = 10 l/min exceeds that at Q = 2 l/min by 15%. This difference,

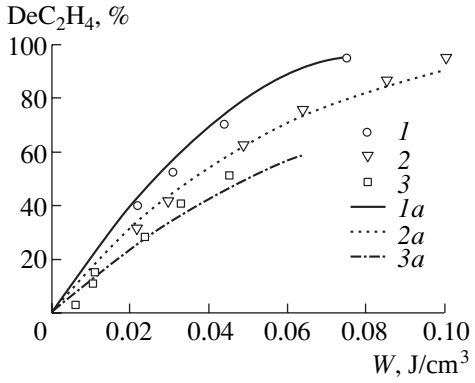

Fig. 6. Degree of ethylene removal from room air vs. specific energy deposition for Q = (*1*, *1a*) 2, (*2*, *2a*) 5, and (*3*, *3a*) 10 l/min at $[C_2H_4]_0$ = 400 ppm and a voltage pulse amplitude of 40 kV. The curves and symbols show the simulation and experimental results, respectively.

which is possibly related to the wall effect, was not taken into account in the simulations.

In the presence of water vapor in the discharge chamber, the reaction of ethylene with hydroxyl (reaction no. 390 in Fig. 2, $k = 3.32 \times 10^{-12}\exp(-483/T)$ cm^3/s [8]) becomes more important. Downstream of the discharge chamber, a decrease in the ethylene concentration is more pronounced than in the case of synthetic air. On the other hand, the presence of hydroxyl radicals reduces the oxygen atom density and impedes ozone production; as a result, the role of the reaction tube decreases. With this tube, under the same conditions, the degree of ethylene removal from room air is lower than that from synthetic air by 2–4% over the entire range of Q under study. At Q = 2 l/min, the energy spent on the conversion of one ethylene molecule is about 50 eV at a conversion efficiency of 90%. Moreover, an additional amount of formaldehyde and methane is produced; their concentrations increase by a factor of 2 as compared to the case of synthetic air and attain 40–50 ppm. The substitution of one toxic component with another (e.g., with unreacted ozone) makes it necessary to determine the total gas toxicity before and after treatment.

5. CONCLUSION

The removal of ethylene from air is simulated under different conditions of the excitation of a pulsed corona discharge. Simulation results are in good agreement with the experiment. Simulations show that it is possible to increase the removal efficiency at a constant total energy deposition by choosing the optimum pulse repetition rate and the energy deposited per discharge pulse and by using a reaction tube placed downstream of the discharge chamber.

It is shown that the removal of ethylene from air is related to the synthesis of ozone, whose concentration in the discharge chamber increases from pulse to pulse. Between the discharge pulses, the ozone concentration in the streamer channel reaches its maximum 10^{-4}–10^{-2} s after the discharge. If the repetition period is longer than this time, then most of the produced ozone has enough time to react with ethylene between the discharge pulses. In the presence of water vapor, the ethylene concentration decreases in reactions with hydroxyl; however, in this case, the concentrations of formaldehyde and methane increase. At Q = 2 l/min, the energy spent on the conversion of one ethylene molecule is ~40 and ~50 eV for voltage pulse amplitudes of 30 and 40 kV, respectively. The dependence of the ethylene removal efficiency on the gas flow rate at a constant energy deposition is related to the different pulse repetition rates and different times during which the gas stays in the reaction tube.

The ozone produced that has not reacted with ethylene in the discharge chamber acts to decrease the ethylene concentration in the reaction tube, thus increasing the overall efficiency of ethylene removal and decreasing the energy spent on the conversion of one ethylene molecule. The rate constant of the reaction between ozone and C_2H_4 is low; hence, an important role is played by the time during which they interact. The same is true for the removal of nitrogen oxides from air with the help of a barrier discharge [22]. For other toxic additives (such as formaldehyde), only the processes in the discharge chamber are important because, in this case, the main reactions are those with hydroxyl and atomic oxygen [15, 22].

ACKNOWLEDGMENTS

We are grateful to R. Rudolph and K.-P. Francke for providing us with the experimental data and for fruitful discussions.

REFERENCES

1. K.-P. Francke and R. Rudolph, in *Proceedings of the XII International Conference on Gas Discharges and Their Applications, Greifswald, 1997*, Vol. 1, p. 397.
2. S. Broer, Th. Hammer, and T. Kishimoto, in *Proceedings of the XII International Conference on Gas Discharges and Their Applications, Greifswald, 1997*, Vol. 1, pp. 188, 192.
3. W. Niessen, O. Wolf, R. Schruft, and M. Neiger, J. Phys. D **31**, 542 (1998).
4. J. Chae, S. Moon, H. Sun, *et al.*, in *Proceedings 14th International Symposium on Plasma Chemistry, Prague, 1999*, p. 2587.
5. R. H. Amirov, E. I. Asinovsky, I. S. Samoilov, and A. V. Shepelin, in *Proceedings of the 2nd International Conference on Applied Electrostatics, Beijing, 1993.*
6. B. M. Zlotopol'skiĭ and T. S. Smolenskaya, Khim. Fiz. **16** (8), 105 (1997).
7. K.-P. Francke and R. Rudolph, *Nichtthermischer Plasmareaktor zum Abbau fluchtiger Kohlenwasserstoffe aus industriellen Prozessgasen*, Projekt der Deutschen Bundesstiftung Umwelt, 1996–1999.

8. M. Bartels, K. Hoyermann, and R. Sievert, in *Proceedings of the 19th International Symposium on Combustion, Combustion Institute, 1982*, p. 61.
9. C. K. Westbrook, F. L. Dryer, and K. P. Schug, in *Proceedings of the 19th International Symposium on Combustion, Combustion Institute, 1982*, p. 153.
10. R. Atkinson, J. Phys. Chem. Ref. Data **26**, 215 (1997).
11. J. J. Orlando, G. S. Tyndall, M. Bilde, *et al.*, J. Phys. Chem. A **102**, 8116 (1998).
12. M. B. Zheleznyak and E. A. Filimonova, Teplofiz. Vys. Temp. **36**, 374 (1998).
13. M. B. Zheleznyak and E. A. Filimonova, Teplofiz. Vys. Temp. **36**, 557 (1998).
14. R. Kh. Amirov, Yu. N. Desyaterik, M. B. Zheleznyak, *et al.*, Fiz. Plazmy **24**, 1141 (1998) [Plasma Phys. Rep. **24**, 1066 (1998)].
15. E. A. Filimonova, R. H. Amirov, H. T. Kim, and I. H. Park, J. Phys. D **33**, 1716 (2000).
16. R. Kh. Amirov, M. B. Zheleznyak, and E. A. Filimonova, Preprint No. 1-403 (Joint Institute for High Temperatures, Russian Academy of Sciences, Moscow, 1997).
17. N. Yu. Babaeva and G. V. Naidis, IEEE Trans. Plasma Sci. **26**, 41 (1998).
18. B. M. Penetrante, in *Non-Thermal Plasma Techniques for Pollution Control*, Ed. by B. M. Penetrante and S. E. Schultheis (Springer-Verlag, Berlin, 1993); NATO ASI Ser., Ser. G **34**, 65 (1993).
19. Y. L. M. Creyghton, E. M. van Veldhuizen, and W. R. Rutgers, in *Non-Thermal Plasma Techniques for Pollution Control*, Ed. by B. M. Penetrante and S. E. Schultheis (Springer-Verlag, Berlin, 1993); NATO ASI Ser., Ser. G **34**, 205 (1993).
20. D. L. Baulch, D. J. Cobos, R. A. Cox, *et al.*, J. Phys. Chem. Ref. Data **21**, 411 (1992).
21. R. Atkinson, D. L. Baulch, R. A. Cox, *et al.*, J. Phys. Chem. Ref. Data **21**, 1125 (1992).
22. E. A. Filimonova, R. Kh. Amirov, H. T. Kim, and I. H. Park, Khim. Fiz. **19** (9), 72 (2000).

Translated by N. N. Ustinovskiĭ

Plasma Physics Reports, Vol. 27, No. 8, 2001, pp. 715–725. Translated from Fizika Plazmy, Vol. 27, No. 8, 2001, pp. 757–768.

LOW-TEMPERATURE PLASMA

Combustion of Methane–Oxygen and Methane–Oxygen–CFC Mixtures Initiated by a High-Current Slipping Surface Discharge

I. A. Kossyĭ, V. P. Silakov, and N. M. Tarasova

Institute of General Physics, Russian Academy of Sciences, ul. Vavilova 38, Moscow, 119991 Russia

Received December 27, 2000

Abstract—Results are presented from experimental studies of the destruction of chlorofluorocarbon (CF_2Cl_2) molecules in a methane–oxygen (air) gas mixture whose combustion is initiated by a high-current slipping surface discharge. It is found that a three-component $CH_4 + O_2$(air)+ CF_2Cl_2 gas mixture (even with a considerable amount of the third component) demonstrates properties of explosive combustion involving chain reactions that are typical of two-component $CH_4 + O_2$ mixtures. Experiments show the high degree of destruction (almost complete decomposition) of chlorofluorocarbons contained in the mixture during one combustion event. The combustion dynamics is studied. It is shown that the combustion initiated by a slipping surface discharge has a number of characteristic features that make it impossible to identify the combustion dynamics with the formation of a combustion or detonation wave. The features of the effects observed can be related to intense UV radiation produced by a pulsed high-current surface discharge. © *2001 MAIK "Nauka/Interperiodica".*

1. INTRODUCTION

At present, the problem of the destruction of chlorine- and/or fluorine-containing materials attracts much attention because these chemical compounds play a major detimental role in worldwide ecology. Here, we should mention, first of all, chlorofluorocarbons (CFCs), which destroy the Earth's ozone layer (e.g., CF_2Cl_2 and $CFCl_3$); compounds capable of contributing to the greenhouse effect (such as CF_4); poison gases accumulated in a number of countries; etc.

The above compounds are usually destroyed in high-temperature furnaces. However, successful attempts have recently been made to use *thermally nonequilibrium* plasma chemistry to solve this problem. For example, in [1], results are presented on the CFC decomposition in pulsed discharges excited by high-power microwave beams. In [2], data are reported on the plasmochemical destruction of CFCs by a slipping surface discharge or a spark excited in a gaseous medium by a pulsed CO_2 laser.

Experiments were performed in nitrogen, argon, or air mixed with different chlorine- and fluorine-containing compounds. Experiments demonstrated a relatively high efficiency of the plasmochemical decomposition that was achieved at the cost of the electric energy expenditure only. The energy cost of decomposition is

$$W = Pt/M \approx 1 \text{ kW h/kg},$$

where P is the mean electric power consumption, t is the treatment time, and M is the mass of material treated. It follows from here that, for $P \simeq 1$ kW, the production rate of a plasmochemical reactor η is on the order of 1 kg/h.

This paper presents the results from experimental studies of the decomposition of chlorine- and fluorine-containing materials in a reactor in which the combustion in a methane–oxygen (air)–CFC mixture is initiated by an electric discharge. This experimental scheme was adopted because it makes it possible to substantially decrease the energy cost of plasmochemical destruction and increase the reactor production rate by utilizing chemical energy (i.e., the energy released during the combustion of the mixture).

2. EXPERIMENTAL SETUP

A schematic of the experimental setup is shown in Fig. 1. The reactor chamber (*1*) is a cylindrical quartz tube with a diameter of ≈ 50 mm and length L = 100–200 mm. The chamber is evacuated down to a pressure of $p_0 < 10^{-2}$ torr and filled with a $CH_4 + O_2$ (air) + CFC mixture at a pressure of $50 \le p \le 300$ torr. Combustion in this three-component gas mixture is initiated with the help of a multispark discharge system (*2*).

The multispark discharge system is a set of electrodes placed in a special way (see [3–6]) on a dielectric (quartz, Teflon, or ceramic) tube with a diameter of 6 mm. The length of the metal–dielectric cylindrical discharge chamber is ≈40 mm. The discharge system is located near one of the end flanges of the reactor chamber.

A high-voltage pulse applied to the electrodes initiates a high-current ($I \le$ 1–10 kA) low-threshold slipping discharge, which results in the formation of an extended plasma sheath around the surface.

1063-780X/01/2708-0715$21.00 © 2001 MAIK "Nauka/Interperiodica"

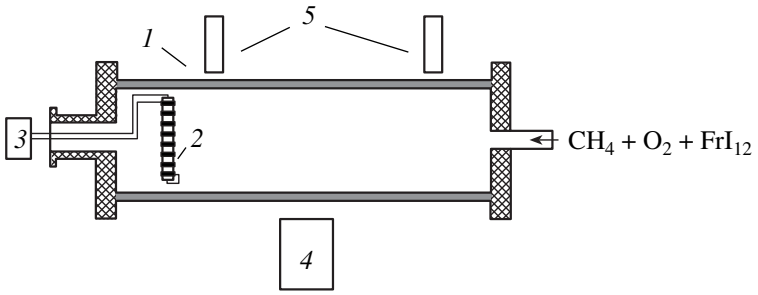

Fig. 1. Experimental setup: (*1*) reactor chamber, (*2*) multispark discharge system, (*3*) high-voltage source, (*4*) FER-7 streak camera, and (*5*) FEU-106 photomultipliers.

Such discharge systems have been widely used at the Institute of General Physics of the Russian Academy of Sciences to generate dense hot collisionless plasmas [3], produce metal plasmas [4], excite converging toroidal shock waves in gaseous media [5, 6], etc.

In this study, a discharge system based on a slipping surface discharge is used for the first time to initiate the combustion of a gas mixture.

The advantage of multielectrode metal–dielectric discharge systems [3–6] is that they can be used in almost any gas and gas mixtures over a wide range of pressures ($10^{-4} \le p \le 760$ torr) and can produce fairly dense plasma sheaths, which are the sources of intense UV radiation [7].

As sources of high-voltage pulses, we used two generators with the following pulse parameters:

(i) A low-energy G_1 generator with a pulse amplitude of $U \simeq 40$ kV, pulse duration of $\tau \simeq 40$ ns, and pulse energy of $E \le 0.2$ J.

(ii) A high-energy G_2 generator with $U \simeq 20$ kV, $\tau \simeq 20$ μs, and $E \le 30$ J.

Below, the operation mode with the use of the G_1 or G_2 generator will be referred to as the G_1 or G_2 mode, respectively.

The content of CFCs and their destruction products was measured from the absorption spectra of the gaseous phase with the help of a SPECORD M-80 infrared spectrometer. The gas samples were taken after combustion initiated by the multielectrode discharge system.

The time evolution of the reactor luminescence was studied with the help of an FER-7 (*4*) streak camera. The slit of the streak camera was oriented along the *Z*-axis of the chamber and its position was adjusted so that one of the discharge gaps was in the viewing field of the camera. The time characteristics of the luminescence integrated over the spectrum were measured with two FEU-106 photomultipliers (*5*); the light was fed to them through fibers positioned at different distances along the *Z*-axis of the reactor chamber (at distances of $Z_1 \le 1$ cm and $Z_2 = 8$ cm from the discharge system).

Pyrometric measurements of the temperature of the reactor chamber allowed us to estimate the temperature of the gaseous medium after combustion initiated by a slipping surface discharge.

3. EXPERIMENTAL RESULTS

The excitation of a pulsed slipping surface discharge near the end of the reactor is accompanied by gas combustion throughout the entire chamber volume. As a result, the chemical composition of the gas mixture changes substantially.

The table lists the characteristic compositions of three-component $CH_4 + O_2 + CF_2Cl_2$ mixtures in which explosive combustion can be initiated with discharges excited along the multielectrode system in the G_1 or G_2 mode. The table also presents the degree of CFC destruction produced by a single discharge initiating combustion (in the table, N_{CFC} is the density of destroyed CFC molecules and φ is the degree of destruction in percent).

As follows from the table, it is possible to initiate combustion accompanied by substantial (from 80 to 99%) decomposition of initial CFC molecules over a wide range of the total and partial pressures of the gas components in the initial mixture. Note that the degree of CFC decomposition depends only slightly on the energy released in a slipping surface discharge initiating combustion. The CFC content in the initial gas mixture is rather high: the partial CFC pressure ranges from 14 to 40% of the total pressure of the working mixture.

In spite of a substantial difference in the energy released in the discharge during the high-voltage pulse, the degree of CFC decomposition in the G_1 and G_2 modes is almost the same. On the other hand, the luminosity dynamics measured by the streak camera and photomultipliers changes significantly when passing over from the G_1 mode to the G_2 mode.

Figure 2 presents typical streak images obtained in the G_2 mode for different proportions of CH_4, O_2, and CF_2Cl_2 in the mixture. Figure 3 shows typical waveforms of the signals from two photomultipliers posi-

Table

Original mixture, torr	Mode	N_{CFC}, cm^{-3}	φ, %	Tube length *L*, cm
$CH_4 : O_2 : Fr_{12} = 30 : 60 : 60$	1	1.7×10^{18}	85	14 (quartz)
Same	2	1.67×10^{18}	83	Same
″	2	1.62×10^{18}	80	″
″	1	1.73×10^{18}	86	″
″	1	1.73×10^{18}	86	″
$CH_4 : O_2 : Fr_{12} = 30 : 60 : 15$	2	4.8×10^{17}	96	″
$CH_4 : O_2 : Fr_{12} = 30 : 60 : 60$	2	1.68×10^{18}	84	″
$CH_4 : O_2 : Fr_{12} = 60 : 60 : 60$	2	1.62×10^{18}	81	″
$CH_4 : O_2 : Fr_{12} = 60 : 120 : 60$	2	1.99×10^{18}	99.4	″
$CH_4 : O_2 : Fr_{12} = 60 : 120 : 90$	2	2.94×10^{18}	97.8	″
$CH_4 : O_2 : Fr_{12} = 60 : 120 : 120$	2	3.6×10^{18}	90	″
$CH_4 : O_2 : Fr_{12} = 60 : 120 : 60$	1	1.98×10^{18}	99	″
$CH_4 : O_2 : Fr_{12} = 60 : 120 : 60$	1	1.98×10^{18}	99	″
$CH_4 : O_2 : Fr_{12} = 30 : 60 : 30$	1	9.54×10^{17}	95.4	″
$CH_4 : O_2 : Fr_{12} = 30 : 60 : 45$	1	1.49×10^{18}	94.6	″
$CH_4 : O_2 : Fr_{12} = 30 : 60 : 60$	1	1.75×10^{18}	87.5	″
$CH_4 : O_2 : Fr_{12} = 15 : 30 : 9$	1	2.87×10^{17}	96	″
$CH_4 : O_2 : Fr_{12} = 15 : 30 : 9$	1	2.94×10^{17}	98	″
$CH_4 : O_2 : Fr_{12} = 15 : 30 : 9$	2	2.86×10^{17}	95.3	″
$CH_4 : O_2 : Fr_{12} = 30 : 60 : 60$	2	1.8×10^{18}	90	″
$CH_4 : O_2 : Fr_{12} = 30 : 60 : 30$	2	9.84×10^{17}	98.4	″
$CH_4 : O_2 : Fr_{12} = 15 : 30 : 15$	2	4.77×10^{17}	95.4	20 (glass)
$CH_4 : O_2 : Fr_{12} = 15 : 30 : 15$	2	4.76×10^{17}	95.2	Same
$CH_4 : O_2 : Fr_{12} = 15 : 30 : 15$	2	4.76×10^{17}	95.2	″
$CH_4 : O_2 : Fr_{12} = 15 : 30 : 15$	2	4.81×10^{17}	96	″
$CH_4 : O_2 : Fr_{12} = 60 : 120 : 30$	1	9.66×10^{17}	96.6	″
$CH_4 : O_2 : Fr_{12} = 60 : 120 : 30$	1	9.9×10^{17}	99	″
$CH_4 : air : Fr_{12} = 30 : 300 : 15$	2	4.6×10^{17}	92	14 (quartz)
$CH_4 : air : Fr_{12} = 15 : 150 : 7.5$	2	2.3×10^{17}	92	″

tioned on the reactor chamber axis (also obtained in the G_2 mode).

Typical streak images obtained with FER-7 in the G_1 mode and the corresponding waveforms of the photomultiplier signal are shown in Figs. 4 and 5.

The horizontal coordinate in the streak images corresponds to time, and the vertical coordinate corresponds to the spatial displacement along the *Z*-axis. The slit of the streak camera was oriented along the *Z*-axis and covered one of the discharge gaps. Thus, it was possible to trace the axial dynamics from the instant of discharge ignition to times substantially exceeding the discharge duration. A vertical strip in the left part of the image indicates the instant when the high-voltage pulse is switched on. A bright spot in the lower part of the strip shows the position of one of the discharge gaps of the discharge system. The viewing field of the streak camera extends to the opposite (free) end of the reactor chamber. It is seen in Fig. 2 that, when the discharge is excited by the G_2 generator, the combustion zone propagates from the discharge system to the chamber in the form of a glowing wave whose velocity varies in the range $v_z \simeq (2.5 – 5.0) \times 10^4$ cm/s depending on the CFC content in the mixture. This

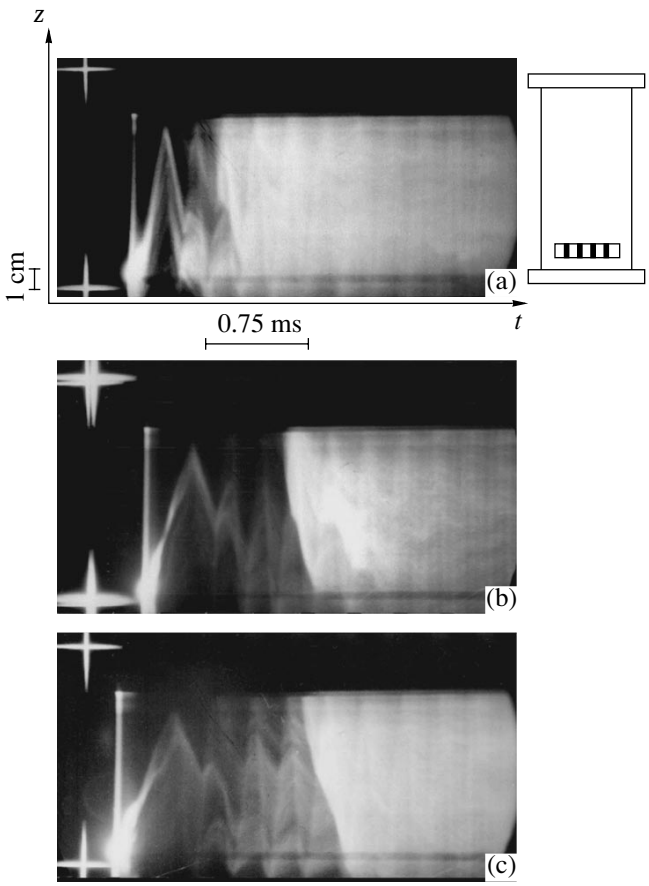

Fig. 2. Typical streak images obtained with FER-7 in the G_2 mode: (a) $CH_4 : O_2 : CF_2Cl_2 = 30 : 60 : 0$ torr, $\tau_d = 0$; (b) $CH_4 : O_2 : CF_2Cl_2 = 30 : 60 : 15$ torr, $\tau_d = 0$; and (c) $CH_4 : O_2 : CF_2Cl_2 = 30 : 60 : 30$ torr, $\tau_d = 0$ (τ_d is the delay time between the high-voltage pulse applied to the discharge system and the start of sweeping).

wave will be referred to as the primary wave. The glow of the gas mixture in this wave is observed in a narrow layer adjacent to the wave front.

It can be seen in Fig. 2 that the wave reaches the opposite end of the chamber, reflects from it, and then makes several oscillations related to the reflections from the opposite ends of the reactor chamber. Then, a secondary glow wave arises at the free end of the chamber and starts propagating toward the discharge system (Figs. 2b, 2c). The structure and propagation velocity of the secondary wave differ from those of the primary wave. The initial velocity of the secondary wave is much higher than that of the primary wave ($v_z \geq 2 \times 10^5$ cm/s). As the secondary wave approaches the discharge system, its velocity decreases to $v_z \approx 2 \times 10^4$ cm/s. Unlike the primary wave, the propagation of the secondary wave is accompanied by a relatively uniform glow throughout the entire reactor volume filled with a gas mixture under study. This allows us to conclude that the secondary wave gives rise to a uniform combustion of the gas mixture throughout the entire volume of the reactor chamber.

A flare that appears near the free end and gives rise to the volume combustion of the mixture also manifests itself in the waveforms of the photomultiplier signals shown in Fig. 3.

In both the streak images and the waveforms of the photomultiplier signals, glow oscillations associated with the waves propagating between the chamber ends are seen against the background of uniform combustion. The frequency of these oscillations depends only slightly on the mixture composition and is determined by the tube length. Thus, as the tube length decreases from $L_1 = 20$ cm to $L_2 = 13$ cm, the oscillation frequency increases from $f_1 = 2.2 \times 10^3$ Hz to $f_2 = 3.3 \times 10^3$ Hz, so that the relation $L_1 f_1 / L_2 f_2 \simeq 1$ holds.

In the G_1 mode, the dynamics of the mixture combustion is generally the same (Figs. 4, 5); in particular, the slipping surface discharge is accompanied by the appearance of a glow wave near the left (initiating) end of the chamber. This wave propagates toward the right (free) end of the chamber. After a certain time delay, the volume combustion begins and then occupies the entire reaction zone of the chamber. However, the combustion processes in the G_1 and G_2 modes differ quantitatively. Thus, the velocity of the primary wave in the G_1 mode is nearly one order of magnitude lower than that in the G_2 mode ($v_z \leq 3 \times 10^3$ cm/s) (Fig. 4a). Another characteristic feature of the combustion process in the G_1 mode is the generation of glow waves that follow the primary wave at nearly the same velocity toward the free end, but have a higher brightness and smaller front width and originate outside the discharge system at a certain distance ΔZ from it (Figs. 4a, 4b).

From a comparison of the waveforms of the photomultiplier signals in Figs. 3 and 5, it follows that the combustion time of the gas mixture depends substantially on the energy released in the initiating discharge (it decreases with the pulse energy). Thus, this time determined from the full width at half-maximum of the photomultiplier signal is equal to nearly $\Delta\tau \approx 11$ ms for the G_1 mode and G_2 – $\Delta\tau \approx 3$ ms for the G_2 mode.

Pyrometric measurements of the temperature of the reactor chamber allowed us to determine the temperature of the gaseous medium after combustion initiated by a slipping surface discharge. The temperature is on the order of 1000 K.

4. DISCUSSION OF THE EXPERIMENTAL RESULTS

Electric discharge is one of the most widely used tools for initiating the combustion of flammable gaseous mixtures (see, e.g., [8, 9]). As a rule, this is a low-power spark excited between two electrodes immersed in a flammable gaseous medium (as in an internal-com-

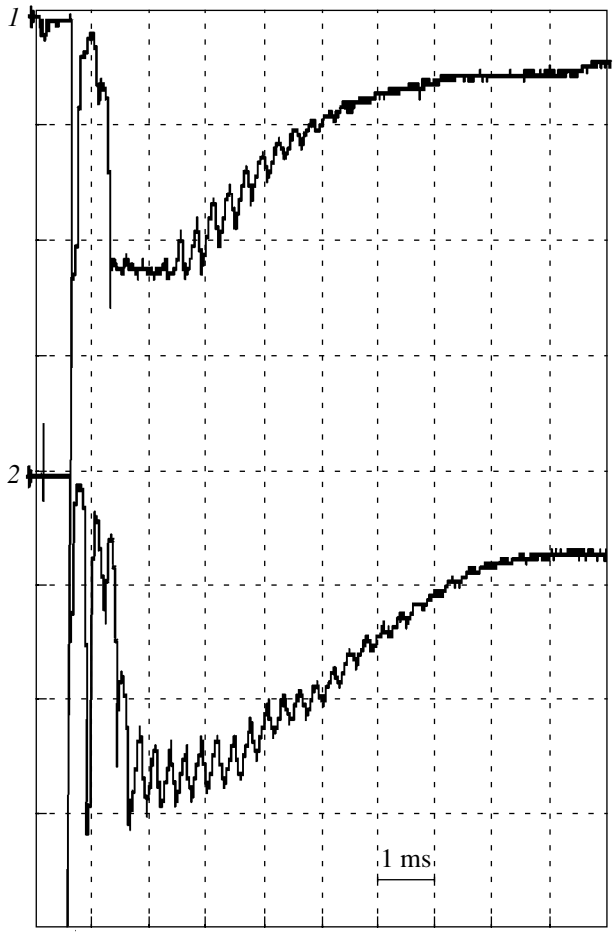

Fig. 3. Typical waveforms of the photomultiplier signals in the G_2 mode for $CH_4 : O_2 : CF_2Cl_2 = 30 : 60 : 15$ torr. The upper and lower curves are the signals from the photomultipliers positioned at distances of $Z_1 \le 1$ cm and $Z_2 = 8$ cm from the discharge system, respectively.

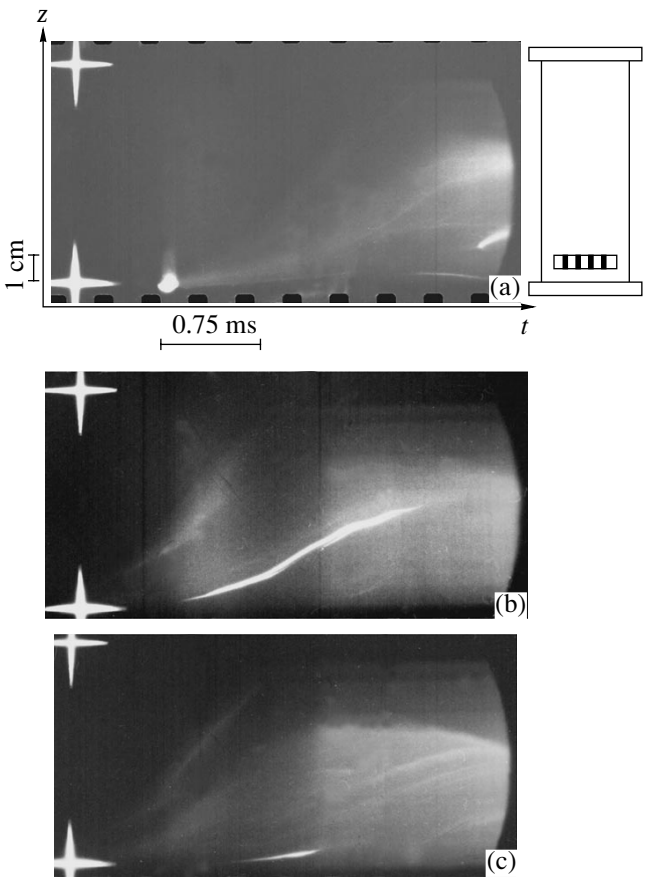

Fig. 4. Typical streak images obtained with FER-7 in the G_1 mode: (a) $CH_4 : O_2 : CF_2Cl_2 = 30 : 60 : 10$ torr, $\tau_d = 0$; (b) $CH_4 : O_2 : CF_2Cl_2 = 30 : 60 : 10$ torr, $\tau_d = 3.0$ ms; and (c) $CH_4 : O_2 : CF_2Cl_2 = 30 : 60 : 10$ torr, $\tau_d = 10.8$ ms (τ_d is the delay time between the high-voltage pulse applied to the discharge system and the start of sweeping).

bustion engine). In this study, instead of a spark, we use a high-current pulsed slipping surface discharge.

First of all, we note that the reactor glow, which is detected by a streak camera and photomultipliers, can certainly be ascribed to either the processes preceding the combustion of a gas mixture under study or the combustion itself. This is evidenced by the following observations:

(i) The characteristic rise time and lifetime of the glow last for ten milliseconds, which substantially exceeds the discharge duration in the multielectrode system (of about 0.5–5 μs) and the recombination time of the discharge plasma.

(ii) The prolonged afterglow exists only in a flammable gas mixture and is not detected, e.g., in argon, nitrogen, or oxygen.

Therefore, the observed behavior of the glow can be explained by neither the plasma propagation into the cylindrical chamber nor gasdynamic processes (a shock wave generated by the discharge).

The measurements of the reactor chamber luminescence reveal the following features that allow us to conclude that combustion initiated by a slipping surface discharge is of particular interest for the physics of combustion and explosion in gases.

The most interesting phenomenon in a *three-component* gas mixture is the high rate of the combustion reaction. Two-component flammable mixtures (such as a methane–oxygen mixture) were studied in detail, e.g., in [8, 10, 11]. The ignition of a methane–oxygen mixture (which is characterized by an explosive energy release) is related to chain branching processes described by the well-known reaction scheme.

With an addition of CFCs as a third component at a partial pressure comparable with the methane and oxygen (air) pressures, the realization of the chain process

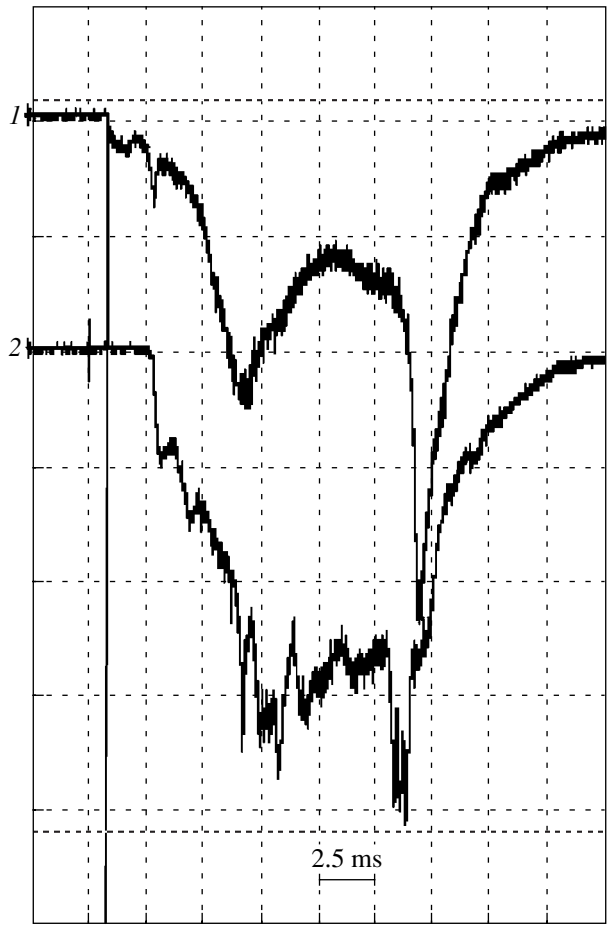

Fig. 5. Typical waveforms of the photomultiplier signals in the G_1 mode for $CH_4 : O_2 : CF_2Cl_2 = 30 : 60 : 15$ torr. The upper and lower curves are the signals from the photomultipliers positioned at distances of $Z_1 \le 1$ cm and $Z_2 = 8$ cm from the discharge system, respectively.

becomes problematic, because the presence of a considerable amount of chlorine- and fluorine-containing molecules can suppress the chain interactions between the constituents of the two-component methane–oxygen mixture.[1] Nevertheless, as follows from our experiments, the chain combustion process occurs even in the presence of the CFC (chlorine- and fluorine-containing) component.

Hence, the new result is that the combustion of a three-component methane–oxygen–CFC mixture is a fast process.

From a physical standpoint, the time evolution of the combustion initiated by a pulsed slipping surface discharge is of considerable interest. When operating in the G_1 or G_2 mode, the combustion of the gas mixture and the destruction of its CFC component can be divided into two stages: an induction stage preceding the volume combustion of the mixture and the main stage in which most of the chemical energy is released and the two- or three-component mixture combusts. The durations of these characteristic combustion stages depend substantially on the energy released in the slipping surface discharge initiating combustion; both of these stages shorten with increasing energy.

A characteristic feature of the induction stage is that, near the initiator surface, a glow wave arises that propagates away from the discharge system toward the free end of the chamber. In the G_2 mode, this wave has time to reflect several times from the ends of the chamber during the induction stage. In the G_1 mode, the primary wave only has time to approach the free end during the induction stage.

The experimentally observed primary glow wave cannot be identified with a slow combustion wave or fast detonation wave described in the literature. First of all, the presence of a relatively narrow glow region adjacent to the wave front is not typical of both these waves: the chain process initiated by a combustion or detonation wave continues to develop explosively behind the front and occupies the entire region through which the wave has propagated. Moreover, the velocity of the observed primary wave is higher than that of a usual combustion wave, but much lower than the detonation wave velocity.

The next combustion stage, in which the oscillatory motion of the primary wave changes to a flare occupying the entire chamber and relatively uniform combustion of the mixture as a whole, seems to be even more unusual.

Hence, when combustion is initiated by a high-current slipping surface discharge, the ignition process in the regions far from the initiator differs substantially from ignition by a usual low-power two-electrode spark or metal filament heater. The conventional combustion dynamics described by a thermal or detonation wave propagating from the local heating (or breakdown) region of a gas changes to a complicated sequence of effects—the excitation of a glow wave propagating away from the initiator and the subsequent relatively uniform gas combustion occurring throughout the reactor volume. In this case, the primary glow wave cannot be identified as a combustion or detonation wave.

The combustion time of the gas mixture depends substantially on the energy released in the initiating discharge and decreases with increasing energy. This feature of the combustion initiated by a high-current slipping surface discharge is also interesting from a physical standpoint. This effect also offers new opportunities for applications, making it possible to influence the combustion time of the methane–oxygen mixture through the initiator parameters.

An analysis of the results obtained allows us to assume that emission from a high-current surface dis-

[1] Indeed, according to [9], under the conditions of high-temperature ignition, even a small addition of a noble gas to a methane–oxygen mixture impedes its fast ignition.

charge plays a decisive role in the observed combustion dynamics. Presumably, the intensity of this emission and its spectrum differ substantially from those of a spark, which is usually employed as an initiator of combustion in gas mixtures.

Specific features of a high-current ($I \simeq 10^2$–5×10^3 A) slipping discharge as a radiating object were previously addressed in a number of papers. In particular, in [12], it was pointed out that the emission spectrum of a slipping discharge contains a considerable fraction of relatively hard UV radiation, which ionizes the gas surrounding the discharge and produces an anomalously long-living plasma. In [13], the efficient volume decomposition of CFCs in a gas mixture (argon–CFC or air–CFC) filling the reactor was also attributed to the specific features of the slipping discharge emission resulting in photoionization, photoexcitation, and photodissociation of the gas far from the region where energy was released. In [7], UV emission from a slipping surface discharge was measured directly for the first time and it was shown that this emission was enriched with the hard component as compared to the Planckian spectrum.

The ability of a high-current surface discharge to substantially influence (through its emission) the properties of a gas medium in a volume substantially exceeding the volume occupied by the plasma can be considered one of the distinctive features of this type of gas discharge.

We may suggest that, in experiments with methane–oxygen–CFC mixtures, a high-current discharge that propagates along the surface of the discharge system and occurs over a short period of time (from tens of nanoseconds to several microseconds) not only initiates plasmochemical reactions in the immediate vicinity of the surface, but also changes the parameters of the gas medium throughout almost the entire reactor volume by irradiating the gas with UV radiation.

We note that the significant role of UV radiation in the initiation and dynamics of combustion in gas mixtures has long been known. As early as 1911, Andreev [14] revealed the chemical action of UV radiation on the water-formation reaction. In [10, 15], a number of experiments were described that demonstrated an increase in the hydrogen-oxidation reaction rate due to the dissociation of hydrogen molecules when a hydrogen–oxygen mixture was irradiated by a UV lamp. In a number of experiments, it was shown that the dissociation of hydrogen molecules (via the sensibilization mechanism) significantly accelerates the combustion of a $H_2 + O_2$ mixture.

In the relatively recent paper [16], the initiation of explosive combustion in a propane–air mixture by a CO_2 laser spark was demonstrated. The authors ascribed the effect observed to the substantial change in the original composition of a flammable gas mixture under the action of a spark.

The process of combustion acceleration by a laser spark is probably similar to the processes occurring in our experiment, in which an open (without quartz walls peculiar to UV lamps) high-power surface discharge determining the specific features of the combustion of a flammable gaseous medium was used for the first time as an irradiating source.

A hypothesized picture of physicochemical processes accompanying a high-current surface discharge in a $CH_4 + O_2$ (air) + CF_2Cl_2 mixture is described in the Appendix. Of course, the general considerations presented here and in the Appendix must be supported by a detailed theoretical analysis based on both the kinetic model and a gasdynamic model describing the specific conditions of our experiment.

We note however that even the first experiments described above are of practical importance, because they indicate the possibility of creating an efficient reactor for the utilization of ozone-destroying CFCs and also CFCs that contribute to the greenhouse effect.

Based on the results our experiments, it is easy to estimate the production rate of a reactor consisting of a discharge system (similar to that described above) that is placed in a cylindrical chamber with the cross section S and length L. To do this, we use the following simple relation:

$$\eta \approx 2 \times 10^{-7}\, p_{\mathrm{CFC}} MSL/\tau_c \text{ kg/h},$$

where p_{CFC} is the partial pressure of CFC to be decomposed (CF_2Cl_2) in torr, M is its molecular weight ($M \simeq 120$), and τ_c is the mixture combustion time in s. For $p_{\mathrm{CFC}} = 100$ torr, $S = 20$ cm^2, $L = 50$ cm, and $\tau_c = 10^{-2}$ s, we obtain

$$\eta \approx 200 \text{ kg/h}.$$

In this case, the consumed electric power will not exceed 50 W. This means that the energy cost of decomposition (related to the electric energy consumption) is approximately equal to

$$W \approx 2 \times 10^{-4} \text{ kW h/kg},$$

which is many orders of magnitude lower than that for the plasmochemical decomposition of nonflammable gas mixtures (see [1, 2]).

To ensure such a high decomposition rate, the gas flow rate through the chamber should be on the order of

$$v \approx L/\tau_c \approx 5 \times 10^3 \text{ cm/s},$$

which can be rather simply realized.

The production rate of the reactor can be controlled by varying the energy deposition in the electric discharge initiating combustion and, thereby, varying the combustion time of the gas mixture τ_c.

ACKNOWLEDGMENTS

We thank S. M. Temchin for contributing to discussions and making valuable remarks. This study was

supported in part by the Russian Foundation for Basic Research (project no. 99-02-16270) and the Netherlands Organization for Scientific Research (NWO) (project no. 047.011.000.01).

APPENDIX

The experimental data were analyzed based on the well-known physicochemical model of the explosive combustion of a methane–oxygen mixture (see [8, 11, 17]). The main point of this model is the following: when the ignition of the mixture is caused by an increase in the temperature to 400–500°C, the combustion can be divided into two stages—the so-called "cold" flame and the subsequent explosive combustion. The chain of reactions leading to explosive combustion originates in the slow endoenergy reaction [8]

$$CH_4 + O_2 \longrightarrow CH_3 + HO_2 - 2.5\ \text{eV},$$

whereas the chains of combustion reactions are formed with the participation of CH_3, OH, HCOH, and HO_2 molecules, e.g.,

$$CH_3 + O_2 \longrightarrow HCOH + OH + 1.5\ \text{eV}.$$

The guiding active particle in subsequent reactions is formaldehyde (HCOH), the accumulation of which transforms slow combustion into explosive combustion.

An analysis shows that, based on the existing models of the explosive combustion of a $CH_4 + O_2$ mixture, it is impossible to explain the relatively rapid appearance of the primary glow wave and the fact that a substantial admixture of CFC-12 (comparable with the methane and oxygen content) does not suppress the mixture ignition.

Hence, it seems reasonable to formulate a kinetic scheme of ignition of $CH_4 + O_2$ and $CH_4 + O_2 + CF_2Cl_2$ gas mixtures, taking into account the effect of the UV component of emission from the slipping surface discharge. We assume that, near the discharge system (in both the G_1 and G_2 modes), the following photoionization reactions occur [18, 19]:

$$\begin{aligned} CH_4 + \hbar\omega &\longrightarrow CH_3 + H + \Delta'_{1(T)} \\ &\longrightarrow CH_2 + H_2 + \Delta''_{1(T)} \\ &\longrightarrow CH + H_2 + H + \Delta'''_{1(T)}, \end{aligned} \quad \text{(A.1)}$$

$$\begin{aligned} O_2 + \hbar\omega &\longrightarrow O(^3P) + O(^3P) + \Delta'_{2(T)} \\ &\longrightarrow O(^3P) + O(^1D) + \Delta''_{2(T)}, \end{aligned} \quad \text{(A.2)}$$

$$\begin{aligned} CF_2Cl_2 + \hbar\omega &\longrightarrow CF_2Cl + Cl + \Delta'_{3(T)} \\ &\longrightarrow CF_2 + Cl_2 + \Delta''_{3(T)}. \end{aligned} \quad \text{(A.3)}$$

A specific feature of these reactions is that a substantial fraction of the photon energy is converted into the translational degrees of freedom of the reaction products.[2] As a result, the gas mixture is heated and the molecular states are excited via VT relaxation. At the same time, the infrared (IR) component of discharge emission provides the nonequilibrium pumping of heteronuclear molecules:

$$\begin{aligned} CH_4 + \hbar\omega &\longrightarrow CH_4^*, \\ CF_2Cl_2 + \hbar\omega &\longrightarrow CF_2Cl_2^*. \end{aligned} \quad \text{(A.4)}$$

Photodissociation and photoexcitation processes lead to the ignition of the heated gas mixture in the vicinity of the discharge according to the scheme

$$H + CH_4^* \longrightarrow H_2 + CH_3\ (\Delta_5 \Rightarrow -0.032\ \text{eV}), \quad \text{(A.5)}$$

$$H + O_2^* \longrightarrow OH + O\ (\Delta_6 \Rightarrow -0.72\ \text{eV}), \quad \text{(A.6)}$$

$$H + CF_2Cl_2 \longrightarrow HCl + CF_2Cl + 0.71\ \text{eV}, \quad \text{(A.7)}$$

$$\begin{aligned} CF_2Cl + CH_4^* &\longrightarrow CHClF_2 + CH_3 \\ &(CHClF_2 \equiv \text{CFC-22}), \end{aligned} \quad \text{(A.8)}$$

$$O + CH_4^* \longrightarrow OH + CH_3\ (\Delta_9 = -0.11\ \text{eV}), \quad \text{(A.9)}$$

$$Cl + CH_4^* \longrightarrow HCl + CH_3\ (\Delta_{10} = -0.08\ \text{eV}), \quad \text{(A.10)}$$

$$\begin{cases} CH_3 + O_2 \longrightarrow HCOH + OH + 1.52\ \text{eV} \\ \qquad (E_a = 0.8\ \text{eV}), \end{cases} \quad \text{(A.11)}$$

$$\begin{cases} OH + CH_4 \longrightarrow H_2O + CH_3 + 0.61\ \text{eV} \\ \qquad (E_a = 0.2\ \text{eV}), \end{cases} \quad \text{(A.12)}$$

$$\begin{cases} OH + CF_2Cl_2 \longrightarrow HCl + CF_2ClO, & \text{(A.13)} \\ CF_2ClO + CH_4 \longrightarrow C_2H_3F_2Cl + OH. & \text{(A.14)} \end{cases}$$

Reactions (A.11) and (A.12) correspond to the catalytic cycle of the combustion of a $CH_4 + O_2$ mixture and lead to the accumulation of HCOH and water molecules.[3] The catalytic cycle represented by reactions

[2] According to [18], for $8.9 \le \hbar\omega \le 9.5$ eV, we have $\Phi'_1 > 0.5$ and $4.4 \le \Delta'_{1(T)} \le 5.0$ eV [where Φ'_1 is the quantum yield of the first channel of reaction (A.1)]. For $\hbar\omega = \hbar\omega_{L\alpha} \Rightarrow 10.2$ eV, we have $\Delta'_{1(T)} \approx 5.69$ eV ($\Phi'_1 \approx 0.44$), $\Delta''_{1(T)} \approx 5.77$ eV ($\Phi''_1 \approx 0.50$), and $\Delta'''_{1(T)} \approx 0.27$ eV ($\Phi'''_1 \approx 0.06$). It follows from [20] that, for $5.1 \le \hbar\omega \le 7.1$ eV, we have $0 \le \Delta'_{2(T)} \le 2$ eV, whereas for $7.1 \le \hbar\omega \le 9.3$ eV, we have $0 \le \Delta''_{2(T)} \le 2.2$ eV. According to [19], for $6.1 \le \hbar\omega \le 7.3$ eV, the values of $\Delta'_{3(T)}$ and $\Delta''_{3(T)}$ fall into the intervals $2.4 \le \Delta'_{3(T)} \le 3.6$ eV and $1.25 \le \Delta''_{3(T)} \le 2.45$ eV ($0.75 \ge \Phi'_3 \ge 0.59$ and $\Phi'_3 + \Phi''_3 = 1$).

[3] The possibility of realizing the selective process of methane oxidation in reactions (A.11) and (A.12) at a high vibrational temperature of oxygen (i.e., at $T_V^{(O_2)} \gg T_g$) was discussed in [21, p. 355]. In our case, these reactions become dominant due to the excitation of vibrational degrees of freedom of the reacting particles in the primary combustion wave.

(A.13) and (A.14) demonstrates the possibility of converting CF_2Cl_2 (CFC-12) into the more stable (against photodissociation) compound $C_2H_3F_2Cl$ (HCFC-142) without suppressing the combustion of a methane–oxygen mixture. However, reactions (A.13) and (A.14) decrease the accumulation rate and quantity of the formaldehyde produced (this, in turn, may result in the additional delay of the volume combustion and a decrease in its rate). Presumably, the described processes of the photochemical action of gas-discharge plasma emission on a $CH_4 + O_2 + CF_2Cl_2$ flammable mixture determine the mechanism for the generation and maintenance of the primary glow wave.

The generation of a secondary glow wave (more precisely, the beginning of volume combustion) is associated with the accumulation of a sufficient amount of HCOH molecules and vibrationally excited molecules in the volume and at the free end of the reactor chamber. It is reasonable to assume that the accumulation is related to the oscillatory propagation of the primary glow wave or, in other words, to the treatment of the gas mixture by this wave. Here, we note that the temperature of the gas mixture is not too high and the concentration of free H, O, Cl, OH, and CH_3 radicals beyond the primary glow wave is fairly low. Otherwise, the conditions for initiating the mixture ignition outside a narrow (3–4 mm wide) combustion region would be satisfied, which contradicts the experimental data. Consequently, it is reasonable to assume that the concentration of free H, O, Cl, OH, and CH_3 radicals in the gas treated by the primary wave is low and the accumulation of HCOH cannot be suppressed by the fast reactions:

$$\begin{gathered}\mathrm{Cl + HCOH \xrightarrow{k_{15}} HCl + HCO + 0.66\ eV},\\ k_{15} = 8.1\times10^{-11}\exp(-30/T),\ \mathrm{cm^3/s}\ \ [22],\end{gathered} \tag{A.15}$$

$$\begin{gathered}\mathrm{OH + HCOH \xrightarrow{k_{16}} H_2O + HCO + 1.35\ eV},\\ k_{16} = 1.1\times10^{-11}\mathrm{cm^3/s}\ \ [22],\end{gathered} \tag{A.16}$$

$$\mathrm{O + HCOH \longrightarrow OH + HCO + 0.63\ eV}, \tag{A.17}$$

$$\mathrm{H + HCOH \longrightarrow H_2 + HCO + 0.71\ eV}, \tag{A.18}$$

$$\mathrm{CH_3 + HCOH \longrightarrow CH_4 + HCO + 0.74\ eV}. \tag{A.19}$$

Furthermore, the concentration of radicals outside the combustion region are governed by the reactions

$$\begin{gathered}\mathrm{Cl + CH_4 \xrightarrow{k_{20}} HCl + CH_3 - 0.08\ eV},\\ k_{20} = 1.1\times10^{-11}\exp(-1400/T),\ \mathrm{cm^3/s}\ \ [22]\\ (\text{for } T = 1000\ \mathrm{K}\ \text{the rate constant is}\\ k_{20}\approx 2.7\times10^{-12}\ \mathrm{cm^3/s}),\end{gathered} \tag{A.20}$$

$$\begin{gathered}\mathrm{CH_3 + O \xrightarrow{k_{21}} H + HCOH + 2.24\ eV},\\ k_{21} = 1.1\times10^{-10}\ \mathrm{cm^3/s},\end{gathered} \tag{A.21}$$

$$\begin{gathered}\mathrm{H + CH_4 \xrightarrow{k_{22}} H_2 + CH_3 - 0.032\ eV}\\ (\text{for } T = 1000\ \mathrm{K} - k_{22} \Rightarrow (3\text{–}5)\times10^{-10}\ \mathrm{cm^3/s}),\end{gathered} \tag{A.22}$$

$$\begin{gathered}\mathrm{OH + O \xrightarrow{k_{23}} O_2 + H + 0.72eV},\\ k_{23} = 2.2\times10^{-11}\exp(120/T)\ \mathrm{cm^3/s}\ [22],\end{gathered} \tag{A.23}$$

$$\mathrm{Cl + CH_3 \longrightarrow HCl + CH_2 + 0.031\ eV}, \tag{A.24}$$

$$\mathrm{O + CH_3 \longrightarrow OH + CH_2 + 0\ eV}, \tag{A.25}$$

$$\mathrm{H + CH_3 \longrightarrow H_2 + CH_2 + 0.078\ eV}, \tag{A.26}$$

$$\mathrm{OH + CH_3 \longrightarrow H_2 + HCOH + 2.32\ eV}. \tag{A.27}$$

Estimates show that, for $T = 1000$ K, the following relations hold: $5\times10^{-12} \le k_j \le 2\times10^{-10}$ cm^3/s, where $j = 17$, 18, 19, 24, 25, 26, and 27.

The primary glow wave, which heats and irradiates the free end, removes various impurities from its surface. For example, in the case of a methane–oxygen mixture, it is the original-gas molecules that should be primarily adsorbed on the cleaned active centers S_a of the surface (see [23], chapter VIII, section 2):

$$\mathrm{O_2 + S_a \rightleftharpoons (O_2S_a)}, \tag{A.28}$$

$$\mathrm{CH_4 + S_a \rightleftharpoons (CH_4S_a)}. \tag{A.29}$$

Then, the following exoenergy reactions occur with a high probability:

$$\begin{aligned}\mathrm{O_2 + (CH_4S_a)} &\longrightarrow \mathrm{H_2O + (HCOHS_a)}\\ &\longrightarrow \mathrm{H_2O + HCOH + S_a}\\ \mathrm{CH_4 + (O_2S_a)} &\longrightarrow \mathrm{HCOH + (H_2OS_a)}.\end{aligned} \tag{A.30}$$

As a result, processes (A.28)–(A.30) ensure a more intense accumulation of HCOH at the wall and in the wall region of the free end than inside the reactor. In this case, the experimentally observed effect that the secondary glow wave usually originates near the free end of the reactor chamber can be consistently explained by the kinetic model based on the following reactions:

$$\mathrm{HCOH + O_2 \longrightarrow H_2O + CO_2 + 5.33\ eV}, \tag{A.31}$$

$$\mathrm{HCOH + O \longrightarrow H_2 + CO_2 + 5.41\ eV}. \tag{A.32}$$

When describing the kinetics of the combustion of $CH_4 + O_2$ and CF_2Cl_2 mixtures initiated by emission from a slipping surface discharge, we tried to reveal the dominant mechanisms for initiating and maintaining the process under study. For this reason, reactions that are of minor importance are omitted in the kinetic scheme.

Hence, it may be suggested that the first stage of combustion is associated with the production of a flammable mixture containing formaldehyde, water vapor, and a certain amount of HCl and HCFC-142 in a narrow glow region. Outside this region, the primary glow wave, which heats and irradiates the gas with UV radiation, creates favorable conditions for transformation

reactions with low activation barriers ($E_a \le 1$ eV). This means that, in most of the volume, the vibrationally excited molecules produced (CH_4^*, HCOH*, $CF_2Cl_2^*$, etc.) accelerate both the reactions

$$\left.\begin{array}{l} CF_2Cl_2 + CH_4^* \\ CF_2Cl_2^* + CH_4 \end{array}\right\} \longrightarrow CH_3Cl + CHClF_2, \quad (A.33)$$

$$\left.\begin{array}{l} HCOH^* + CF_2Cl_2 \\ HCOH + CF_2Cl_2^* \end{array}\right\} \longrightarrow HCClO + CHClF_2 \quad (A.34)$$

(where CH_3Cl, HCClO, and $CHClF_2$ are methyl chloride, formyl chloride, and CFC-22 molecules) and the reactions revealed in [1, 2]:

$$CF_2Cl_2 + CF_2Cl_2^* \longrightarrow CF_3Cl + CFCl_3, \quad (A.35)$$

$$CF_2Cl_2 + CF_2Cl_2^* \longrightarrow CF_4 + CCl_4, \quad (A.36)$$

$$CF_2Cl_2 + CF_2Cl_2^* \longrightarrow C_2F_4Cl_2 + Cl_2, \quad (A.37)$$

$$CF_3Cl + CF_3Cl^* \longrightarrow CF_4 + CF_2Cl_2, \quad (A.38)$$

$$CFCl_3 + CFCl_3^* \longrightarrow CF_2Cl_2 + CCl_4, \quad (A.39)$$

$$CF_3Cl + CF_3Cl^* \longrightarrow C_2F_6 + Cl_2. \quad (A.40)$$

Here, $CF_3Cl \Rightarrow$ CFC-13, $CFCl_3 \Rightarrow$ CFC-11, $CF_4 \Rightarrow$ CFC-14, $C_2F_4Cl_2 \Rightarrow$ CFC-114, and $C_2F_6 \Rightarrow$ CFC-116.

The second stage of the combustion of $CH_4 + O_2 + CF_2Cl_2$ mixtures is the volume ignition of the gas treated by the primary glow wave; this process is associated with reactions (A.31) and (A.32). The second stage is characterized by a rapid growth of the temperature and intense photodissociation and thermodissociation reactions. First of all, unstable CCl_4 halocarbons and $CFCl_3$ and CF_2Cl_2 chlorofluorocarbons will be involved in the reactions of photodissociative decomposition [18, 20]:

$$CCl_4 + \hbar\omega \left\{\begin{array}{l} \longrightarrow CCl_3 + Cl \\ \longrightarrow CCl_2 + Cl_2 \\ \longrightarrow CCl + Cl_2 + Cl \end{array}\right. \text{for } \hbar\omega \ge 5.5 \text{ eV}, \quad (A.41)$$

$$CFCl_3 + \hbar\omega \left\{\begin{array}{l} \longrightarrow CFCl_2 + Cl \\ \longrightarrow CFCl + Cl_2 \end{array}\right. \text{for } \hbar\omega \ge 5.8 \text{ eV}, \quad (A.42)$$

$$CF_2Cl_2 + \hbar\omega \left\{\begin{array}{l} \longrightarrow CF_2Cl + Cl \\ \longrightarrow CF_2 + Cl_2 \end{array}\right. \text{for } \hbar\omega \ge 6.1 \text{ eV}. \quad (A.43)$$

We illustrate the thermodissociation process by the example of the decomposition of carbon tetrachloride:

$$CCl_4^* + M \longrightarrow CCl_3 + Cl + M, \quad (A.44)$$

$$CCl_3^* + M \longrightarrow CCl_2 + Cl + M, \quad (A.45)$$

$$CCl_2^* + M \longrightarrow CCl + Cl + M, \quad (A.46)$$

$$CCl^* + M \longrightarrow C + Cl + M. \quad (A.47)$$

The appearance of a large amount of radicals (Cl, CCl, C, etc.) during volume combustion can lead to the formation of Cl_2 and C_2 gas components, e.g., in the reactions

$$CCl + CCl^* \longrightarrow C_2 + Cl_2 \ (\Delta_{48} \Rightarrow 1.1 \text{ eV}), \quad (A.48)$$

$$Cl + Cl + M \longrightarrow Cl_2 + M, \quad (A.49)$$

$$C + C + M \longrightarrow C_2 + M. \quad (A.50)$$

The above said agrees with the experimental observation that, if CFC-12 is added to a methane–oxygen mixture, then both the duration and intensity of the light burst in the reactor volume decrease. Furthermore, taking into account the present-day concepts and the experimental data on the mechanisms for oxidation of hydrogen and hydrocarbons (see [11, 24]), as well as our concept of the mechanism for the combustion of $CH_4 + O_2 + CF_2Cl_2$ mixtures, it may be suggested that, at the optimum content of oxygen in a flammable gas mixture, the final products of the combustion of a methane–CFC mixture will be CFCs that are relatively stable against photodissociation (such as CFC-13, CFC-116, CFC-114, CFC-22, and CFC-14) and H_2O, CO_2, and Cl_2 molecules (the content of C_2, H_2, HCl, and other molecules in the resulting mixture will be small).

REFERENCES

1. S. I. Gritsinin, I. A. Kossyĭ, M. A. Misakyan, and V. P. Silakov, Fiz. Plazmy **23**, 264 (1997) [Plasma Phys. Rep. **23**, 242 (1997)].
2. Z. G. Akhvlediani, É. M. Barkhudarov, G. V. Gelashvili, *et al.*, Fiz. Plazmy **22**, 470 (1996) [Plasma Phys. Rep. **22**, 428 (1996)].
3. É. M. Barkhudarov, N. K. Berezhetskaya, E. F. Bol'shakov, *et al.*, Zh. Tekh. Fiz. **54**, 1219 (1984) [Sov. Phys. Tech. Phys. **29**, 701 (1984)].
4. A. M. Anpilov, E. M. Barkhudarov, N. K. Berezhetskaya, *et al.*, Plasma Sources Sci. Technol. **7**, 1 (1998).
5. N. K. Berezhetskaya, E. F. Bol'shakov, S. K. Golubev, *et al.*, Zh. Éksp. Teor. Fiz. **87**, 1926 (1984) [Sov. Phys. JETP **60**, 1108 (1984)].
6. I. A. Kossyĭ, K. V. Krasnobaev, I. V. Sokolov, and V. E. Terekhin, Kratk. Soobshch. Fiz., No. 11, 3 (1987).
7. Yu. B. Bark, E. M. Barkhudarov, Yu. N. Kozlov, *et al.*, J. Phys. D **33**, 859 (2000).
8. N. N. Semenov, *Some Problems of Chemical Kinetics and Reactivity* (Akad. Nauk SSSR, Moscow, 1958).
9. B. Lewis and G. Elbe, *Combustion, Flames, and Explosions in Gases* (Academic, New York, 1961; Mir, Moscow, 1968).
10. L. N. Khitrin, *Physics of Combustion and Explosion* (Mosk. Gos. Univ., Moscow, 1957).

11. V. S. Arutyunov and O. V. Krylov, *Oxidative Transformations of Methane* (Nauka, Moscow, 1998).
12. S. I. Gritsinin, I. A. Kossyĭ, V. P. Silakov, *et al.*, Teplofiz. Vys. Temp. **24**, 662 (1986).
13. G. A. Askar'yan, G. M. Batanov, S. I. Gritsinin, *et al.*, in *Microwave Plasma and Its Applications*, Ed. by Yu. A. Lebedev (Moscow Physical Society, Moscow, 1995), p. 24.
14. I. I. Andreev, Zh. Russ. Fiz.-Khim. Obshch. **43**, 1342 (1911).
15. A. B. Nalbandyan and V. V. Voevodskiĭ, *Mechanisms for Oxidation and Combustion of Hydrogen* (Akad. Nauk SSSR, Moscow, 1949).
16. G. I. Kozlov, V. A. Kuznetsov, and A. D. Sokurenko, Pis'ma Zh. Tekh. Fiz. **17** (11), 25 (1991) [Sov. Tech. Phys. Lett. **17**, 398 (1991)].
17. E. S. Shchetinkov, *Physics of Gas Combustion* (Nauka, Moscow, 1965).
18. H. Okabe, *Photochemistry of Small Molecules* (Wiley, New York, 1978; Mir, Moscow, 1981).
19. D. L. Baulch, R. A. Cox, P. J. Crutzen, *et al.*, J. Phys. Chem. Ref. Data **11**, 327 (1982).
20. A. M. Pravilov, in *Plasma Chemistry*, Ed. by B. M. Smirnov (Énergoatomizdat, Moscow, 1987), Vol. 14, p. 65.
21. V. D. Rusanov and A. A. Fridman, *Physics of Chemically Active Plasmas* (Nauka, Moscow, 1984).
22. É. L. Aleksandrov, Yu. A. Izraél', I. L. Karol', and A. Kh. Khrgian, *Earth's Ozone Layer and Its Variations* (Gidrometeoizdat, St. Petersburg, 1992).
23. D. I. Slovetskiĭ, *Mechanisms for Chemical Reactions in Nonequilibrium Plasmas* (Nauka, Moscow, 1980).
24. V. N. Kondrat'ev and E. E. Nikitin, *Kinetics and Mechanism of Gasophase Reactions* (Nauka, Moscow, 1974).

Translated by N. F. Larionova